Particle Type Dependence in Di-Hadron Correlations

for Identified Strange Hadrons in Heavy Ion Collisions

By
Zillay Huma Khan
B.S., University of Illinois at Chicago, 2010

Thesis submitted in partial fulfillment of the requirements
for the degree of Doctor of Philosophy in Physics
in the Graduate College of the
University of Illinois at Chicago, 2017

Chicago, Illinois

Defense Committee:

Olga Evdokimov, Chair and Advisor
David Hofman
Zhenyu Ye
Anjum Ansari, Biophysics
Adnan Chawdhry, California University of Pennsylvania

All the praises and thanks be to Allah, Lord of the worlds, The most Gracious, the most Merciful, Master of the Day of Judgement. You alone we worship and You alone we ask for help.

Al-Qur'an (Surah Fatiha: 1-4)

ACKNOWLEDGEMENTS

First and foremost, I would like to express my sincere gratitude to my advisor, Olga Evdokimov, for her enormous support, motivation, guidance and endless patience throughout the course of this work. I would also like to thank the rest of my thesis committee: David Hofman, Zhenyu Ye, Anjum Ansari, and Adnan Chawdhry for their support and kindness. I am greatly indebted to my fellow students and postdocs who were always ready and eager to help. In particular, I would like to thank my former colleague and friend Kolja Kauder, who taught me everything from Root to C++, and beyond, when I first started my research. Finally, I would like to thank my family: my husband, kids, parents and my sister, for supporting me, believing in me and for always being there for me.

TABLE OF CONTENTS

TABLE OF CONTENTS (Continued)

TABLE OF CONTENTS (Continued)

LIST OF TABLES

LIST OF FIGURES

LIST OF FIGURES (Continued)

LIST OF FIGURES (Continued)

LIST OF FIGURES (Continued)

LIST OF FIGURES (Continued)

LIST OF FIGURES (Continued)

LIST OF ABBREVIATIONS

DCA	Distance of Closest Approach
QED	Quantum Electro-Dynamics
QCD	Quantum Chromo-Dynamics
QGP	Quark Gluon Plasma
LHC	Large Hadron Collider
CERN	Conseil Européen pour la Recherche Nucléaire (European Council for Nuclear Research)
BNL	Brookhaven National Lab
RHIC	Relativistic Heavy Ion Collider
AGS	Alternating Gradient Synchrotron
SPS	Super Proton Synchrotron
LINAC	LINear ACcelerator
STAR	Solenoidal Tracker At RHIC
BRAHMS	Broad RAnge Hadron Magnetic Spectrometer
PHENIX	Pioneering High Energy Nuclear Interaction eXperiment
TPC	Time Projection Chamber

LIST OF ABBREVIATIONS (Continued)

ZDC	Zero Degree Calorimeter
TOF	Time Of Flight
EMC	Electro-Magnetic Calorimeter
FTPC	Forward Time Projection Chamber
HFT	Heavy Flavor Tracker
VPD	Vertex Position Detector
BBC	Beam-Beam Counter
MWPC	Multi-Wire Proportional Chamber
GEANT	GEometry ANd Tracking
MC	Monte Carlo
GMC	Glauber Monte Carlo
NCQ	Number of Constituent Quarks

CHAPTER 1

INTRODUCTION

The study of ultra-relativistic heavy ion physics is strongly connected to the evolution of our universe. The experiments conducted at the Relativistic Heavy Ion Collider (RHIC) are believed to create a phase of matter very much similar to the one present in early universe, right after the Big Bang [1]. Understanding how the constituents of matter react under a wide range of physical conditions, is key to understanding the origin of our universe. In contrast to the Big Bang, the strongly interacting hot and dense medium created in heavy-ion collisions, is short lived and extremely small in size; presenting daunting challenges to study such medium. During its evolution, this strongly interacting medium, known as the Quark Gluon Plasma (QGP) goes through many stages, governed by different underlying physics.

Our current understanding of the visible universe comes from the standard model which presents a comprehensive picture of how the matter in the universe is made up of. However, no one theoretical model has yet been able to successfully describe the entire dynamic evolution of QGP, although the effort to develop a “Standard Model of relativistic heavy Ion collision” is an active field of study. The work presented in this thesis was done in the field of ultra-relativistic nuclear physics. The field of Quantum Chromodynamics (QCD) describes the strong interactions between the constituents of QGP which are of primary interest in this work.

In order to be sure that a state of QGP is created, many experimental probes have been put forth and studied over the years. Signs of de-confinement can be extracted by studying

certain properties of the transverse momentum spectra and ratios of produced particles. Hadronic yields, chemical saturations and abundances can provide information on the chemical composition, size, dynamic evolution and collective flow of the medium from which they originated. This work uses strange hadrons as probes to focus on particle production mechanisms at mid transverse momentum. The goal is to use the unique properties of strange hadrons, such as, longer lifetimes, to investigate how they interact with the medium when compared to non-strange hadrons.

During an ultra-relativistic heavy-ion collision, high energy partons are produced as a result of hard scattering between the constituents of the colliding nuclei. These high energy partons lose energy and fragment into jets while travelling through the medium created. Di-hadron azimuthal correlations capture the properties of the remnants of these jets as they transpire from the medium. Azimuthal di-hadron correlations with strange hadrons are measured in this work. High energy strange hadrons, so-called trigger particles, are chosen as a representation of the jets. The direction of the trigger particles is used to identify the jet axes and the measured correlations are used to study the energy loss experienced in the medium by these jets. The measured correlations also allow us to investigate other observed phenomenon like collective flow, particle yields and particle ratios. How the measured final results of the strange particles conform or differ from their non-strange counterparts is also explored.

1.1 THE STANDARD MODEL

The Standard Model of QCD explains how the building blocks of the visible matter or the fundamental particles interact via four fundamental forces [2]. From its development in early 1970s to recent years, the Standard Model has successfully described many experimental results in high energy particle physics and had made accurate predictions about a wide variety of phenomena.

All visible, non-dark matter, which makes up a relatively small fraction of all the matter in the Universe, is made up of two types of fundamental particles, quarks and leptons. Quarks are spin-1/2 fermions with fractional electric charge (i.e. 2/3e and -1/3e), whereas leptons, like elections and neutrinos, are neutral or carry integral charge. Each of the groups of quarks and leptons consists of 6 particles and their anti-particles, divided into pairs called “generations”. All stable, visible matter in the universe is made up of the first generation of these fundamental particles. The higher generation heavy particles quickly decay into the next lighter generation. The three generations of quarks are Up and Down, Charm and Strange, and Top and Bottom. Along with the electric charge, the quarks also come in three different color charges and can only combine in two’s (quark-antiquark pairs) and three’s in such a way to form colorless hadrons, called mesons and baryons, respectively. The three generations of leptons include: electron and electron neutrino; muon and muon neutrino; and tau and tau neutrino. All the neutrinos are neutral and are very light, whereas, the electron, muon and tau have sizeable mass and carry an electric charge. **Figure 1** shows a graphic representation of the constituents of the Standard Model.

In the Standard Model, quarks and leptons interact via the exchange of various fundamental particles known as bosons. Bosons are integral spin particles, and are the carriers of the four fundamental forces described in the Standard Model as gravity, electromagnetic, weak and strong interactions. The bosons have a characteristic coupling to the charge of the respective force and the strength of the force depends on this coupling along with the mass of the carrier. Apart from gravity, which is weakest of all forces and whose mediating boson is yet to be discovered, electromagnetic interactions have the longest range and account for most extra-nuclear phenomena in physics. Both weak and strong forces are effective over a short range, ~1fm = 10^{-15}m. The carriers for electromagnetic, weak and strong forces are the massless photon, the massive Z^0 and $W^{\pm}$ bosons, and a color charge carrying boson, called gluon, respectively. At high enough energies, well over the mass scale of the Z^0 and $W^{\pm}$ bosons, the electromagnetic and weak forces combine into one 'electro-weak' interaction, i.e. have comparable strength.

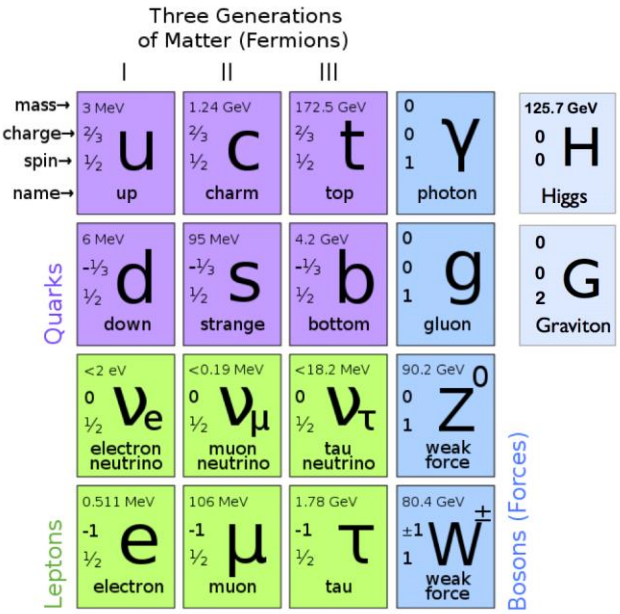

Figure 1: The graphic representation of the Standard Model of particle physics. It shows the three families of the quarks and leptons as well as the gauge bosons for the four fundamental forces.

1.2 QUANTUM CHROMODYNAMICS

Quantum Chromodynamics (QCD) is the study of strong interactions which take place between the constituent quarks that make up hadrons [2], [3]. QCD has a running coupling constant, $\alpha_s = \frac{g_s^2}{4\pi}$, (where g_s is the strong charge of quark s) which is large at low energies and small at high energies. Analogous to the photon in QED, the strong force is mediated via a neutral, massless boson, but unlike photons, the gluons carry a color charge. QCD has many of freedom, i.e. a quark can carry one of the three color charges, and an anti-quark the corresponding anti-

color. The strength of the strong coupling between quarks is independent of the color. The strong coupling constant is determined as a function of momentum transfer Q^2 and the scale dependence of the coupling at short distances or high momentum transfer is expressed as perturbative series of β-functions.

$$\beta(\alpha_s) = -(\frac{\alpha_s}{4\pi})^2 \sum_{n=0} (\frac{\alpha_s}{4\pi})^n \beta_n \qquad \textbf{Eq. 1}$$

At small distances, in the perturbative QCD, only one or two quark-anti-quark loops are dominant, hence the higher order β-terms are often not included in the perturbative calculations. The exact first order solution for the strong coupling constant is given in Eq.3, and is plotted in **Figure 2**.

$$\alpha_s(Q^2) = \frac{4\pi}{\beta_0 \ln(Q^2/\Lambda^2)} \qquad \textbf{Eq. 2}$$

where $\beta_0 = 11 - \frac{2}{3} n_f$; n_f the number of quark flavors with $m_q^2 << Q^2$, and $\Lambda^2 \equiv \mu^2 \exp(-\frac{4\pi}{\beta_0 \alpha_s(\mu^2)})$ with Λ being the QCD scale parameter. Λ is determined by non-perturbative calculations or actual measurements.

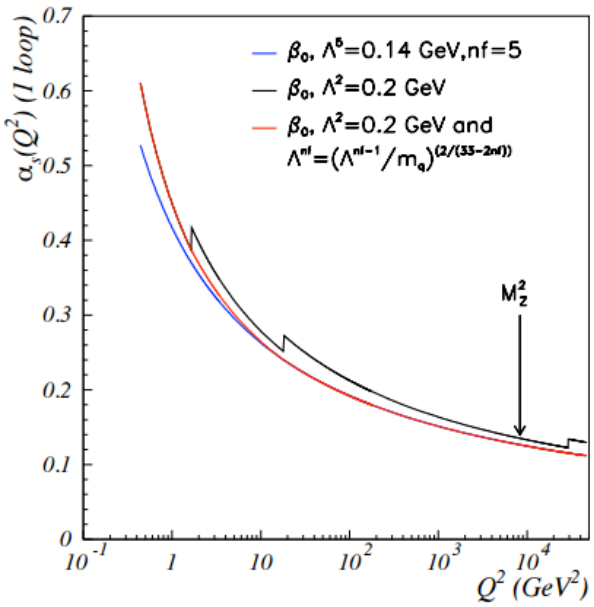

Figure 2: (Taken from [4]) The first order running coupling constant for number of active quark flavors $n_f = 5$ where Λ^5 was adjusted to match data, is plotted in blue. The red curve corrects for the effect of quarks becoming active, i.e. when $m_q^2 << Q^2$ (black curve). The arrow shows the experimental coupling value at $Q^2 = M_Z^2$ (M_z^2=Mass of the z-boson)

Having a running coupling constant and a color charge carrying mediator gives rise to unique phenomena, like confinement and asymptotic freedom. Confinement means that color charged objects can only be found in the form of color-neutral hadrons. Potential between two quarks as a function of the distance between them *r*, can be described as:

$$V_s = -\frac{4}{3}\frac{\alpha_s}{r} + kr \quad , \qquad \textbf{Eq. 3}$$

where, α_s is the strong coupling constant, and the second linear term is associated with confinement. In QCD color lines of force between quarks are pulled in form of flux tubes or strings and the term *kr* (k being the spring constant) gives the potential energy stored in those strings. When the quarks are pulled apart to large distances, the potential energy eventually reaches a point where it is energetically more favorable to produce a quark-anti-quark ($q\bar{q}$) pair.

The asymptotic freedom can be thought of as the 'flip side' of confinement, as it explains how the strong force behaves at very short distances. David Gross, while recalling about the discovery of asymptotic freedom wrote "If we were to heat the world to a temperature of a few hundred MeV, hadrons would melt into a plasma of liberated quarks and gluons" [5].

1.2.1 QCD Phase Diagram

An analytical study of QCD is only possible in certain limits, such as high values of temperature and/or baryo-chemical potential μ_B, at short distances, where QCD dynamics are dominant due to the asymptotic freedom [6]. The lattice approach has proven to be a powerful tool in studying the QCD thermodynamics, and is being vigorously pursued especially in the most interesting experimental regions, where the thermodynamic variables T and μ_B are of the order of the confinement scale Λ_{QCD} ~ 1fm^{-1}.

Figure 3 shows the QCD phase diagram. The region of interest, currently accessible through ultra-relativistic heavy ion collisions, is at high temperature and low μ_B. Lattice and some model calculations, incorporating three flavors of quarks; two light (up and down) and one heavier (strange); show that the transition begins as a crossover at μ_B=0 and changes to a first order transition for higher μ_B. The point where the first order transition line ends is known as the

critical point. Its exact location on the phase transition line is still unknown and the order of transition at the critical point is still unclear. Lattice QCD results predict that the critical point where the hadron gas changes into QGP occurs at temperature T_c = 160-170 MeV for μ_B=0.

The region of interest in this work is at low μ_B and high temperature in the QCD phase diagram where two states of matter coexist along the transition line, hadron gas for lower T and quark gluon plasma for higher T. Since this region is found to be accessible through heavy ion collision experiments, it is expected that these collisions encompass the phase transition of QGP into the hadron gas.

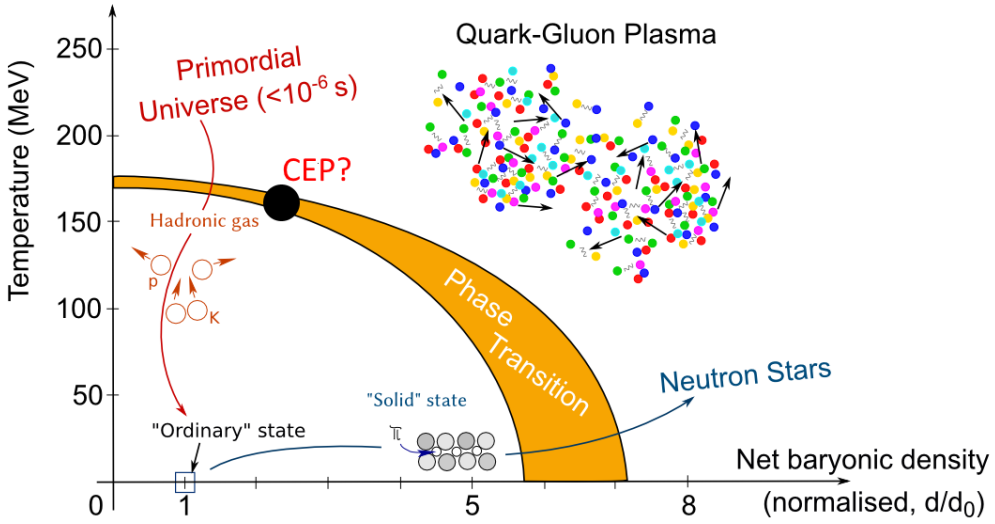

Figure 3: A contemporary sketch of the QCD phase diagram

1.3 HEAVY ION COLLISIONS AND THE CREATION OF QGP

The prime goal of the ultra-relativistic heavy ion collisions is to explore the QCD phase diagram and the properties of the state of matter created under extreme conditions of high density and temperature, known as QGP. Critical temperature of 173 ± 8 MeV, corresponding to a critical energy density of 0.6 ± 0.3 GeV/ fm^3, is needed for de-confinement as predicted by the lattice gauge theory for two-flavor QCD. A comparison of theoretical results and energy densities expected in ultra-relativistic heavy ion collisions have shown that these collisions provide conditions sufficient to produce matter in a de-confined state of quarks and gluons [7]. The initial conditions required to achieve de-confinement come from lattice QCD calculations and Monte-Carlo simulations. The energy density of gluons; the most prominent constituent of QGP; scales with the fourth power of temperature by the number of degrees of freedom. Various lattice gauge theory calculations predict (**Figure 4**) an abrupt increase in the energy density around the critical temperature which is indicative of a system with phase transition. At temperatures less than T_c, quarks and gluons are bound in hadrons, but at temperatures greater than T_c, larger degrees of freedom implies that the system exists in a QGP state, where quarks are gluons can travel a distance larger than the size of a typical nucleus. The saturation of the energy density at higher temperature occurs at the significantly lower value than that of calculation based on Stefan-Boltzmann limit for ideal gas. This change show the presence of strong interactions between the quarks and gluon in the QGP phase [8].

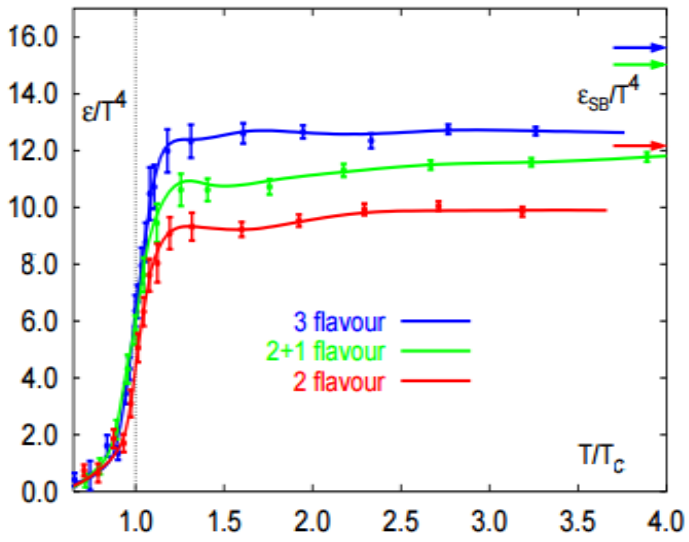

Figure 4: (Taken from [7]) Lattice gauge theory calculations for different number of flavors is shown. Energy density scaled by the fourth power of temperature is plotted versus temperature scaled by the critical temperature. The arrows indicate the ideal gas results.

In experiments, initial energy density for heavy ion collisions could be estimated from the measured transverse energy [7], [9]. An estimate of thermalization time required for such a calculation is derived using various theoretical models. Initial temperatures reached in Au+Au collisions at RHIC are estimated to be around 210-600 MeV exceeding the critical value. To acquire a state of QGP, a thermal equilibrium within the constituents along with a high energy density is required. Assuming the thermal nature of the medium is conserved through hadronization, the final state particles should provide useful tools to probe such medium.

From the creation of QGP to the final state particles, the system goes through a number of phases as shown in **Figure 5**. The initial hard scattering between the constituents of the

incoming nucleons result in the creation of the QGP which reaches local equilibrium and lives for about 1-10 fm/c (about 10^{-22} s) [10], [11]. As the system expands and cools down it reaches temperatures and densities where partonic interactions no longer exist. This stage is known as hadronization and occurs at the point in the evolution called the chemical freeze-out. The final hadron fractions are determined at this point and their relative abundances can no longer change. The system further expands and cools down and reaches the stage called thermal freeze-out, when the all the hadronic collisions stop and the produced hadrons acquire their final momenta. Production mechanism and interaction time within the medium dictate how the measured final state particles get affected by the various phases during the evolution of the collision fireball.

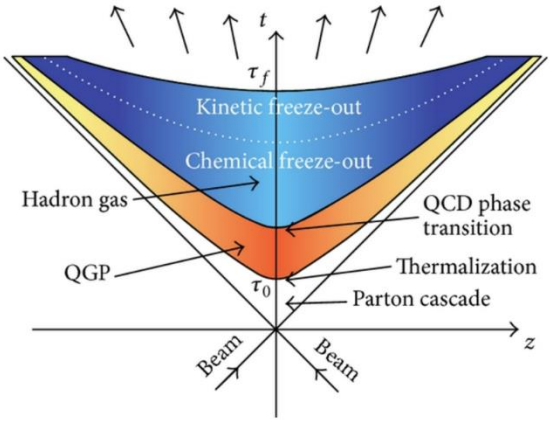

Figure 5: Schematic space-time view of heavy ion collision, showing the basic stages in the evolution of the collision fireball.

CHAPTER 2

HEAVY ION COLLISIONS

One of the goal of heavy-ion collisions is to understand the dynamics and evolution of the state of matter created under extreme conditions. To study this short lived, primordial soup of quarks and gluons (QGP) created under extreme conditions of high density and temperature, we need well-defined measurable probes, ideally from the earliest times of the collision, having maximum possible interaction with the medium. The effects of interaction with the medium must be quantifiable so that they can shed light on the properties of the medium created.

Conducting heavy-ion collisions is a massive and complex task and needs special laboratories capable of accelerating heavy ions to extremely high energy and colliding them. Currently two facilities are running heavy-ion collision experiments, Large Hadron Collider (LHC) at CERN and Relativistic Heavy Ion Collider (RHIC) at Brookhaven National Lab (BNL). In this work data from Au+Au collisions at energies 200 GeV per nucleon, collected at RHIC during run year 2011, is used. Details about the experimental facilities are discussed in Chapter 3 and data selection is further described in Chapter 4.

2.1 KINEMATIC VARIABLES

In heavy-ion collisions, origin, momentum, and charge of the measured particles are the main observables. Cartesian coordinates are used to describe the position in the lab frame and by convention the direction along the beam pipe is taken as the z-axis. The position where collision occurs and most particles originate from is called the *primary* vertex, and its position is

given as V_x, V_y and V_z. Many particles decay into other particles within the detectors and the position of this secondary decay is referred to as the *secondary* vertex. Secondary vertices corresponding to neutral particle decays are sometimes called V^0 (0 referring to zero charge).

In relativistic heavy-ion collision it is convenient to use kinematic variables that are boost invariant. One such variable is the transverse momentum, defined as:

$$p_T \equiv \sqrt{p_x^2 + p_y^2}\,. \qquad \textbf{Eq. 4}$$

In relativistic kinematics, energy and momentum of a particle with mass *m*, form the 4-vector momentum $p = (E, p_x, p_y, p_z)$, and the velocity of the particle is given by $\beta = \frac{\vec{p}}{E}$. The polar angle θ, and the momentum in the z-direction are not boost invariant hence it is convenient to use a variable known as rapidity,

$$y \equiv \frac{1}{2}\ln\frac{E + p_z}{E - p_z}. \qquad \textbf{Eq. 5}$$

Rapidity is a useful variables because it is additive under boosts in the z-direction i.e. rapidity of a particle in frame moving with respect to an inertial frame is simply *y+dy*, where *y* and *dy* are the particle's rapidities in the inertial and moving frames, respectively. Rapidity is related to the polar angle θ as follows:

$$y = \frac{1}{2}\ln\frac{\sqrt{m^2 + p^2} + p\cos\theta}{\sqrt{m^2 + p^2} - p\cos\theta}. \qquad \textbf{Eq. 6}$$

At very high energies, *p>>m*, equation 2.3 can be written as:

$$y = \frac{1}{2}\ln\frac{p + p\cos\theta}{p - p\cos\theta} = -\ln\tan\frac{\theta}{2} \equiv \eta\,, \qquad \textbf{Eq. 7}$$

where, η is called pseudo-rapidity. In ultra-relativistic high-energy experiments, pseudo-rapidity serves as an extremely useful variable in cases where the mass or momentum of the particle is not known. Relationship between the pseudo-rapidity and the polar angle are shown in **Figure 6**. The azimuthal direction is properly defined as:

$$\phi \equiv \tan^{-1}\frac{p_y}{p_z}\,, \qquad \textbf{Eq. 8}$$

And the Lorentz invariant differential yield is given by:

$$E\frac{d^3N}{d^3p} = E\frac{d^3N}{d^2p_T dp_z} = \frac{d^3N}{d^2p_T dy}\,, \qquad \textbf{Eq. 9}$$

where, $dy = {}^{dp_z}\!/_{E}$.

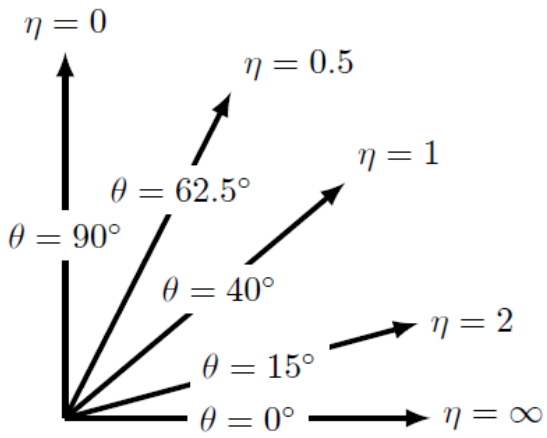

Figure 6: Representation of the relationship between pseudo-rapidity η and polar angle θ.

2.2 CENTRALITY

The nuclei colliding in a heavy ion collision create a range of systems depending on their impact parameter, i.e. the degree of overlap between the two nuclei. This impact parameter, b, is commonly referred to as a measure of the centrality of the collision. Collisions with the maximum overlap (small b) are called *central* collisions, whereas, collisions in which the incoming nuclei barely glance each other (large b) are called *peripheral* collisions. A perfectly head-on collision (most central) would correspond to the impact parameter of b = 0. Systems created in a central versus a peripheral collision can be very different. Higher multiplicities are expected in central collisions which can lead to the creation of QGP. Not all nucleon present in the colliding nuclei may take part in the collision. Each nucleon that take part in the collision is called a *participating* nucleon and each such collision is called a *binary* collision. The number of participating nucleon (N_{part}) and the number of binary collisions (N_{coll}) are estimated using the Glauber model.

2.2.1. The Glauber Model

Thousands of particles are produced in an ultra-relativistic heavy-ion collisions and hence present a much more complex picture when compared to a simpler collision system like proton-proton collision. Given the small length scales involved, a direct observation of the geometrical parameters, such as impact parameter (b), number of participating nucleons, and binary nucleon-nucleon collisions is not possible. The theoretical technique commonly used to calculate these parameter, is known as the Glauber Model, which uses the quantum mechanical scattering

theory to describe complex collision systems, such as nucleus-nucleus (A+B) or proton-nucleus (p+A).

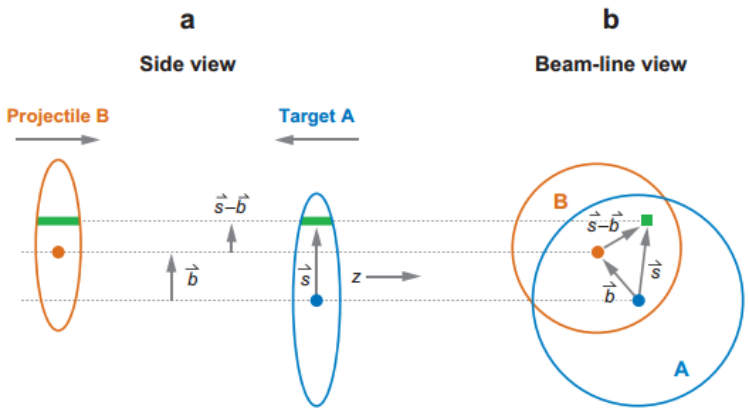

Figure 7: (Taken from [12]) Transverse (a), Longitudinal (b) views of the schematic representation of the Optical Glauber model.

With the assumption that the nucleons have independent linear trajectories, the Galuber model describes a nucleus-nucleus interaction cross section in terms of the basic nucleon-nucleon cross section. In the Optical Limit approximation of the Glauber model, the geometrical parameters are calculated using the probabilities of finding nucleons in the overlap region (**Figure 7**). On the other hand, the Glauber Monte Carlo (GMC) approach, where the two colliding nuclei are assembled by a computer as a three dimensional collection of independent nucleons distributed by their respective nuclear densities (**Figure 8**), and several simulated collisions are used to calculate the geometrical parameters.

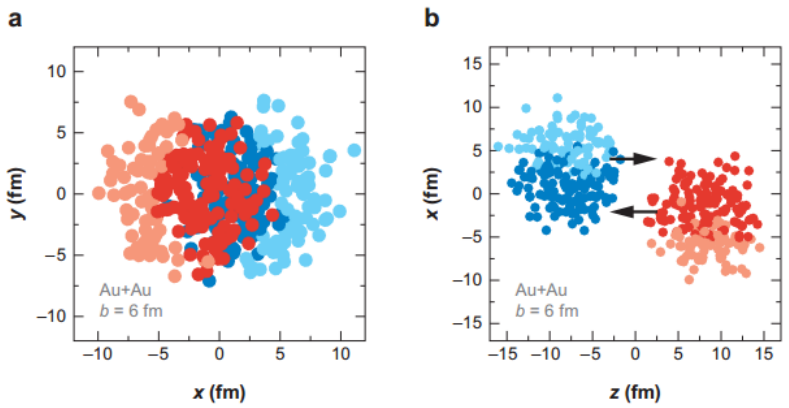

Figure 8: (Taken from **[12]**) A Galuber Monte Carlo event simulated for Au+Au at $\sqrt{s_{NN}} = 200$ GeV with impact parameter b = 6 fm is shown a) in the transverse plane, b) along the beam axis. The participating nucleons are shown as darker circles.

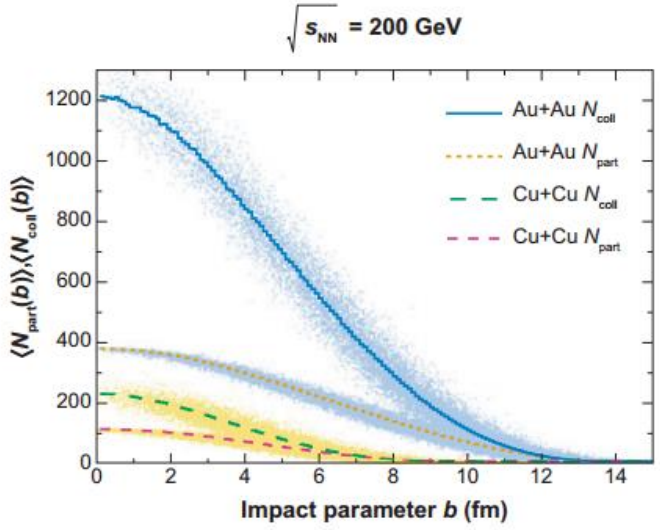

Figure 9: (Taken from **[12]**) Glauber calculated N_{part} and N_{coll} for Au+Au at 200 GeV, along with the event-by-event fluctuations as a function of the impact parameter b.

Figure 9 shows average number of participants, $<N_{part}>$ and binary nucleon-nucleon collisions $<N_{coll}>$ as a function of the impact parameter (b) calculated by the Glauber Monte Carlo, along with the event-by-event fluctuations illustrated by the scatter plots. Unfortunately, these calculated geometric quantities, N_{part} and N_{coll}, cannot be directly measured in experiments. Centrality classes are defined for both measured and calculated distributions, using N_{part} and impact parameter from Glauber Monte Carlo and the total charged particle (N_{ch}) multiplicities measured in the experiments. N_{ch} is measured using a variety of different methods by different detector systems, e.g in STAR TPC N_{ch} is measured by counting charged tracks while in other detectors it can be estimated by dividing the total energy deposited in the detector by energy deposition per charged particle. Larger charged multiplicities and small number of non-participating (spectator) nucleons are expected for central events. Correspondingly, for peripheral collisions, multiplicities at mid-rapidity are expected to be small with a large number of spectator nucleons. **Figure 10** shows an illustrated correlation of the calculated and measured quantities, identifying the typical centrality binning by the dashed lines.

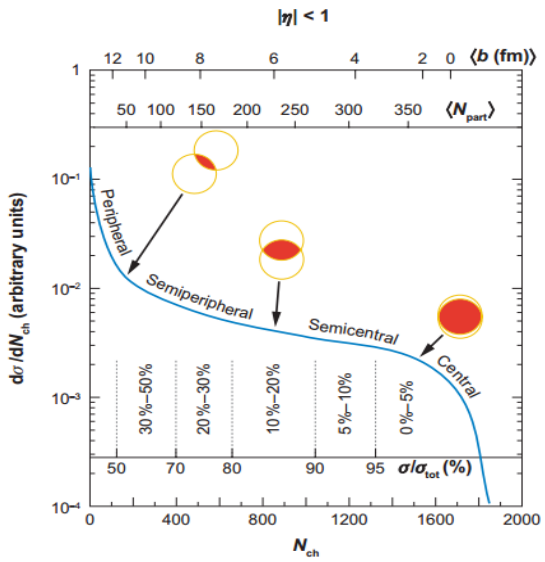

Figure 10: (Taken from **[12]**) An illustrated example of the Correlation of measured charged multiplicity with the calculated impact parameter b, and N_{part} is plotted for mid-rapidity.

The top 5% of the total multiplicity events correspond to the 0-5% most central events, similarly the next 5% events correspond to 5-10% most central events, and so on. Often after the first two most central bins, the rest of the distribution is divided into increments of 10% events, referring to 10-20%, 20-30%, 30-40%, 40-50%, 50-60%, 60-70% and 70-80% most central events. Centrality bins are often added to tackle issues relating to low statistics or per some analysis specific needs. In this work, three centrality bins are studied, namely 0-20%, 20-40% and 40-80%, mainly due to the limited statistic in peripheral events. Details on event selection and choses centrality definitions for the work presented here are presented in Chapter 4.

2.3 Temperature and Energy Density

Energy density of the system created in ultra-relativistic heavy ion collisions cannot be measured directly, hence it is estimated from the properties of the particles detected. The initial energy density is estimated using the Bjorkens formula [13]:

$$\varepsilon = \frac{1}{\pi R^2 \tau} \frac{d\langle E_T \rangle}{dy} \qquad \textbf{Eq. 10}$$

where *R* is the radius of the overlap region between the colliding nuclei and τ is the formation time. Total multiplicity measured in a Au+Au collision at RHIC for the 5% most central collisions is about 7000 particles. Using the measured multiplicities at mid-rapidity, the initial energy density is estimated to be around 5-15 GeV/fm^3 [14]. Assuming the formation time to be on the order of 1fm/c the energy density is found to be ~5 GeV/fm3 which is a factor of 5 times higher than the energy density of QGP predicted by lattice QCD [13]. Initial temperature corresponding to the estimated energy density is found to be about 240-320 MeV for top RHIC energy, using lattice QCD calculations. **Figure 11** shows the measured energy densities for different collision energies at RHIC as a function of N_{par}. It can be seen that the energy density increases with both increasing centrality and system energy and for more central collisions is well above the critical density of 1 GeV/fm predicted for phase transition [15].

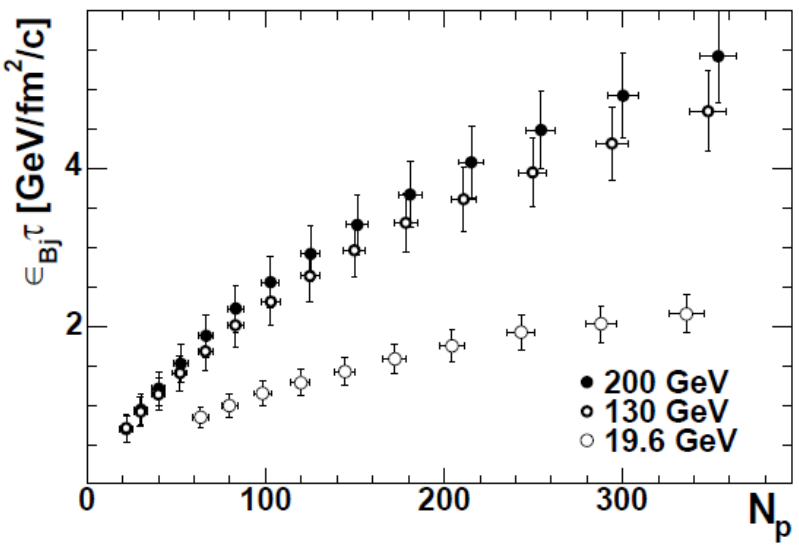

Figure 11: (Taken from **[15]** Product of energy density and the formation time calculated form PHENIX data at RHIC for three different energies as a function of the number of participating nucleons.

The extremely dense and hot system expands and hadronizes and the final hadron yields can be described statistically by the following equation [14]:

$$n_i = \frac{N_i}{V} = \frac{g_i}{2\pi^2}\int_0^\infty \frac{p^2 dp}{\exp[(E_i - \mu_i)/T] \pm 1} \qquad \textbf{Eq. 11}$$

where N_i is the total number of hadrons for the species *i*, gi is the spin degeneration factor, E_i is the total energy, μ_i is the chemical potential, *V* is the total volume and positive and negative signs in the denominator are used for fermions and bosons respectively. Assuming zero total strangeness and isospin of the system and using $\mu_i = \mu_b$, where μ_b is the baryonic chemical potential, hadron yield ratios can be predicted using the chemical freeze-out temperature and

the baryonic potential. **Figure 12** shows statistical model predictions for full equilibrium of strange particles and agrees very well with particle yields measured at mid-rapidity in heavy ion data at $\sqrt{s_{NN}}$ = 200 GeV. The freeze-out temperature and baryonic potential at RHIC extracted from these fits is ~160 MeV and ~20 MeV respectively.

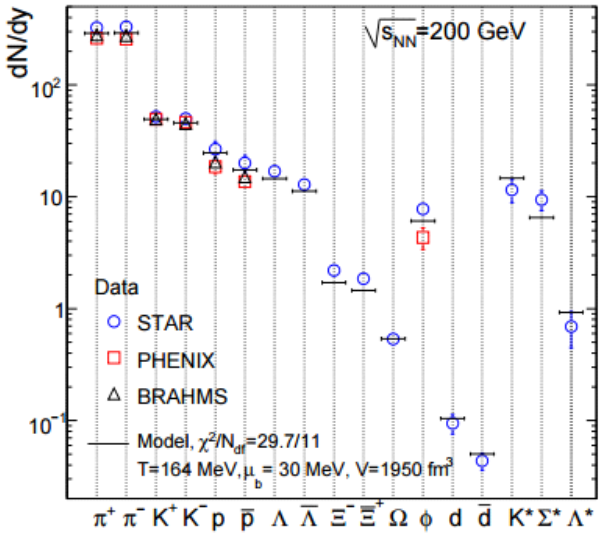

Figure 12: (Taken from **[16]**) Statistical model fits for measured particle yields at mid-rapidity for Au+Au collisions at $\sqrt{s_{NN}}$ = 200 GeV

2.4 BULK PROPERTIES

2.4.1 Collective flow

The bulk QGP matter produced in the heavy ion collisions is often termed as the collision "fireball" which quickly expands and cools down and evolves into the final state hadrons detected by the experiment. In heavy-ion collision, transverse flow (flow perpendicular to the beam direction) builds up in response to the pressure gradients in the initial state due to the asymmetric overlap region of the colliding nuclei (**Figure 13**). Early in the mid-1990's when transverse flow was first observed, theoretical advancements were made in the field of relativistic ideal fluid dynamics to explain the data [17].

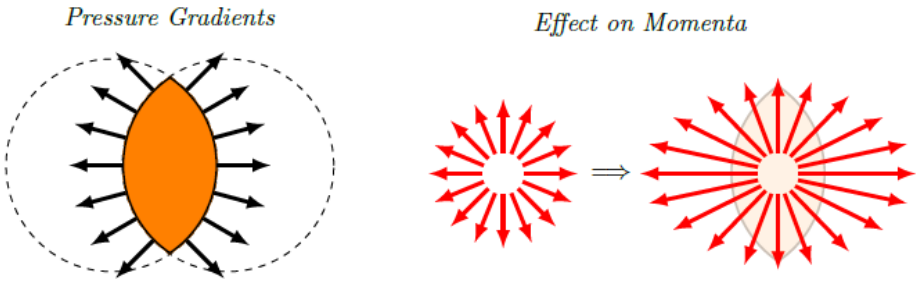

Figure 13: (Taken from **[18]**) Illustration of the initial pressure gradient created in non-central collisions translated into the final state momentum anisotropy.

2.4.1.1 Elliptic Flow

In non-central heavy-ion collisions, the spatial distribution of the nucleons is not symmetric and resembles an elliptic shape due to the overlap region of the colliding nuclei. Initial hard scattering in this asymmetrical initial geometry is translated into the final state anisotropy in the transverse momentum distribution.

Particle yields produced in a heavy ion collision with respect to the reaction plane, plane is defined by the beam direction and the impact parameter, can be described as [19]:

$$\frac{d^3N}{dp_t^2 d\phi dy} = \frac{d^2N}{2\pi dp_t^2 dy}[1 + 2\sum_n v_n \cos(n(\phi - \Psi_R))], \qquad \textbf{Eq. 12}$$

where p_T, ϕ, y are the transverse momentum, azimuthal angle and rapidity of the particle and Ψ_R is the reaction plane angle (**Figure 14**). The reaction plane changes event-by-event. The coefficients in the Fourier series describe the anisotropy observed in the final momentum-space distribution. The first and second coefficients in this series (v_1, v_2) are commonly referred to as "directed flow" and "elliptic flow".

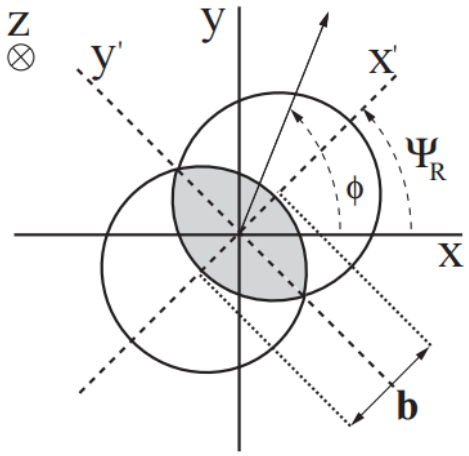

Figure 14: (Taken from **[19]**) Schematic view of nucleus-nucleus collision in the transverse plane

The elliptic flow measured in the heavy ion collisions serves as one of the key observables to compare with the hydrodynamic predictions (**Figure 15**). Despite over-predicting the data by about 50% at higher energy, the ideal fluid dynamics was able to explain the production of particles at lower momenta very well [17].

The fact that the anisotropies survive in the final state suggest that the medium created after the initial collision quickly acquired local thermal equilibrium and a pressure gradient was formed early on in the collision. In order to reproduce the elliptic flow measurements at RHIC, a small thermalization time 0.6-1.0 fm/c is required by the hydro-dynamical models [20]. Since the spatial asymmetry dissipates quickly, a small thermalization time means that the pressure gradient would be largest in the shortest direction resulting in higher momenta in that direction. A small thermalization time would also reflects into small viscosity, since the viscosity of a fluid is the measure of its ability to reach a local thermal equilibrium.

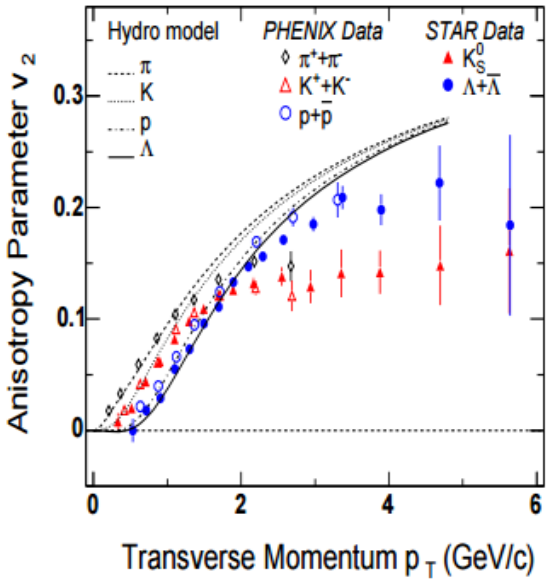

Figure 15: Measurements of elliptic flow v_2, taken at STAR and PHENIX for different particle species compared with hydrodynamic flow predictions **[21]**.

The degree to which the ideal hydrodynamics was able to reproduce experimental results led to the conclusion that the QGP does in fact flows like a viscous liquid and the early success of ideal fluid dynamics also suggested that the viscosity must be very small. A hybrid theoretical approach was introduced to incorporate two separate phases of the fireball evolution combining a viscous hydrodynamics with a microscopic description of the hadronic phase. Theoretical model prediction put a lower limit of $1/4\pi$ for the sheer viscosity divided by the entropy density, η/s, of the QGP.

2.4.1.2 Higher Order Flow Harmonics

Theoretically, in heavy-ion collisions, initial state of the incoming nuclei is often demonstrated by two different theoretical models [10]. The Monte Carlo Glauber model, discussed in Section 2.2.1. The Glauber Model, where the nucleons are treated as a collection of independent particles and are positioned in the colliding nuclei according the measured nuclear density distribution. According to the Monte Carlo Kharzeev-Levin-Nardi (MC-KLN) model, at high energy, the gluon density saturates and the gluons form a coherent state similar to a Bose condensate, known as the Color Glass Condensate [17], [13], [22]. In both models, the initial state transverse position of the nucleons inside the colliding nuclei does not follow a smooth distribution and the initial shape of the overlap region experiences event-by-event fluctuations. **Figure 16** shows a MC Glauber model simulation of a mid-central collision illustrating the fluctuating initial shape. These fluctuations give rise to a non-uniform initial overlap shape, translating into non-zero higher order terms in the Fourier series and are characterized by the eccentricity (ε):

$$\varepsilon \equiv \frac{\sum y_i'^2 - \sum x_i'^2}{\sum y_i'^2 + \sum x_i'^2} \qquad \textbf{Eq. 13}$$

where, x_i' and y_i' are the coordinates (see **Figure 14**) of the nucleons in the transverse plane (perpendicular to the beam axis) and x' is in the reaction plane.

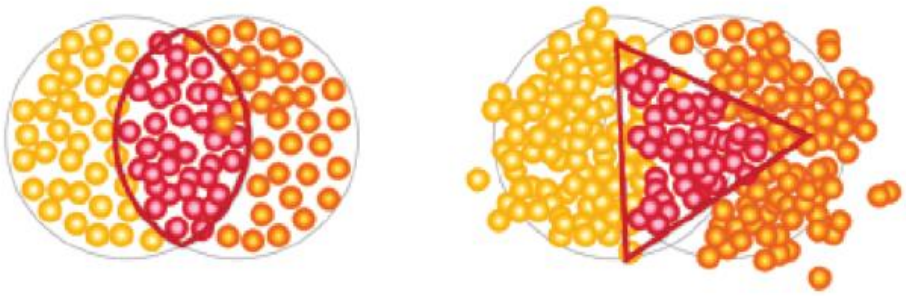

Figure 16: (Taken from **[18]**) MC Glauber simulation for a mid-central collision. Event-by-event fluctuations in the initial state give rise to elliptic (left) or triangular (right) flow patterns.

Eccentricity ε is the driving force behind the elliptic flow and quantifies the centrality dependent aspect of v_2. A ratio of elliptic flow over eccentricity, v_2/ε, essentially removes any geometrical aspects such as initial conditions, or different experimental methods used to calculate v_2, which could have an effect on the eccentricity, and only depends on the specific sheer viscosity of the QGP $(\eta/s)_{QGP}$. **Figure 17** plots this ratio as a function of charged hadron multiplicity density per unit overlap area. Different initialization models were used for the left and right plots, and since the difference in eccentricity calculated by these models differ by about 20%, the estimated value for the specific viscosity differs by a factor of about 2-2.5 [17]. The theoretical curves are calculated using VISHNU hybrid model which uses temperature independent specific sheer viscosity of QGP as an input and agrees well with the centrality dependence of the measured data.

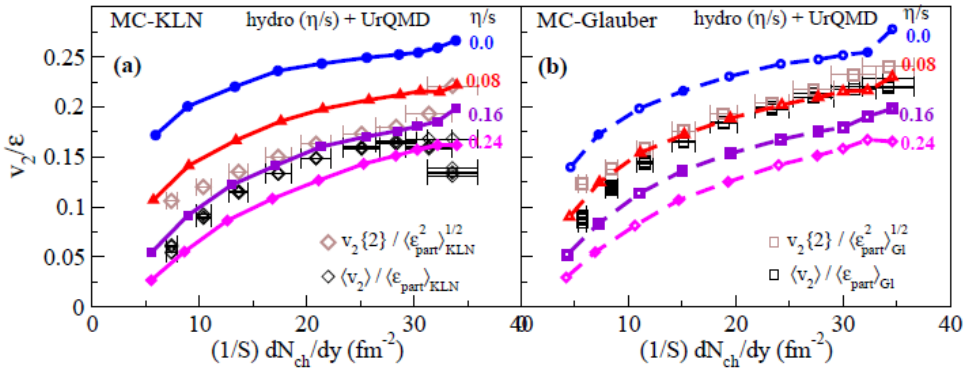

Figure 17: (Taken from **[17]**) Elliptic flow scaled by eccentricity is plotted from 200 GeV Au+Au collisions at RHIC as a function of total charged multiplicity density per unit overlap area. Both panels use the same data set but different initialization models. Theoretical curves are calculated with the VISHNU model using different specific sheer viscosity values, printed on the right of the curves.

2.4.2 Strangeness Enhancement

It has been suggested that an enhanced production of strange particles in heavy-ion collisions compared to elementary collisions could be taken as a signature of QGP creation [16], [23]. This prediction relied on two important points, a) the production threshold and b) equilibration timescales being substantially smaller in QGP than in hadron gas. In QGP the strange-anti-strange pair could be produced via gluon or light quark fusion. **Figure 18** shows the Feynman diagrams for such processes.

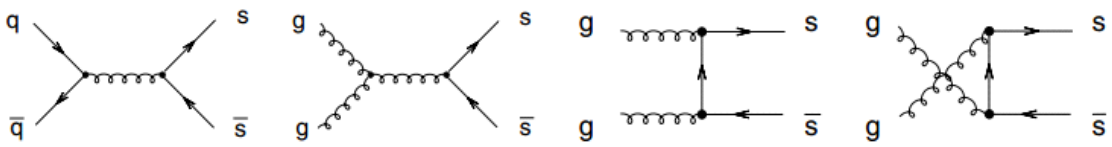

Figure 18: (Taken form **[23]**) Feynman diagrams for perturbative QCD for the production of strange-anti-strange quarks

Eq. 14 and Eq. 15 describe the production processes of strange quarks in QGP and hadron gas, respective, along with the threshold energies. It can be noted that a much larger energy is required to produce strange hadron via associated process in hadron gas.

$g + g \leftrightarrow s + \bar{s}$; $q + \bar{q} \leftrightarrow s + \bar{s}$ ($Q_{QGP} = 2m_s \approx 200$ MeV), **Eq. 14**

$N + N \rightarrow N + \Lambda + K$ ($Q_{ass.} = m_\Lambda + m_K - m_N \approx 670$ MeV), **Eq. 15**

Strangeness enhancement is measured by comparing strange hadron production in different system sizes, e.g. Pb+Pb and p+Be or Au+Au and p+p. The strangeness enhancement factor is defined as follows:

$$E_S = \left(\frac{1}{\langle N_{part} \rangle} \frac{dN(Pb+Pb)}{dy}\Big|_{y=0} \right) / \left(\frac{1}{2} \frac{dN(p+p(Be))}{dy}\Big|_{y=0} \right) \quad \textbf{Eq. 16}$$

Where the average number of participating nucleons, $\langle N_{part} \rangle$ is calculated using the Glauber model. It has been found that the strangeness enhancement increases with the strangeness content and decreases with increasing energy (**Figure 19**). It can also be seen that the

enhancement of baryons is higher than mesons and a larger baryon enhancement is observed at lower energies [16].

Strangeness enhancement can already be seen while comparing p+p collisions to p+A collisions, which shows that multiple hard scattering or the formation of hadron resonance gas can also be the source of this enhancement [16]. Canonical models suggest that for smaller systems, Npart < 50, strangeness production is suppressed due to small effective volume. Moreover, some statistical models predict that large enough volumes needed for equilibration of strangeness production are created for Npart > 50. Thermal model fit performed on experimental data estimates that strangeness suppression due to volume effects is no longer present for Npart = 100, hinting that any enhancement after this point may be coming from a deconfined medium. **Figure 20** shows the measurements from STAR and NA57 experiments at $\sqrt{S_{NN}} = 200$ GeV and $\sqrt{S_{NN}} = 17.3$ GeV, respectively. Contrary to predictions from statistical models of a saturation, a steady enhancement of strange hadrons production is observed with increasing N_{part} and increasing strangeness content, which could mean that the multi-strange particles are not fully equilibrated even for the most central events [16]. Further investigation of strange hadron production is needed to understand how much of the strangeness enhancement observed can indeed be attributed to the formation of QGP.

Although, strangeness enhancement has been established experimentally, recent developments in theoretical models, i.e. other explanations for the enhancement not necessarily involving the QGP formation, and some observations in heavy ion collisions, such as strange-non-strange particle ratios, energy and centrality dependence of strangeness enhancement, particle

yields and elliptic flow of strange particles at intermediate p_T, etc. have initiated new debate on the importance of studying strange hadrons in heavy ion collisions.

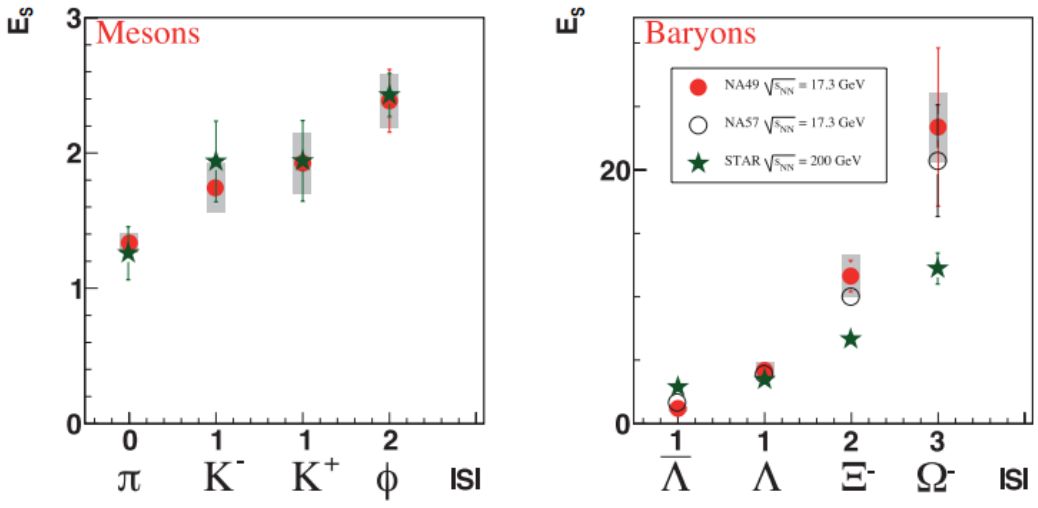

Figure 19: (Taken from **[16]**) The enhancement of strange particles as a function of number of valence quark for mesons and baryons for Pb+Pb at $\sqrt{S_{NN}} = 17.3$ GeV and Au+Au at $\sqrt{S_{NN}} = 200$ GeV. Experiments NA49 and STAR used p+p collisions, whereas experiment NA57 used p+Be collisions as reference to calculate E_s.

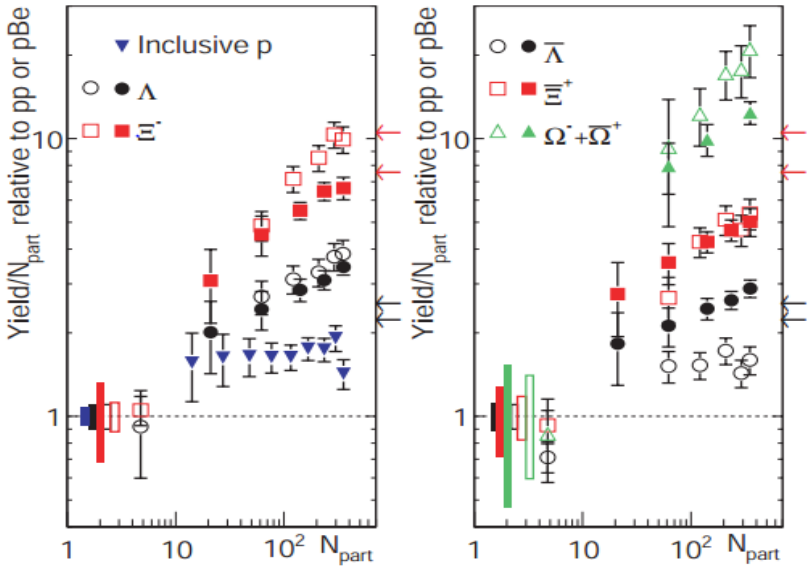

Figure 20: (Taken from **[16]**) The enhancement of inclusive protons and various strange hadrons around mid-rapidity is plotted. The boxes around 1 show the combined statistical and systematical errors in the reference systems (p+p or p+Be). The arrows (red corresponding to $\Xi^-(\bar{\Xi}^+)$ and black corresponding to $\Lambda(\bar{\Lambda})$) mark statistical predictions for temperatures T_{ch}=165 MeV and T_{ch}=170 MeV.

2.5 PARTICLE PRODUCTION IN QGP

Over the years, the results from heavy ion collisions have triggered new and important advances on the theoretical front to explain the properties of the strongly interacting matter produced and the propagation of partons through that medium [24]. The lattice QCD with its analytical limitation in the non-perturbative regime must be supplemented by various other models to describe the evolution of heavy ion collisions.

2.5.1 Strange Hadron Production

There are mainly two types of theoretical models that are used to describe the strangeness production in heavy ion collision, i.e. Transport models and Statistical models. Transport models such as Ultra-relativistic Quantum Molecular Dynamics (UrQMD), Relativistic Quantum Molecular Dynamics (RQMD), Hadron-String Dynamics (HSD), A-Multi-Phase-Transport (AMPT), are based on hadronic degrees of freedom and hence are used to provide a baseline for strangeness production observed in experiments. Statistical models are based on partition functions: canonical, micro-canonical or grand-canonical. Mean hadron multiplicities, allowing the possibility of non-equilibrated strangeness are defined as [16]:

$$\langle N_i \rangle = (2J_i + 1)\frac{V}{(2\pi)^3}\int d^3p \frac{1}{\gamma_s^{-s_i}\exp[(E_i - \mu.q_i)/T_{ch}] \pm 1} \qquad \textbf{Eq. 17}$$

Where T_{ch} is the chemical freeze-out temperature, μ is the chemical potentials, V represent the volume, γ_s is the strange quark fugacity (a measure for the equilibration of strange quarks) and s_i, and J_i represent the number of strange quarks and spin for a given particle type *i*, respectively. Strange quark fugacity, γ_s =1, assumes full equilibrium (equal number of strange and anti-strange quarks) while γ_s < 1 means that the strangeness might not be fully equilibrated. The QGP phase is strangeness neutral, i.e. γ_s =1, since the quarks exist in unbound states. In models that do not assume full equilibrium of strange particles, γ_s is found be larger than 0.6-0.7, indicating the system is close to equilibrium. **Figure 21** shows statistical model fit, using γ_s as a free parameter, to particle yields measured at SPS and RHIC energies. A clear energy dependence is observed when γ_s increases slowly, with the increasing energy, from 0.6-0.7 at SPS to about 1 at RHIC [16].

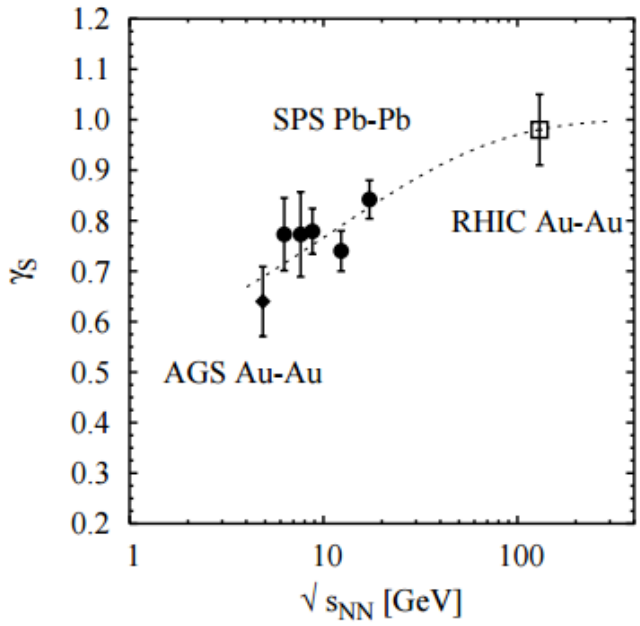

Figure 21: (Taken from **[16]**) Strange quark fugacity at chemical freeze-out is plotted as a function of system energy. The dashed line represents the model fit, satisfying $\gamma_s \to 1$ for $\sqrt{S_{NN}} \to \infty$.

Calculation of the equilibration timescale involves taking an average cross section of the incoming particles. For a typical temperature of about T = 200 GeV the timescale is found to be τ_{eqQGP} ~ 10 fm at, which is about the same timescale for a heavy ion collision from initial collision to final freeze out. However, the equilibration time depends on the temperature and is shorter for higher temperatures. **Figure 22** shows time needed for strange quark densities to reach equilibrium for various temperatures. It can be seen that the time needed to fully equilibrate strangeness depends strongly on temperature (faster for higher temperature) and is about 3 fm and 20 fm for a temperature of 300 MeV and 160 MeV, respectively [23]. Due to smaller

equilibration times, strange particles provide a better probe to extract information on constituent quarks at the hadronization stage [25]. Moreover, some studies have found that the partonic degrees of freedom play an important role in the measurements taken in heavy ion collisions and due to the difference in mass of light and strange quarks, strange quarks might be able to expand our understanding of the partonic dynamics in the QGP [26].

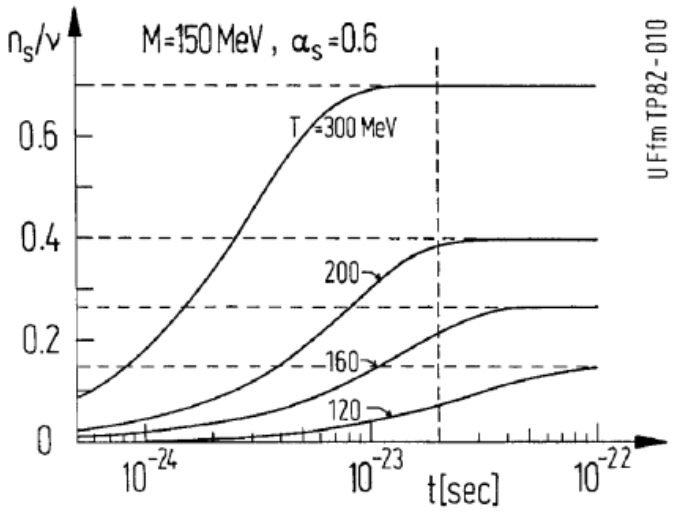

Figure 22: (Taken from **[23]**) Strange quark densities per baryon number are plotted as a function of time. The solid horizontal lines represent the quark densities in equilibrium at various temperatures.

2.5.2 Recombination/Coalescence Models

Some striking features were observed in early RHIC results for heavy ion collisions, in particular, measurements relating to the enhanced baryon production at intermediate p_T, sometimes collectively termed as “the baryon puzzle” [27]. The observables deviating from traditional theoretical and model predictions include: enhanced baryon to meson ratio; the nuclear modification factor R_{AA}, and scaling of elliptic anisotropy (v_2) of particle production at azimuthal angle relative to the reaction plane. Similar observations were made for strange hadrons. Theoretical advancements to explain these observations forced the revival of the recombination models.

Hadronization via recombination was suggested in the 1970s to explain the 'leading particle effect' and formed the basis of the algebraic coalescence rehadronization (ALCOR) model in the 1990s which proved to be a very successful model in predicting the hadron multiplicities at lower energies and focused on the hadron production at lower p_T ($p_T < 1.5$ GeV/c).

Recombination seems to provide a natural explanation to some of these experimental observations, such as the enhanced baryon production at intermediate p_T shown in **Figure 23**. The relative yields of anti-protons with respect to pions and anti-Lambda with respect to K^0-short, at intermediate p_T, show that the measured baryon-to-meson ratios in Au+Au collisions are significantly higher than those in e^++e^- or p+p collisions, indicating that the hadronization process in these systems are different. The plotted baryon to meson ratio is ~ 1, around $p_T = 2$ GeV/c, and could be explained if the hadrons were formed via recombination of thermal quarks. An

abundance of thermal quarks in the QGP makes the formation of baryons or mesons equally probable, explaining the ratio of $p/\pi \sim 1$ at intermediate p_T [28].

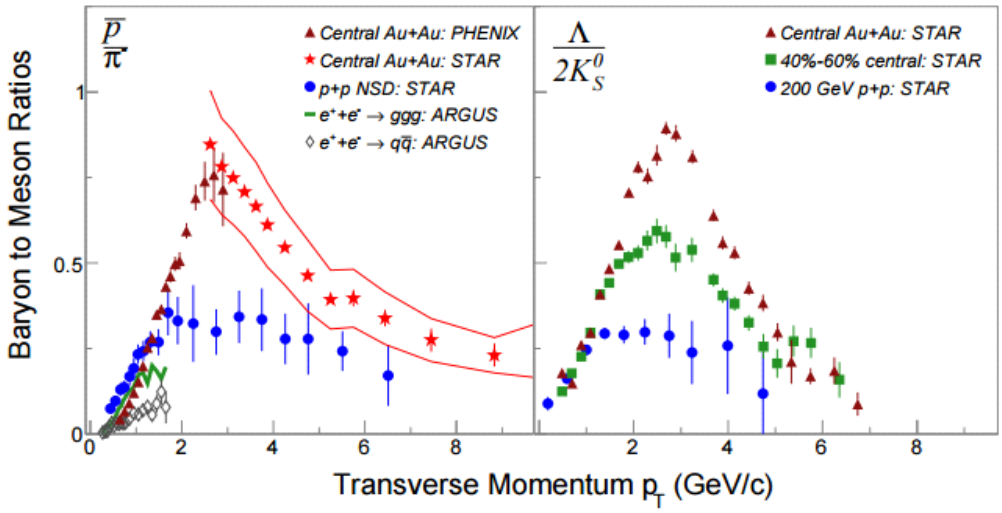

Figure 23: (Taken from **[27]**) $\bar{p}/\pi$- (Left) and $\Lambda/2K^0_s$ (Right) ratios for various collisions at $\sqrt{s_{NN}}$ = 200 GeV are plotted. The $\bar{\Lambda}/K^0_s$ ratio in the right plot is scaled by a factor of two for comparison.

High p_T partons have limited availability due to a steeply falling transverse momentum spectra, therefore, fragmentation is not sufficient to form high p_T hadrons since it requires a fragmenting parton with even higher p_T. The baryon enhancement at intermediate p_T has been explained well using the recombination models, including the contributions from coalescence of two or three quarks to produce a meson or a baryons. **Figure 24** shows the ratios of (anti-) proton to pion ratio with the calculations with two different recombination models. **Figure 25**

demonstrates the success of theoretical models using an interplay of recombination and fragmentation to describe the p_T spectra for neutral pions and kaons for different centralities.

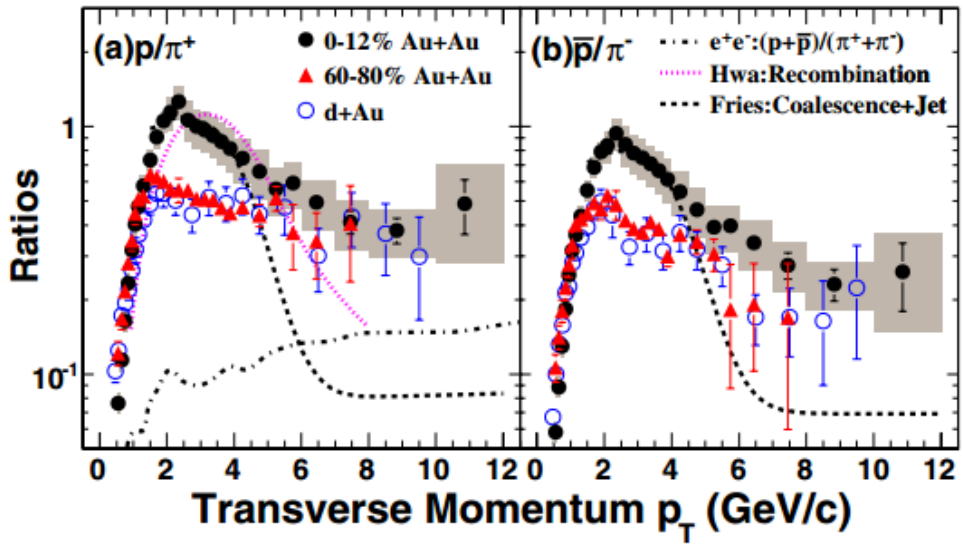

Figure 24: (Taken from **[29]**) Enhancement of (anti-)pronton to pion ratio in central Au+Au collisions at $\sqrt{S_{NN}} = 200$ GeV compared to peripheral Au+Au and d+Au collisions is shown along with model calculation in central Au+Au collisions.

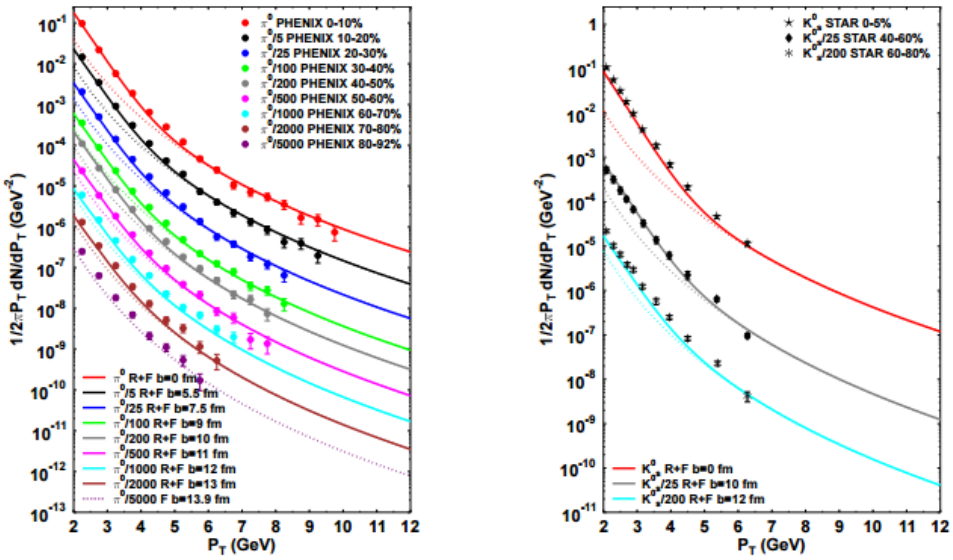

Figure 25: (Taken from **[30]**) Centrality dependence of (Left) π^0 and (Right) K^0_s spectra is plotted with data from PHENIX and STAR, respectively. Model calculations for fragmentation and sum contributions from fragmentation and recombination are also shown.

Nuclear Modification Factor:

To quantify the large suppression of yields of single-particles at high p_T observed in heavy ion collision when compared to particle yields in elementary collisions an observable, called the nuclear modification factor, R_{AA}, is used and can be described as follows:

$$R_{AA} = \frac{(1/N_{evt}^{AA})}{\langle N_{coll}\rangle (1/N_{evt}^{pp})} \frac{d^2N_{ch}^{AA}/dp_T d\eta}{d^2N_{ch}^{pp}/dp_T d\mu} \qquad \textbf{Eq. 18}$$

Where $\langle N_{coll}\rangle$ represents the average number of binary collisions for a given centrality, N_{evt}^{AA} and N_{evt}^{pp} are the number of events in heavy-ion and proton-proton collisions, respectively.

When p+p reference is unavailable, a slightly modified version of the nuclear modification factor R_{AA}, called the R_{CP} is used, in which particle yields from central to peripheral collisions in nucleon-nucleon collisions are compared instead of using p+p collisions as reference. **Figure 26** shows the nuclear modification factor, R_{CP}, for charged and neutral strange hadrons (i.e. K^0_s and $\Lambda + \overline{\Lambda}$).

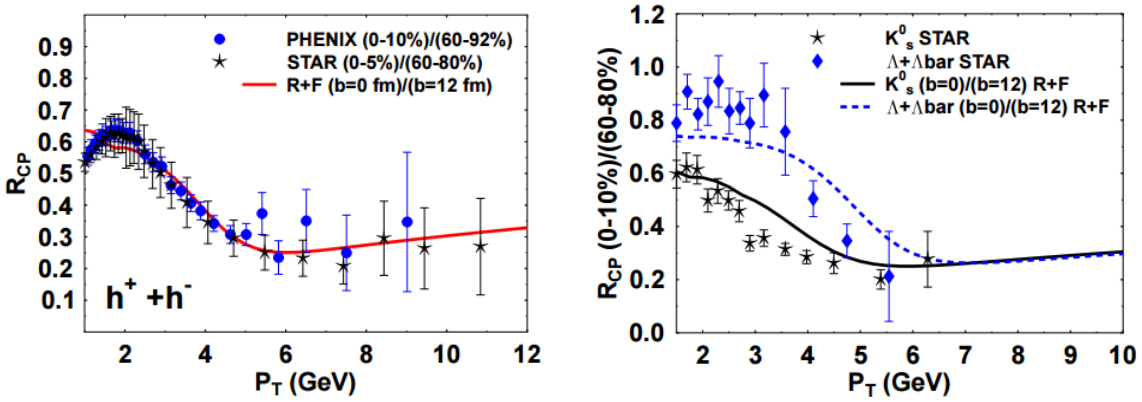

Figure 26: (Taken from **[30]**) Nuclear modification factor R_{cp} measured at PHENIX and STAR for (Left) charged hadrons and (Right) K^0_s and $\Lambda + \overline{\Lambda}$. Model calculations incorporating an interplay of recombination and fragmentation is used to describe the data.

As seen earlier in **Figure 15** of Section 2.4.1.1, a large elliptic flow, v_2, measured in the bulk region (p_T < 1.5 GeV/c) agrees well with the hydrodynamic model, suggesting mass ordering i.e. heavier particles have smaller v_2 than light particles, but for p_T > 1.5 GeV/c the values clearly deviate from the model predictions. At intermediate p_T, a 50% increase has been

found in the v_2 of baryons showing particle type dependence, which rules out particle production described by pure fragmentation or simple hydrodynamics. Moreover, when the elliptic flow of various particle species is plotted per number of constituent quarks (**Figure 27**), an approximate scaling is observed, commonly known as the number of constituent quark (NCQ) scaling. This scaling of the elliptic flow further strengthens the recombination models that suggest that collectively moving quarks in the QGP are recombined into hadrons.

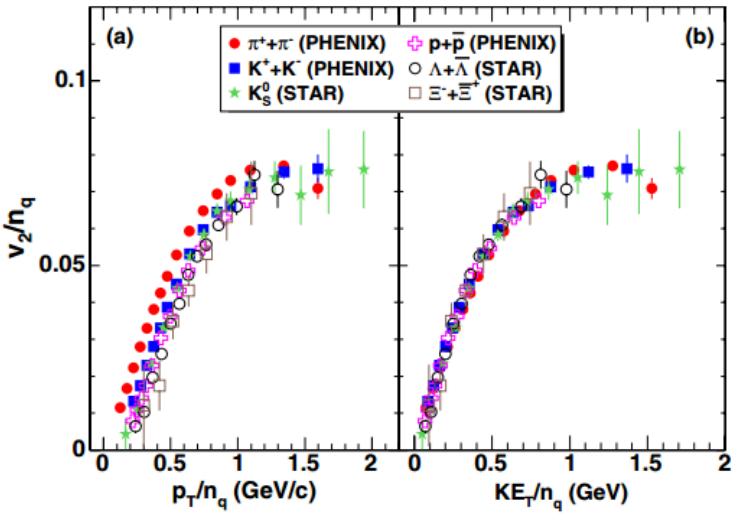

Figure 27: (Taken from **[31]**) Elliptic flow per number of constituent quarks v_2/n_q is plotted versus scaled (a) p_T and (b) Kinetic energy for various hadron measured in minimum-bias Au+Au collisions

2.6 JET QUENCHING

Hard probes, i.e. particles produces via hard processes in the earliest stage of heavy ion collisions, are extremely useful in studying the dynamic and evolution of the QGP [8], [32], [33]. These particles are primarily produced in the initial collision via fragmentation of high p_T partons in the form of collimated sprays of particles, known as jets. The leading particle in a jet is "slowed" down as a result of a medium induces energy loss and this effect has been termed as "jet quenching" in heavy ion collisions. Measurements of jet quenching or single-particle suppression can be used to extract initial parton density in the hot and dense QGP.

Figure 28 compares the R_{AA} in central Au+Au collision measured at LHC to measurements taken at STAR and PHENIX. If the particle yields scaled with the number of binary collisions, R_{AA} should equal to 1, while suppression at high p_T can be taken as a sign of jet quenching in the QGP. It can be seen that for p_T up to 2 GeV/c measured R_{AA} at RHIC and LHC are similar, however at higher p_T the LHC data has smaller R_{AA}, i.e. more suppression of charged hadrons at LHC. Since, suppression is mainly attributed to energy loss experienced by partons while traversing through a strongly interacting medium, this enhanced suppression at LHC could suggest the creation of a denser medium [34].

The parton energy loss depends on the parton density of the medium and according to some theoretical estimates is proportional to the gluon density in the medium. Gluon densities can be calculated using the following expression [35]:

$$\rho(\tau) = (\tau_0/\tau)\rho(\tau_0) \qquad \textbf{Eq. 19}$$

where $\tau_0 \rho_0 = (1/\pi R_A^2) dN^8/dy$, and dN^8/dy is the effective initial gluon density.

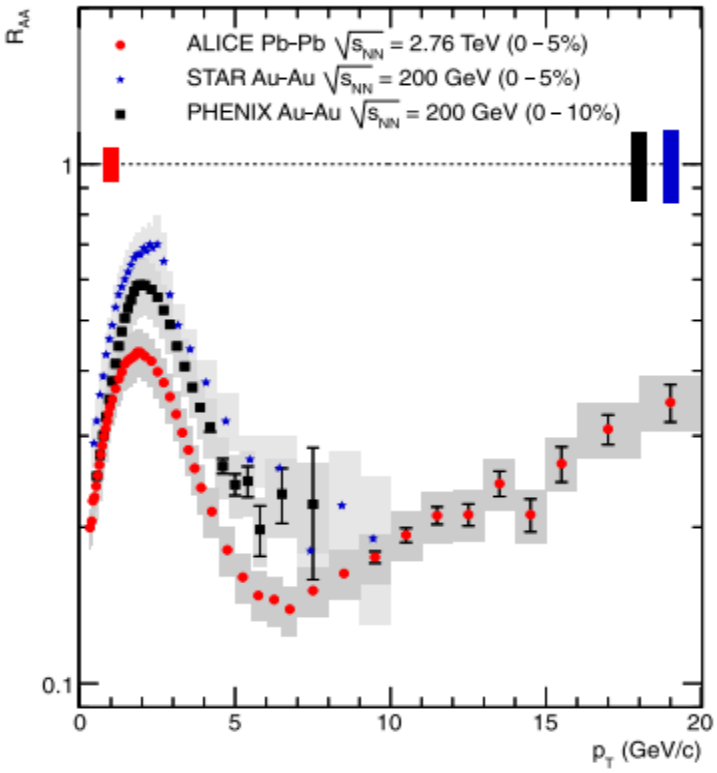

Figure 28: (Taken from **[34]**) Measurement of Nuclear modification factor, R_{AA} of charged hadrons, in central Au+Au at STAR and PHENIX is compared to measurements taken at LHC at $\sqrt{S_{NN}}$ =200 GeV. p_T independent scaling errors are represented by the vertical bars around R_{AA}=1.

Theoretical calculations show that initial gluon density at RHIC top energy is around 2000-3500. Assuming transverse energy per nucleon of 0.5 GeV, this corresponds to the initial energy

density of 15 GeV/fm^3 (100 times larger than the energy density of cold nuclear matter) [35], [36].

Figure 29 shows the difference in nuclear modification factor R_{CP} of baryon and mesons. Lower R_{CP} corresponds to larger suppression and it can be seen that at low p_T the suppression for baryon (e.g. $\Lambda + \overline{\Lambda}$, $\Xi + \overline{\Xi}$, and $\Omega + \overline{\Omega}$) and mesons (e.g. $K^{\pm}$, K^0_s, and ϕ) is comparable. However, for intermediate and higher p_T > 2 GeV/c, the trend changes, and the baryons show less suppression. The baryon enhancement indicates that number of valence quark is a more important factor in particle production than the particle's mass at higher p_T.

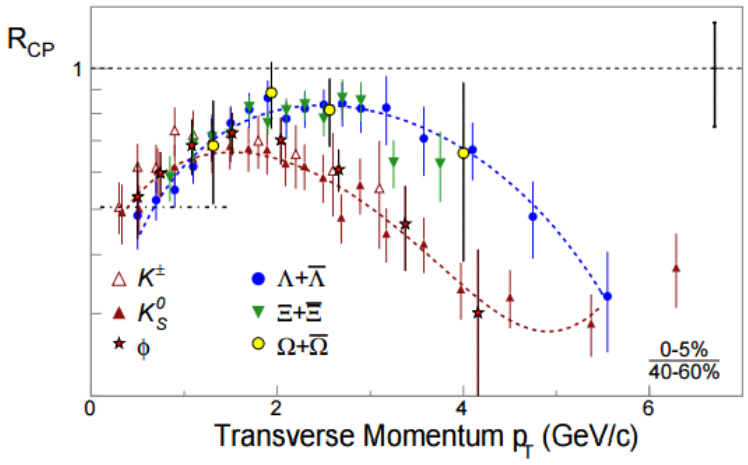

Figure 29: (Taken from **[27]**) Nuclear modification factor for different baryons and mesons measured in Au+Au collisions at $\sqrt{s_{NN}}$ = 200 GeV

CHAPTER 3

DETECTOR SETUP

3.1 THE RELATIVISTIC HEAVY ION COLLIDER

The Relativistic Heavy Ion Collider (RHIC) is located at the Brookhaven National Laboratory (BNL) on Long Island, NY. The idea to build RHIC was conceived in the early 80's and the construction was completed in 1999. The main objective of RHIC was to collide heavy ions, but colliding intense beams of polarized protons has later become an important part of RHIC. Some of the most crucial and novel features of RHIC are the ability to provide collisions between beams of different species, as well as colliding gold (Au)-ions over a range of energies. The first Au+Au collisions at the top RHIC beam energy of 200 GeV/nucleon pair were performed in year 2001.

A schematic diagram of BNL collider facility is shown in **Figure 31**. The overall complex consists of two concentric rings, the Alternating Gradient Synchrotron (AGS), Electron Beam Ion Source (EBIS), the Booster, the proton linear accelerator (Linac). The rings are about 3.8 km in diameter and have six interaction points. The two rings accelerate, store and collide various types of ions.

Fully charged ions are generated in the Electron Beam Ion Source (EBIS) residing in the Linac area, whereas polarized protons are produced and accelerated in the Linac. The EBIS replaced the two Tandem Van de Graaff accelerators that had been used as the heavy ion source for over 40 years. EBIS can create highly charged ions of any element from deuterons to uranium. The EBIS became fully functional in September, 2010 [37]. The produced ions are first accelerated

in the linear accelerator before going into the Booster Synchrotron, where they are boosted to 95 MeV per nucleon. The Booster feeds the ions to the AGS, where they go from 37% to 99.7% the speed of light, reaching the energy of 10.8 GeV per nucleon [38], [39]. The ions are then sent to the RHIC beam lines as bunches by a switching magnet directing them to either of the two rings. Once these counter-rotating ion beams are in the rings; they are accelerated to designated energy and can be stored for up to 10 hours at the top energy.

The bending and focusing of the ion beams is achieved by superconducting ring magnets. A magnetic field of about 3.458 T is applied which yields top energy of 200 GeV/nucleon pair for Au-ions and 500 GeV for protons. The magnets are kept at a temperature below 4.6 K. The cooling system comprises of a cold circulator, providing forced circulation of supercritical helium; heat exchangers called 'recoolers', periodically cooling the circulating helium by heat exchange with liquid helium; and a 25 kW helium refrigerator.

An important requirement in the design of the ring magnets was the need to achieve high-luminosity collisions over a range of energies 30-100 GeV/nucleon. Luminosity can be used as a measure of detector performance and is described by the number of interactions per unit time per unit cross-section. The nominal luminosities reached at RHIC, as per original design, averaged over the 10 hour storage time, are about 2×10^{26} cm^{-2} s^{-1}, corresponding to a rate of 800 Hz [38], [14].

To improve luminosity, upgrades and improvements were made to RHIC experiment and accelerator after the completion of run year 2010. In run year 2011, Au+Au collision at three different energies; 19.6, 27 and 200 GeV/nucleon pair were conducted at RHIC. Average

luminosity recorded, for the 200 GeV/nucleon pair run, was 30 × 10^{26}cm^{-2}sec^{-1}. Even higher luminosities were reached in the following years. **Table 1** lists a summary of some recorded parameters for Au+Au runs at 200 GeV per nucleon pair. At the time, achievement of high integrated luminosities made the run year 2011 a great success. A new peak instantaneous luminosity was also reached which superseded previous run years [40]. **Figure 30** show the integrated luminosity for STAR and PHENIX at 200 GeV/nucleon pair. Minimum bias Au+Au data at 200 GeV taken by STAR during Run-11 was selected for the present analysis because it was the largest dataset available at that time, and allowed us to explore a wide range of system sizes, i.e. centralities.

Two of the six interaction points on the accelerator rings house experiments that are currently active, namely the Solenoidal Tracker at RHIC (STAR) and the Pioneering Hadron Electron Nuclear Interaction eXperiment (PHENIX). Two other experiments, Broad RAnge Hadron Magnetic Spectrometers Experiment (BRAHMS), and PHOBOS concluded their experiments and were decommissioned in 2006. STAR and PHENIX are large, multi-purpose detectors whereas PHOBOS and BRAHMS were smaller systems.

	Run2	***Run4***	***Run7***	***Run10***	***Run11***	***Run14***	***Run16***
No. of bunches	*55*	*45*	*103*	*111*	*111*	*111*	*111*
Ions/bunch [10^9]	*0.6*	*1.1*	*1.1*	*1.1*	*1.3*	*1.6*	*2.0*
Peak luminosity [$10^{26}cm^{-2}s^{-1}$]	*4*	*15*	*30*	*40*	*50*	*84*	*155*
Avg. store luminosity [$10^{26}cm^{-2}s^{-1}$]	*1.5*	*5*	*12*	*20*	*30*	*50*	*87*
Luminosity per week [μb^{-1}/week]	*24*	*160*	*380*	*650*	*1000*	*.0022*	*.003*
Run length [weeks of physics]	*15.9*	*12*	*12.8*	*10.9*	*6.4*	*13.3*	*14.4*
Time in store [% of calendar time]	*26*	*53*	*49*	*53*	*59*	*68*	*65*

Table 1: Run parameters for 100 GeV Au+Au runs **[40]**, **[41]**

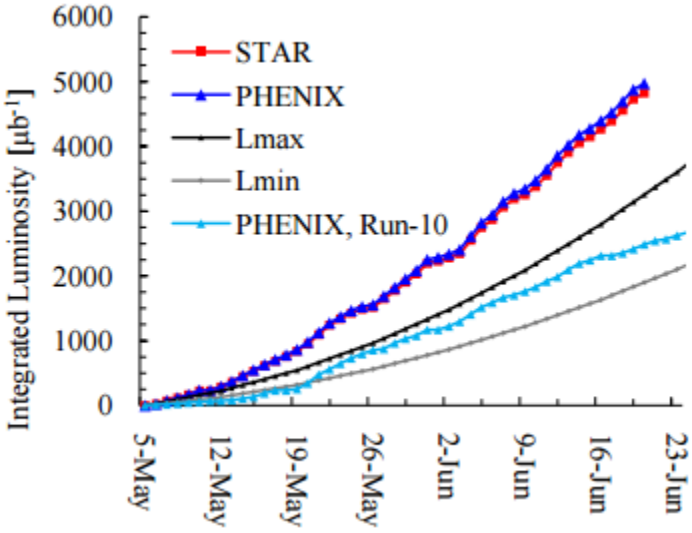

Figure 30: (Taken from **[40]**) Integrated luminosities for STAR and PHENIX at 100 GeV. Conservative predictions for minimum (L_{min}) and maximum (L_{max}) luminosities for Run-11 and luminosity recorded for PHENIX during Run-10 is also shown for reference.

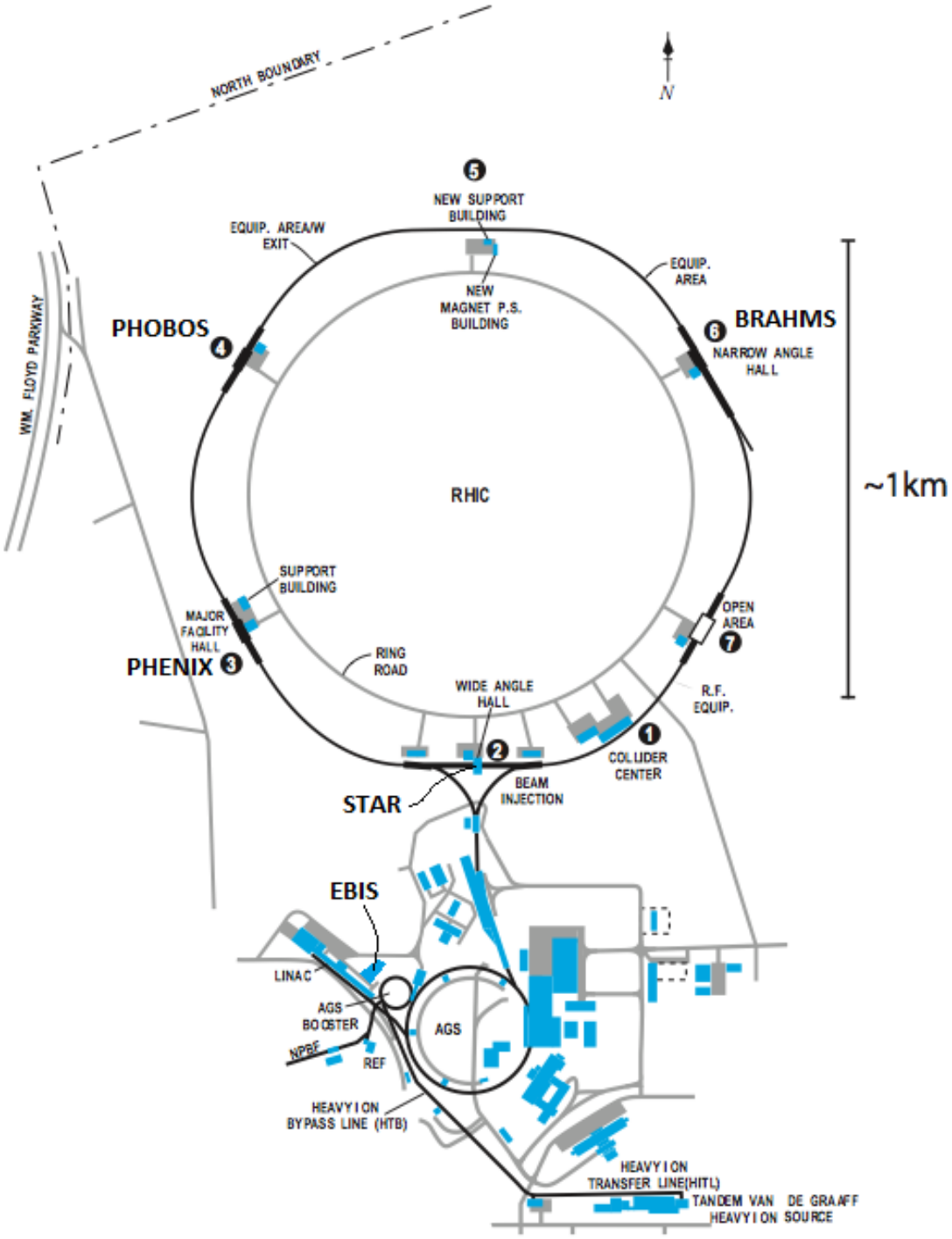

Figure 31: (Taken from **[15]** - Edited) Schematic diagram showing the Brookhaven National Laboratory collider complex

3.2 THE STAR DETECTOR

The Solenoidal Tracker at RHIC (STAR) is one of the two large detectors currently conducting experiments at RHIC. The main goal of STAR was to create QGP and study its properties and behavior.

The STAR detector consists of many sub-detectors that work together to track thousands of particles produced in heavy-ion collisions at RHIC. A layout of the STAR detector is shown in **Figure 32**. The large acceptance of STAR, covering a large solid angle ($|\phi| < \pi$, and $|\eta| < 1.8$), enables it to perform high precision tracking, and particle identification, and most importantly an event by event characterization of heavy-ion collisions. The Time Projection Chamber (TPC), STAR's primary tracking device, sits at the heart of STAR encased by the solenoidal magnet. Event selection, i.e. triggering, is done by fast detectors such as the Zero Degree Calorimeter (ZDC), Beam-Beam Counter (BBC) and the Vertex Position Detector (VPD). Other subsystems of STAR include Forward Time Projection Chamber (fTPC), Time of Flight (TOF), Electro-Magnetic Calorimeters (EMC), and the Heavy-Flavor Tracker (HFT). The current analysis uses measurements taken by the TPC only. TPC and subsystems, relevant to our study, are discussed in the following sections.

3.2.1 STAR Magnet System

The STAR magnet is one of the most important parts of the STAR detector, and provides a nearly uniform magnetic field parallel to the beam direction within the detector volume. The magnet is a large solenoid, with an inner and outer diameter of 5.27m and 6.28m respectively,

that houses many of the STAR subsystems including TPC. A detailed view of the STAR magnet system is shown in **Figure 33**.

The STAR magnet consists of three types of coils, main, space trims and poletip trims, which are kept at a mean temperature of about 29^{o} C by circulating cold water through them. The cooling system uses heat exchangers which in turn are cooled using an outside water cooling tower. The magnet can operate at 0.25 T or 0.5 T, values referred to as half-field and full field, respectively. The field is reversible, allowing for systematic cross-checks, and the magnetic field of a negative value is called the reversed field.

The design requirement of the magnet includes the tracking accuracy of high energy electrons with the estimate of their position reconstruction accuracy of about 200μm. The long term drift in the absolute field was found to be within 0.1 Gauss over a period of 12 hours. The field is reproducible to within 0.5 Gauss and both positive and negative fields in full and half field settings are same within 0.25 Gauss [42].

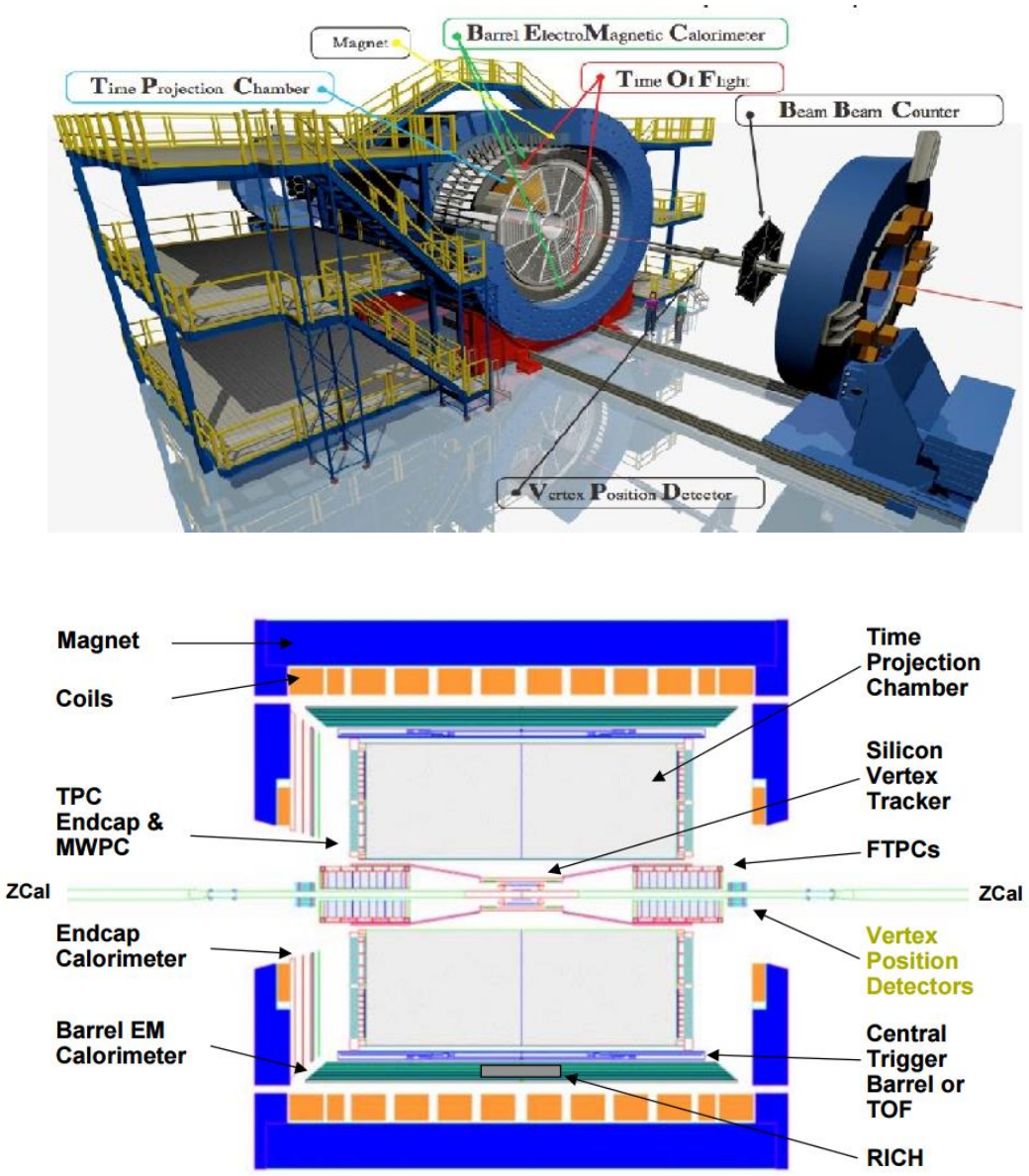

Figure 32: (Top) Layout of major components of the STAR detector at RHIC (Bottom) Detailed cutout view of the STAR detector

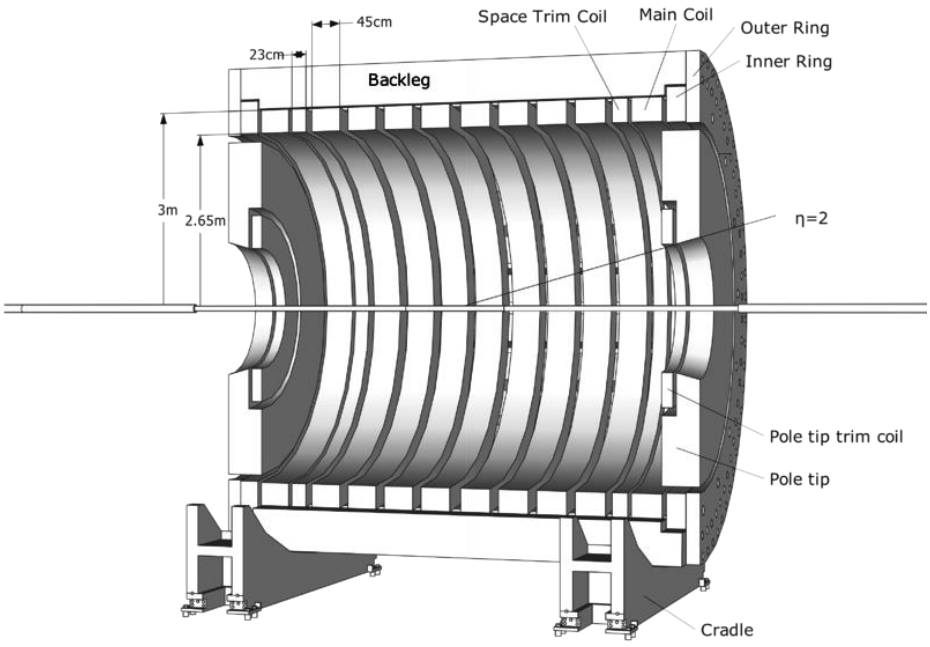

Figure 33: Detailed intersection of the STAR Magnet System

3.2.2 STAR Trigger Detectors

STAR trigger system is composed of a number of fast detectors including, Zero-Degree Calorimeter (ZDC), Beam-Beam Counter (BBC), and Vertex Position Detector (VPD), which are responsible of making the decision to record an event. The processing times for these detectors range from 1.5μs to 5ms. These triggers are designed to meet various requirements such as, selecting central, ultra-peripheral, or jet events required for specific studies. Moreover, fast triggers are also used to reject background (beam-gas interaction). The background rate is expected to be ~ 100 Hz at maximum luminosity. Given that the bunch crossing rate at RHIC is

~10 MHz some background must be rejected when the interaction rate approaches the bunch crossing rate [43].

3.2.2.1 Zero-Degree Calorimeter

The Zero-Degree Calorimeter (ZDC) detects the spectator (non-participating) neutrons that are produced when a high energy collision takes place. No signal in the ZDC's would mean that the collision didn't take place. A small number of spectator neutrons is indicative of central collision and vice versa. Two identical ZDC's are installed on either side of all RHIC experiments. They are located at identical positions on either side of the interaction region (16-18 meters from the nominal interaction point). Neutrons produced during heavy-ion collisions at beam energy 200 GeV/nucleon pair stay within 1mrad of the beam and are detected by the ZDC's which are only 10cm wide [43], [44]. A coincidence of summed signal in both ZDC's is required to be greater than 40% of a single neutron signal to be used as a part of the minimum bias trigger. The coincidence is also used as a tool to measure luminosity and to eliminate the backgrounds resulting from single beam interactions with residual gas in the detector. The time recorded by ZDC east and ZDC west also gives a measure for the position of primary interaction.

3.2.2.2 Vertex Position Detector

The Vertex Position Detector (VPD) at STAR is used as a primary minimum bias trigger in Au+Au collisions, starting in run year 2007 [45]. It provides the position of the primary collision vertex and the event 'start time' [46]. This system consists of two identical VPD's on each side, 5.7m from the center of STAR, and each made up of nineteen readout detectors. Upon getting a signal from STAR ZDC's that an event has occurred, data is collected from the VPD's about the

primary vertex position $V_z = c(T_{east} + T_{west})/2$ and start time of an event $T_{start} = (T_{east} + T_{west})/2 - L/c$; where *L* is the distance from either VPD to center of STAR. Along with a coincidence signal from both ZDC's, a cut on V_z measured by the VPD can be used as a minimum bias trigger [45].

The resolution of measuring the primary vertex location is determined by comparing the position measured by the VPD's and the position obtained by the reconstructed primary tracks in the TPC. A Gaussian fit is used on the difference $\Delta Z = V_z^{VPD} - V_z^{TPC}$ of these positions to determine the vertex resolution. The average resolution of a single detector is 94 ps for top energy of 200 GeV and goes up to 150 ps for intermediate energies for Au+Au collisions. The start time resolution is observed to be very small, 20-30 ps in top energy Au+Au and ~80 ps in p+p collisions.

3.2.3 STAR Time Projection Chamber

The Time Projection Chamber (TPC) surrounds the beam-beam interaction region and is used as a primary tracking device in the STAR experiment at RHIC. The chamber measures 4.2 meters in length and 4 meters in height and is divided into two halves by a central membrane. The central membrane is kept at a constant potential of about 28 kV, producing uniform electric field in opposite directions in the two halves, pointing from the membrane to the anodes in the end-caps, which are maintained at a potential of 0 V.

A schematic diagram of the TPC is shown in **Figure 34**. The inner radius measures 50 cm and covers a pseudo-rapidity range of $|\eta| < 2$, while the outer radius covers a pseudo-rapidity range of $|\eta| < 1$.

The TPC chamber is filled with P10 gas (10% methane, 90% argon), kept at 2 mbar above atmospheric pressure. In addition to P10 the TPC gas system also supplies a mixture of 50% He + 50% C_2H_6 for purging when TPC is not in use; during that time the system operates in an open system configuration [47]. The TPC gas system is primarily used to circulate the gas and maintain the purity, temperature and pressure of the gasses. The P10 gas has been chosen for its relatively fast drift velocity which peaks and saturates to ~5.45 cm/μs at low electric field (130 V/cm).

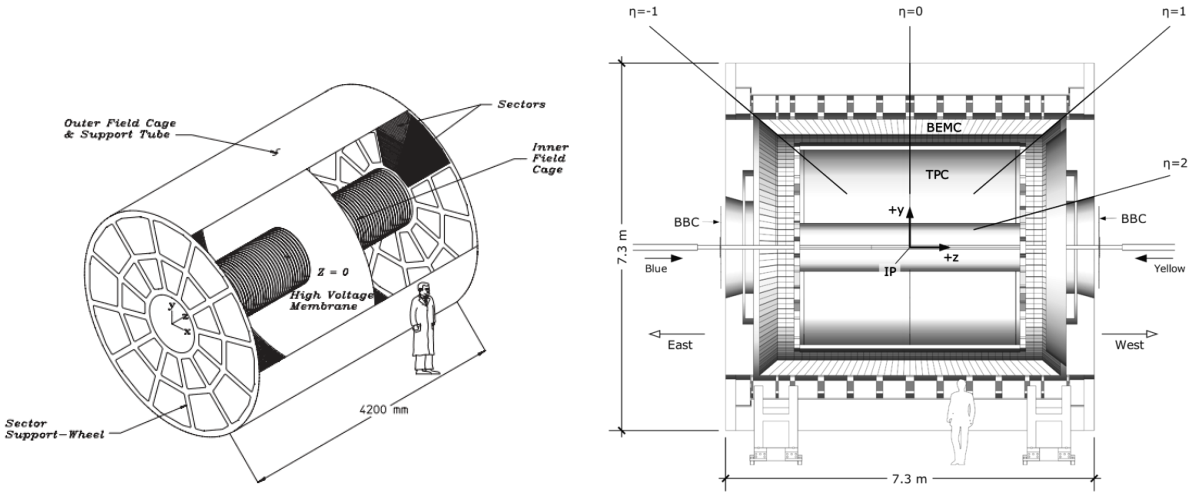

Figure 34: (Left) Schematic diagram of the TPC, showing inner/outer field cages, central membrane and the readout sectors (Right) Sectional view of STAR showing beam direction and TPC acceptance.

Each end-cap consists of 12 sectors which are arranged in 45 pad rows. Each sector is further divided into an inner and outer sub-sector (**Figure 35**). The inner and outer sub-sectors consist of 1750 and 3942 readout pads each, respectively, with a total of 136,608 total pads in the system. The inner sub-sectors contain smaller pads to ensure better two hit resolution since they cover the region of high track density. The principle of Multi-Wire Proportional Chamber (MWPC) with readout pads is utilized in the readout system. The chamber consists of three 20μm anode wire planes sandwiched between the readout plane and a ground wire plane.

During a collision many primary and secondary charged particles are produces [48]. The secondary particles are produced as a result of the decay of some short-lived primary particles, or the interaction of particles with the detector material. All charged particles produced in the collision travel in a helical path under the uniform magnetic field, ionizing the gas inside TPC, leaving a trail of ionization electrons. The electrons drift through the gas towards the nearest end-cap with a well-defined velocity and get recorded by the readout pads. The electron drift paths are up to 2.1 m long and a uniform electric field is required to ensure accurate track reconstruction. The drifting electrons are amplified by avalanching in the high electric field present in the chamber. The charge induced by the positive ions created during the avalanche is shared by a maximum of three adjacent readout pads. The width of the pads is designed to achieve the best possible position resolution, typically better than 20% of the pad dimension, for a high-p_T track.

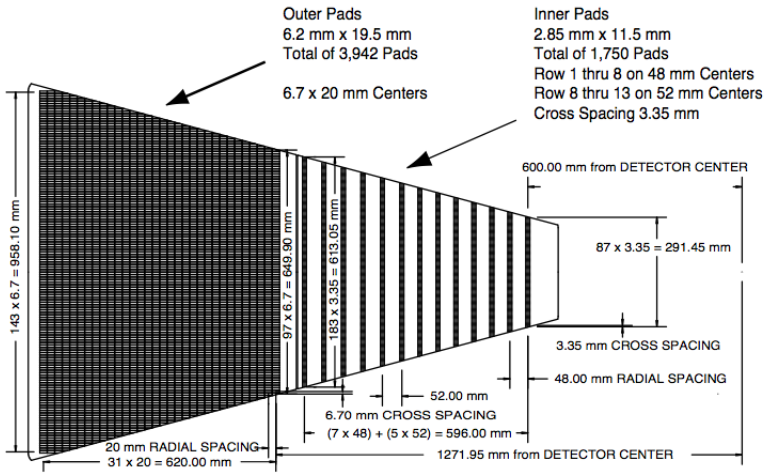

Figure 35: Schematic diagram of one TPC sector readout plane

3.2.3.1 Tracking in the TPC

The three dimensional position where the ionization takes place along the path length of a charged track can be reconstructed from the information and is called a 'hit', A central heavy-ion collision can produce hundreds of thousands of hits. Calculating the accurate position of these hits is crucial in order to achieve the intended physics goals. Knowing the time and location in the readout pads it is possible to reconstruct the three dimensional position, called a 'hit', where the ionization took place. The track of a particle passing through TPC is found by locating ionization clusters along its path. These clusters are measured separately in x-y and z space.

The position of the hit in the x-y plane, perpendicular to the beam, is calculated by fitting a Gaussian to the avalanche signal deposited on three adjacent pads in a single pad row. A

weighted mean method is used to determine the position if the signal is found in more than 3 pads, which could happen when a track crosses the pad at large angles.

The position of the hit parallel to the beam direction, local z-axis, is determined by dividing the time it took the drifting electrons to reach the anodes on the endcap by the drift velocity. Time is measured in 100 ns intervals, called 'time buckets'. In order to convert time into position the drift velocity must be known within 0.1% [48]. The changes in the drift velocity are minimized by maintaining a uniform electric field and independently measuring the drift velocity every few hours by using lasers to create artificial tracks.

Once all the raw hits have been found, track reconstruction process begins using the Kalman Filter approach [15], [49]. TPC hits before and after the track reconstruction process are shown in **Figure 36**. The process can be broadly divided into two steps; track finding and fitting. During track finding, the primary interaction point is not taken into account and tracks (charged particle trajectories) are treated as independent objects. Starting from the outer most pad row, where track densities are smaller, going inwards all possible combinations of hits are considered to form possible tracks. Any charged particle's trajectory under a uniform magnetic field can be described very well by a helix, therefore all possible tracks are fitted to a helix.

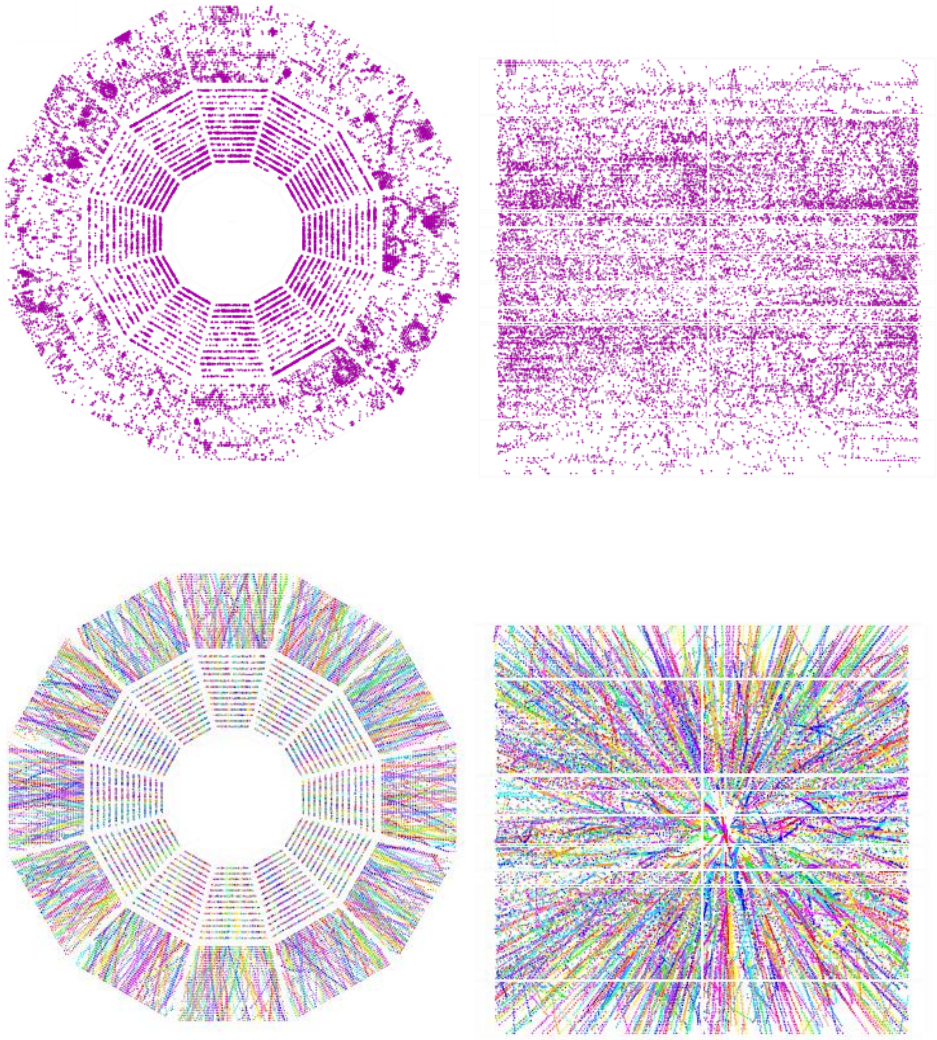

Figure 36: (Taken from **[40]**) (Left) Projection of all hits in the TPC volume onto one single pad plane (Right) The lateral view of the same hit volume. (Top) Raw TPC hits before track reconstruction. (Bottom) Same data after track reconstruction

Tracks constructed at this point are called “global tracks” and do not have any correlation with the primary interaction point. Global tracks within 3.0 cm of the nominal interaction point are used to find the primary vertex position. All tracks with their distance of closest approach (DCA) less than 3 cm to the primary vertex are refitted again, requiring them to go through the primary vertex, to construct tracks, called “primary tracks”. The fitting parameters like the direction and radius of curvature are used to calculate the charge and momentum of the track. A small fraction of the ionization energy is lost due to interaction with the TPC gas. This energy loss can be measured by the amount of energy deposited on the readout pads. Kalman Filter corrects for these losses assuming pion mass for all charged tracks. Given the kinematic range being considered the energy loss can be used for particle identification [18].

CHAPTER 4

ANALYSIS DETAILS

4.1 DATA SELECTION

Data selection process is done both on-line, using hardware trigger selection in real time, and offline through event and track selection criteria. Data used in this analysis is Minimum Bias data from Au+Au collisions at $\sqrt{s_{NN}}$ = 200 GeV, taken at RHIC in year 2011 by the STAR detector. Name and identifiers of the triggers used in this analysis are listed in **Table 2**.

4.1.1 Trigger Selection

The decision making process of choosing which events to record is called triggering. Triggering is mainly done for practical purpose of reducing data rate, and is also used to select events of certain interest. The events recorded with simplest selection criteria are called the minimum bias events. In run year 2011, Vertex Position Detector (*VPD*) along with the Zero Degree Calorimeter (*ZDC*) was used as a primary minimum bias trigger. The *VPD* measures the primary interaction position along the beam line and *ZDC* determines the number of spectator neutrons (see Sections 3.2.2.1 and 3.2.2.2). For Run-11 the minimum bias trigger consisted of two conditions; the primary interaction position, as measured by VPD, within $|z| < 30$ cm of the TPC center, and a coincidence of at least one neutron in both ZDC's.

Triggers selected for this analysis also provide protection against 'pile-up', a situation when tracks of particles from a previous event are still present in the TPC, and are read out with the tracks of particles produced in the current event. Pile-up occurs as a consequence of high

luminosity, i.e. very large number of collisions per bunch crossing. Protection from pile-up can be provided by selecting events if no ZDC incidence was recorded within ±45 microseconds of that event.

Collision Type	$\sqrt{s_{NN}}$	***Trigger Id***	***Trigger Name***
		350003	
		350013	
Au+Au	*200 GeV*	*350023*	*vpd-zdc-mb-protected*
		350033	
		350043	

Table 2. Id's and name Id's and name of the Trigger used in this analysis.

4.1.2 Event Selection

Event selection is an offline process and is specific to the analysis. For an event to be considered, it is made sure that a proper vertex has been found and that its position is within a certain range, fitting to the analysis. In addition to the primary interaction position measured by the VPD, positions of other vertices are also calculated using TPC data, during the track reconstruction process. These vertices could be the main interaction point, a secondary decay vertex, or some other interaction center. All vertices are then ranked and a primary vertex is chosen by applying various quality cuts, such as number of tracks pointing towards it. Tracking performance of TPC is best near its center; therefore, primary vertex was chosen to be within 25 cm of the TPC center. To avoid falsely identified primary vertex due to pile-up, highest ranking

vertex was chosen with its reconstructed Vz within 3cm of the vertex position determined by the VPD. **T**otal number of events in the dataset, events satisfying the minimum bias triggers and number of events with primary vertex position within 25 cm of the TPC center with at least one particle with transverse momentum p_T > 3.0 GeV/c are presented in **Table 3**.

4.1.3 Track Selection

To ensure that only 'good' reconstructed tracks, tracks with optimal momentum and position resolution, are used in the analysis, some quality control cuts are applied to each track. **Table 4** lists these cuts and their values used in this analysis. The distance of closest approach of a global track to the primary vertex is a good measure to make sure that the primary track reconstructed using said global track is a good primary track. This DCA is required to be within *1cm* to get more accurate values for the dynamic variable (p_T, η, ϕ) which are calculated with respect to the primary vertex.

	Events Processed		**Events Used in Analysis**
	Total Events	**Events Satisfying Trigger**	**Events with |Vz| < 25 cm**
Full Magnetic Field	320,056,858	235,330,039	87,561,827
Reversed Full Magnetic Field	284,832,169	235,214,651	86,292,839

Table 3: Number of events for year 2011 Au+Au 200 GeV/c minimum-bias data

A track can have a maximum of 45 hit points in the TPC (number of TPC pad rows) that are used to reconstruct that track. Exceptions to this maximum are some low momentum tracks that lose all their energy within the bounds of the TPC, and might end up with more than 45 hit points. Number of hit points of a track can also vary due to detector acceptance, particle decay or overlap with other tracks. Tracks with a minimum of 20 hit points are selected. Not all the possible points available are used to reconstruct a track, therefore to increase precision, tracks for which at least 51% of the available hit points were used to determine its helix were selected.

An additional constraint is placed on the pseudo-rapidity of the track to fall within the acceptance range of the outer TPC barrel. This cut ensures that sufficient path length of a track in the TPC is available for reconstruction.

Track Quality Cuts
$DCA_{global} < 1cm$
$N_{fitpoints} \geq 20$
$\frac{N_{fitpoints}}{N_{possiblefitpoints}} > 0.51$
$\lvert\eta\rvert < 1.0$

Table 4: Track quality cuts used in this analysis

4.1.4 Centrality Selection

Number of charged tracks detected by TPC in an event is referred to as the Reference multiplicity (Refmult) of that event. A sample reference multiplicity at mid-rapidity, $|\eta| < 0.5$ is used to define centrality classes using MC Glauber Model as discussed in section 2.2. To

account and correct for any luminosity dependence, a standard class StRefMultCorr is used in STAR. This class corrects for luminosity dependence and redefines centrality bins. For year 2011 Au+Au minimum bias dataset, centrality is divided into nine bins, which correspond to 0-5%, 5-10%, 10-20%, 20-30%, 30-40%, 40-50%, 50-60%, 60-70% and 70-80%; 0-5% being the most central 5% events. Cuts defining these centrality bins are presented in **Table 5**.

For this analysis these nine centrality bins are combined into three consolidated bins, namely; 0-20%, 20-40%, and 40-80%, mainly for statistical purposes. Distributions of the luminosity corrected reference multiplicities are shown in **Figure 37**. The left plot represents the Refmult distribution of all events, whereas the right plot shows Refmult for events with at least one particle with p_T > 3.0 GeV/c.

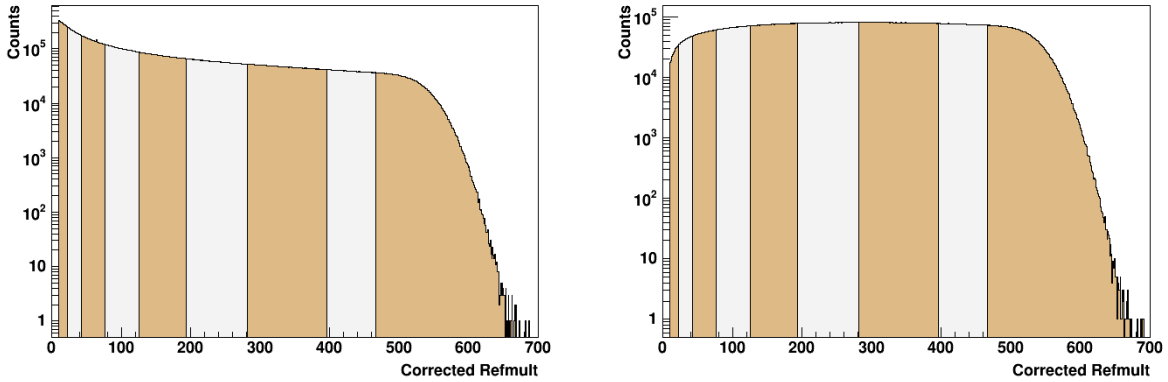

Figure 37: Luminosity corrected Refmult distribution (Left) for all events (Right) for events with at least one particle with pT > 3.0 GeV/c. Alternating shaded regions represents nine centrality bins.

Centrality Bin	Corss Section	Corrected Refmult
1	70-80%	≥10
2	60-70%	≥22
3	50-60%	≥43
4	40-50%	≥76
5	30-40%	≥125
6	20-30%	≥193
7	10-20%	≥281
8	5-10%	≥396
9	0-5%	≥466

Table 5: Luminosity corrected centrality definition for year 2011 Au+Au 200 GeV/c

4.1.5 Dataset QA:

A number of runs were excluded from the analysis based on some problems found during the QA process. The QA cautioned about an unusual Refmult distribution for some runs. A strange 'dip', was observed, for which the cause was not found. **Figure 38** is taken from the QA analysis and shows the Refmult distribution for some runs. It was found that around runs 350003 to 3500013, the average number of track, Refmult, was lower than other runs. Most likely, this loss of track was due to some detector related problem, hence those runs were rejected to avoid any non-physics related issue influencing our results.

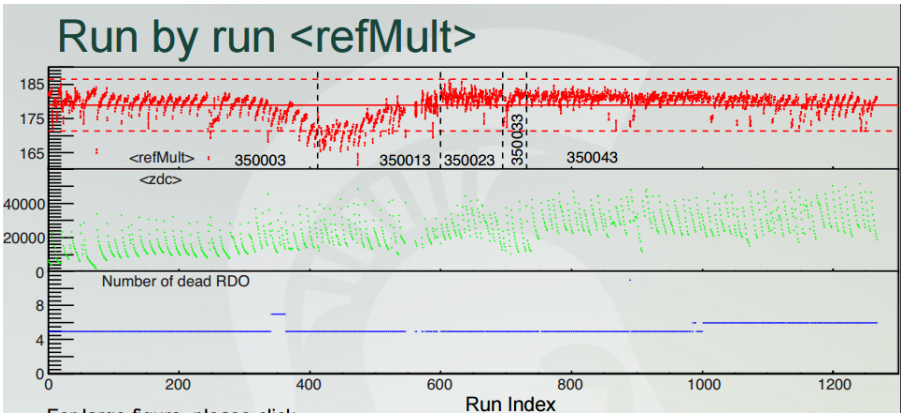

Figure 38: Taken from QA analysis for year 2011 Au+Au 200 GeV/c. Un-corrected reference multiplicity distribution is shown for various run numbers. **[50]**.

4.2 V^0 RECONSTRUCTION

Strange neutral particles such as K^0_s and $\Lambda(\overline{\Lambda})$ in the intermediate p_T region (3-6 GeV/c) are studied in this analysis. These are weakly decaying particles and have a relatively long lifetimes with decay length $c\tau$ of about several centimeters. After being produced at the initial interaction region, where the heavy-ion collision occurs, these particles travel some distance before decaying into their daughter particles. Neutral particles are not detected in the TPC and most of these strange particles decay before reaching the TPC. However, their decay daughters (pions and protons) can be detected in the TPC, and are used to reconstruct the strange particle using their decay topology. The weak decay channels used for reconstruction in this analysis for K^0_s and $\Lambda+\overline{\Lambda}$ are listed in **Table 6**. All of these particles decay into two oppositely charged particles; pions and protons (anti-protons).

Particles	Mass (GeV/c^2)	cτ (cm)	Decay Channel	Branching Ratio
K^0_s	0.4976	2.6842	$\pi^+\pi^-$	69.20%
Λ	1.116	7.89	$p\pi^-$	63.90%
$\overline{\Lambda}$	1.116	7.89	$\overline{p}\pi^+$	63.90%

Table 6: Invariant Mass, Decay length and Weak Decay Channels of Strange Particles

To reconstruct the strange particle, all possible combinations of two oppositely charged global tracks are considered as decay daughters of strange particle candidate. Topology of the strange particle decay is used to place cuts on various decay parameters. **Figure 39** shows the decay topology sketch for a strange neutral particle.

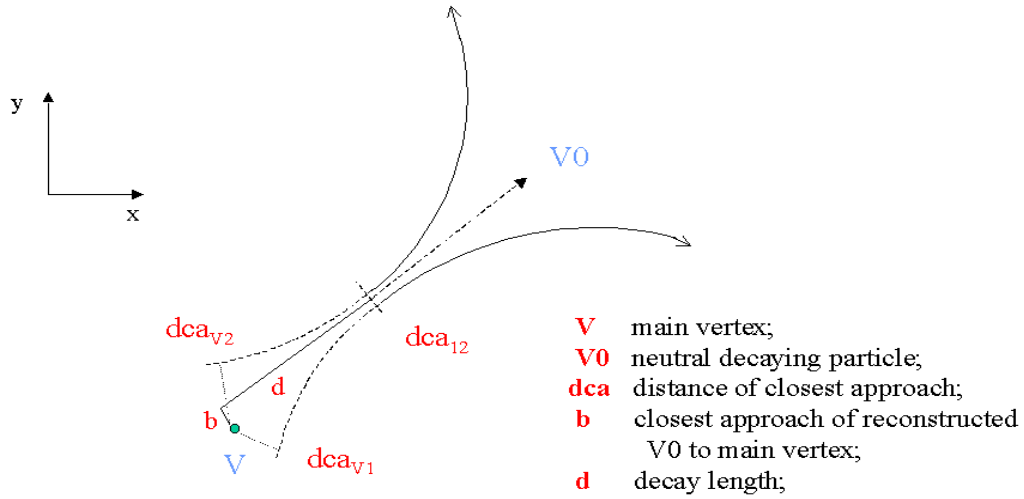

Figure 39: Decay topology of a neutral particle.

The strange particle produced at the primary vertex during the collision decays at the secondary vertex after travelling some distance. Distance between the primary and the secondary vertex refers to the decay length *d* of the candidate particle. If the selected particle pair really comes from the same secondary vertex, then theoretically, the distance of closest approach between the two tracks dca_{12} should be zero. This distance (dca_{12}) is calculated using track helix information of the corresponding global track. Detailed math derivation of the method is discussed in a former STAR thesis [51]. To account for practical limitations on detector resolution this distance is allowed to be greater than zero and a cut is placed to reduce combinatorics background in selection of a possible daughter track pair. Momenta of the decay daughters at the secondary vertex are also calculated. The average position of the closest points of the candidate pair is taken as the position of the secondary vertex.

After assigning masses appropriate for the corresponding weak-decay channel, invariant mass of the candidate strange particle is calculated using Eq. 20, taking energy and momentum conservations into account. Momentum of the reconstructed strange particle candidate is the sum of the momenta of the two decay daughter tracks.

$$M = \sqrt{E^2 - \vec{p}^{\,2}} = \sqrt{(E_+ + E_-)^2 - (\vec{p}_+ + \vec{p}_-)^2} \qquad \textbf{Eq. 20}$$

where, $E_{+,-} = \sqrt{m_{+,-}^2 + \vec{p}_{+,-}^{\,2}}$.

If the strange particles are produced in the collision at the primary vertex then its DCA to the primary vertex *b* should also be zero. A cut on this distance is placed to reduce random combination of oppositely charged tracks.

Secondly, since the charged particles travel on a helical path in the presence of a magnetic and electric field, their radius of curvature is proportional to their momentum, i.e. $r \propto mv$. Therefore, particles with higher momenta would have a larger radius and consequently should have smaller DCA to the primary vertex considering the kinematics of the decay. Cuts on the distance of closest approach of individual tracks (DCA_{v1} and DCA_{v2}) are selected based on the decay kinematics, mass and momentum of the track.

To further tune the topological cuts and optimize the signal to background ratio, a small sample of the reconstructed strange particles is created with loose topological cuts. Efficiency of a cut is calculated by studying the cut value in two mass regions; around and away from the expected mass of the strange hadron, referred to as 'peak' and 'sidebands' regions, respectively. Boundaries of these regions used in this analysis are listed in **Table 7**. **Figure 40** shows these mass regions for a sample invariant mass distribution.

	K^0_s (GeV/c^2)	Λ (GeV/c^2)
Peak region (S+C)	0.48-0.52	1.11-1.122
Left Sideband (A)	0.42-0.46	1.09-1.10
Right Sideband (B)	0.54-0.58	1.135-1.155

Table 7: Peak and sideband mass region boundaries selected for this analysis

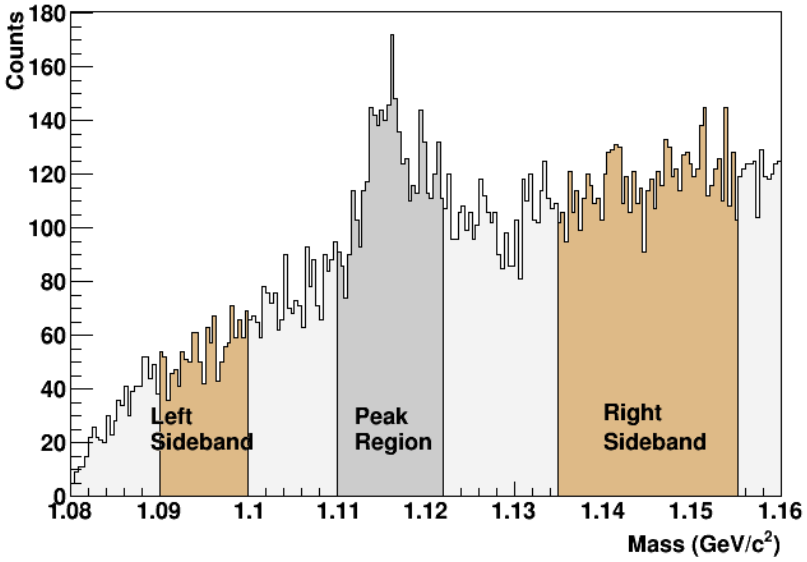

Figure 40: Sample invariant mass distribution is shown. Shaded region in the middle 'peak region' represents the region around the expected mass of the strange hadron. Two shaded regions on the sides 'left and right sidebands' are chosen away from the expected mass to estimate the background

To estimate the background in the peak region, a combination of a Gaussian function and a 2nd order polynomial function (Eq. 21) is fitted to the invariant mass distribution. The polynomial is used to describe the background. **Figure 41** shows the fit for $\Lambda+\overline{\Lambda}$ signal in the sample dataset with fit parameter a_1 fixed at the expected mass of the $\Lambda(\overline{\Lambda})$ baryon.

$$f(x) = a_0 \exp(-(\frac{x-a_1}{a_2}))^2 + b_0 + b_1 x + b_2 x^2, \qquad \text{Eq. 21}$$

where, α_0 and α_2 are the amplitude and width of the mass peak, respectively, α_1 is fixed at the expected mass of the measured particle. Coefficients b_0, b_1 and b_2 belong to the 2nd order polynomial used to describe the background.

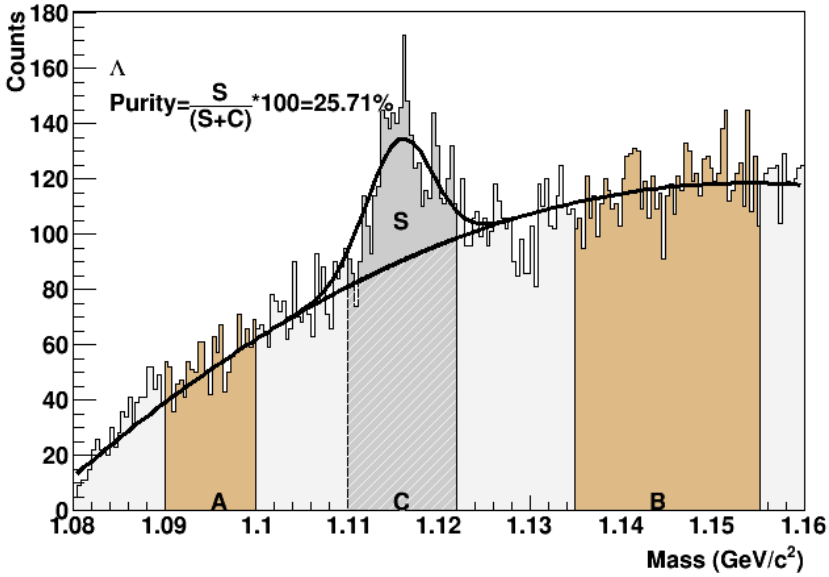

Figure 41: Sample Λ invariant mass distribution fitted with a combination of a Gaussian and a 2nd order polynomial function. Sideband regions are marked A and B, Signal in peak region is marked S and estimated background in peak region is marked C.

Number of particles in the peak region S+C, and in sideband regions A and B are calculated by bin counting. The polynomial fit function is used to calculate the number of background particles C in the peak region. To account for the differences in the widths of mass regions selected, a scaling factor λ is calculated using Eq. 22

$$\lambda = \frac{N_C}{N_A + N_B} \qquad \text{Eq. 22}$$

where N_A, N_B, and N_C are number of particles in regions A, B, and C in **Figure 41**.

To obtain a distribution of a given cut for 'pure' signal, background needs to be subtracted from the peak region. Therefore, cut distribution of particles in sideband are subtracted from the cut distribution of particles in the peak region, after scaling the sidebands by λ. Number of particles in 'pure signal' and 'sideband' regions are then used to calculate signal and background efficiencies and signal to background ratio for all possible cut values. Purity of the signal is calculated by taking ratio of particles in 'pure signal' and the total number of particles in the peak region. A cut value is then chosen where the efficiency of the cut is maximized. The goal is to lose as much background as possible while optimizing the signal to background ratio. Cut efficiencies are plotted for various topological variables are plotted and shown in **Figure 42**. The vertical lines in the figure represent the cut values chosen for each kinematic quantity. No differences were found in the cut efficiencies for Λ and Λ-bar, hence same cuts are used. **Table 8** lists the optimized cuts. Same cuts were used for all p_T and centrality bins.

	DCA V^0 to PV	**DCA Daughters**	**DCA $\pi^{\pm}$ to PV**	**DCA $p^{\pm}$ to PV**	**Decay Length**
K^0_s	<0.4cm	<0.5cm	>0.8cm	-	>0.0cm
$\Lambda(\bar{\Lambda})$	<0.5cm	<0.5cm	>1.0cm	>0.3cm	>10.0cm

Table 8: Optimized topological cuts for K0s and $\Lambda(\bar{\Lambda})$ for all centralities and $3.0<p_T<6.0$ GeV/c

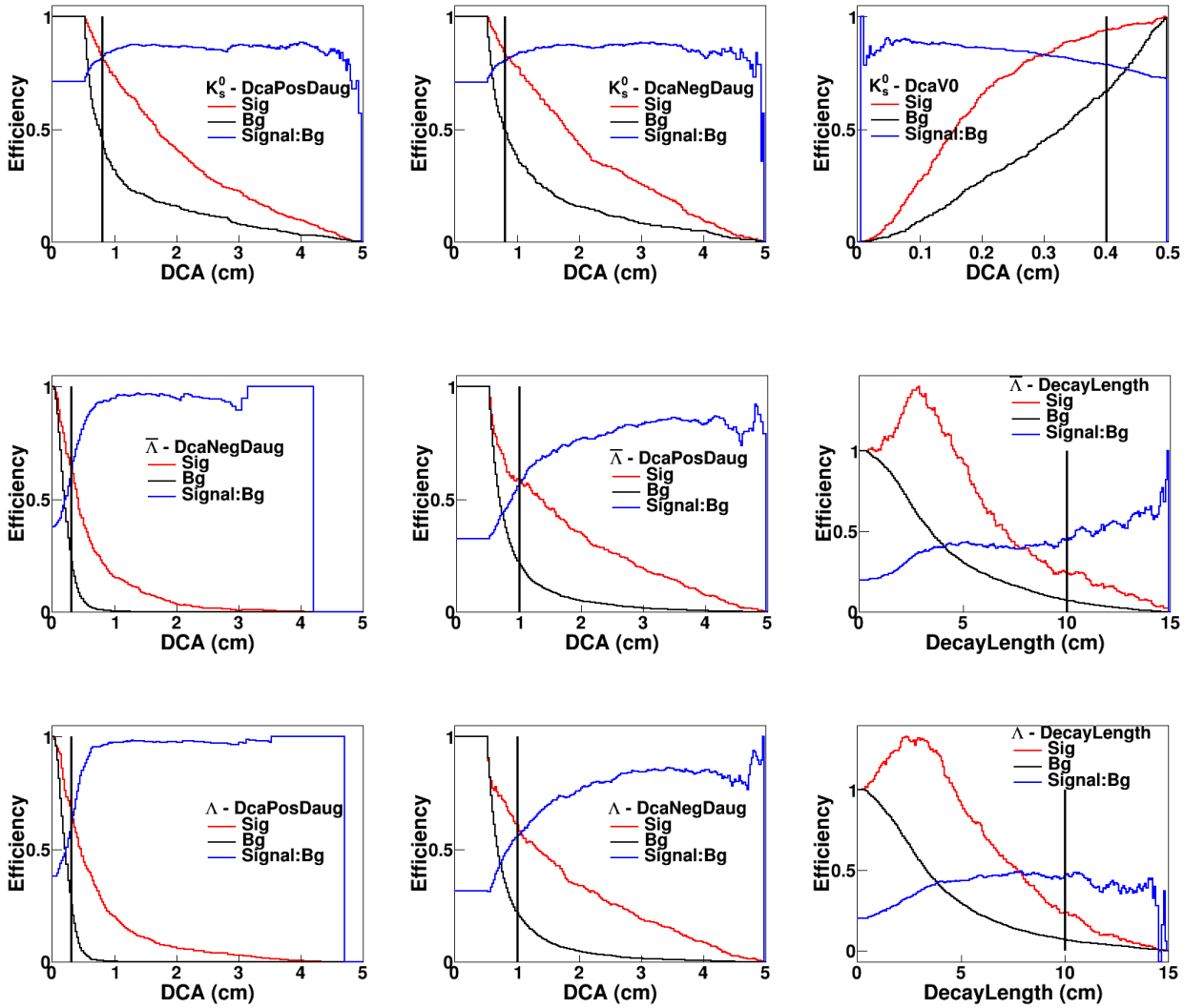

Figure 42: (Top to Bottom) Cut Efficiencies for K^0_s (top), Λ (middle), and (bottom) with p_T=[4.0-6.0 GeV/c]. Signal efficiency, background efficiency and Signal purity (cut efficiency) are plotted in Cyan, Red and Black, respectively. Left to Right (top row:) a) DCA of negative daughter; b) DCA of positive daughter; c) DCA of candidate particle; Left to Right (middle and bottom rows:) a) DCA of negative daughter; b) DCA of positive daughter; c) Decay Length of candidate particle

Invariant mass signal, in the sample data, after applying optimal topological cuts are shown in **Figure 43**. Full dataset with the optimized cuts is then produced. **Figure 44** shows the final reconstructed signals for K^0_s and $\Lambda+\overline{\Lambda}$ in different centrality bins. Only one highest p_T particle is selected per event.

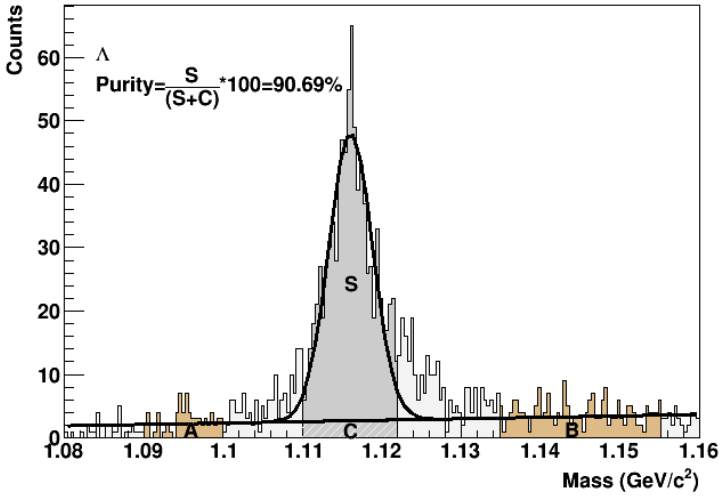

Figure 43: Sample invariant mass distribution after applying the optimized topological cuts. Shaded regions labeled A and B represent left and right sidebands, region C represents the background, under the signal in peak region, derived from the fit function, and region S represents 'pure signal' after subtracting background C from the peak region

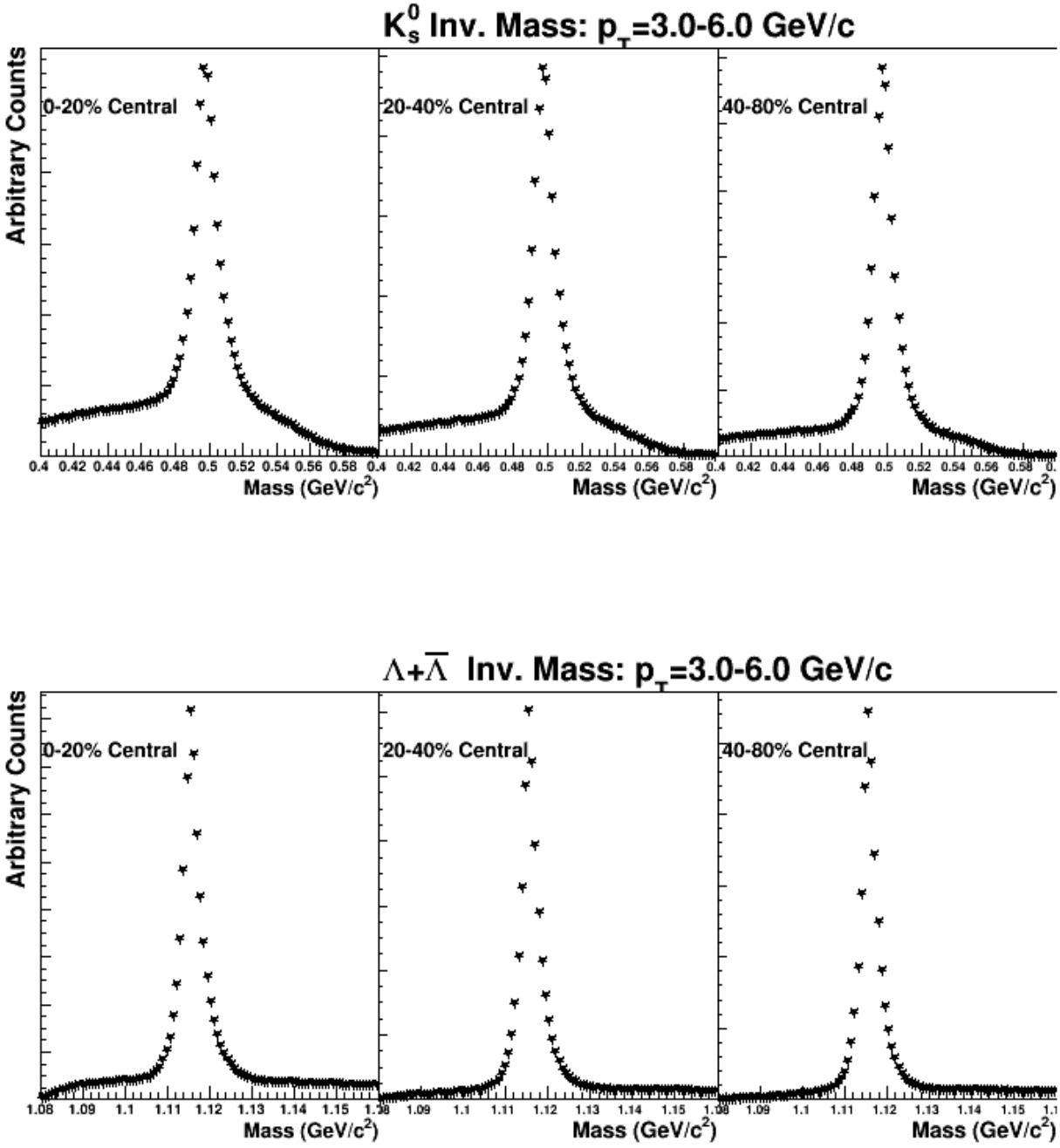

Figure 44: Reconstructed signal for K0s (top), and Λ+ (bottom) with pT=[3.0-6.0 (GeV/c)] are plotted for three centrality bins used in the analysis.

4.3 DI-HADRON CORRELATIONS

Di-hadron correlations studied in this work are described as the relative angular distributions of all charged particles, called 'associated tracks' or hadrons, with respect to the direction of a selected particle, called 'trigger'. Trigger particle here is defined as a reconstructed strange particle satisfying two conditions; 1) it is the highest p_T particle of an event, and 2) its transverse momentum is at least 3.0 GeV/c. The associated particles are selected with transverse momentum within 1.5-3.0 GeV/c.

The relative azimuth and relative pseudo-rapidity are defined as:

- $\Delta\phi = \Phi_{trigger} - \phi_{associate}$
- $\Delta\eta = \eta_{trigger} - \eta_{associate}$

The correlation function can be described by the following equation:

$$\frac{1}{N_{trig}}\frac{d^2N}{d\Delta\phi d\Delta\eta} = \frac{1}{\varepsilon(\eta, p_T)}\frac{1}{\varepsilon(\Delta\phi, \Delta\eta)}\frac{d^2N^{raw}}{N_{trig}\Delta\phi\Delta\eta}, \qquad \text{Eq. 23}$$

where, N is the final corrected count of all associated charged particles, and N^{raw} is the uncorrected count. Final yield is normalized per trigger. $\epsilon(\eta,p_T)$ is the single track efficiency (see Section 4.3.1), and $\epsilon(\Delta\phi,\Delta\eta)$ is the pair acceptance correction factor (see Section 4.3.4) applied to each track.

4.3.1 Single Track Reconstruction Efficiency

Not all tracks measured by TPC can be reconstructed. Some tracks are lost due to physical conditions and structure of the detector, large number of hits, electronics inefficiencies, etc.

Lower momentum tracks, that spiral inwards and do not pass through the active volume of the TPC might also get lost in the reconstruction chain. These losses must be corrected for in order to get accurate physics result of any measurement.

To correct for these losses, single track reconstruction efficiency is calculated using Monte Carlo simulation. Trajectories of some (usually 5% of total multiplicity) particles of interest are simulated using GEANT-3 [52], taking into account the real time conditions and geometry of the detector. These tracks are then embedded in real data. Same track reconstruction techniques are used as for the real data. After applying desired quality cuts, same as used for data, ratio of tracks reconstructed and number of total tracks embedded gives us track reconstruction efficiency.

For the current analysis, the tracking efficiency were calculated using charged pion (π^+, π^-) embedded data. Charged pions make up majority of the particles detected in the final state of the collisions and it has been seen that the effective efficiency for reconstructed charged particles (kaons, protons and pions) are similar for particles with p_T > 1.0 GeV/c. Charged pion embedded data from year 2004 and 2011 was analyzed, and tracking efficiency calculated from the run-04 data was selected due to some un-resolved issues with run-11 embedding data (see section 4.3.2). Single track efficiency depends on both p_T and η.

Figure 45 shows the p_T dependence of the 2004 efficiency for various centrality bins. The efficiency was parameterized using the following two dimensional function:

$$F(p_T,\eta) = F(x,y) = c_0 + c_1x^2 + c_2x^4 + c_3x^6 + c_4x^8 + c_5e^{c_6y} + c_7y + c_8y^2 \qquad \text{Eq. 4.2}$$

where, the variables c_n's are derived by fitting this function to efficiency calculated from the embedding data. **Table 9** lists these values for all centrality bins. The parameterization was

chosen purely to reproduce the shape of the efficiency. **Figure 46** shows sample parameterization of the efficiency for 0-5% most central data.

Single track efficiency correction is applied by using the inverse of the efficiency calculated as weight for every associate track. Since the results are normalized per trigger efficiency correction applied to only associate tracks is sufficient.

In order to properly account for the differences in the data sets of year 2004 and year 2011, a data-driven approach was used. Two-dimensional maps, ϕ:η, were prepared for both year 2004 and 2011 minimum bias data for all centrality bins. **Figure 47** shows these maps for *5%* most central data for both years. For both years 2004 and 2011, data was collected using two magnetic field settings, Full Field and Reverse Full Field. To account for any differences arising from these settings two sets of ϕ:η maps were created corresponding to each magnetic field setting. Tracks within $1.5 < p_T < 3.0$ GeV/c were included in these maps after applying further quality cuts as used for associate tracks.

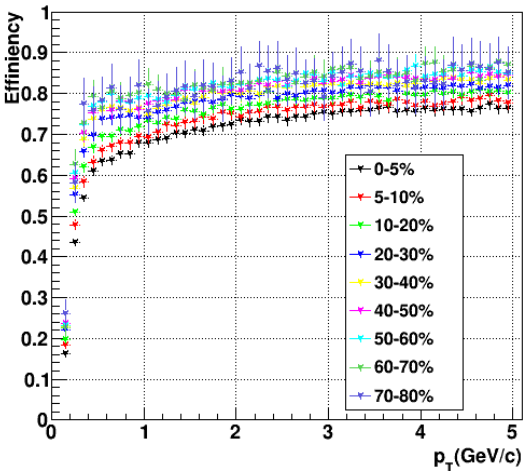

Figure 45: Year 2004 π± Efficiency Vs. pT is is shown for various centrality bins; 0-5% being the 5% most central events for Au+Au 200 GeV.

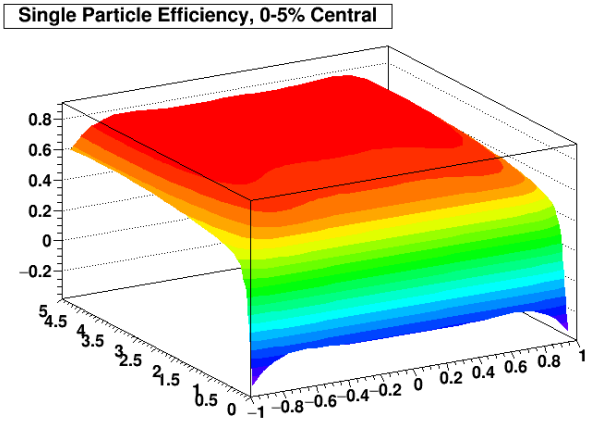

Figure 46: Year 2004 parameterized efficiency fit for 0-5% central events for Au+Au 200 GeV

	0-5%	5-10%	10-20%	20-30%	30-40%
C_0	0.618034	0.643162	0.685657	0.721186	0.739045
C_1	-0.0837758	-0.0312013	-0.0869841	0.0163749	-0.0298143
C_2	0.777011	0.285862	0.646615	0.0452373	0.274268
C_3	-1.30819	-0.321645	-1.08308	-0.0279497	-0.403919
C_4	0.400507	-0.163406	0.313978	-0.261357	-0.0656258
C_5	-1.52736	-1.66035	-1.88648	-2.00331	-2.46673
C_6	-7.98367	-8.44102	-8.91262	-9.13054	-0.103708
C_7	0.0769166	0.0746654	0.0615317	0.0512645	0.0466928
C_8	-0.00940549	-0.00920344	-0.00713399	-0.00597879	-0.0050243

	40-50%	50-60%	60-70%	70-80%
C_0	0.748151	0.754028	0.777113	0.705604
C_1	0.0367997	-0.00766688	0.0444908	0.113575
C_2	-0.110651	0.0461481	-0.302917	0.143447
C_3	0.198323	0.00377836	0.672338	-0.912715
C_4	-0.338684	-0.259026	-0.695591	0.461372
C_5	-2.73071	-2.95293	-1.85981	-1.84134
C_6	-0.108512	-0.111304	-8.15266	-9.19443
C_7	0.0461091	0.0454114	0.02345	0.0505106
C_8	-0.00501508	-0.00474997	-0.000922917	-0.00574011

Table 9: Parameterization variables derived from fit, for year 2004

To correct for geometry and acceptance differences between the two years, a η-ϕ-dependent "translation" map is constructed by taking a ratio of 2004/2011 maps. The translation maps were used as a means to transform 2011 data to match 2004 data, so that track efficiency from year 2004 can be applied. A ϕ–averaged version of these maps was used to minimize the error propagation due to lower statistics in lower reference multiplicity bins. Every associated track is weighted according to these translation maps.

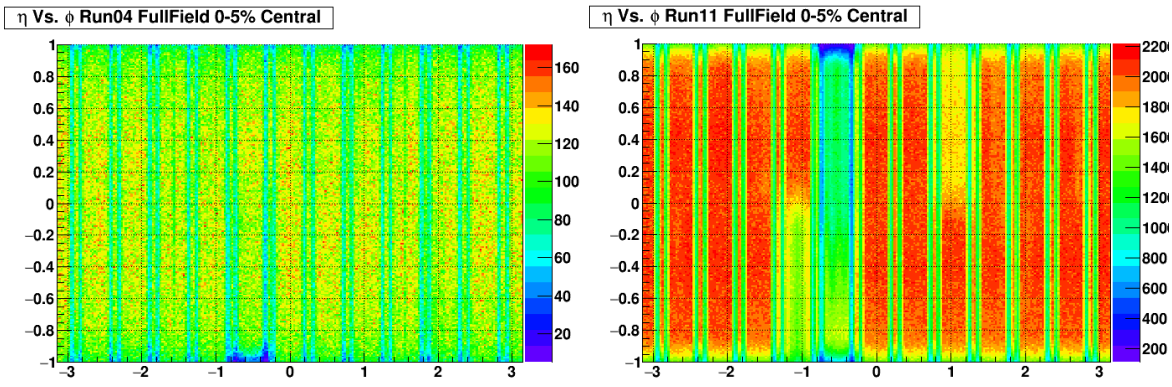

Figure 47: Associate tracks ϕ:η maps for Run04 (left) and Run11 (right) for 0-5% Central data for FullField

In 2011 maps, in addition to a dead TPC sector, some other centrality and magnetic field dependent "bad performing" sectors were also found. These sectors were masked, i.e. excluded from the analysis. Any associated particle, reconstructed strange particles or their daughter particles tracks found in the masked region were discarded. Ranges for the sectors that were excluded are listed in **Table 10**.

Centrality	FullField	Reversed FullField
0-20%	$-1.35<\phi<-0.2$	$-1.85<\phi<-0.2$
	$-1.0<\eta<1.0$	$-1.0<\eta<1.0$
20-80%	$-0.85<\phi<-0.2$	$-0.85<\phi<-0.2$
	$-1.0<\eta<1.0$	$-1.0<\eta<1.0$

Table 10: Centrality and b-field dependent TPC regions masked in this analysis of year 2011 Minimum bias dataset.

4.3.2 2011 Efficiency

Single track efficiency was also calculated for data taken in year 2011. During a cross check some discrepancies were observed which suggested potential problems in the 2011 embedded data. For this cross check, corrected p_T distributions from Run 04 and Run 11 were compared and a difference of more than *10%* was observed. **Figure 48** shows the raw and corrected distributions and their differences for year 2004 and 2011. The source of these discrepancies was not found therefore it was decided not to use year 2011 single track efficiency in this analysis.

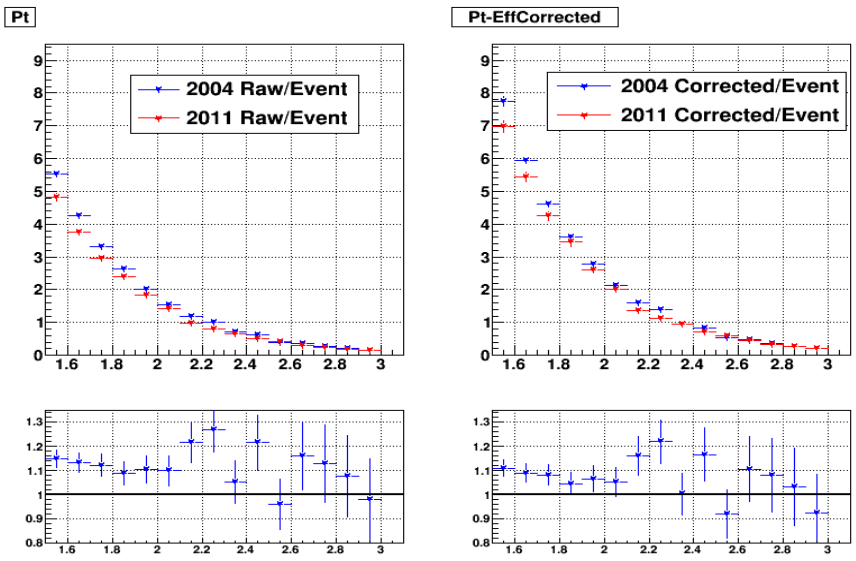

Figure 48: p_T distributions, normalized per event, for Run year 2004 and 2011 are plotted (Left) raw, (Right) corrected by tracking efficiencies of respective years. The differences amongst the two years are plotted in the bottom panels

4.3.3 Raw Di-hadron Correlations

Algorithm used to construct the raw di-hadron correlations is described here. Same algorithm was used for all data. An event is selected using the event selection criteria, described in Section 4.1.2. Global and primary tracks are then analyzed for each event.

High transverse momentum (p_T > 3.0 GeV/c) strange neutral particles are used as trigger particles. For comparison, correlations are also constructed with unidentified charged particle triggers. Strange trigger candidates are reconstructed from global tracks using techniques described in Section 4.2, whereas primary tracks are used to select unidentified charged trigger

candidates and associated particles. All particles found in the masked sectors are discarded to avoid issues arising from any dead or significantly low performing TPC sectors.

Highest p_T trigger particle is selected for each event and the following information is saved for its track. In case of reconstructed trigger particle, track specific information is saved for the daughter tracks, e.g. track id.

- Run number
- Event number
- Vz (vertex position along the beam axis)
- Centrality
- Track id
- ϕ, η, and p_T

Finally, angular distributions of all associated particles, relative to the trigger particle, are calculated. For this analysis, three distributions were made corresponding to the three centrality bins (Section 4.1.4) chosen for this study. Primary tracks associated with global tracks of the daughter particles of the neutral trigger are excluded from the correlation measurements to avoid self-correlation.

4.3.4 Pair Acceptance Correction

After applying the single particle efficiency, additional corrections are needed to tackle some other acceptance effects pertaining to the acceptance of particle pairs. The $\Delta\phi$ distribution is affected by the physical gaps between the TPC sectors. The relative azimuthal value for an associated track with respect to the trigger particle depends on their position in regards to the

sector gaps. Therefore, the $\Delta\phi$ distribution shows a non-uniform structure. A hypothetical ϕ distribution was studied to see the effects of the sector gaps on the $\Delta\phi$ distribution and results are shown in **Figure 49** [15].

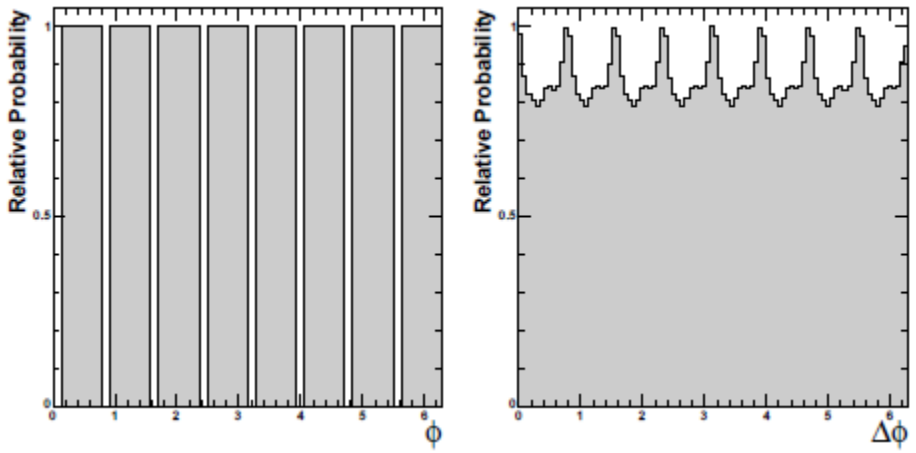

Figure 49: (Taken from **[15]**) (Left) A hypothetical TPC azimuthal acceptance with sector gaps, (Right) Relative angular difference constructed, normalized to unity for maximum acceptance.

Selective acceptance in η, $|\eta| < 1$ for trigger and associated tracks, also creates a unique structure in the $\Delta\eta$ distribution. To understand this effect, a simple simulation was used to construct a sample TPC acceptance in pseudo-rapidity with the $|\eta|<1$ cut applied. The resulting $\Delta\eta$ distribution exhibits a triangular shaped distribution, shown in **Figure 50**. Both of these effects have some p_T dependence hence corrections are derived from data for each p_T bin separately, using mixed-event method. Unlike the single track reconstruction efficiency, the

pair acceptance correction is applied after the data has been processed.

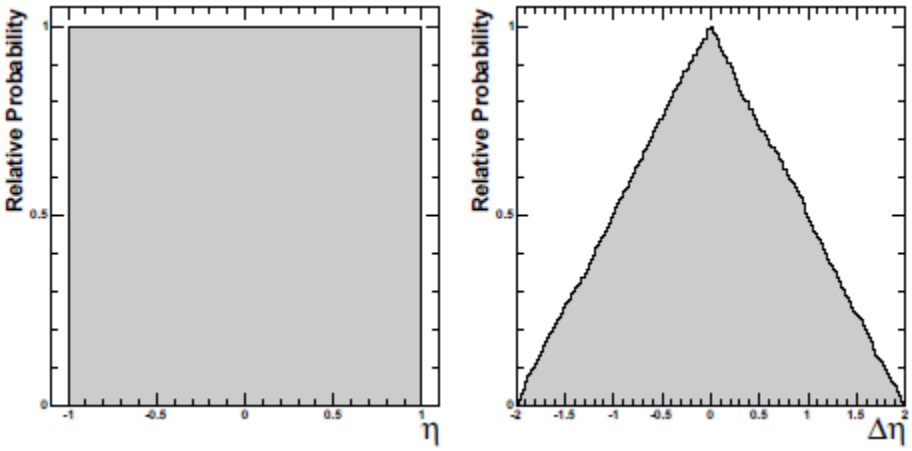

Figure 50: (Taken from **[15]**) (Left) Simulated η acceptance in TPC for |η|<1, (Right) Resulting $\Delta\eta$ distribution, normalized to unity for maximum acceptance.

To calculate pair acceptance corrections; a di-hadron correlation needs to be constructed that doesn't have any physical correlation, and can only be described by geometrical and acceptance effects. This is achieved by using the exact same method as the real correlation but the trigger particle is selected from a different event than the associated particle, process commonly used and referred to as the 'event mixing technique'. To account for multiplicity and vertex position dependences, the two different events are required to have same centrality and their vertex position V_z be within 1 cm of each other. Each geometrically similar event is mixed with exactly 25 real triggers.

4.3.5 Masking

As discussed earlier in Section 4.3.1 Single Track Reconstruction Efficiency, some TPC sectors are excluded from the analysis. Because of this exclusion the $\Delta\phi$ distribution shows new sub-structures, most prominent at small angles. To study the effects of the number of sectors masked and their relative position on the real and mixed-event background correlations, sample correlations were constructed with different masked sectors. The results are shown in **Figure 51**.

It is observed that the $\Delta\eta$ distribution retains its triangular shape. However, a considerable change in the $\Delta\phi$ distribution is seen in the form of new sub-structures. The effects of masking only one TPC sector can be understood by realizing that when a trigger is selected, it must come from an un-masked sector, hence all the associated tracks close to it are available. Although, for any given trigger, it's position relative to the masked sector is different and loss of tracks due to that masking gets distributed evenly over all $\Delta\phi$. Therefore, it results in a 'hump' created at small angles, around $\Delta\phi$=0.

It can also be noted in **Figure 51** that the structures developed in the $\Delta\phi$ distribution change, depending on the position of the masked sectors. In both the second and third row of **Figure 51**, two sectors are masked. In second row the sectors masked are symmetric around $\Delta\phi$=0, whereas in the third row, they are anti-symmetric. Finally in row three, all of the three sectors are masked at once. The overall sub-structures change with respect to the different masking schemes although, the maximum around $\Delta\phi$=0 and $\Delta\eta$=0, representing maximum acceptance in the mixed-event correlation histogram, remains unchanged.

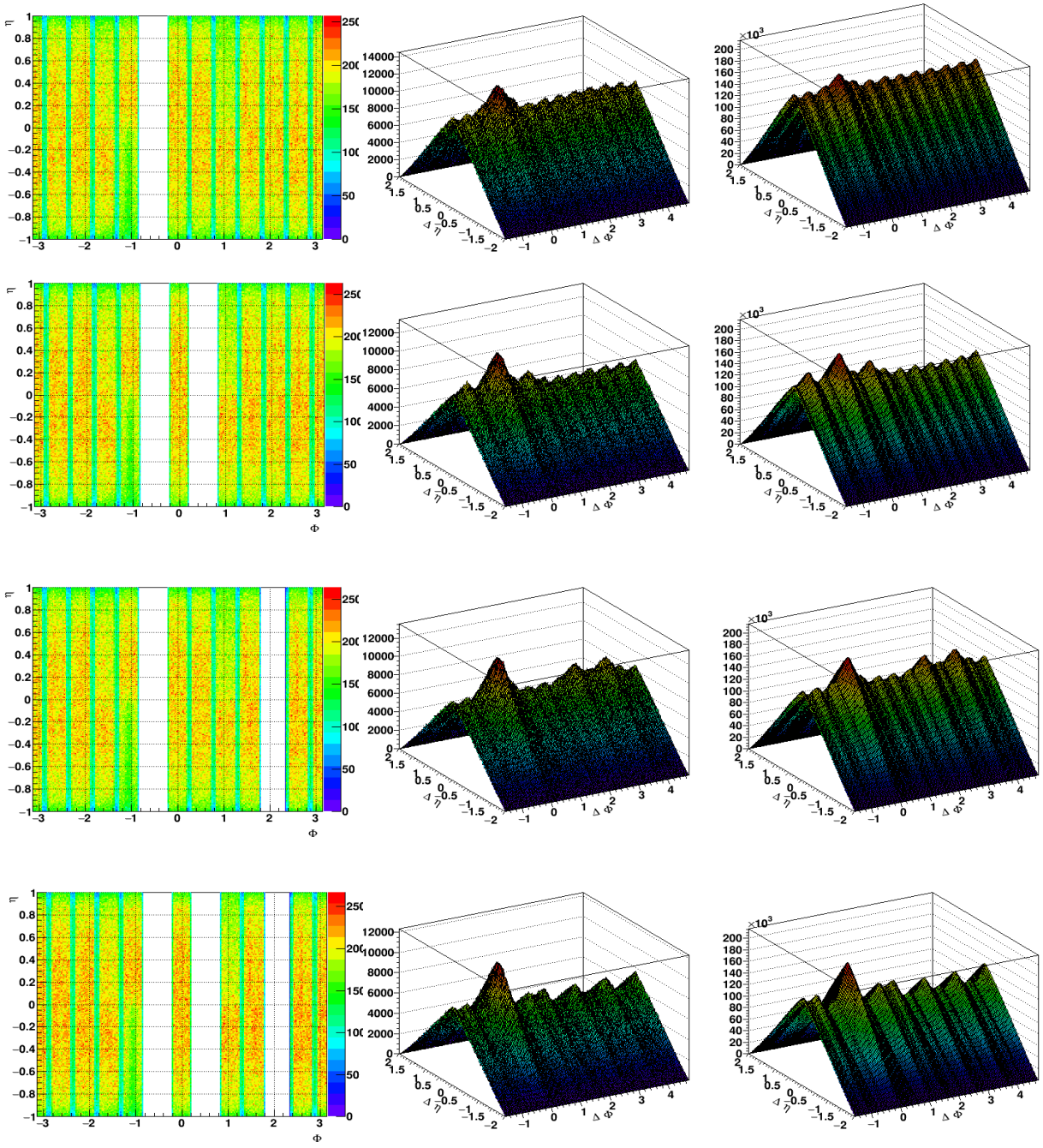

Figure 51: Sample h-h correlations constructed by masking different TPC sectors. Left plots show the masking scheme. Middle and right plots are correlation histograms, and mixed-event background correlation histograms respectively for the corresponding masking scheme

4.3.6 Normalization

To apply the pair acceptance correction, the mixed-event background need to be normalized to unity, to represent 100% acceptance where the maximum occurs (around $\Delta\phi$=0 and $\Delta\eta$=0). Under normal conditions, when no TPC sector needs to be excluded from the analysis, a $\Delta\phi$-averaged $\Delta\eta$ distribution is used to find this maximum. However, in the presence of the unusual sub-structures in the $\Delta\phi$ distribution, due to the masked sectors, using a $\Delta\phi$-averaged maximum is not possible. Therefore, maximum is found by taking the value at $\Delta\phi$=0 and $\Delta\eta$=0. Practically this is done by taking an average of four bins around zero in the two-dimensional mixed-event background distribution. The raw correlations are then divided by the normalized mixed-background to obtain pair acceptance corrected correlations.

4.3.7 Background Subtraction

In addition to the jet-like correlations, all particles are also correlated with the reaction plane which give rise to the underlying background. A commonly accepted explanation of these correlations is given due to anisotropy in the initial state overlap region of the colliding nuclei [53]. These flow contributions can be determined by measuring different flow harmonics as discussed in Section 2.4.1 and must be subtracted to extract jet-like yields. In this analysis, the following functional form was used to describe the underlying background:

$$B(\Delta\phi, p_T) = A(1 + 2\sum_{n=1}^{4} v_n(p_T^{trig}) v_n(p_T^{assoc}) \cos(n\Delta\phi)), \qquad \text{Eq. 24}$$

where, A is the background level, determined by fitting a Gaussian to the $\Delta\eta$ distributions for different centrality bins. A sample fit to data of the above function along with an overlay of individual flow harmonics are shown in **Figure 52**.

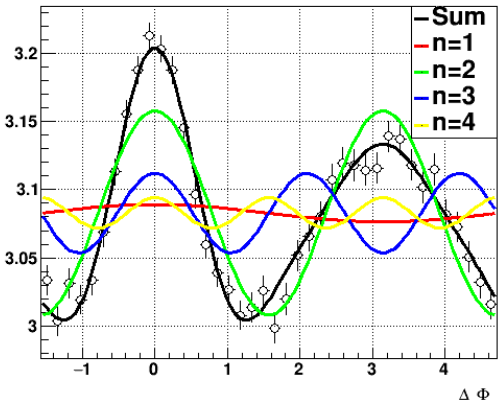

Figure 52: Sample fit to data used to subtract background and measure the coefficients of various flow harmonics. $\Delta\phi$ distribution in region $0.95 < |\Delta\eta| < 1.4$ is plotted which is represented by open symbols. Solid colored lines represent flow harmonics for n=1,2,3, and 4, whereas, the black solid line represents the sum.

The background can be subtracted before or after correcting for track merging effects (see Section 4.3 8). Both options were carried out to calculate systematic uncertainties on final yields resulting from the differences in the methods used. One approach is to describe the correlations in terms of a two-dimensional function (see Section 4.3.8.1) which incorporates the jet-like correlation peak at small angles and uncorrelated background at large $|\Delta\eta|$ in a single function. The background can then be subtracted to extract final corrected yields. An alternate

method is to use the functional fit given in Eq. 24, to describe the one-dimensional $\Delta\phi$ distribution in region $0.95 < |\Delta\eta| < 1.4$, where jet-like contributions are expected to be marginal [15]. The uncorrected jet-like correlation signal or 'pure cone' extracted after subtracting the background can then be fitted with a two-dimensional Gaussian function (see Section 4.3.8.2) to correct for track merging effects. Fits to all p_T and centrality bins used in this analysis are presented in Appendices A and B.

4.3.7.1 Combinatorial Background

Most of the combinatorial background in the trigger selection (coming from a 'fake' neutral particle reconstructed from a random particle pair) is eliminated by using tuned topological cuts. However, in some cases, the background is non-negligible and can dilute the final measurements. For example, in case of a fake (anti-)Lambda, the actual contributions might be coming from a high p_T (anti-)Proton as a result of a random particle combination. To subtract these contributions, another set of correlations were constructed from the neutral particles selected from the side band regions of the invariant mass range (see Section 4.2).

To calculate the number of 'fake' triggers in the 'peak' region, fits were used to describe the invariant mass signal (see **Figure 43**). A normal Gaussian or a generalized Gaussian were used to describe the peak, and background or 'side band' region was described using polynomial functions of different degrees that best described the background shape. 'Side band' correlations were scaled by the scaling factor calculated from the fit and subtracted from the raw correlations. Appendix E shows the fits used for all p_T and centrality bins used in this analysis.

4.4 TRACK MERGING/SPLITTING

One prominent feature of the raw correlations is a significant 'dip' at small angles. This depletion of the correlation signal can be seen (**Figure 53**) in the inclusive charged particle correlations, and is attributed to the phenomena called track merging or track splitting. To extract any final results from the correlations, corrections need to be made to account for the missing tracks.

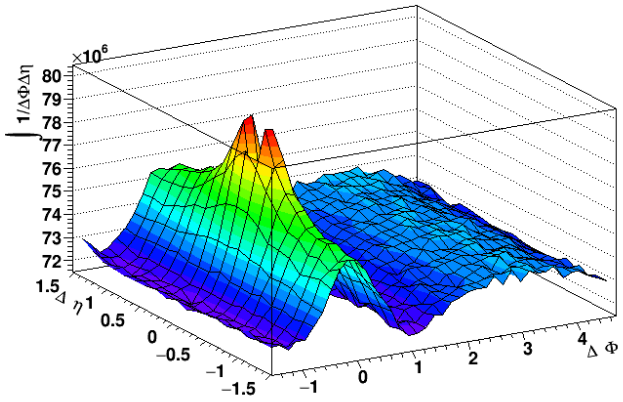

Figure 53: 2D h-h correlations are plotted with $3.0 < p_T^{trigger} < 6.0$ GeV/c and $1.5 < p_T^{assoc} < 3.0$ GeV/c in 0-10% central Au+Au minimum bias data

Track merging or track splitting effects are encountered during the track reconstruction process. Track splitting occurs when two tracks cross each other, and one of the intersected tracks is reconstructed as two smaller tracks. These tracks are then usually discarded during the analysis because they no longer satisfy the track quality cuts. Track merging can happen when two tracks are very close to each other. In that case, if they share enough hits, these two tracks

can be reconstructed as one. **Figure 54** illustrates the possible track merging or track splitting scenarios. The conventional method used to correct for these effects involves constructing correlations for separate charge combinations, used and discussed in detail in a previous STAR thesis [18]. In this method a trigger particle of a specific charge is correlated with only positive and only negative associated particles separately. The different charge combinations result in a slight shift in the depletion about the origin and the corrections are made by symmetrizing the correlations.

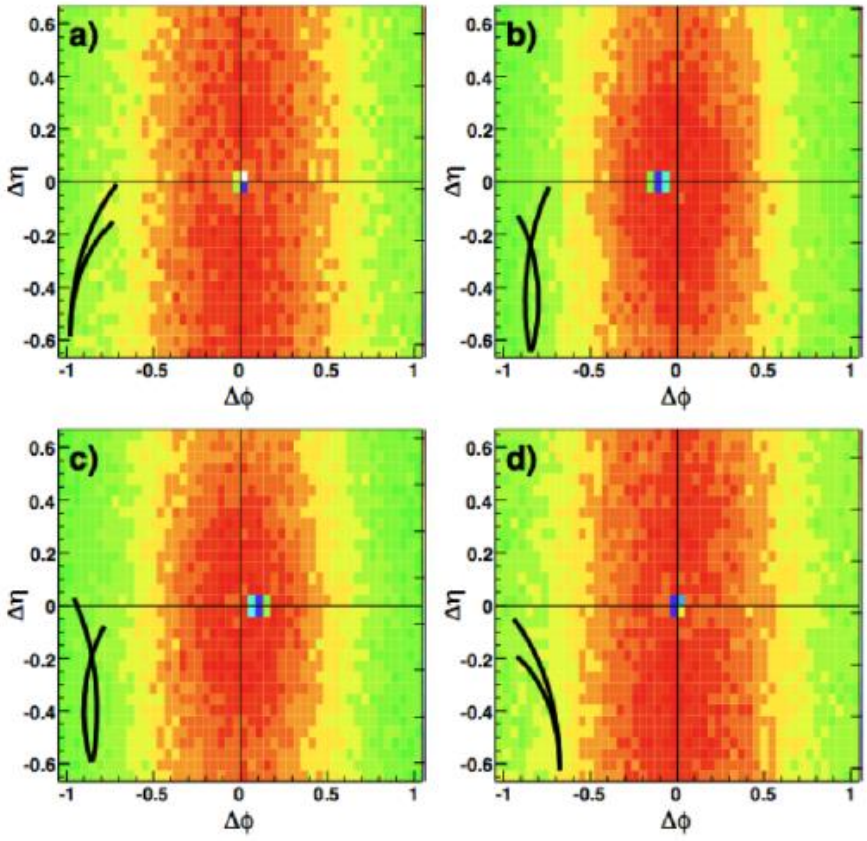

Figure 54: (Taken from **[18]**) Track merging/splitting illustrations

The trigger particles used in this analysis are neutral strange hadrons that are reconstructed from two oppositely charged particles, called 'daughter' particles. The depletion observed in the correlations can have contributions from both of the daughter particles. Therefore, Using charge separation cannot fully eliminate the contribution coming from the other charge. In the current work, charge separation method was used as a reference for the Lambda (anti-Lambda) particles (see Section 4.3.8.3).

4.4.1 Track Merging Correction – 2D Fit Method

It has been described, in detail, in a previous study [18] that the two-dimensional correlations can be described very well by performing a two dimensional fit using the following function:

$$f(\Delta\phi,\Delta\eta) = A(1+\sum_{n=1}^{4} 2V_n \cos(n\Delta\phi)) + B\exp[-(\frac{|\Delta\phi|}{\alpha_\phi})^{\beta_\phi}]\exp[-(\frac{|\Delta\eta|}{\alpha_\eta})^{\beta_\eta}], \qquad \textbf{Eq. 25}$$

where *A* is the uncorrelated background level and *B* is proportional to the strength of the jet-like signal. β_ϕ, $\beta_\eta = 2$ gives a normal Gaussian distribution. The Fourier expansion terms are used to describe the various flow harmonics and the two dimensional generalized Gaussian is used to describe the jet-like yield at small angles.

The two-dimensional fit was performed excluding the region affected by track merging, i.e. at small angles. Data to fit ratio in the bins around $\Delta\eta=0$ and $\Delta\phi=0$ were used as correction factors. **Figure 55** shows sample 2D fit function and the correlations before and after the track merging corrections. The corrections are only applied to the bins that were excluded from the fit.

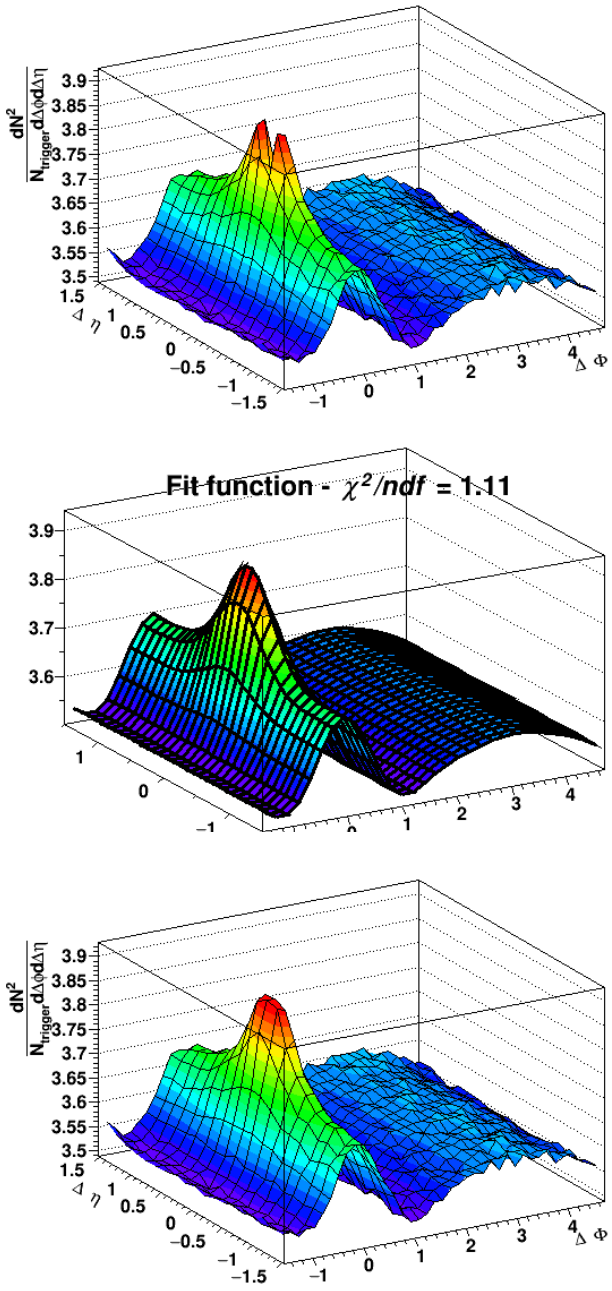

Figure 55: h-h Correlation with $3.0 < p_T < 6.0$ GeV/c in 0-10% central Au+Au minimum bias data. (Top) 2D fit, (Middle) correlations before correction, (Right) Correlations after correction

The two-dimensional fit method has worked well in describing the unidentified charged particle correlations, however, since the exact shape of the correlations is not known, ambiguities in the fit results remain in case of neutral particles. The fit procedure was repeated multiple times varying exclusion ranges and the Gaussian function (standard or generalized). Differences in the fits was used to calculate systematic uncertainty on final yields. **Figure 56**, and **Figure 57** show the best possible fit achieved for a K^0_s-h and Λ-h correlations, respectively, with $3.0 < p_T^{trigger} < 4.0$ GeV/c in 0-20% central events. Correlations, before and after corrections are also plotted.

4.4.2 Track Merging Correction – 2D Fit Method on 'Pure Cone'

To correct for track merging effect after the background has been subtracted a two-dimensional Gaussian function fit is performed on the jet-like peak or the 'pure cone'. Final particle yields calculated using the two-dimensional fits before or after the background subtraction were found to be within 5%. The exclusion ranges chosen for various centrality and p_T ranges are given in **Table 11** and **Table 12** for K^0_s-h and Λ-h, respectively.

	0-20%		**20-40%**		**40-80%**		**60-80%**	
p_T^{trig} (GeV/c)	**$\|\Delta\phi\|<$**	**$\|\Delta\eta\|<$**	**$\|\Delta\phi\|<$**	**$\|\Delta\eta\|<$**	**$\|\Delta\phi\|<$**	**$\|\Delta\eta\|<$**	**$\|\Delta\phi\|<$**	**$\|\Delta\eta\|<$**
3.0-3.5	0.24	0.48	0.24	0.16	0.16	0.16		
3.5-4.5	0.31	0.16	0.16	0.32	0.16	0.16		
4.5-5.5	0.16	0.08	0.16	0.08	0.16	0.16		
3.0-4.0	0.24	0.24					0.16	0.16
4.0-6.0	0.16	0.16					0.16	0.16

Table 11: $\Delta\eta$ and $\Delta\phi$ ranges excluded from the two-dimensional fits for K^0_s trigger particles.

	0-20%		20-40%		40-80%		60-80%	
p_T^{trig} (GeV/c)	$\|\Delta\phi\|<$	$\|\Delta\eta\|<$	$\|\Delta\phi\|<$	$\|\Delta\eta\|<$	$\|\Delta\phi\|<$	$\|\Delta\eta\|<$	$\|\Delta\phi\|<$	$\|\Delta\eta\|<$
3.0-3.5	0.31	0.32	0.24	0.32	0.16	0.16		
3.5-4.5	0.24	0.24	0.16	0.24	0.16	0.08		
4.5-5.5	0.16	0.24	0.16	0.08	0.24	0.24		
3.0-4.0	0.24	0.24					0.16	0.08
4.0-6.0	0.24	0.24					0.0	0.0

Table 12: $\Delta\eta$ and $\Delta\phi$ ranges excluded from the two-dimensional fits for Λ trigger particles.

4.4.3 Track Merging Correction – Embedding Method

A new data-driven method was introduced in this work that used Embedding to correct for the track merging affect. The goal was to capture and calculate the effect of track merging of daughter tracks on angular correlations of high p_T neutral particles. The embedded particles should have no correlations with real data and if two dimensional angular correlations were constructed using these particles only the effects of track merging at small angles should be present.

Tracks simulating the decay of neutral particles with flat p_T = 3.0 – 6.0 GeV/c were embedded in real data uniformly in $0 < \phi < 2\pi$ and $|\eta| < 1.0$, such that two embedded tracks were associated with each simulated decay. To magnify the effect of track merging, 100 V^0 particles were embedded in each real event for 20% most central events. Two separate embedding samples were produced for the two strange particles studied in this analysis: K^0_s and

Λ. Each dataset contains about 1 million real events embedded with 100 trigger particles embedded in each event.

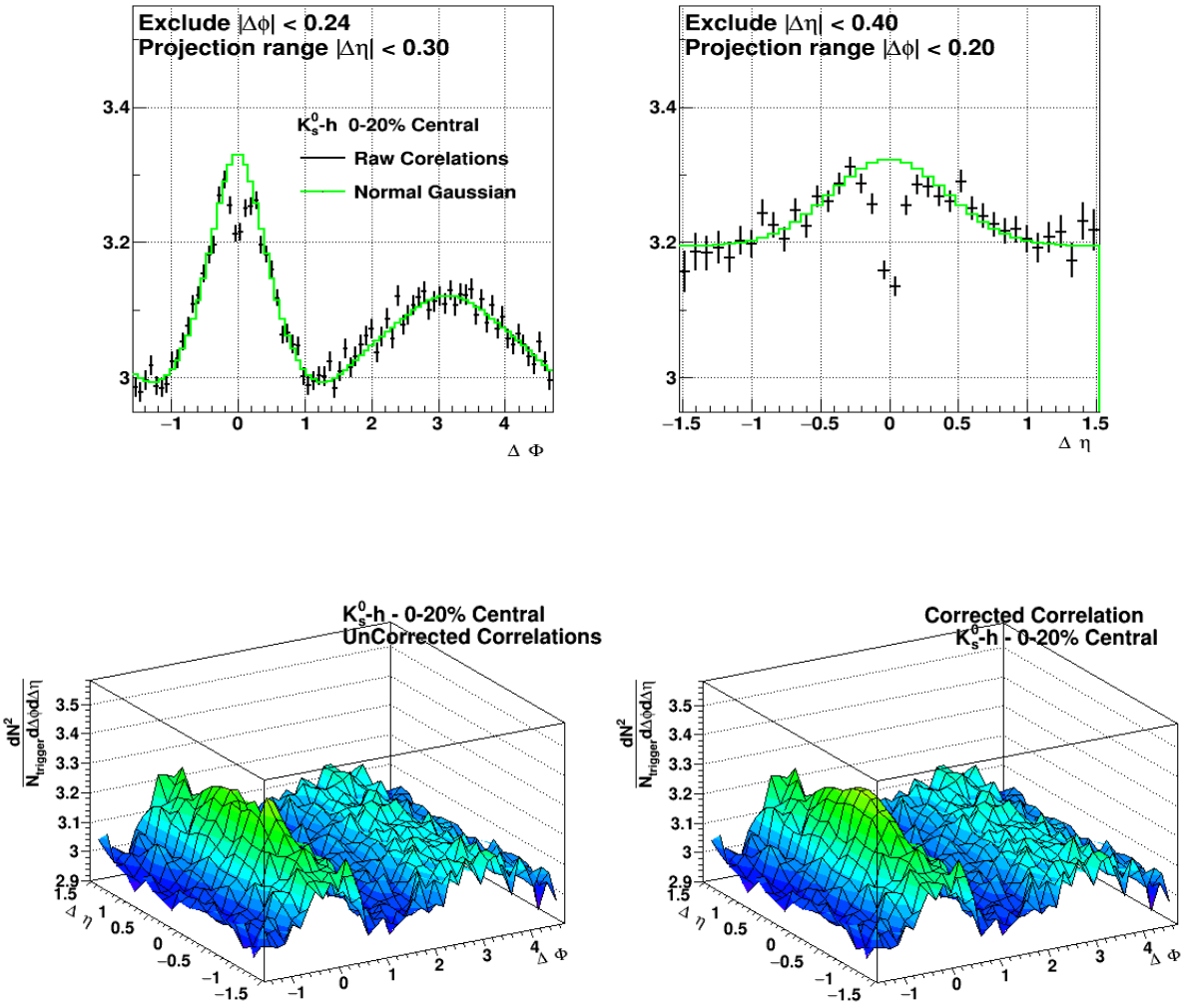

Figure 56: K^0_s-h Correlations with $3.0 < p_T^{trig} < 4.0$ GeV/c and $1.5 < p_T^{assoc} < 3.0$ GeV/c in 0-20% most central $\sqrt{s_{NN}}$ =200 GeV Au+Au Collisions. Top: Δϕ and Δη projections with the fit function are plotted, in black and green respectively. Bottom-Left: Correlations before correction, Bottom-right: Correlations after correction.

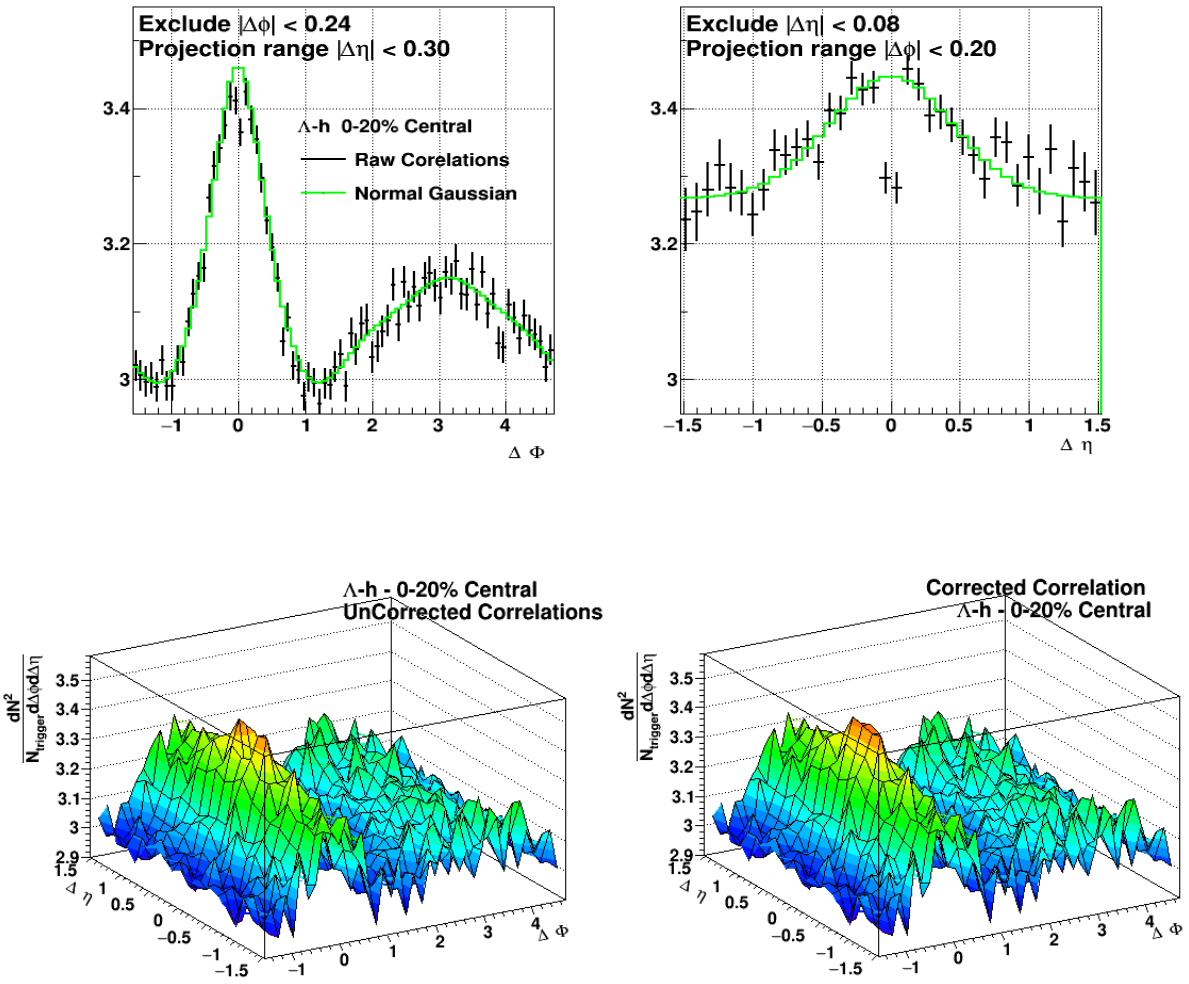

Figure 57: Λ-h Correlations with 4.0 < p_T^{trig} < 6.0 GeV/c and 1.5 < p_T^{assoc} < 3.0 GeV/c in 0-20% most central $\sqrt{s_{NN}}$ =200 GeV Au+Au Collisions. Top: Δϕ and Δη projections with the fit function are plotted, in black and green respectively. Bottom-Left: Correlations before correction, Bottom-right: Correlations after correction

Track reconstruction was performed after the embedding. Simulated tracks that were matched with the global tracks with at least 10 common hits were used to reconstruct the neutral particle. Exact same track quality cuts and decay topological cuts were applied to these tracks in order to reproduce a sample of trigger particle closely matching to those found in data. Ideally, correlations with these embedded trigger particles need to be constructed with reconstructed tracks from 'real' data. Reconstructed tracks that did not match any simulated tracks or those that were matched to primary tracks are stored in separate branches. All unmatched reconstructed primary tracks, after applying track quality cuts, were used as associated particle tracks in the correlations. Tracks that matched with the embedded tracks are most likely 'fake' tracks, i.e. they do not come from the real event, and should not be included in the correlations. Considering the possibility that some 'real' primary tracks, with a small number of common hits, could have coincidently labeled as 'matched' and excluded from the correlations, matched tracks with less than 10 common hits were also considered to be used as associated particle tracks. **Figure 58** shows number of common hits distribution of the matched tracks and the p_T spectra for various cuts on the number of common hits. A falling p_T spectra for common hits < 10 suggests that those tracks might be real, although they only make up less than 1% of the total number of associated tracks available. Difference in embedding correlation with and without including these matched tracks are plotted in **Figure 63**.

Low performing TPC sectors masked in data were also blocked in embedding and separate raw and mixed-event correlations were constructed using the exact same method as real data for full field (FF) and reverse full field (RFF) magnetic field setting. **Figure 59** shows these correlations for Λ and K^0_s.

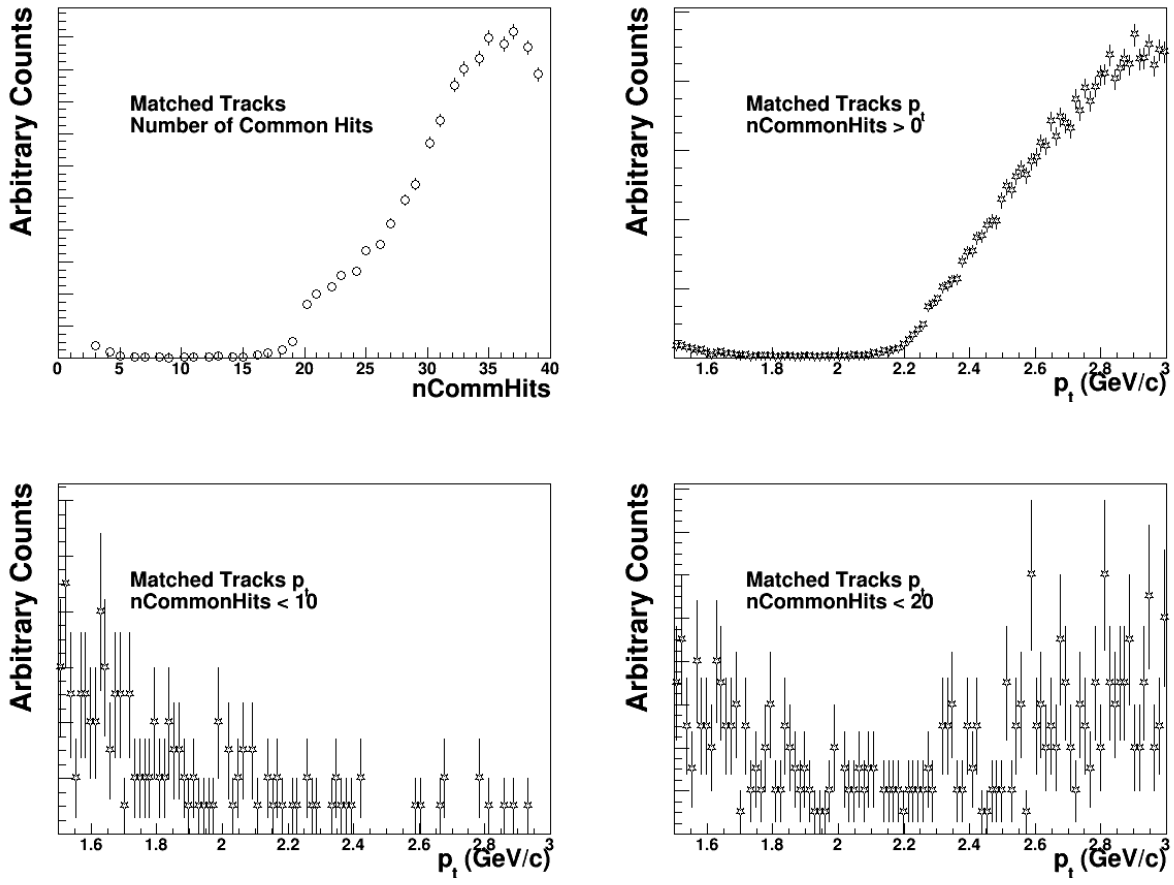

Figure 58: Number of common hits and transverse momentum distributions for various cuts on number of common hits are plotted for reconstructed primary tracks that matched embedded MC tracks.

Correlations for different magnetic field setting (FF, or RFF) were corrected for acceptance and detector geometry using their respective mixed-event correlations (**Figure 60**) and were then added and normalized per trigger. The overall background in the acceptance corrected normalized correlations (**Figure 60** (a)) was found to be around 10% lower than in data. The source of this loss of tracks could not be established. To bypass this issue, the final normalized

embedding correlations were calculated by individually normalizing raw correlations and mixed-event correlations by their respective number of triggers before performing the acceptance correction, i.e. normalized per trigger raw correlations were divided by normalized per trigger mixed-event correlations. These acceptance corrected correlations provide the track merging effect per trigger particle (**Figure 60** (b)).

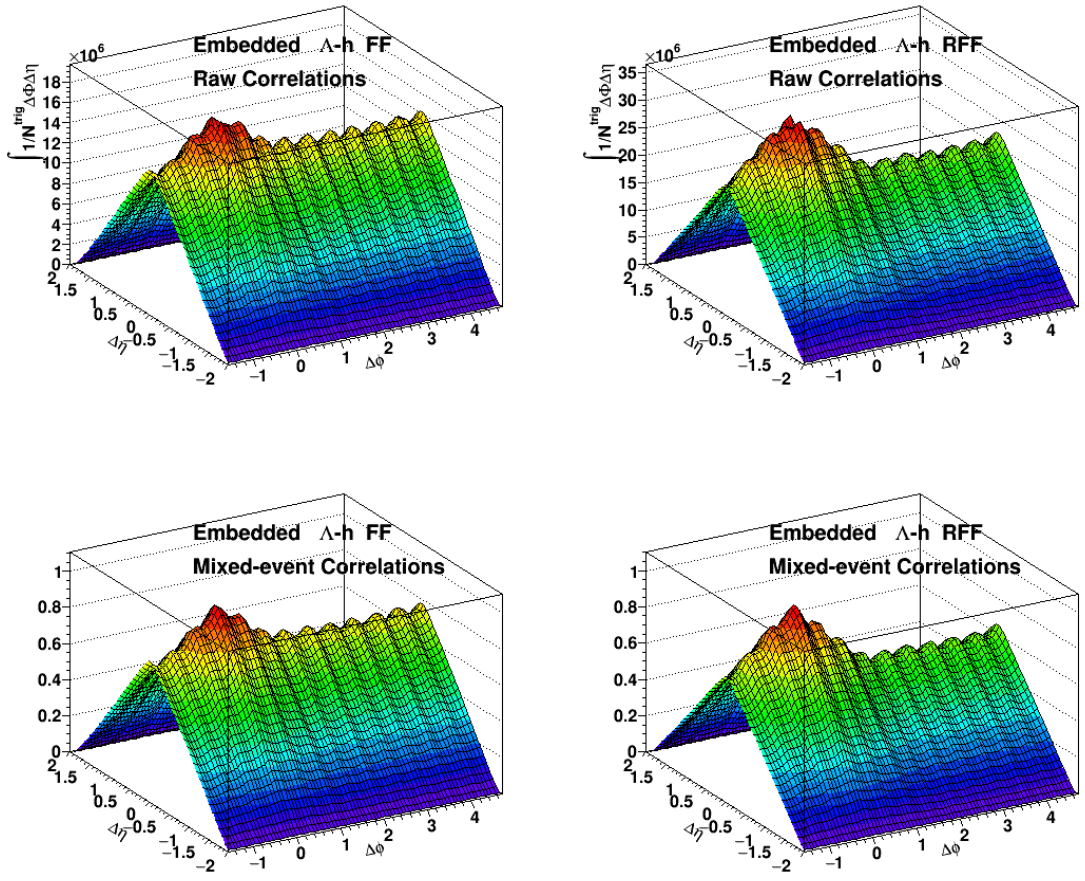

Figure 59: Raw (top) and mixed-event (bottom) correlations are plotted for embedded particles with $3.0 < p_T^{trigger} < 6.0$ GeV/c and $1.5 < p_T^{assoc} < 3.0$ GeV/c for data with full field, FF (Left) and reverse full field, RFF (right) magnetic field settings. Mixed- event correlations are normalized to 1 at average maximum around $\Delta\eta = 0$ and $\Delta\phi = 0$

The reconstructed neutral particle should have no correlations with other real or reconstructed particles, and as expected no such signature structures were found in the correlations. However, we did expect to see an enhanced track merging effect due to a large number of embedded tracks. This effect was clearly seen in the embedded correlations in the form of a significant loss of tracks or 'dip' at small angles.

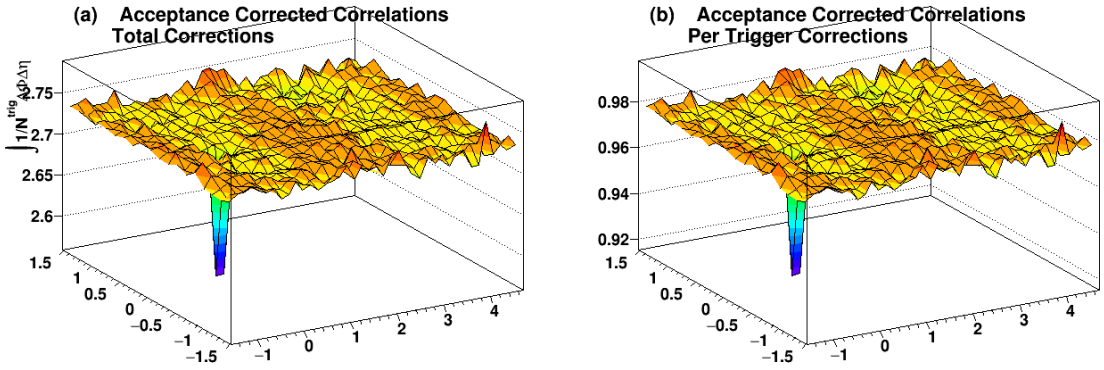

Figure 60: Sample embedded Λ-h correlations with $3.0 < p_T^{trigger} < 6.0$ GeV/c and $1.5 < p_T^{assoc} <$ 3.0 GeV/c. Total (a) and per trigger (b) acceptance corrected correlations are plotted.

When a Lambda particle decays, most of its energy is carried away by the daughter proton, which more or less keeps travelling in the same direction. **Figure 61** shows the relative angular differences and p_T distributions for Lambda with respect to its daughters; proton and π^+.

In case of the embedded Lambda particles two separate 'dips', with unequal magnitudes, were observed presumably resulting from the track splitting of the daughter proton. The separation in the dips can be attributed to the small relative difference in the direction of the

Lambda and its daughter proton. A two-dimensional view of these dips is shown in **Figure 62** for different magnetic field settings. The embedding sample was not produced for anti-Lambda, however due to symmetry Lambda in a positive field setting behaves exactly as an anti-Lambda in a negative field setting. Therefore, a combined full field and reverse full field embedding can be used for correcting our $\Lambda + \overline{\Lambda}$ data.

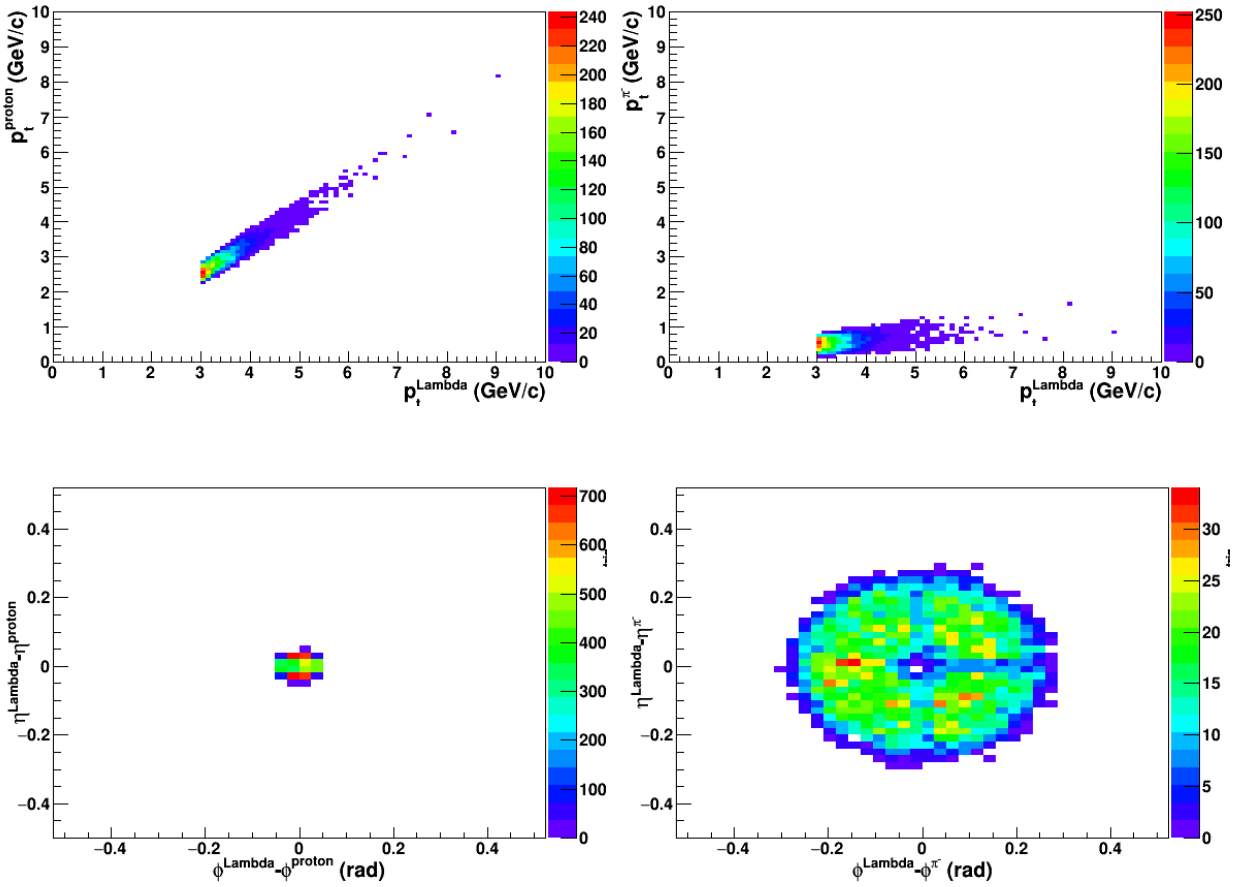

Figure 61: Transverse momentum and relative angular difference of Lambad with respect to its decay duaghters proton and pion are plotted.

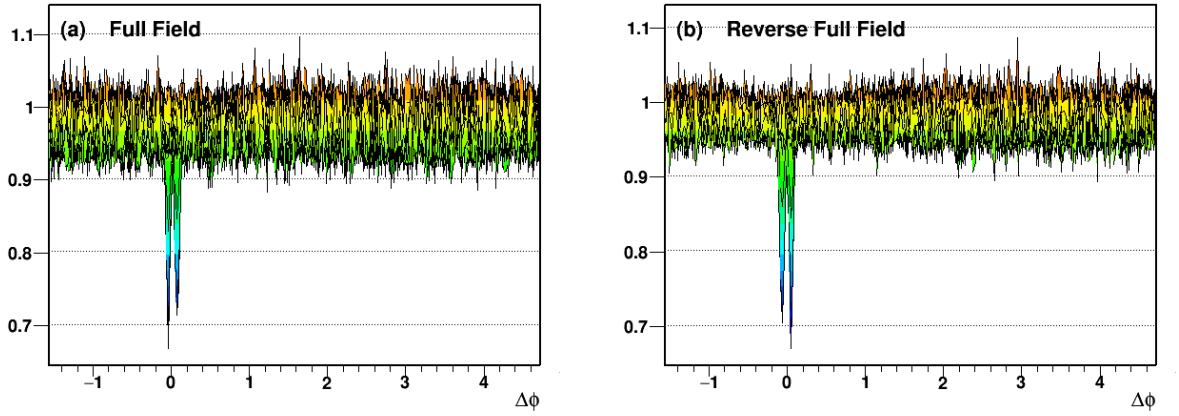

Figure 62: Two-dimensional view in $\Delta\phi$ of the two track merging 'dips' in the embedded Lambda correlation are shown for full field (a) and reverse full field (b) magnetic field settings.

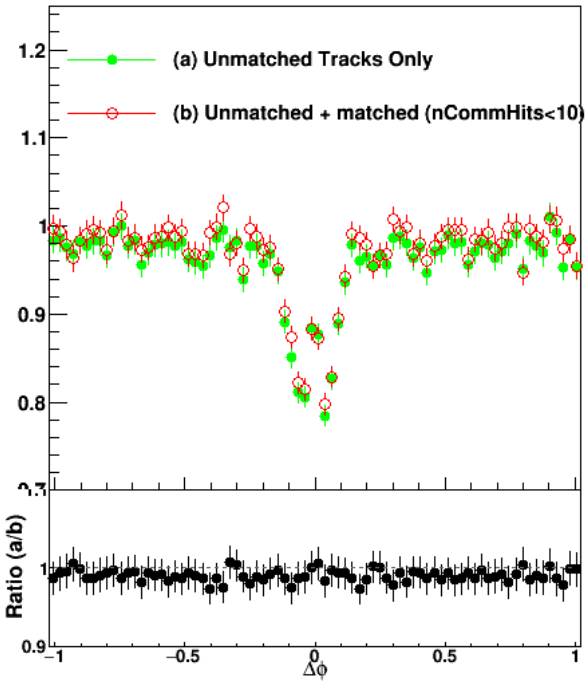

Figure 63: Embedding correlations constructed with (a) primary tracks that did not match any MC tracks (b) unmatched and primary tracks that matched MC tracks with less than 10 common hits. The Ratio of the two is plotted at the bottom.

Track merging corrections were applied bin by bin at small relative angles using the ratio of data over embedding. Corrections were applied separately to each p_T bin analyzed in this analysis. Data vs. embedding correlations are plotted for $3.0 < p_T^{trigger} < 3.5$ GeV/c and $4.0 < p_T^{trigger} < 6.0$ GeV/c in **Figure 64**(a) and **Figure 65** (a), where the data has been scaled by the background level for comparison. Correlations before and after the corrections are also plotted in **Figure 64**(b),(c),(d) and **Figure 65**(b),(c),(d). Corrected correlations using the two-dimensional fit is also plotted in **Figure 64**(b) and **Figure 65**(b) for reference. It can be seen that at lower p_T, a small dip is still present at very small angles around $\Delta\phi$ and $\Delta\eta = 0$. We believe that the embedding should correct for any track merging/splitting effect and any remaining depletion might have sources other than track merging or splitting. Similar results were obtained using the charge separation method (Section 4.4.4 Track Merging Correction – Charge Separation). For this analysis the difference in the correction are used as systematic uncertainties on the final particle yields.

4.4.4 Track Merging Correction – Charge Separation

As discussed earlier, daughter proton of a high p_T Lambda retains the direction of its parent particle and takes away most of its energy. Therefore, the Λ-h correlations could be treated as a p-h correlations and the charge separation method to correct for track merging/splitting corrections, commonly used in case of charged hadrons can be used. However, for K^0_s-h correlations, this method would not work, since its decay is symmetric, with both daughters moving away and carrying about half the energy of the parent particle in opposite direction. **Figure 66** plots the transverse momentum and relative angular distributions of K^0_s with respect to its decay daughter π^+ and π^-.

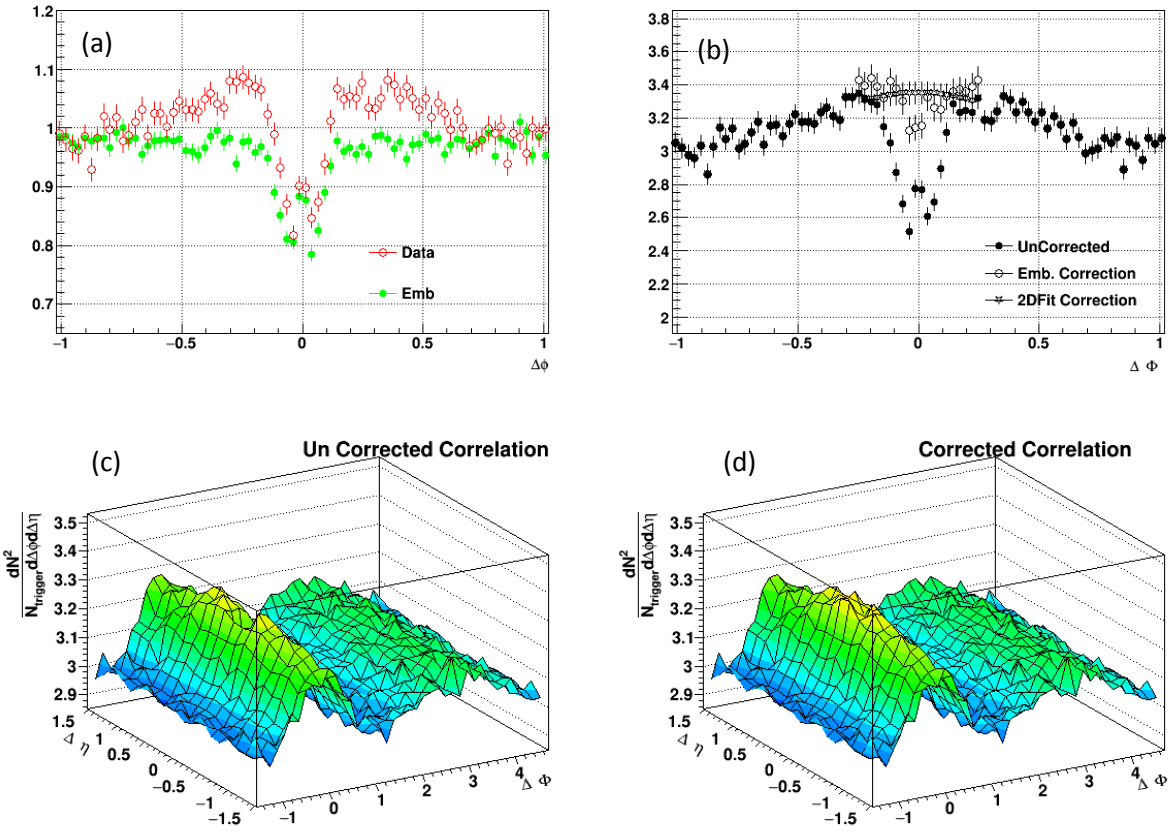

Figure 64: Λ-h Correlations for $3.0 < p_T^{trigger} < 3.5$ GeV/c with $1.5 < p_T^{asscociate} < 3.0$ GeV/c are plotted; (a) Δϕ projections with an overlay of embedding correlations is plotted (data has been scaled down by the background level for comparison); (b) Correlation projection before and after corrections are plotted, corrections using two-dimensional fit method is also plotted for reference. (c) Shows the uncorrected correlations, and (d) shows the corrected correlations using embedding method.

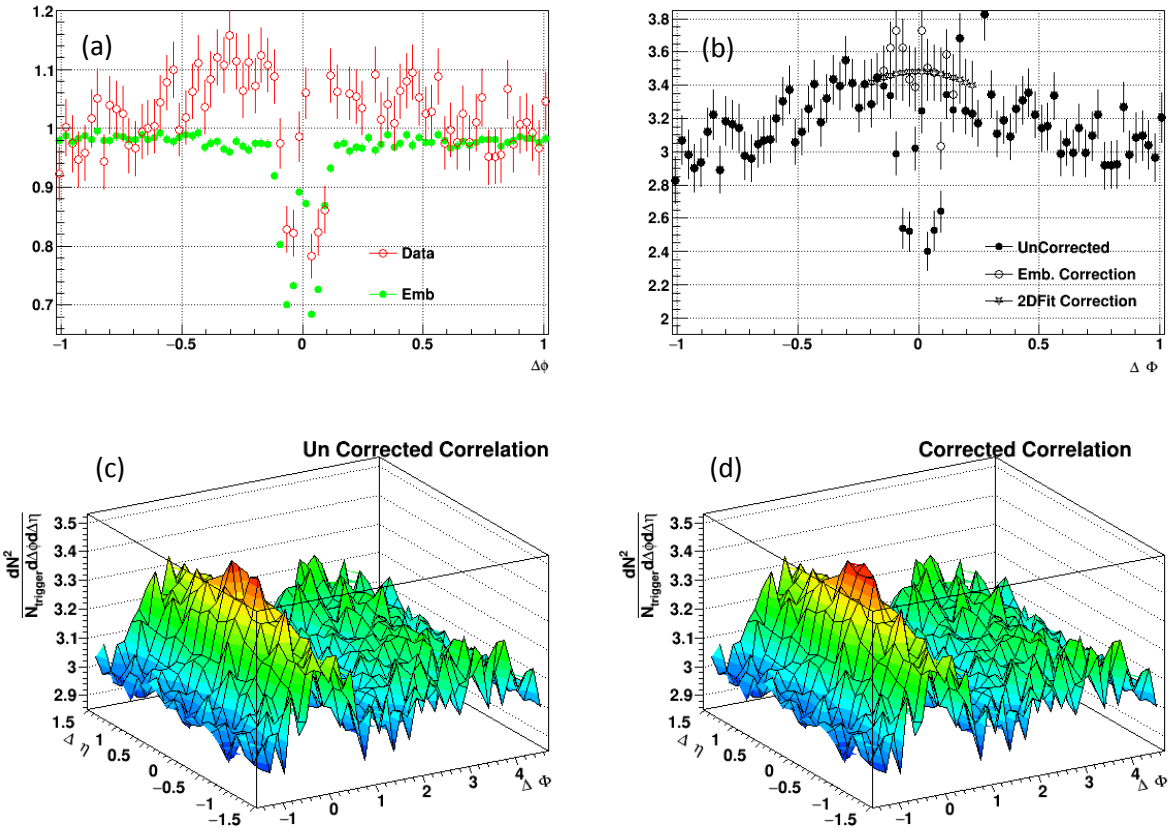

Figure 65: Λ-h Correlations for $4.0 < p_T^{trigger} < 6.0$ GeV/c with $1.5 < p_T^{asscociate} < 3.0$ GeV/c are plotted; (a) $\Delta\phi$ projections with an overlay of embedding correlations is plotted (data has been scaled down by the background level for comparison); (b) Correlation projection before and after corrections are plotted, corrections using two-dimensional fit method is also plotted for reference. (c) Shows the uncorrected correlations, and (d) shows the corrected correlations using embedding method.

Unlike charged hadron correlations, where four different combinations of positive and negative charged particles are used (used and discussed in detailed in a previous STAR thesis [18], only two combinations are possible in case of a neutral Lambda or Anit-Lambda, considering the charge of the daughter proton or anti-proton.

Correlations of Lambda and anti-Lambda were constructed separately with positive and negative associated particles. A clear separation of the dips was seen similar to charged hadron correlations from [18]. Corrections were made by mirroring the signal around $\Delta\phi = 0$, i.e. replacing the bin content of the dip by its bin reflection. **Figure 67** and **Figure 68** show these dips and their corrections for Lambda and anti-Lambdas, respectively. Corrected correlations were then added and normalized per trigger to get the final corrected result.

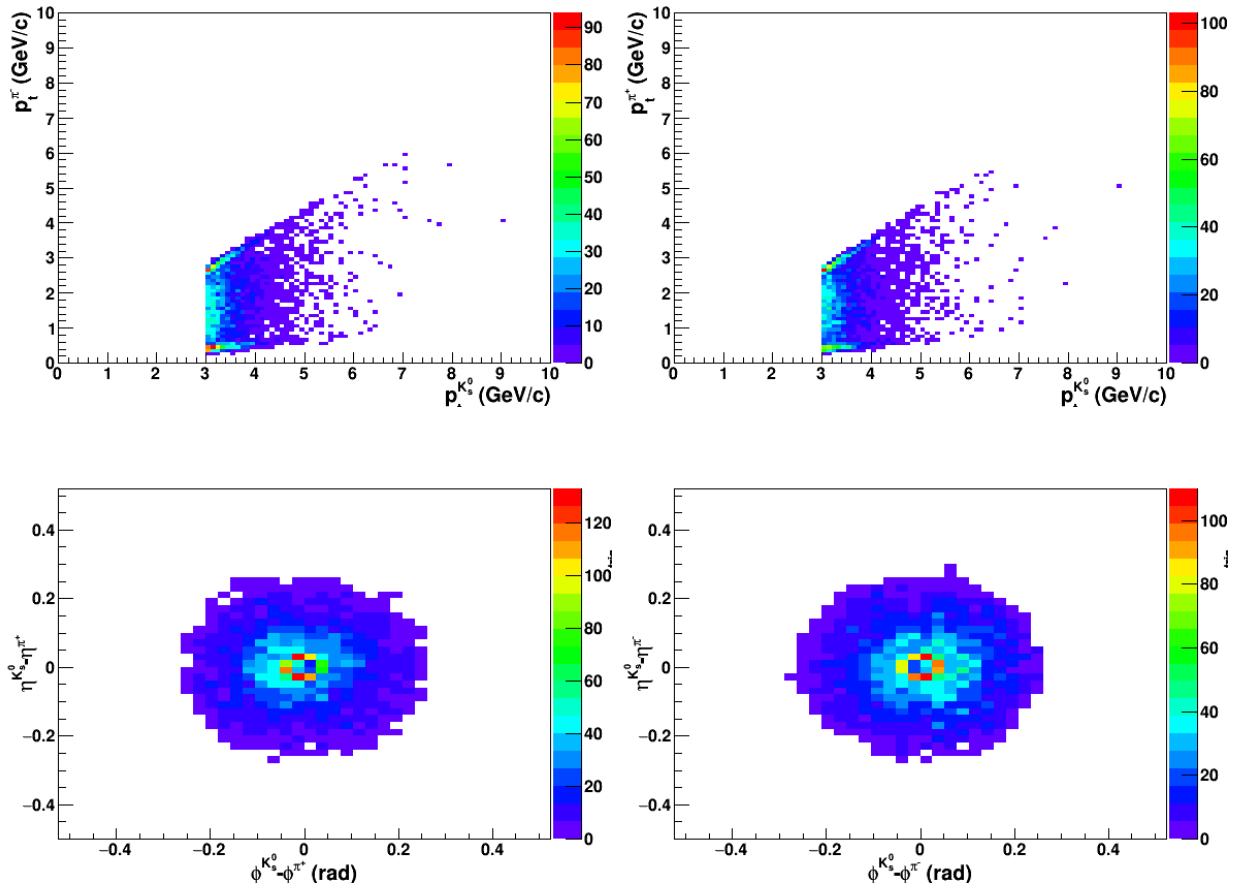

Figure 66: Transverse momentum and relative angular difference of K^0_s with respect to its decay duaghters pion$^+$ and pion$^-$ are plotted.

A comparison of track merging corrections performed using three different methods, namely, 2D fit method, Embedding method, and charge separation method is plotted in **Figure 69** for two p_T bins. Embedding and charge separation methods show good agreement.

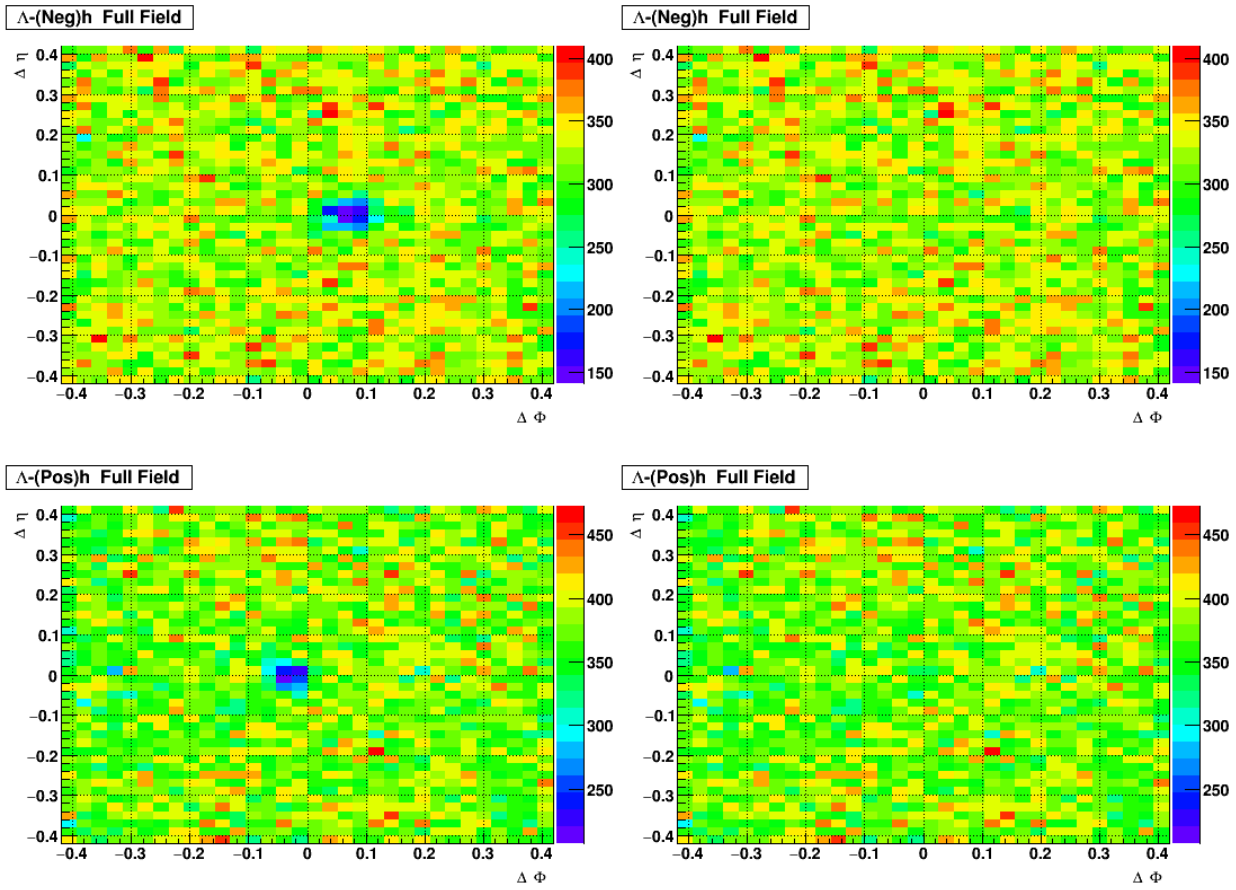

Figure 67: Lambda correlations, in 0-20% most central events, with positive (top) and negative (bottom) associate particles are shown before (left) and after (right) the track merging correction.

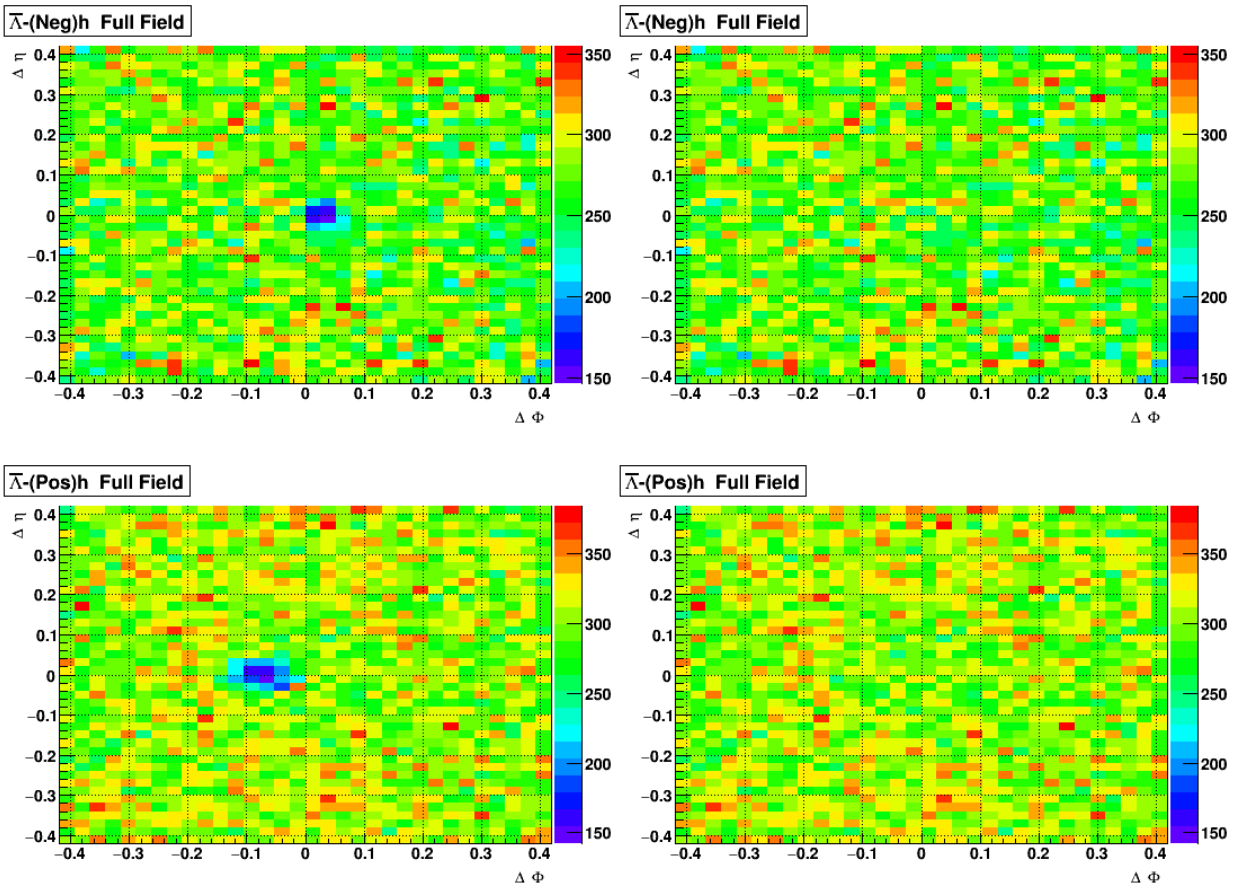

Figure 68: Anti-Lambda correlations, in 0-20% most central events, with positive (top) and negative (bottom) associate particles are shown before (left) and after (right) the track merging correction.

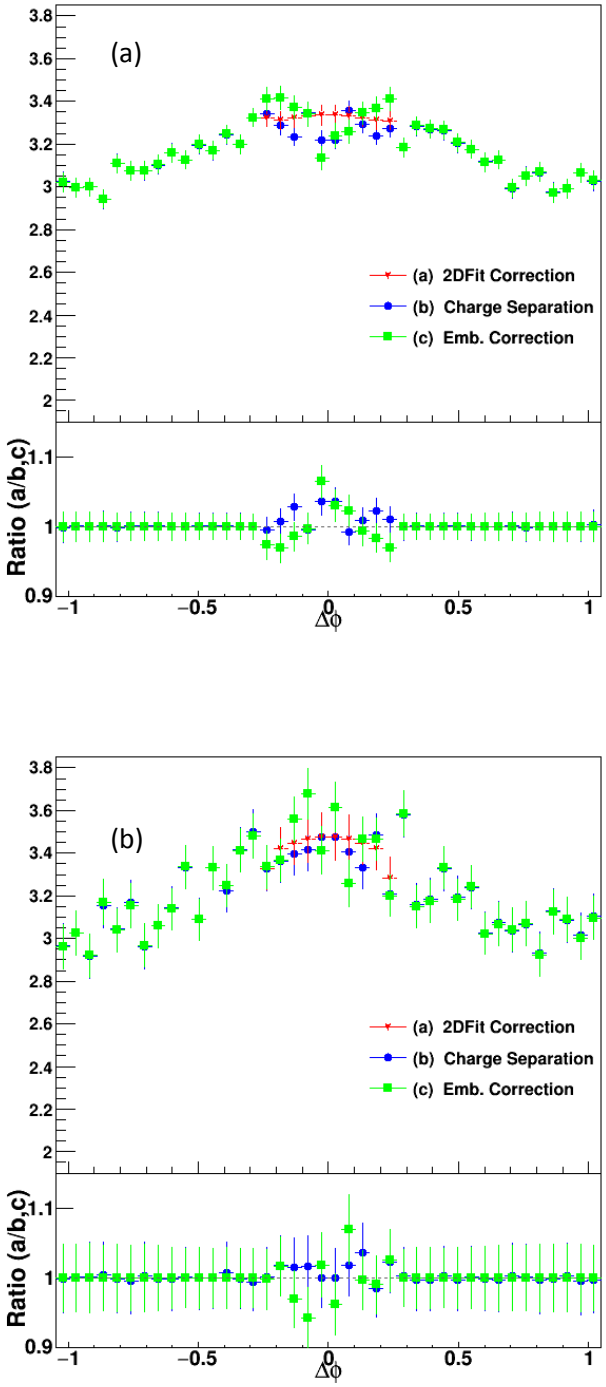

Figure 69: Corrected Λ-h correlations for (a) $3.0 < p_T^{trigger} < 3.5$ GeV/c and (b) $4.0 < p_T^{trigger} < 6.0$ GeV/c are plotted using three different method to correct for track merging effect. The bottom panel shows the ratio of the 2D fit method to the embedding and charge separation method.

4.5 CROSS CHECK

Charged hadron yields calculated for 0-20% most central data in this analysis were compared to two previously published results. Results from run year 2004 is for 0-12% most central and run year 2011 for 0-10% most central events. Plot shows that the results amongst the three run years agree very well.

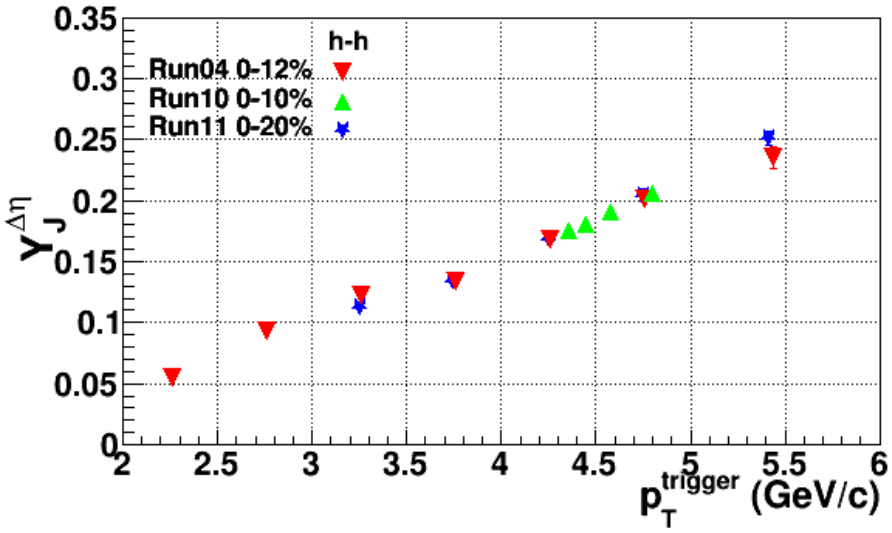

Figure 70: Associated particle yields for unidentified charged hadron correlations are compared with previously published results for cross check.

4.6 JET-LIKE YIELDS

Jet-like yields at small relative angles are extracted by subtracting the background as discussed in Section 4.36 and 4.37. Assuming that the jet-like correlations are contained at smaller relative angles, random pair, or flow contributions can be removed by subtracting correlations averaged over large relative pseudo-rapidity [18]. Contributions from random combinatorial background or ‘fake’ triggers are removed by subtracting the correlations

constructed from reconstructed charged track pairs with invariant mass away from the expected mass of the strange triggers (see **Figure 40**). The background was obtained by fitting the long range correlations over the range of $0.95 < |\Delta\eta| < 1.4$.

Loss of yields at small relative angles due to track merging was corrected using two dimensional fits. However, for 0-20% most central collisions, where the track merging effect is largest, two additional methods (see Section 4.4) were also used. The conventional charge separation method, and a new data driven method developed and tried for the first time, using embedding. All three methods were consistent within statistical errors (<5%). However, in the lowest p_T bin (3.0-3.5 GeV/c) both the charge separation method and the embedding method couldn't fully recover the depletion in the correlation signal at small relative angles around $\Delta\phi$ =0, and $\Delta\eta$ = 0. The two dimensional fit, however, artificially corrects for this depletion by construction but the actual shape of these correlations is not known.

Figure 71 shows the differences resulting from two correction methods, at small relative angles for two p_T ranges, 3.0-3.5 GeV/c and 3.5-4.5 GeV/c. The depletion is slightly larger in the lower p_T range, but in both cases, the overall difference in associated hadron yield is within or close to statistical errors (<6.0% and 3.2%, respectively). However, it should be noted that most of this depletion is confined to very small relative angles ($\Delta\phi < 0.08$, and $\Delta\eta < 0.06$). A similar depletion at low transverse momentum ($1 < p_T^{trig} < 3$ GeV/c), at small relative angles in the most central collisions was also reported recently in two-particle correlations at collision energy of 2.76TeV [54]. It was argued that the depletion could be a result of an interplay of flow and jet fragmentation. The depletion reported in [54] is less than 3%, after excluding all possible

secondary contributions coming from particle pairs with small opening angles or from correlation of secondary decay particles (neutral or γ-conversions).

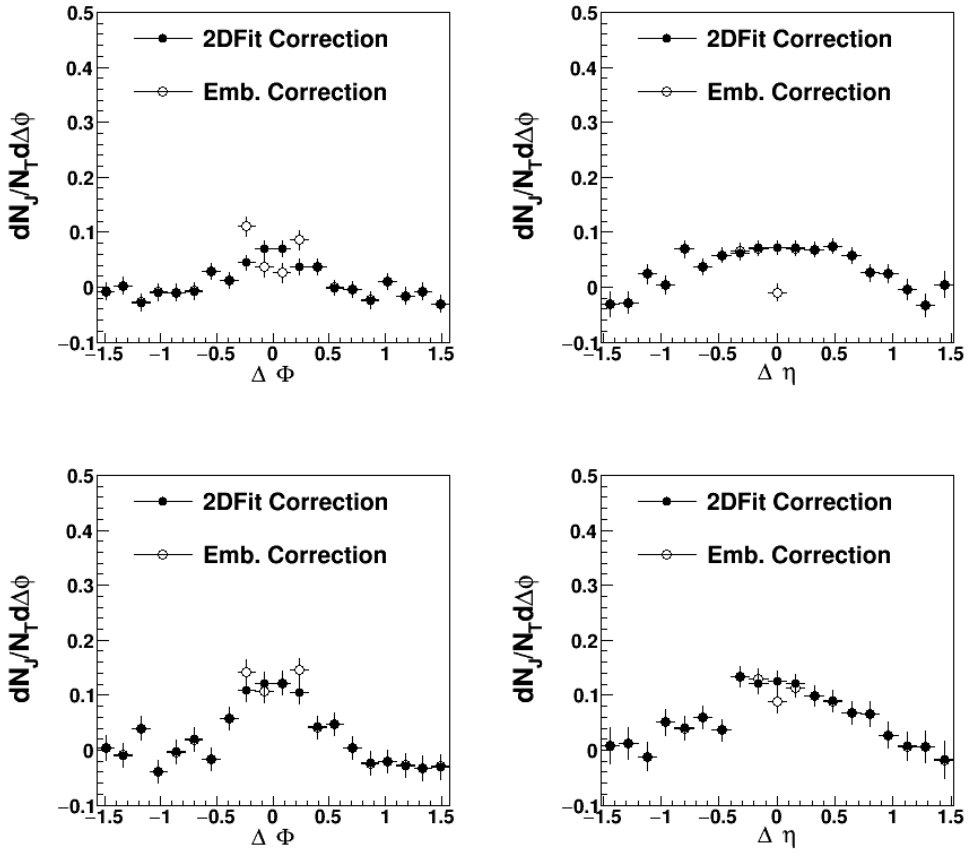

Figure 71: Corrected pure cone projections in $|\Delta\phi| < 0.08$ and $|\Delta\eta| < 0.06$, exhibiting the differences from different correction methods (two-dimensional fit and embedding) for $3.0<p_T^{trig}<3.5$ GeV/c (top) and $3.5<p_T^{trig}<4.5$ GeV/c (bottom)

4.7 SYSTEMATIC UNCERTAINTIES IN PARTICLE YIELDS

4.7.1 Background Subtraction

A major source of uncertainty comes from the background subtraction, which is much larger in the most central collisions due to higher track multiplicities. Greater errors are also seen in higher p_T bins, where the data sample is limited and uncertainties in determining the background level are larger.

The distribution of background was described by an average taken over $0.95 < |\Delta\eta| < 1.4$. The region was varied in eight steps from $0.9 < |\Delta\eta| < 1.5$, and the standard deviation of the particle yields obtained as a result of these variation was used as systematic uncertainty on the final yields (see Appendix C for plots). The errors were larger in the most central bin due to higher multiplicities and larger underlying background and for higher p_T bins where statistical fluctuation are larger due to lower number of triggers. The effects on yields range from under 5% in the 40-80% most central collisions for up to 8.7% in 0-20% most central collisions.

Two types of fits were used to describe the background that was subtracted to calculate the 'pure cone' as described in Section 4.3.6 and 4.3 7. One dimensional fit on $\Delta\phi$ distribution averaged over the background range stated above and a two dimensional combined fit on complete two dimensional correlation signal, including the ridge and the jet-like correlations. The difference in the fits also introduced systematic uncertainties in the final yields and were found to be the source of the largest errors. Both fits described the background well, and hence neither could be discarded as 'bad' fit. An example of the two fits is shown in **Figure 72**. Differences in fits for all p_T, and centrality bins used in this analysis are presented in Appendix D. These errors

were found to be larger for the Lambda (anti-Lambda) triggers for the most central collisions. For K^0_s, the errors range from under 0.5% in lower p_T bins to up to 12% in the highest p_T bin. For Lambda, the errors range from 0.5% to 17.2%. The systematic uncertainties from the two sources described above for background subtraction are listed in Table 13.

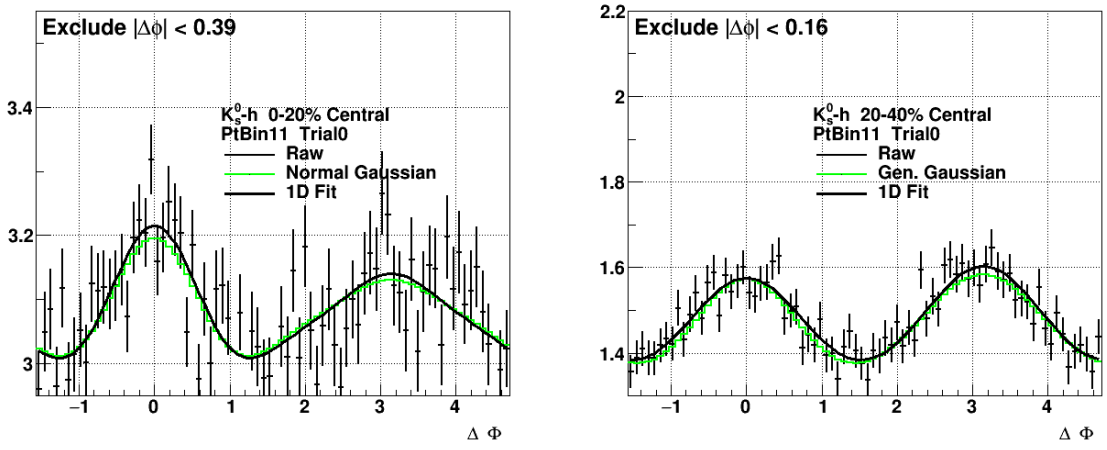

Figure 72: A sample of the difference between the two-dimensional and one-dimensional fits is shown.

	K^0_s Triggers			Λ Triggers		
p_T^{trig} (GeV/c)	3.0-3.5	3.5-4.5	4.5-5.5	3.0-3.5	3.5-4.5	4.5-5.5
Source	Value (%)					
	0-20% Central					
Vary Δη range	3.5%	4.4%	7.9%	5.8%	4.6%	8.7%
1D Vs. 2D Fit	0.5%	4.7%	12.0%	13.8%	15.4%	17.2%
	20-40% Central					
Vary Δη range	3.8%	7.3%	6.8%	3.4%	5.8%	4.1%
1D Vs. 2D Fit	2.7%	3.6%	8.8%	8.6%	9.1%	8.4%
	40-80% Central					
Vary Δη range	1.2%	2.6%	4.6%	2.5%	2.5%	3.1%
1D Vs. 2D Fit	4.5%	3.0%	7.8%	0.5%	4.7%	5.1%

Table 13: Systematical uncertainties due to background subtraction

4.7.2 Track Merging Correction

Three different methods were used and compared to correct for the track merging correction. **Table 14** lists the uncertainties in jet-like yields due to the correction methods. Uncertainties from these methods were found to be less than 5%. Two dimensional fits, used to correct for track merging, were performed by excluding the region affected by track merging. The exclusion ranges were varied and the standard deviation of the resulted yields were used as systematic uncertainties on the final yields. These uncertainties were also found to be less than 5%.

	K^0_s Triggers			Λ Triggers		
p_T^{trig} (GeV/c)	3.0-3.5	3.5-4.5	4.5-5.5	3.0-3.5	3.5-4.5	4.5-5.5
Source	Value (%)					
0-20% Central						
Correction Type	3.0%	1.9%	2.9%	4.1%	1.6%	4.2%
Exclusion range (a)	3.3%	0.9%	2.2%	1.7%	1.1%	1.7%
Exclusion range (b)	4.8%	0.9%	0.8%	0.0%	4.3%	4.0%
20-40% Central						
Correction Type	0.0%	4.4%	0.2%	2.1%	1.6%	3.1%
Exclusion range (a)	1.1%	1.5%	2.2%	1.9%	1.1%	3.0%
Exclusion range (b)	1.7%	0.7%	1.8%	2.4%	0.6%	2.6%
40-80% Central						
Correction Type	0.4%	0.1%	0.6%	0.2%	0.0%	0.1%
Exclusion range (a)	1.7%	1.9%	2.3%	0.2%	0.8%	1.4%
Exclusion range (b)	1.4%	2.9%	4.9%	0.3%	0.2%	1.2%

Table 14: Systematic uncertainties due to correction method. Exclusion ranges (a) and (b) refer to ranges in two-dimensional fits perform after and before the background subtraction, respectively.

4.8 SYSTEMATIC UNCERTAINTIES IN ELLIPTIC FLOW

Uncertainties in the elliptic flow measurements were calculated by varying the ranges of the $\Delta\phi$ distributions. The standard deviation in the values obtained was used as systematic error on v_2 results presented in Section 5. The error was found to be less than 5% except for the highest p_T bin ($6.0 < p_T^{trigger} < 10.0$ GeV/c), where it varies from 3%-16% for K^0_s and 5%-10% for Λ triggers.. Appendix F contains plots displaying the variation ranges for all p_T and centralities used in this analysis. Another source for uncertainties in measuring the elliptic flow is estimating the background in the invariant mass, using 'side band' correlations. The range of the side bands were varied and the percent difference in the v_2 values taken as uncertainties due to the background estimation. These uncertainties were also found to be less than 5%, except for highest p_T bin, where it was found to be 5%-13% for K^0_s and 9%-26% for Λ triggers. The errors from the two sources were added in quadrature to get total systematic uncertainty.

CHAPTER 5

RESULTS

The final fully corrected 2D correlations for K^0_s and $\Lambda+\overline{\Lambda}$ with $p_T^{trigger}$ = 3.0 – 6.0 GeV/c are shown in **Figure 73** for 0-20%, 20-40%, 40-60%, and 60-80% most central Au+Au 200 GeV collisions. Unidentified h-h correlations are also shown for comparison and were measured using the same method and collision system. The jet-like correlation strength at small relative angles is stronger for K^0_s, whereas a much larger long-range ridge structure is present in Λ-h correlations in all centralities. These differences in the correlation signal for K^0_s and $\Lambda+\overline{\Lambda}$ are consistent with trends seen in [18] for pion and non-pion triggers.

5.1 JET-LIKE YIELDS

Background subtracted jet-like peak projections on $\Delta\eta$ and $\Delta\phi$ for three different centralities are plotted for various p_T ranges for both K^0_s and Λ in **Figure 74**. The peak shapes from different centrality classes, in $\Delta\phi$ projections are similar, but broadening can be seen developing, at low p_T, in the $\Delta\eta$ projections with centrality.

The associated particle yields for each trigger selection are calculated by integrating the data over $|\Delta\eta| < 0.78$ and $|\Delta\phi| < \pi/4$, as in [55] and [18], and the results, along with the ratio of Λ yields to K^0_s associated yields, are listed in **Table 15**. In **Figure 75**, the calculated associated yields are plotted for three different centralities along with some published results from [55]. **Figure 76** compares associated yields in three centrality ranges for K^0_s and Λ triggers.

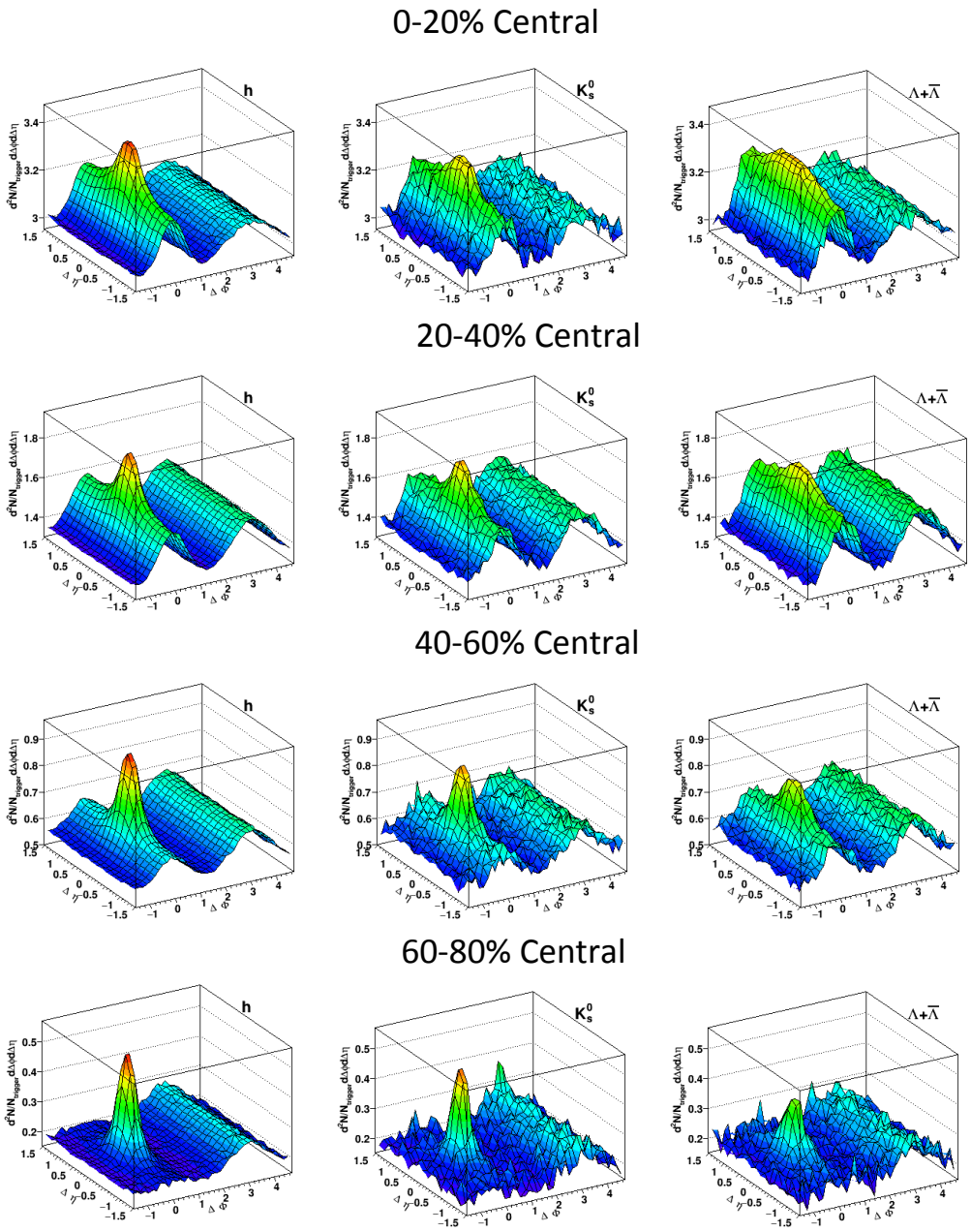

Figure 73: Two-dimensional azimuthal correlations for h-h (left), K^0_s-h (middle) and Λ-h (right) are plotted for 0-20% (top), 20-40% (2^{nd} row), 40-60% (3^{rd} row) and 60-80% (bottom) most central Au+Au collisions at 200 GeV with trigger and associated particles in transverse momentum ranges $3.0 < p_T^{trigger} < 6.0$ GeV/c and $1.5 < p_T^{associate} < 3.0$ GeV/c

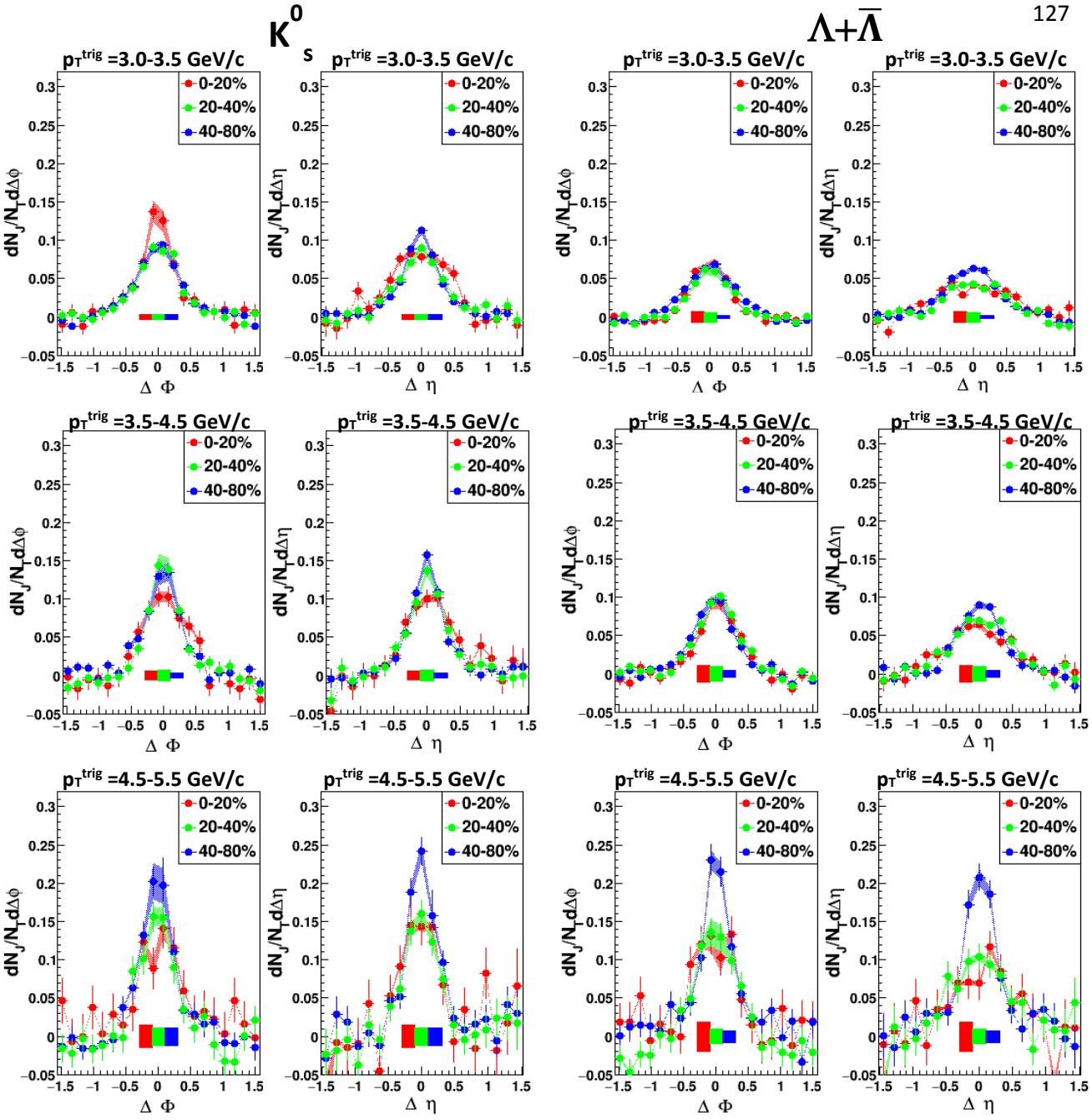

Figure 74: The $\Delta\eta$ and $\Delta\phi$ projections of the background subtracted jet-like correlations in $|\Delta\eta| < 0.78$ and $|\Delta\phi| < \pi/4$ for K^0_s (left two panels) and Λ (right two panels) triggers. Three p_T selections for trigger hadrons are shown: 3.0-3.5 GeV/c (top), 3.5-4.5 GeV/c (middle) and 4.5-5.5 GeV/c (bottom). Three different centrality bins represented by different colors. Corresponding colored boxes show systematic uncertainties due to background subtraction in respective centrality range; colored bands show the rest of the systematic uncertainty.

		K^0_s Trigger	Λ Trigger	$Y_J(\Lambda)/Y_J(K^0_s)$
Centrality	**p_T^{trig} (GeV/c)**	**Associated Yields ± stat. errors ± sys. uncertainties**		
0-20%	3.0-3.5	0.133±0.007±0.010	0.077±0.004±0.012	0.059±0.005±0.010
	3.5-4.5	0.133±0.010±0.009	0.107±0.006±0.018	0.0705±0.007±0.014
	4.5-5.5	0.163±0.021±0.024	0.156±0.018±0.032	0.957±0.166±0.240
20-40%	3.0-3.5	0.111±0.005±0.006	0.070±0.003+0.007	0.631±0.040±0.071
	3.5-4.5	0.137±0.006±0.013	0.117±0.005±0.013	0.854±0.052±0.123
	4.5-5.5	0.162±0.015±0.019	0.156±0.014±0.017	0.963±0.124±0.151
40-80%	3.0-3.5	0.115±0.004±0.006	0.091±0.003±0.002	0.791±0.038±0.046
	3.5-4.5	0.141±0.006+0.007	0.113±0.004+0.006	0.801±0.044±0.060
	4.5-5.5	0.200±0.015±0.021	0.199±0.013±0.013	0.995±0.096±0.131

Table 15: Jet-like yields in $|\Delta\eta| < 0.78$ and $|\Delta\phi| < \pi/4$ and their ratio as a function of p_T^{trig} for K^0_s and Λ triggers are presented for Au+Au collisions at 200 GeV.

In order to separate the medium effect from initial state nuclear effects, most central (0-20%) data were compared with the most peripheral (60-80%) collisions, where medium induced modifications are expected to be the least. Associated yields for K^0_s triggers are larger than those associated with Λ triggers in all centralities, confirming the general trends seen in [18]. The relative suppression for Λ triggers, with respect to K^0_s triggers, is found to be decreasing with increasing p_T, however, no suppression is seen in the highest p_T bin. Other than a possible broadening in $|\Delta\eta|$ for central collisions at low p_T, which is attributed to an expanding and collectively flowing medium, no significant centrality dependence in the total associated yields is seen (**Figure 76**).

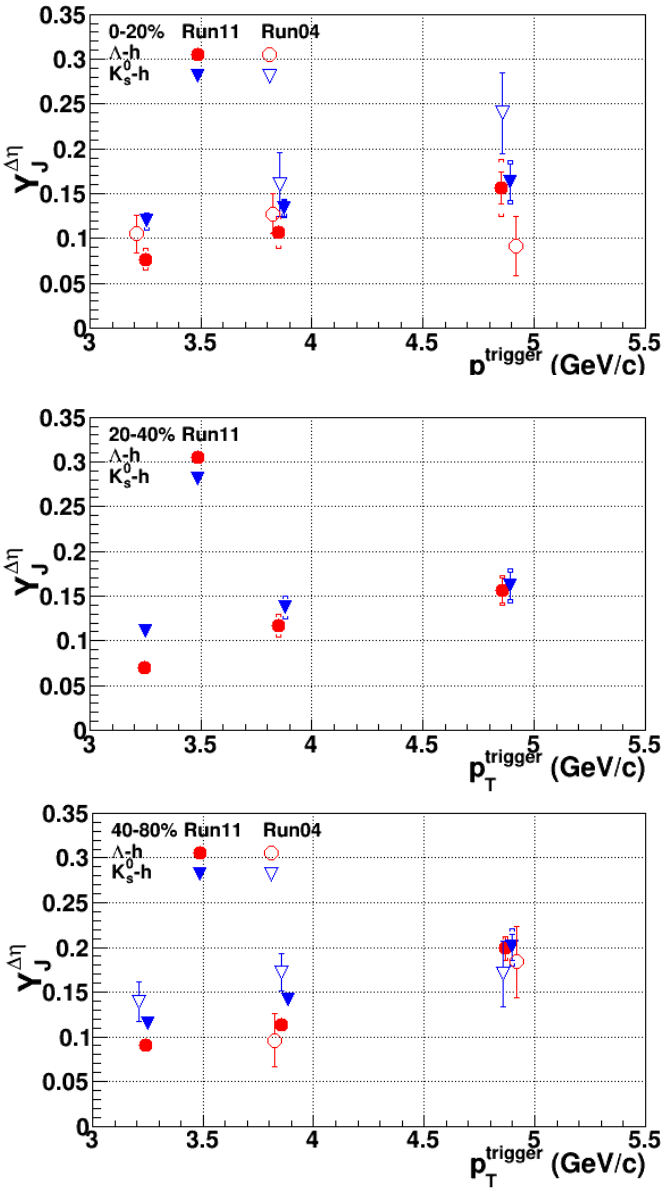

Figure 75: Jet-like yields in $|\Delta\eta| < 0.78$ and $|\Delta\phi| < \pi/4$ are plotted as a function of $p_T^{trigger}$ for K^0_s -h and Λ-h for Au+Au collisions at 200 GeV. Error bars show statistical errors and the brackets around the error bars represent systematical uncertainties. For comparison, published K^0_s -h and Λ-h correlations from **[55]** at the same collision energy are also plotted. Note that for many points the combined uncertainties are smaller than the marker size.

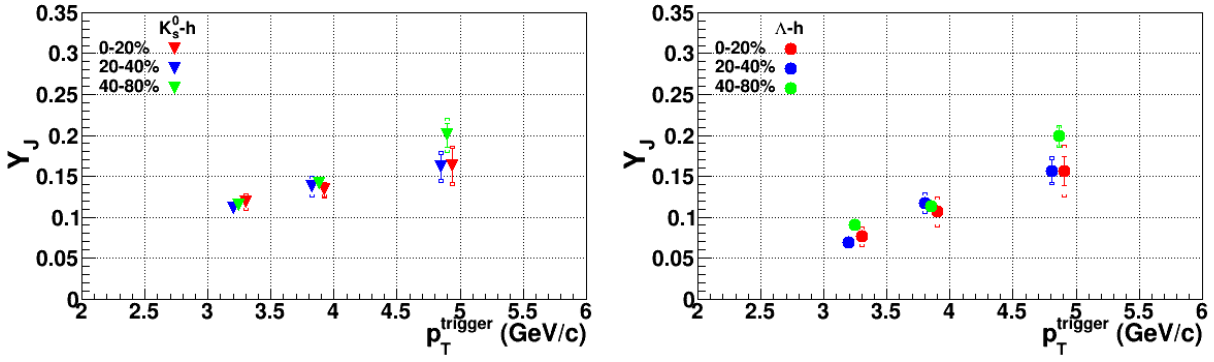

Figure 76: Associated hadron yield as a function of trigger p_T is plotted for three different centralities for K^0_s (left) and Λ (right) triggers. Error bars show statistical errors and the brackets around the error bars represent systematical uncertainties. Note that the statistical errors on some points are smaller than the marker size. Data points for 0-20% and 20-40% are shifted for in $p_T^{trigger}$ for visibility.

5.1.1 Medium Effects

Least amount of QGP with shorter lifetime is produced in the most peripheral collisions, hence these collision are expected to be similar to elementary collisions. 0-20% central data were directly compared to 60-80% central data to study the medium effects on the correlations. The resulting pure cone projections are plotted in **Figure 78.** The calculated associated yields are presented in **Table 16** for quantitative comparison and are plotted for both trigger particles in **Figure 77**. Relative associated yields for trigger types in both centrality bins are consistent within uncertainties.

	p_T^{trig} (GeV/c)	0-20%	60-80%
$Y_J(K^0_s)$	3.0-4.0	0.117±0.006(stat.)±0.010(sys.)	0.122±0.005(stat.)±0.007(sys.)
	4.0-6.0	0.170±0.014(stat.)± 0.026(sys.)	0.186±0.015(stat.)±0.020(sys.)
$Y_J(\Lambda)$	3.0-4.0	0.079±0.003(stat.)± 0.014(sys.)	0.096±0.004(stat.)±0.004(sys.)
	4.0-6.0	0.138±0.010(stat.)± 0.030(sys.)	0.162±0.013(stat.)±0.011(sys.)
$Y_J(\Lambda)/Y_J(K^0_s)$	3.0-4.0	0.674±0.045(stat.)±0.132(sys.)	0.781±0.049(stat.)±0.054(sys.)
	4.0-6.0	0.808±0.086(stat.)±0.215(sys.)	0.959±0.088(stat.)±0.123(sys.)

Table 16: Associated hadron yields per trigger for 0-20% and 60-80% most central collisions for K^0_s and Λ triggers.

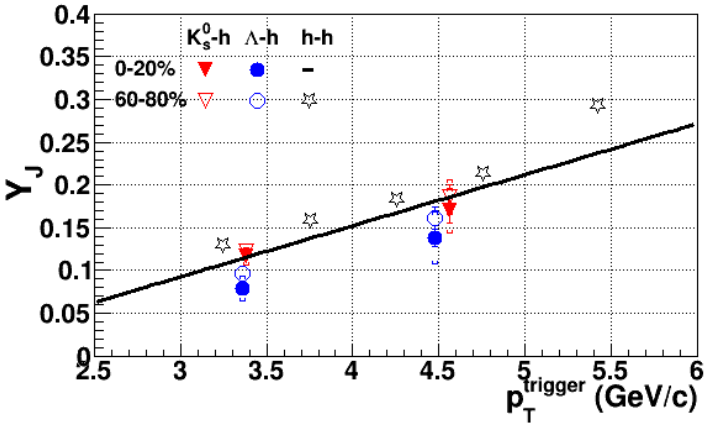

Figure 77: Associated yields for K^0_s, Λ and unidentified charged hadron triggers are plotted for 0-20% and 60-80% most central Au+Au 200 GeV collisions. Unidentified charged hadron yields are used as a reference and a fit to 0-20% results is used for better visibility.

A previous study made similar measurements using K^0_s and Λ triggers in different collision systems [55]. An enhancement in associated yields for K^0_s triggers was reported in 0-12% most central Au+Au 200 GeV collisions, however, due to large uncertainties in the results the findings were not conclusive. Data from this earlier study has been plotted for comparison in **Figure 75,** along with our data. Another previous work studied jet-like yields for identified pion and non-pion triggers [18], in a slightly different transverse momentum range for the associated hadrons, with $1.5<p_T^{assoc}<4.0$ GeV/c in 0-10% most central collisions, compared to the range studied in this work of $1.5<p_T^{assoc}<3.0$ GeV/c in 0-20% most central collisions, and an enhancement of jet-like yields associated with pion triggers was observed in the central Au+Au collisions when compared to d+Au collisions.

To quantify any relative suppression/enhancement of associated yields due to medium effects, a ratio of yields, I_{cp}, is often used in di-hadron correlations. In this study I_{cp} was calculated as:

$$I_{cp} = Y_{central} / Y_{peripheral} \quad . \qquad \textbf{Eq. 26}$$

The ratio of the I_{CP} for the two trigger types will represent the relative enhancement or suppression between the two types of triggers in different centralities. The ratio of I_{CP}'s or a 'double-ratio' is taken as:

$$R \equiv I_{cp}^{\Lambda} / I_{cp}^{K_s^0} . \qquad \textbf{Eq. 27}$$

The calculated values for I_{CP} and their ratios for both trigger types are presented in **Table 17**. A relative suppression of 17%±6%(stat.)±4%(sys.) is found for the Λ triggers with p_T^{trig}=3.0-

4.0 GeV/c in the 0-20% most central collisions with respect to the 60-80% peripheral collision. This suppression hints towards the presence of the trigger dilution effect, where thermal triggers, produced via recombination/coalescence from the medium dilute the associated yields. However, given the uncertainties in the measurements this result remains inconclusive with respect to thermal trigger dilution effect. Relative yield ratios in transverse momentum range of p_T^{trig}=4.0-6.0 GeV/c are consistent with unity, meaning no evidence or hint of suppression/enhancement was seen.

p_T^{trig} (GeV/c)	I_{cp} (Λ)	I_{cp} (K^0_s)	I_{cp} (Λ)/I_{cp} (K^0_s)
3.0-4.0	0.826±0.052(stat.) ±0.150(sys.)	0.958±0.064(stat.) ±0.096(sys.)	0.863±0.079(stat.) ±0.179(sys.)
4.0-6.0	0.850±0.090(stat.) ±0.195(sys.)	0.916±0.104(stat.) ±0.172(sys.)	0.927±0.144(stat.) ±0.274(sys.)

Table 17: Ratios of associated charged hadron yields for Λ triggers to K^0_s triggers in central (0-20%) with respect to peripheral (60-80%) collisions.

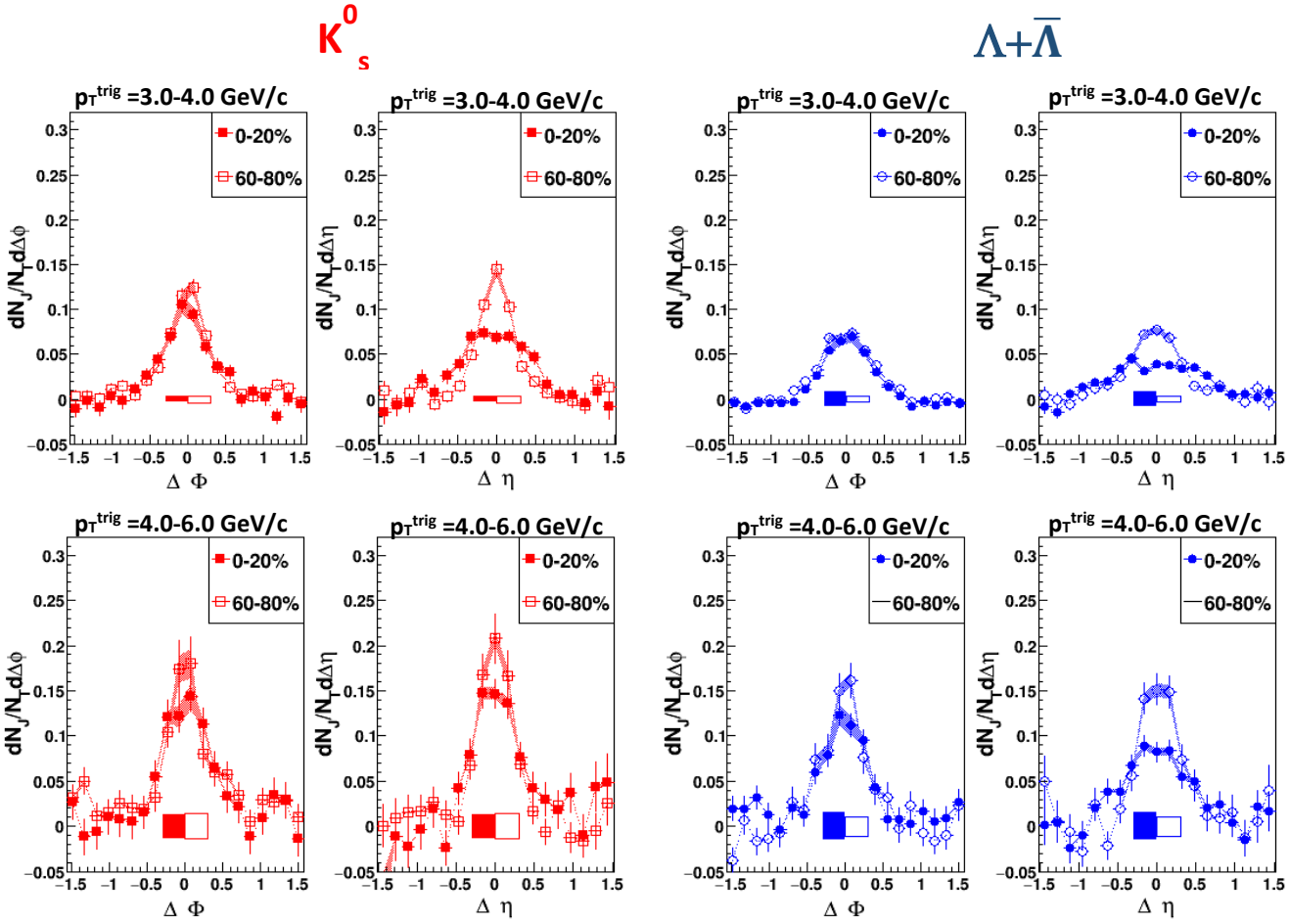

Figure 78: Pure cone projections in $|\Delta\eta| < 0.78$ and $|\Delta\phi| < \pi/4$, for K^0_s-h (left two panels) and Λ-h (right two panels) correlations are plotted for $3.0 < p_T^{trig} < 4.0$ GeV/c (top) and $4.0 < p_T^{trig} < 6.0$ GeV/c (bottom) for 0-20% and 60-80% most central collisions. Corresponding colored boxes show systematic uncertainties due to background subtraction in respective centrality range; colored bands show the rest of the systematic uncertainty.

5.2 LONG-RANGE $\Delta\eta$ CORRELATIONS

The long-range $\Delta\eta$ independent correlations can be explained in terms of higher-order anisotropies due to hydrodynamic flow. To characterize these anisotropies, the $\Delta\eta$-averaged projection over the range of $0.95 < |\Delta\eta| < 1.4$ is described via the Fourier expansion:

$$B(p_T, \Delta\phi) = A(1 + \sum_{n=1}^{N} 2V_n \cos(n\Delta\phi)), \qquad \textbf{Eq. 28}$$

where A is the uncorrelated background level and the first four Fourier terms (N=1-4) are used to describe the distribution. Including higher order (N>4) terms did not have significant effect on the fit result. In fact, the higher-order terms were found to be consistent with zero within errors when two-dimensional fits were performed to correct for track merging.

It is widely assumed that the coefficients of the Fourier expansion factorize into azimuthal anisotropies of the trigger and associated particles, i.e. $V_n = \langle v_n^{trig} \rangle \langle v_n^{assoc} \rangle$, for two-particle correlations outside the small jet-like correlation range, [18]. The coefficient of the second term in the Fourier expansion, v_2, known as the elliptic flow, is dominant in the long range correlations. Fragmentation contribution to the away side correlations were not excluded from the fit, however, they are negligible compared to flow effects [18]. Elliptic flow measurements were made for K^0_s and Λ to compare with previous results [56]. Elliptic flow for charged hadrons from [57] was used to calculate the average v_2 for associated particles. In **Figure 79**, v_2 for K^0_s and Λ are plotted along with published charged hadron v_2 for three different centralities. The measured v_2 values for K^0_s and Λ triggers are listed in **Table 18** and **Table 19**, respectively. The magnitude of the v_2 increases with centrality with similar trends of increasing with p_T, reaching a plateau at

intermediate p_T and decreasing for higher p_T. The value of v_2 and p_T at saturation are particle-type and centrality dependent. A decrease in v_2 at higher p_T could be explained using theoretical model incorporating hydrodynamics and jet-quenching [58]. Measured v_2 for Λ is found to be larger than K^0_s in all centralities, which is consistent with previous results in [56].

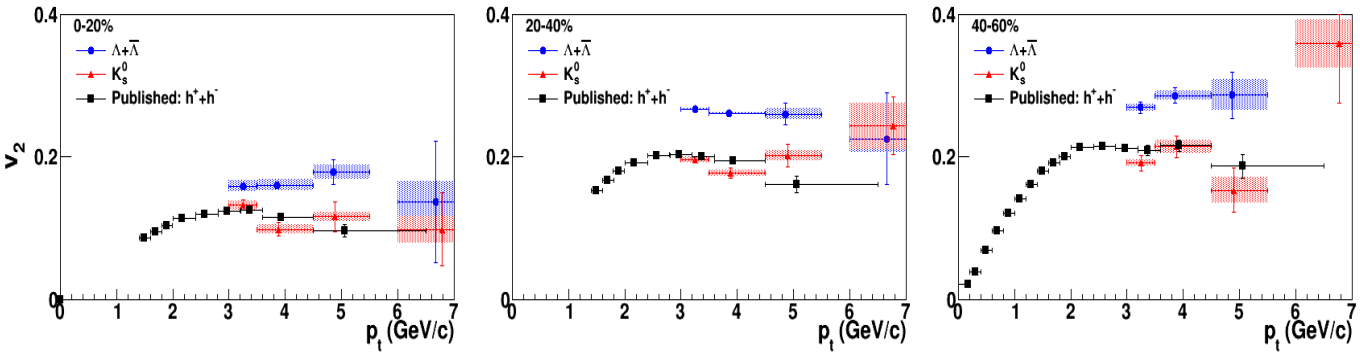

Figure 79: Elliptic flow (v_2) vs. p_T is plotted for K^0_s and Λ triggers along with published results for charged hadron v_2 from [57]. Shaded blocked represent the systematic uncertainties.

Centrality	0-20%			20-40%			40-60%		
p_T^{trig} (GeV/c)	v_2	stat.	sys.	v_2	stat.	sys.	v_2	stat.	sys.
3.0-3.5	0.132	5.6%	5.0%	0.197	2.8%	2.3%	0.192	5.6%	2.6%
3.5-4.5	0.098	10.0%	6.4%	0.177	3.9%	2.3%	0.214	6.9%	4.3%
4.5-5.5	0.116	18.1%	5.4%	0.202	7.9%	3.7%	0.153	20.7%	12.1%
6.0-10	0.098	52.1%	18.9%	0.243	16.6%	13.4%	0.359	23.1%	9.3%

Table 18: Elliptic flow for K^0_s triggers in different centralities

Centrality		0-20%			20-40%			40-60%	
p_T^{trig} (GeV/c)	v_2	stat.	sys.	v_2	stat.	sys.	v_2	stat.	sys.
3.0-3.5	0.159	2.5%	5.1%	0.267	1.2%	0.6%	0.269	2.8%	2.0%
3.5-4.5	0.161	3.5%	5.2%	0.262	1.8%	0.4%	0.286	3.8%	2.1%
4.5-5.5	0.179	10.0%	5.8%	0.26	5.7%	3.0%	0.287	11.3%	7.4%
6.0-10	0.137	62.5%	21.6%	0.226	28.4%	8.7%	0.811	18.5%	29.6%

Table 19: Elliptic flow for Lambda triggers in different centralities

Scaling behavior of the elliptic flow with the number of constituent quarks is interpreted as evidence of collective flow at partonic level and has been well explained via hadron production through recombination/coalescence (see Section 2.52). The ratio of v_2 to the number of constituent quarks (n=2 for K^0_s and n=3 for Λ) was measured for the strange triggers and are plotted in **Figure 80**. These results are in agreement with previously published results from [56] (also plotted for comparison in Figure 80). Measured values for v_2 in 0-80% most central collisions are listed in Table 20 for K^0_s and Λ triggers.

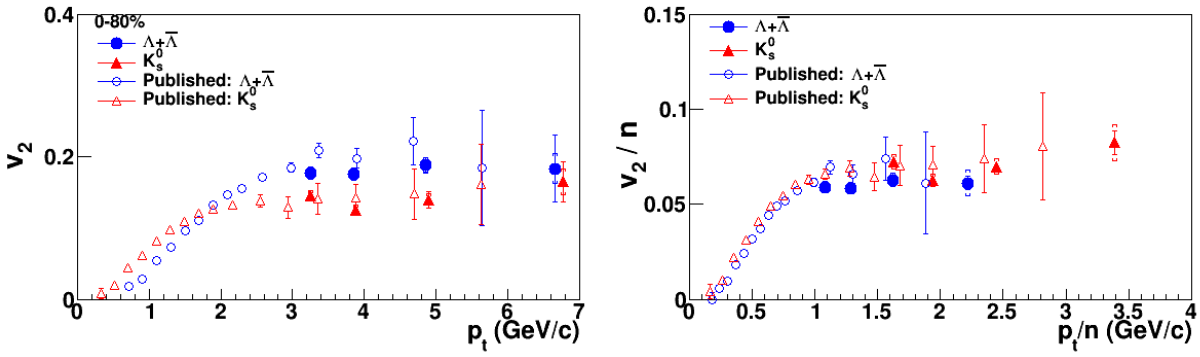

Figure 80: Elliptic flow vs. p_T (left) and v_2/n vs. p_T/n (right) for K^0_s (n=2) and Λ (n=3) is plotted for Au+Au 200 GeV minimum bias collisions. Error bars denote statistical errors and the brackets around the error bars represent systematic uncertainties. Published results from **[57]** are plotted for comparison.

	K^0_s Triggers			Λ Triggers		
p_T^{trig} (GeV/c)	v_2	stat.	sys.	v_2	stat.	sys.
3.0-3.5	0.149	1.9%	0.7%	0.173	1.2%	0.6%
3.5-4.5	0.138	2.7%	1.4%	0.171	1.6%	0.5%
4.5-5.5	0.148	6.2%	2.9%	0.179	4.7%	2.5%
6.0-10	0.167	14.6%	5.2%	0.167	19.4%	4.8%

Table 20: Elliptic flow for K^0_s and Lambda triggers in 0-80% most central collisions

5.3 SUMMARY

Di-hadron correlation were studied for K^0_s and Λ triggers in transverse momentum ranges of 3.0-3.5 GeV/c, 3.5-4.5 GeV/c and 4.5-5.5 GeV/c for 0-20%, 20-40% and 40-80% most central collisions to investigate particle-type dependence for identified strange hadrons in Au+Au collisions at 200 GeV with the STAR experiment. Correlations in 0-20% most central collisions were also directly compared to correlations in 60-80% peripheral collisions.

Jet-like associated hadron yields in transverse momentum range of 1.5-3.0 GeV/c were calculated. No significant centrality dependence was seen in the total associated charged hadron yields, however, a clear particle-type dependence is present in all centralities which is consistent with previous studies. Yields associated with K^0_s triggers were found larger than Λ triggers at intermediate transverse momentum and at higher transverse momentum (> 4.5 GeV/c) the yields were comparable within uncertainties.

A small relative suppression was seen for the Λ triggers with p_T^{trig} = 3.0 – 4.0 GeV/c in the 0-20% most central collisions with respect to 60-80% peripheral collisions, where medium induced modifications are expected to be minimum. These results hint a possible trigger pool dilution at intermediate p_T due to recombination/coalescence. Similar suppression can also be attributed to an enhanced strange hadron production in the QGP, due to an abundance of strange quarks present in the medium. The absence of such suppression in the associated yields for the K^0_s triggers might be due to a competing effects such as interplay of trigger dilution effect and enhancement of soft associated yields due to jet quenching.

The new measurements presented in this work significantly improve statistical and systematical uncertainties of previous results.

Elliptic flow coefficient, v_2, for K^0_s and Λ was calculated in different collision centralities and was found consistent with previous measured trends for the same particles. A larger v_2 was measured for Λ triggers than K^0_s triggers, in agreement with the concept of particles acquiring v_2 at quark level in the de-confined QGP phase. Measurements of v_2 in Au+Au minimum bias data (0-80%) were also made and compared to previous measurements. Our values are consistent with the previously published results and confirm the constituent quark scaling of the elliptic flow, providing plausible evidence for particle production via recombination/coalescence.

APPENDIX A

TWO-DIMENSIONAL FITS ON PURE CONES – VARY EXCLUSION RAGNES

Plots here show the $\Delta\eta$ and $\Delta\phi$ projections of uncorrected pure cones with two-dimensional fits. Exclusion ranges were varied to calculate systematic uncertainties in total associated yields. Exclusion ranges and ranges over which projections were taken are labeled on top of the plots. In the legend 'Raw' represents uncorrected data and 'Gaussian' or 'Gen. Gaussian' denote if a normal or generalized Gaussian fit was used.

K^0_S-h: 0-20% $3.0 < p_T^{trig} < 3.5$ GeV/c

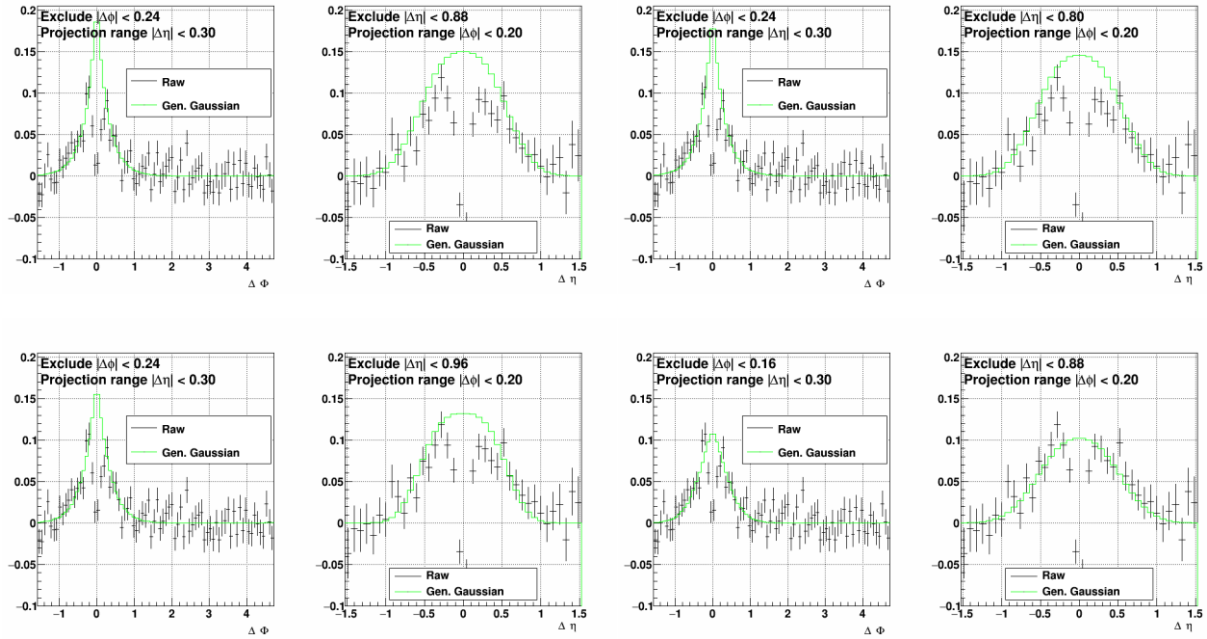

APPENDIX A (Continued)

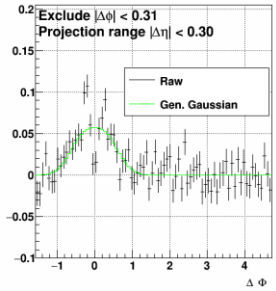

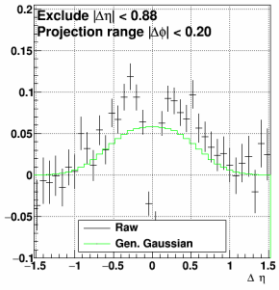

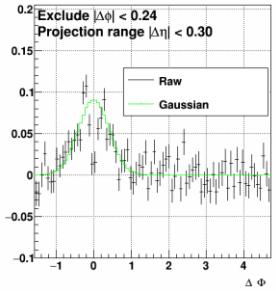

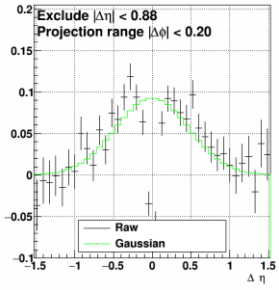

K^0_S-h: 0-20% $3.5 < p_T^{trig} < 4.5$ GeV/c

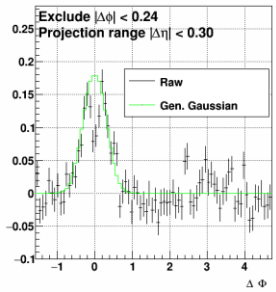

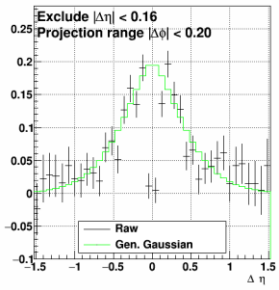

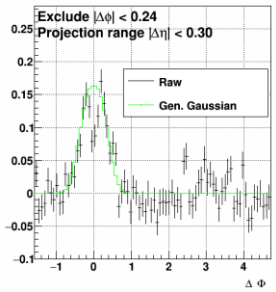

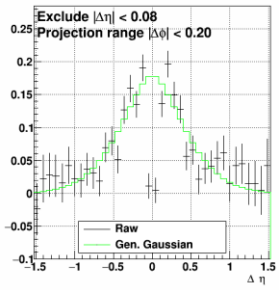

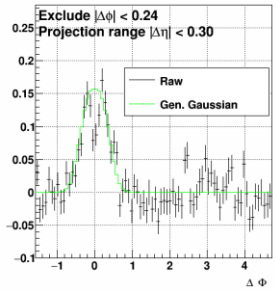

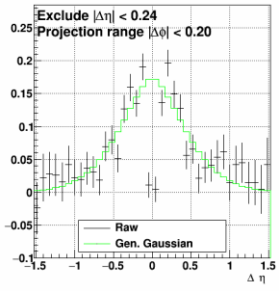

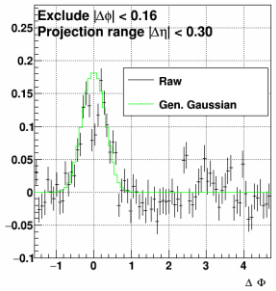

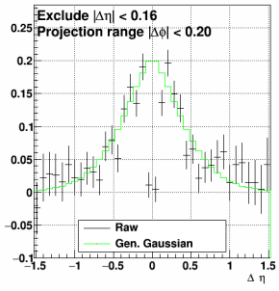

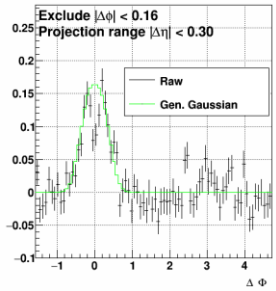

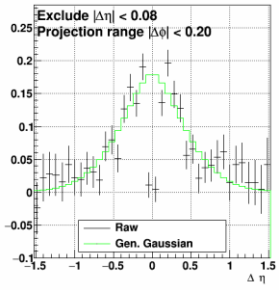

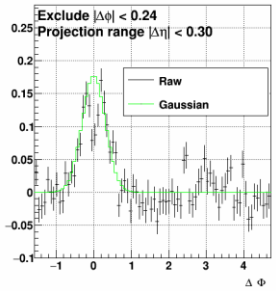

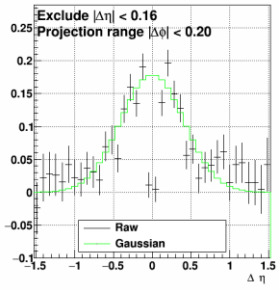

APPENDIX A (Continued)

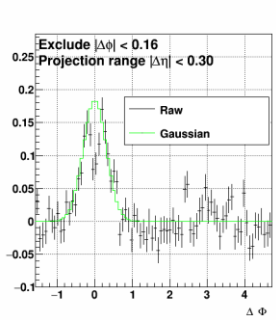

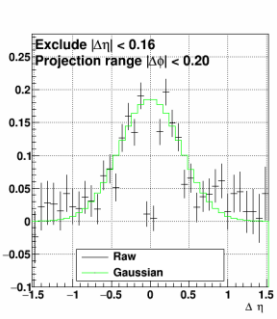

K^0_S-h: 0-20% $4.5 < p_T^{trig} < 5.5$ GeV/c

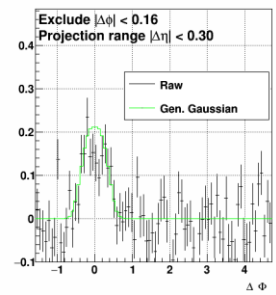

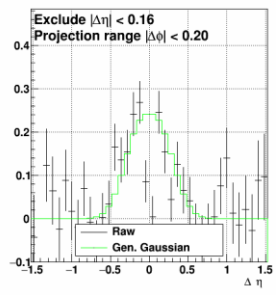

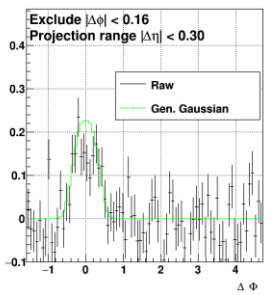

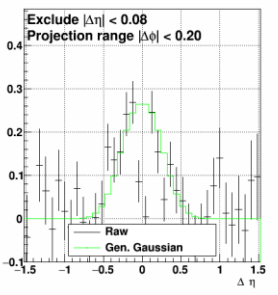

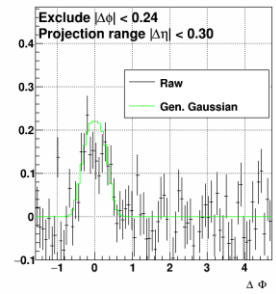

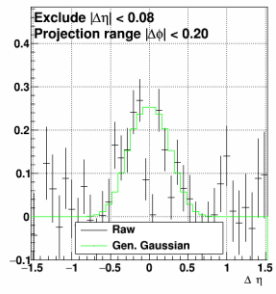

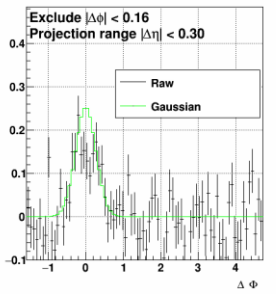

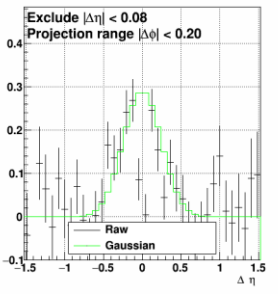

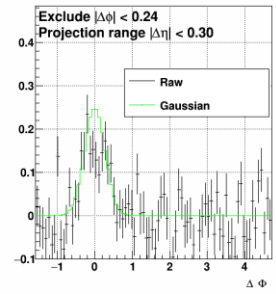

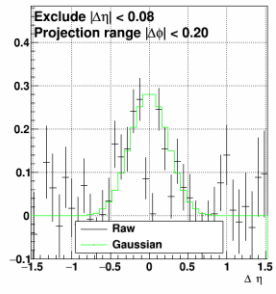

APPENDIX A (Continued)

K^0_S-h: 20-40% $3.0 < p_T^{trig} < 3.5$ GeV/c

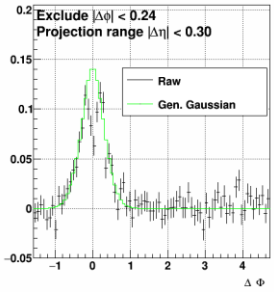

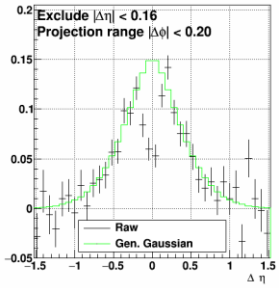

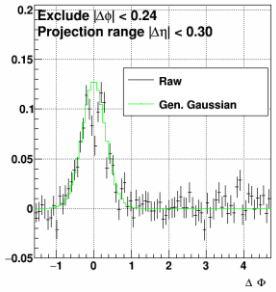

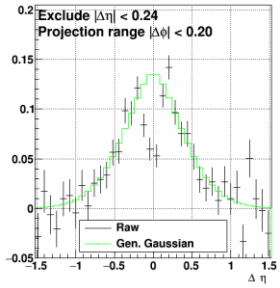

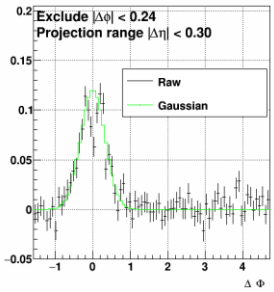

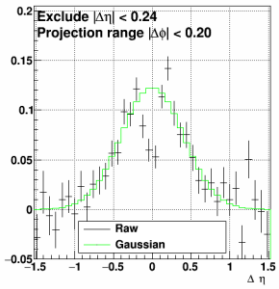

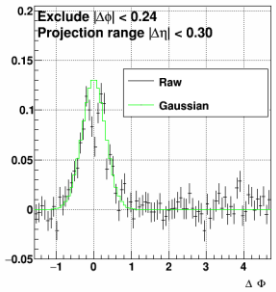

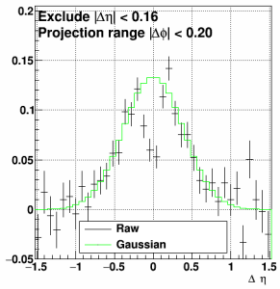

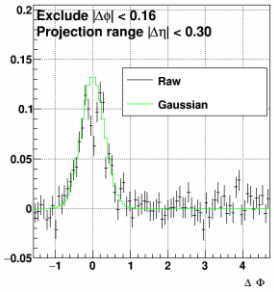

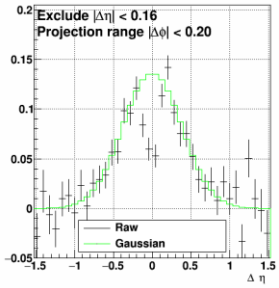

APPENDIX A (Continued)

K^0_S-h: 20-40% $3.5 < p_T^{trig} < 4.5$ GeV/c

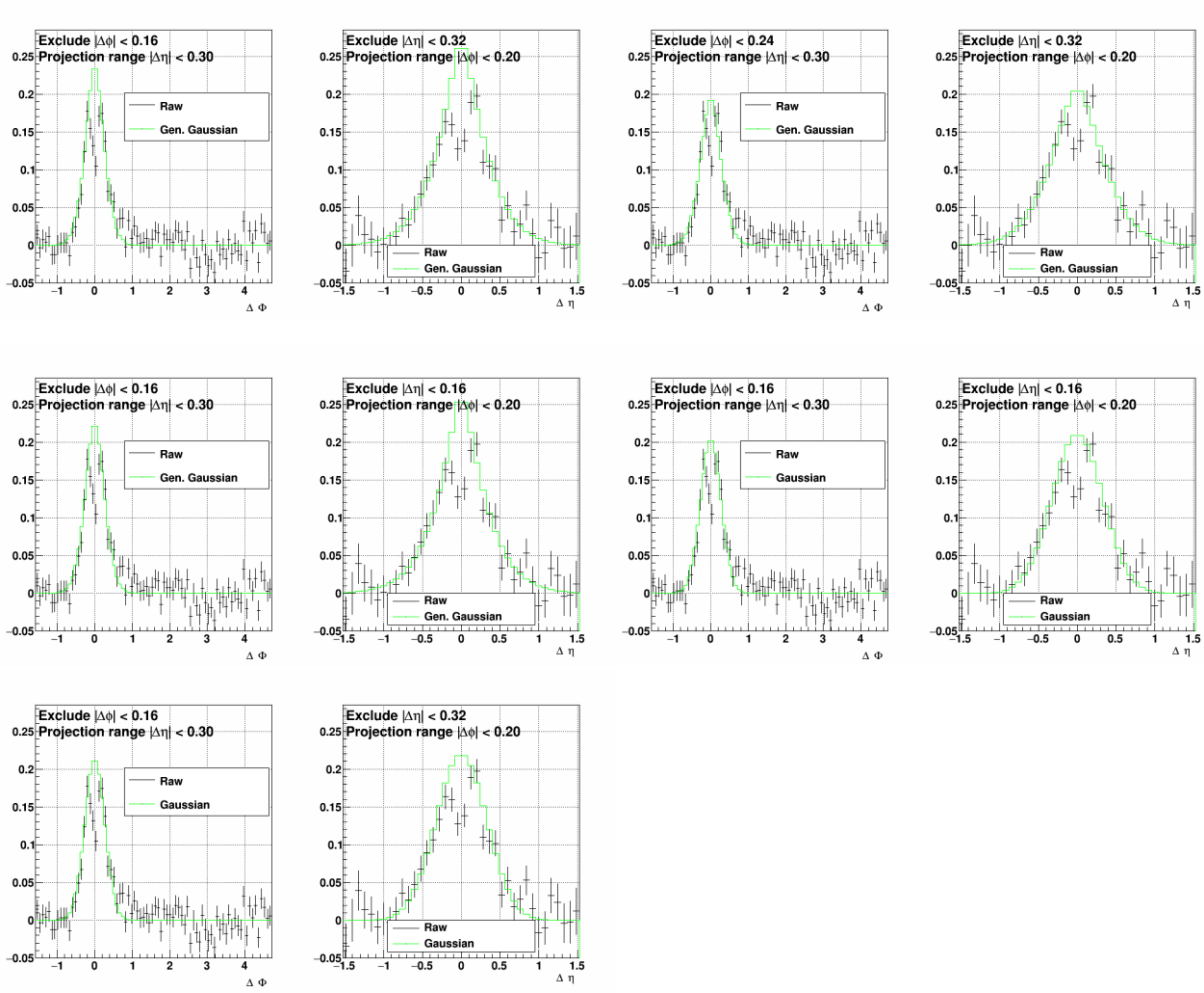

APPENDIX A (Continued)

K^0_S-h: 20-40% $4.5 < p_T^{trig} < 5.5$ GeV/c

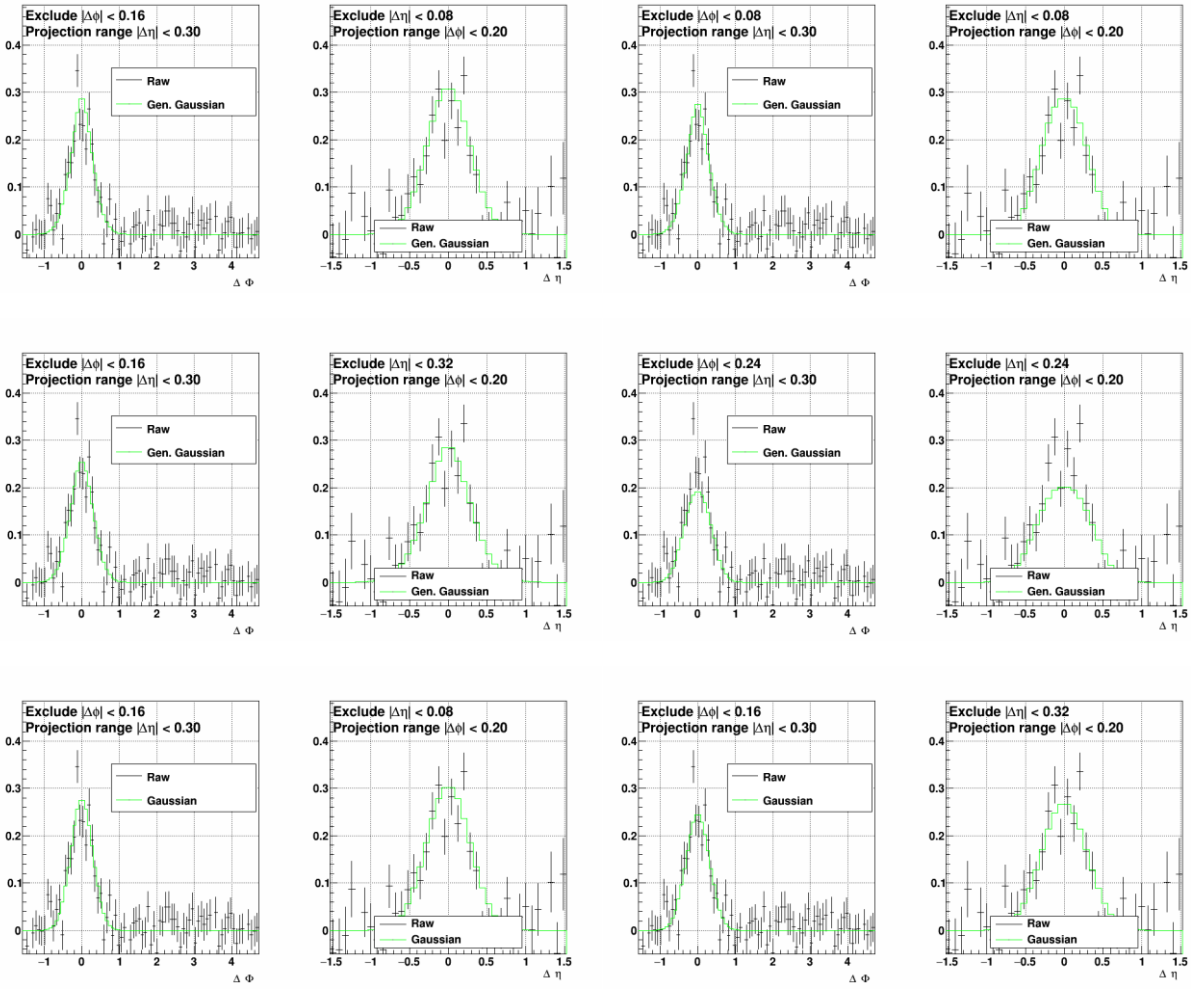

APPENDIX A (Continued)

K^0_S-h: 40-80% $3.0 < p_T^{trig} < 3.5$ GeV/c

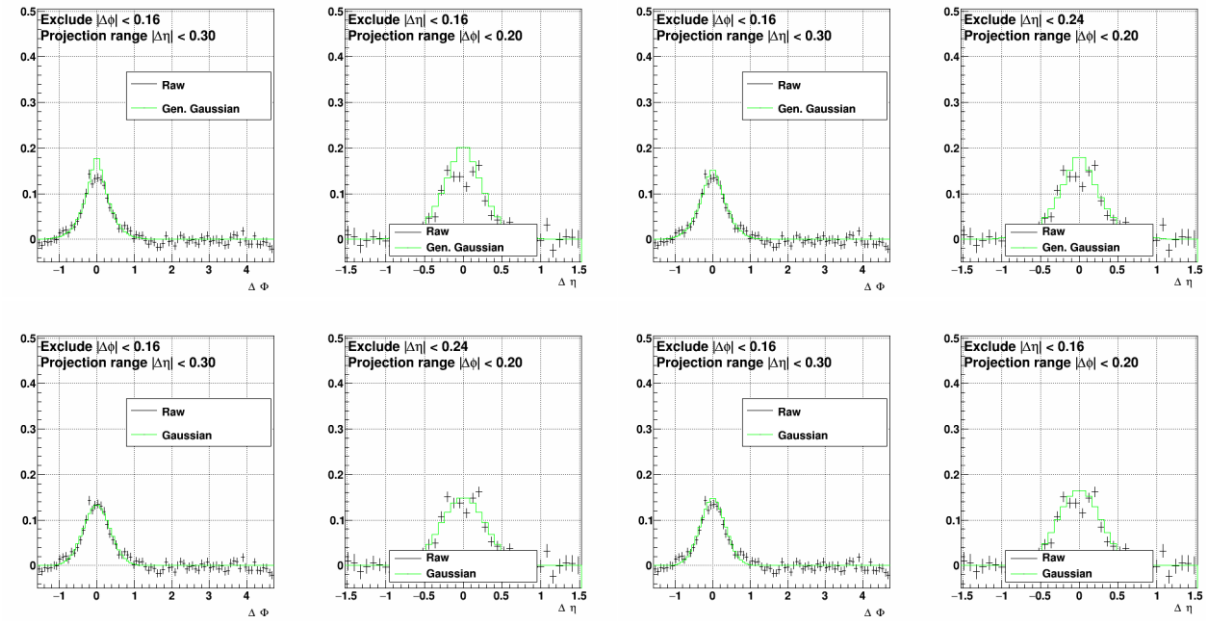

K^0_S-h: 40-80% $3.5 < p_T^{trig} < 4.5$ GeV/c

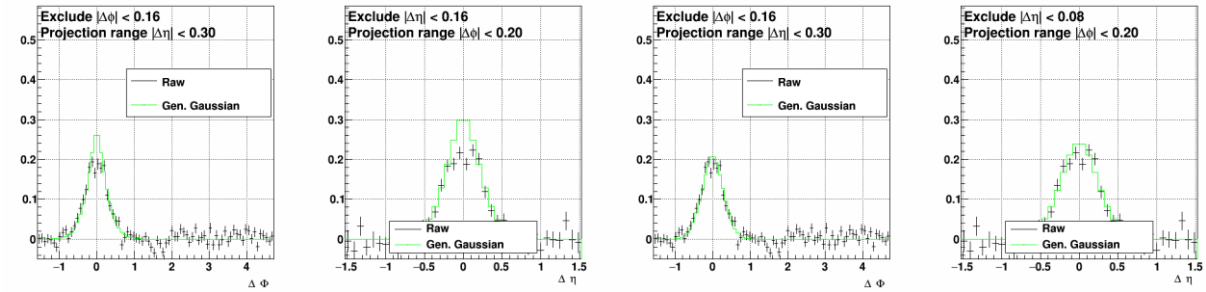

APPENDIX A (Continued)

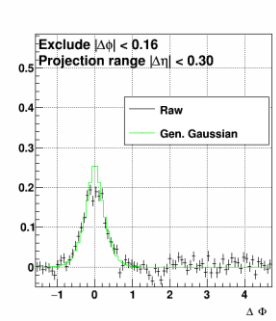

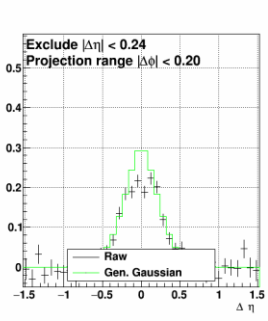

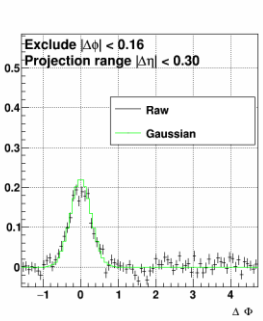

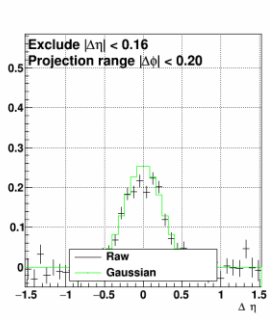

K^0_S-h: 40-80% $4.5 < p_T^{trig} < 5.5$ GeV/c

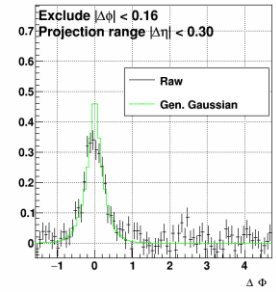

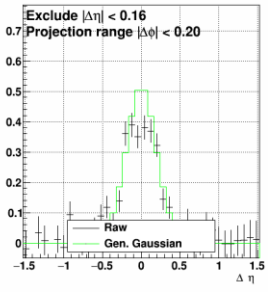

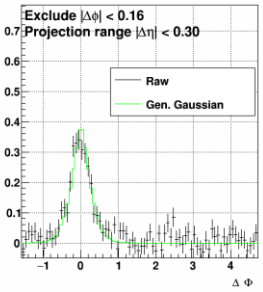

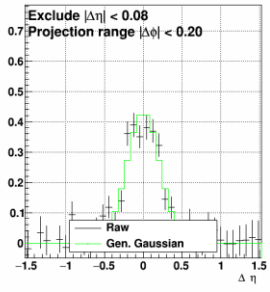

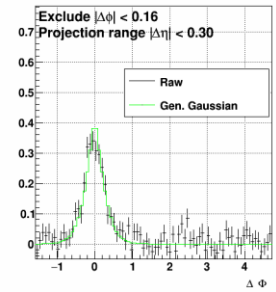

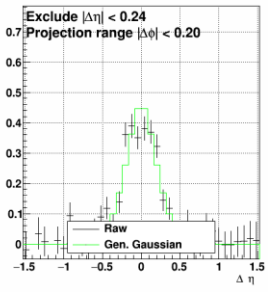

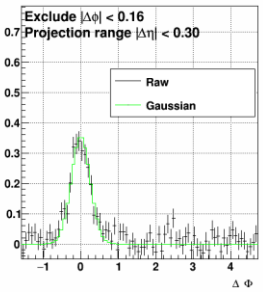

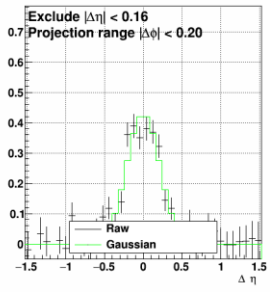

APPENDIX A (Continued)

Λ-h: 0-20% 3.0 < p_T^{trig} < 3.5 GeV/c

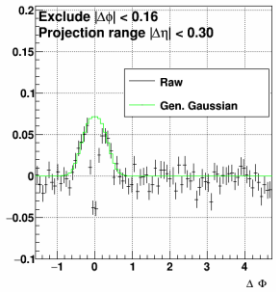

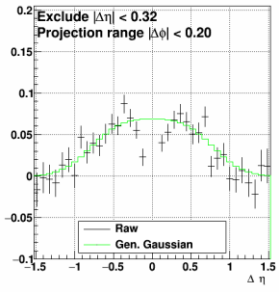

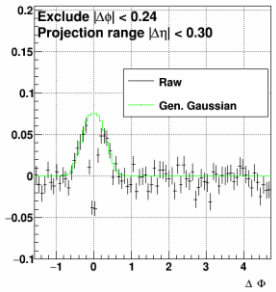

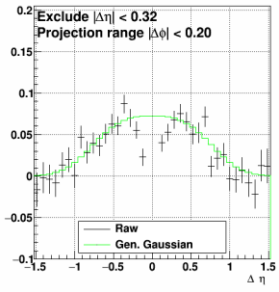

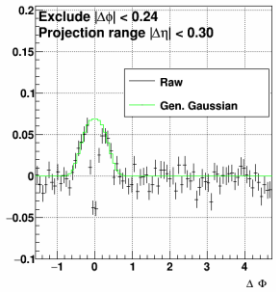

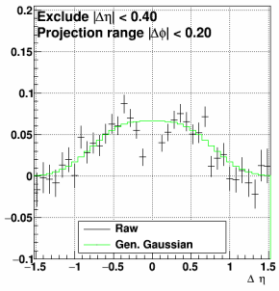

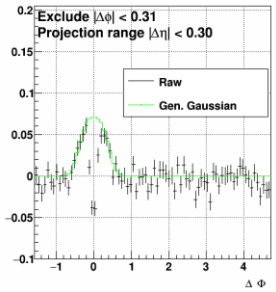

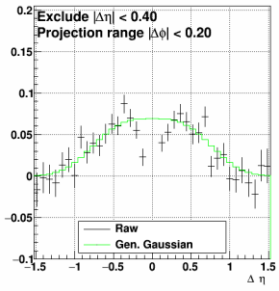

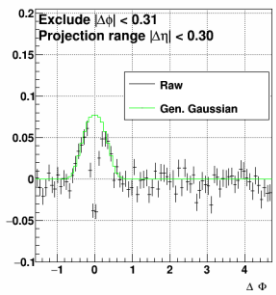

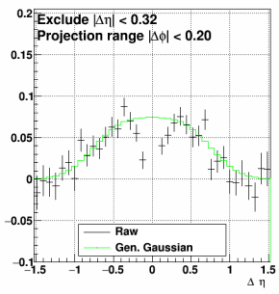

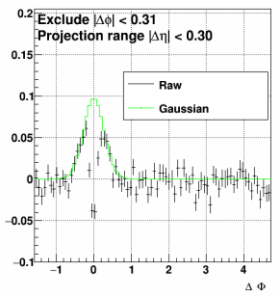

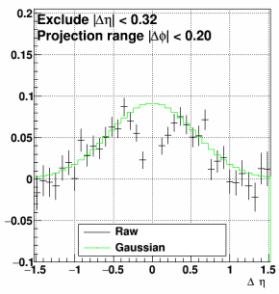

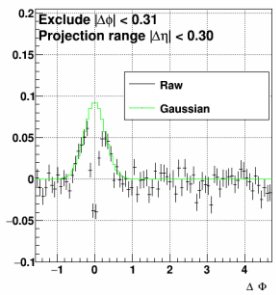

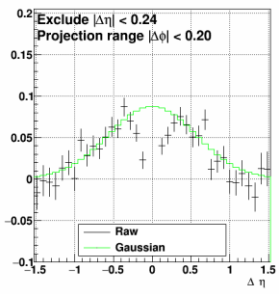

APPENDIX A (Continued)

Λ-h: 0-20% 3.5 < p_T^{trig} < 4.5 GeV/c

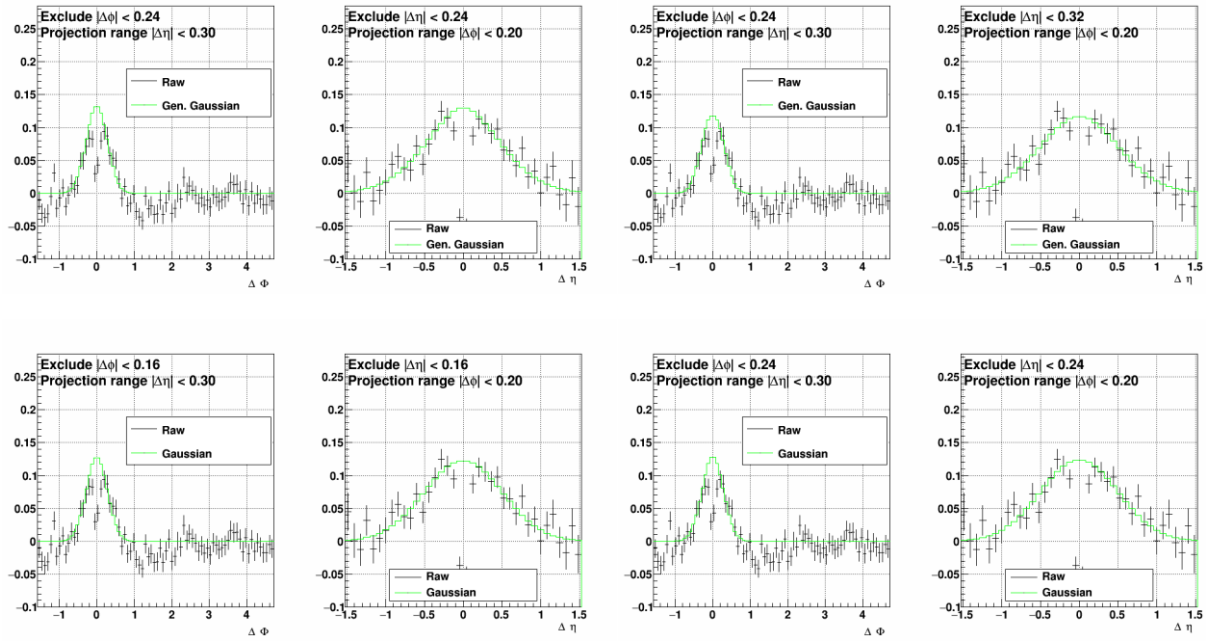

Λ-h: 0-20% 4.5 < p_T^{trig} < 5.5 GeV/c

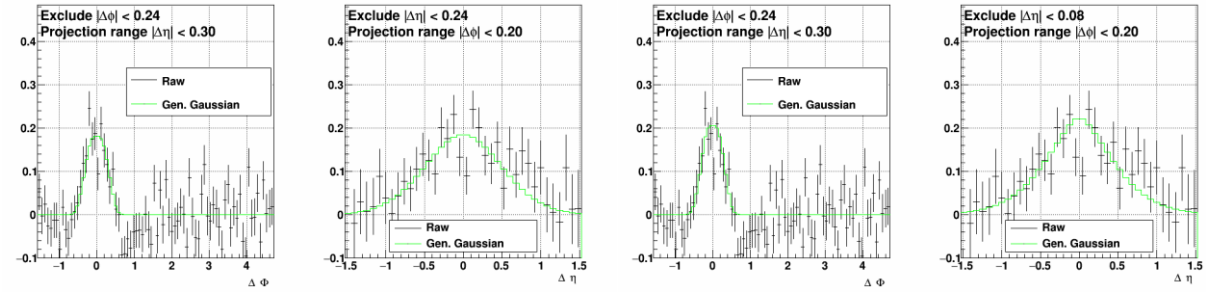

APPENDIX A (Continued)

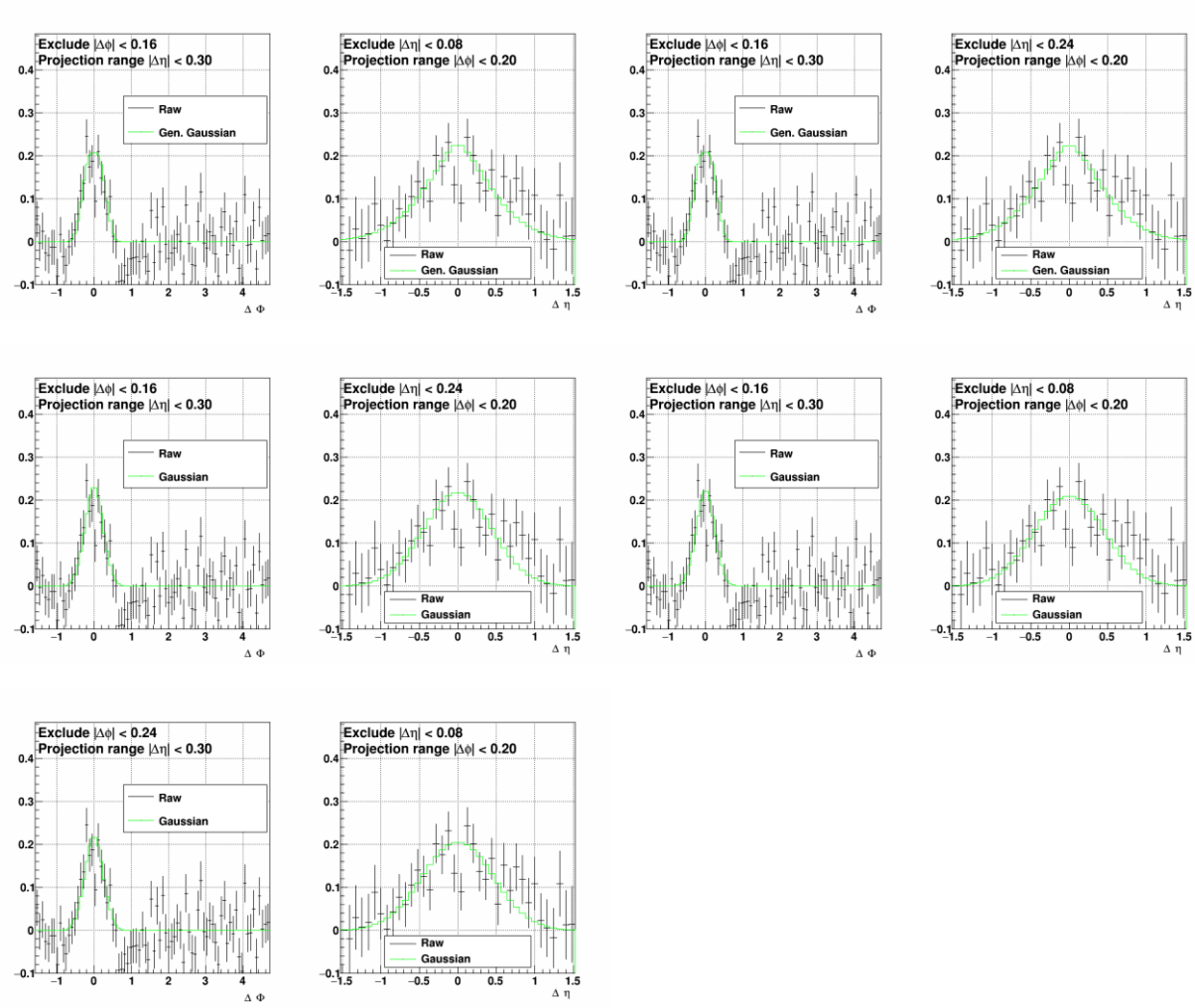

Λ-h: 20-40% 3.0 < p_T^{trig} < 3.5 GeV/c

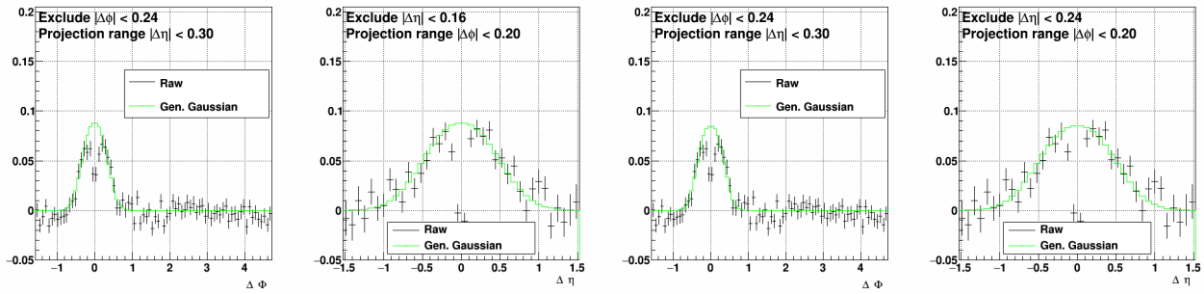

APPENDIX A (Continued)

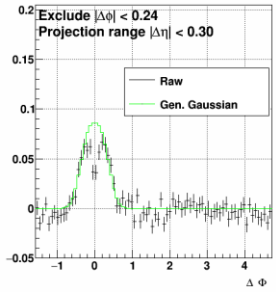

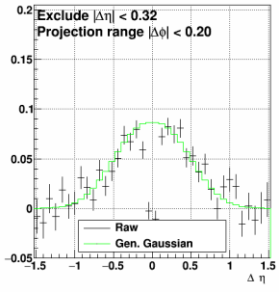

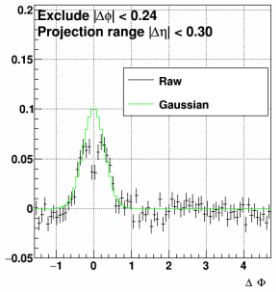

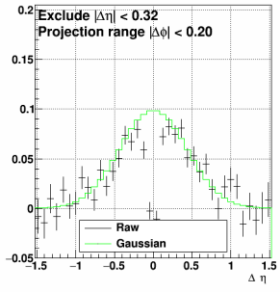

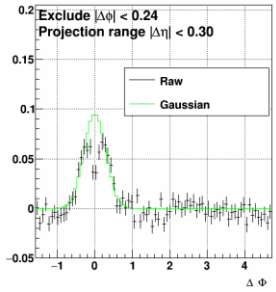

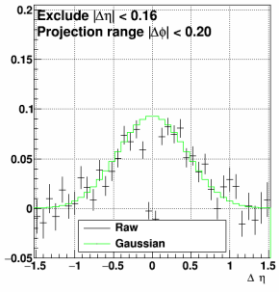

Λ-h: 20-40% 3.5 < p_T^{trig} < 4.5 GeV/c

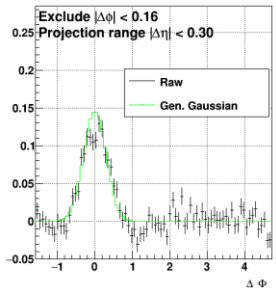

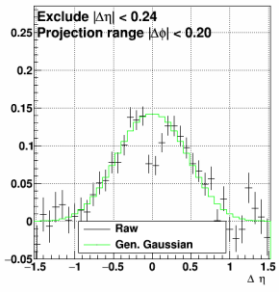

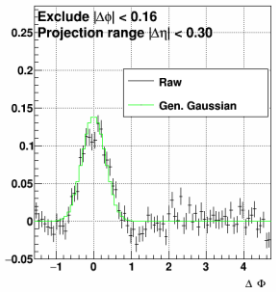

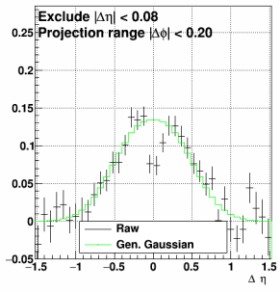

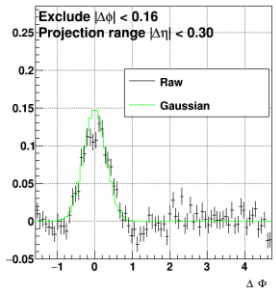

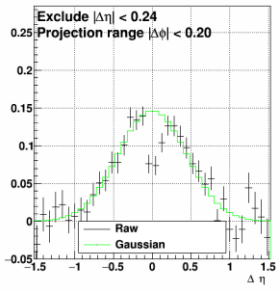

APPENDIX A (Continued)

Λ-h: 20-40% 4.5 < p_T^{trig} < 5.5 GeV/c

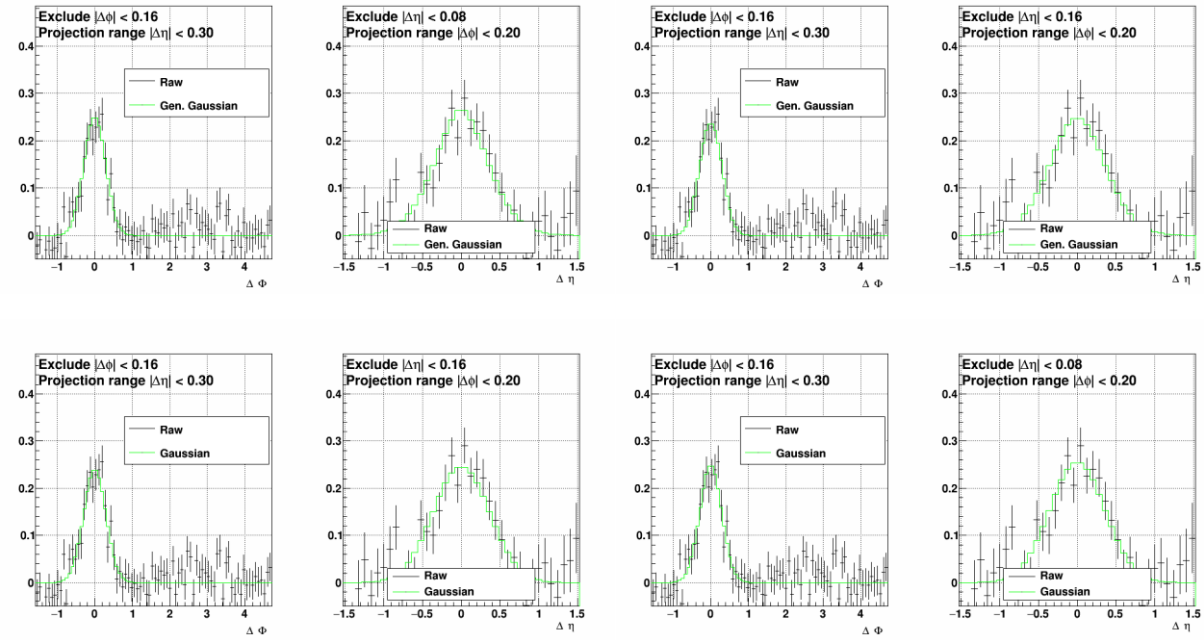

Λ-h: 40-80% 3.0 < p_T^{trig} < 3.5 GeV/c

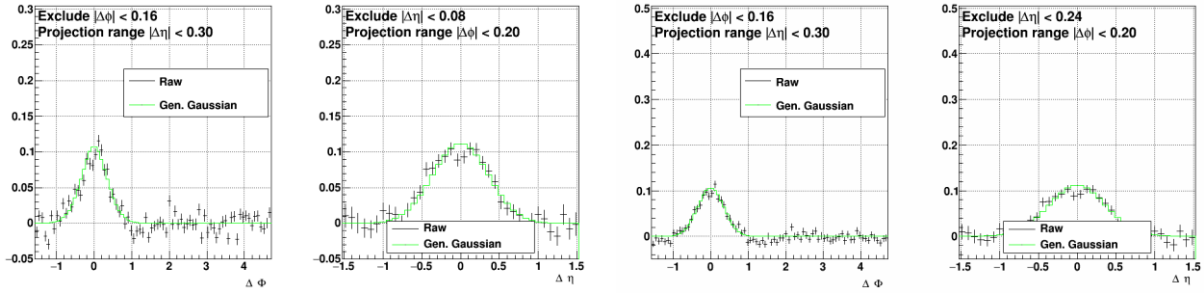

APPENDIX A (Continued)

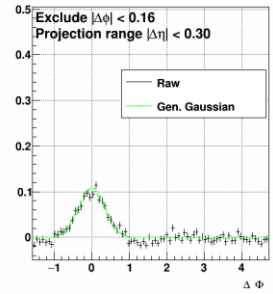

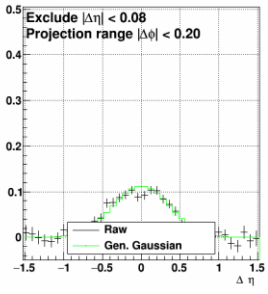

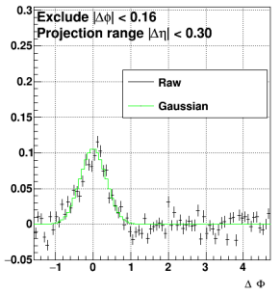

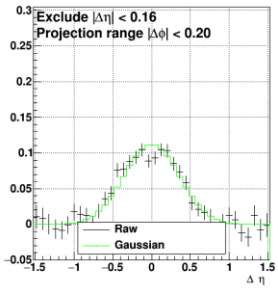

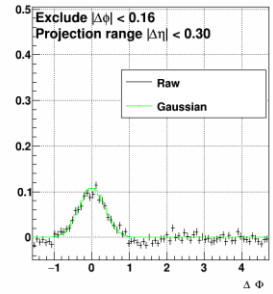

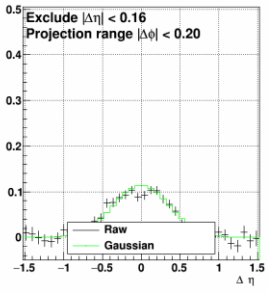

<u>Λ-h: 40-80% 3.5 < p_T^{trig} < 4.5 GeV/c</u>

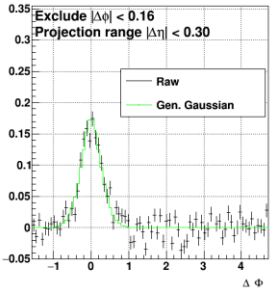

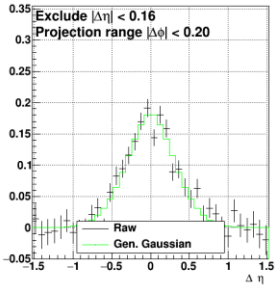

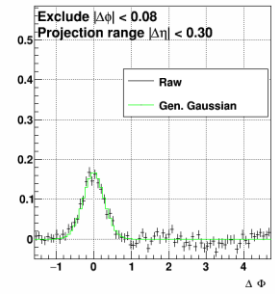

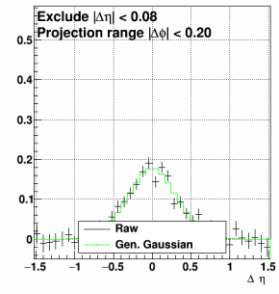

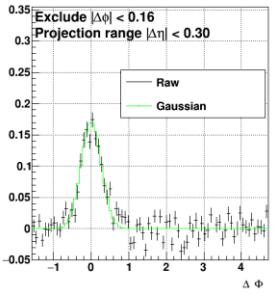

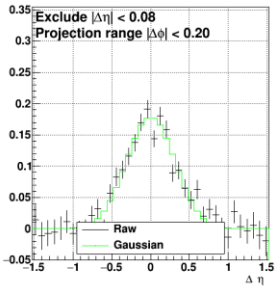

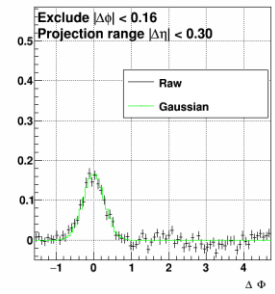

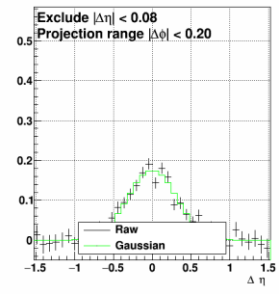

APPENDIX A (Continued)

Λ-h: 40-80% 4.5 < p_T^{trig} < 5.5 GeV/c

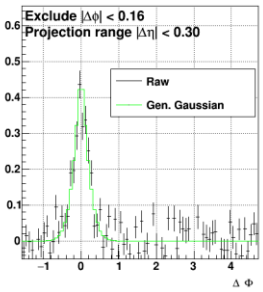

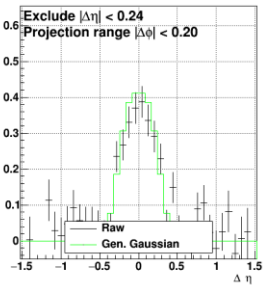

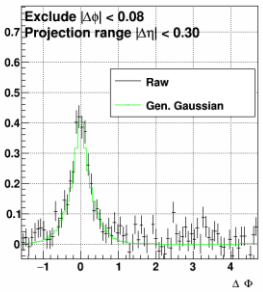

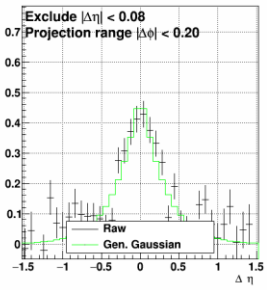

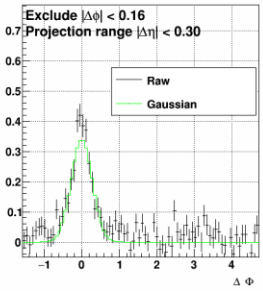

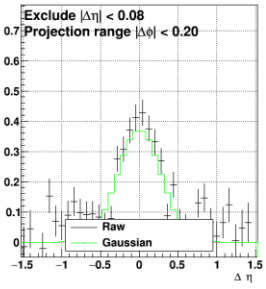

APPENDIX B

TWO-DIMENSIONAL FITS ON TOTAL CORRELATIONS – VARY EXCLUSION RAGNES

Plots here show the $\Delta\eta$ and $\Delta\phi$ projections of uncorrected pure cones with two-dimensional fits. Exclusion ranges were varied to calculate systematic uncertainties in total associated yields. Exclusion ranges and ranges over which projections were taken are labeled on top of the plots. In the legend 'Raw' represents uncorrected data and 'Gaussian' or 'Gen. Gaussian' denote if a normal or generalized Gaussian fit was used.

K^0_S-h: 0-20% $3.0 < p_T^{trig} < 3.5$ GeV/c

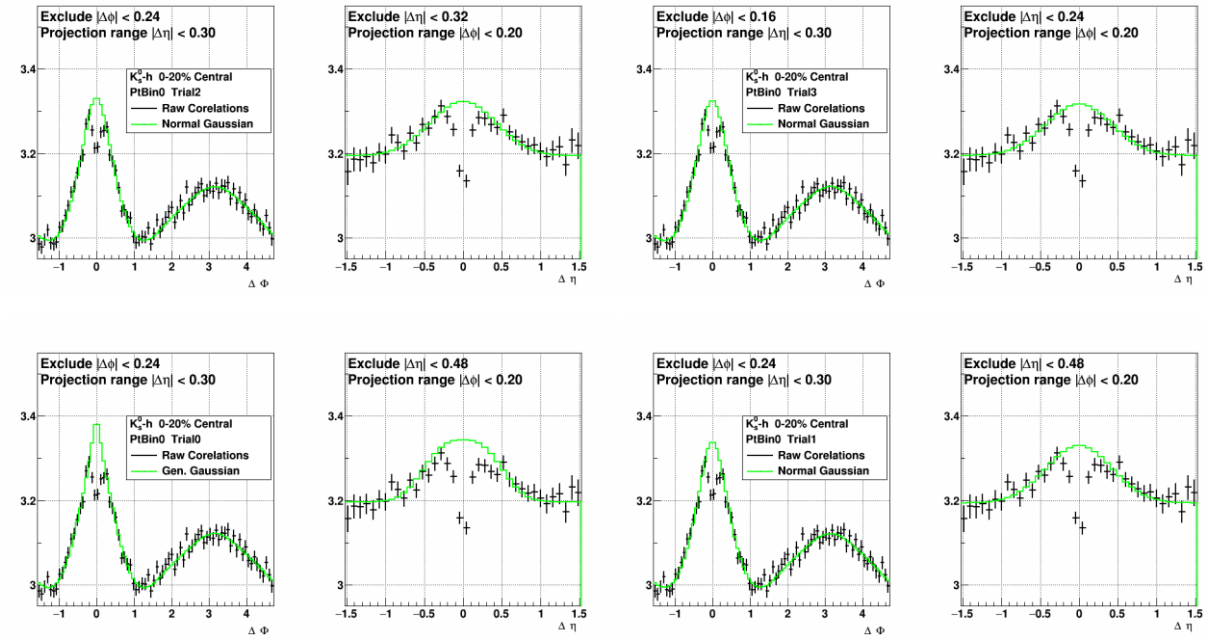

APPENDIX B (Continued)

K^0_S-h: 0-20% 3.5 < p_T^{trig} < 4.5 GeV/c

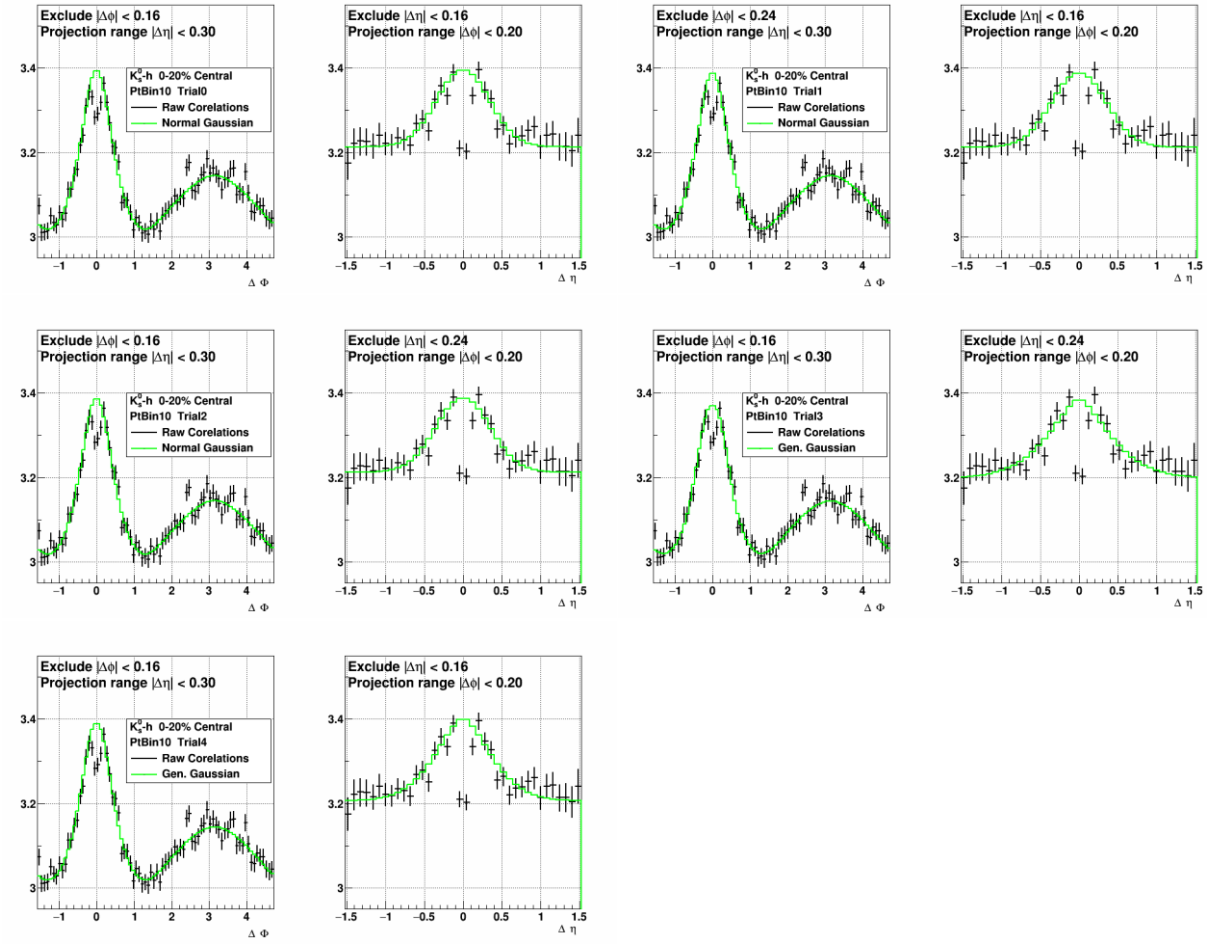

K^0_S-h: 0-20% 4.5 < p_T^{trig} < 5.5 GeV/c

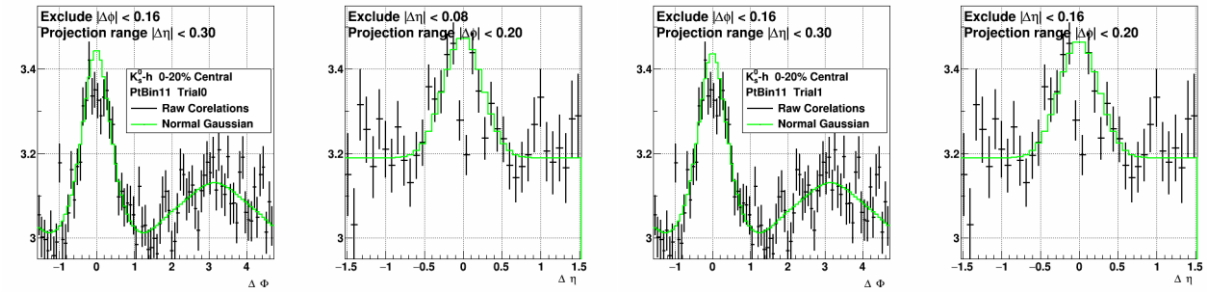

APPENDIX B (Continued)

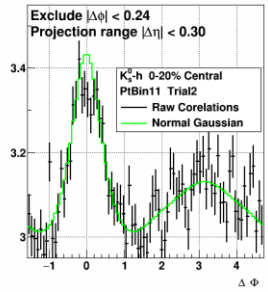

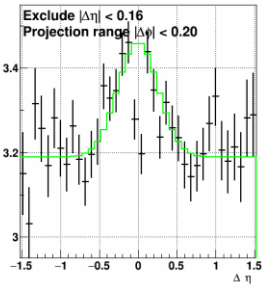

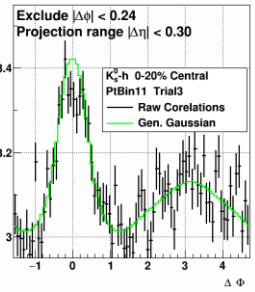

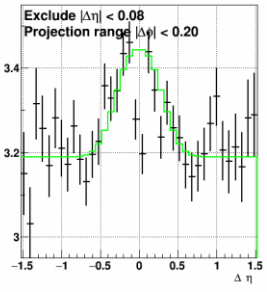

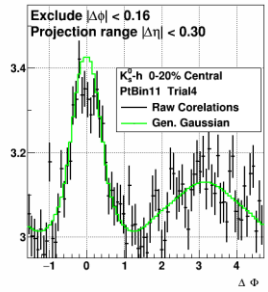

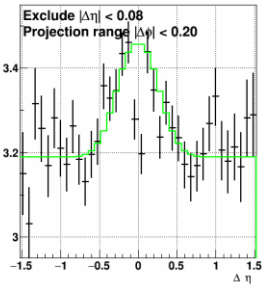

K^0_S-h: 20-40% 3.0 < p_T^{trig} < 3.5 GeV/c

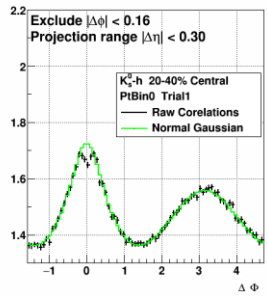

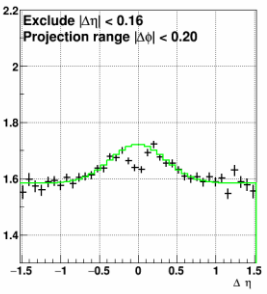

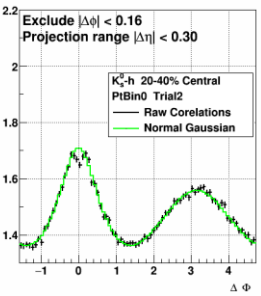

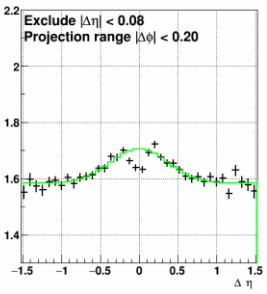

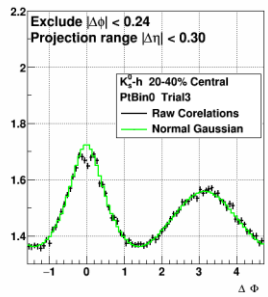

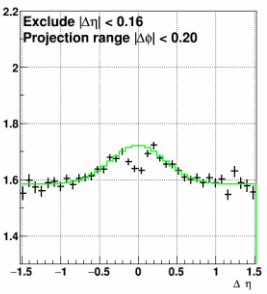

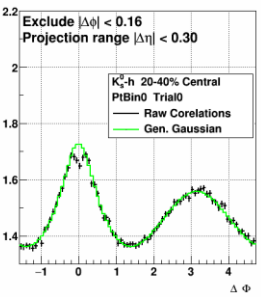

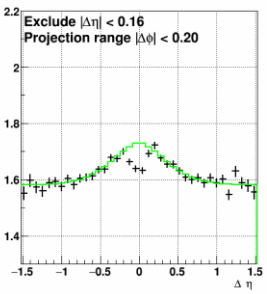

APPENDIX B (Continued)

K^0_S-h: 20-40% $3.5 < p_T^{trig} < 4.5$ GeV/c

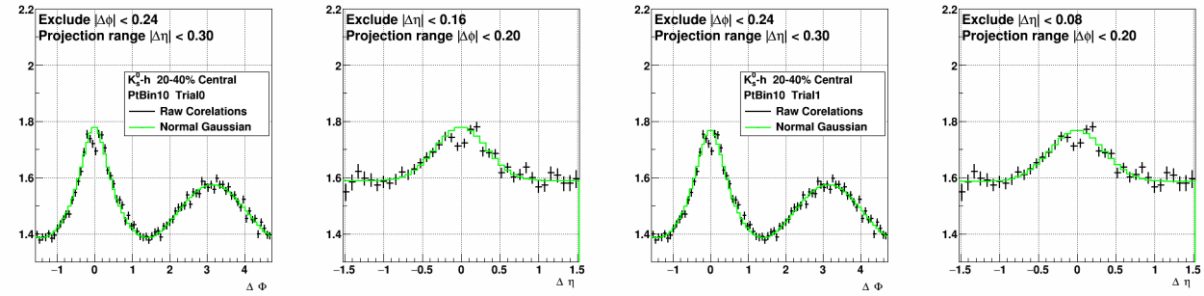

K^0_S-h: 20-40% $4.5 < p_T^{trig} < 5.5$ GeV/c

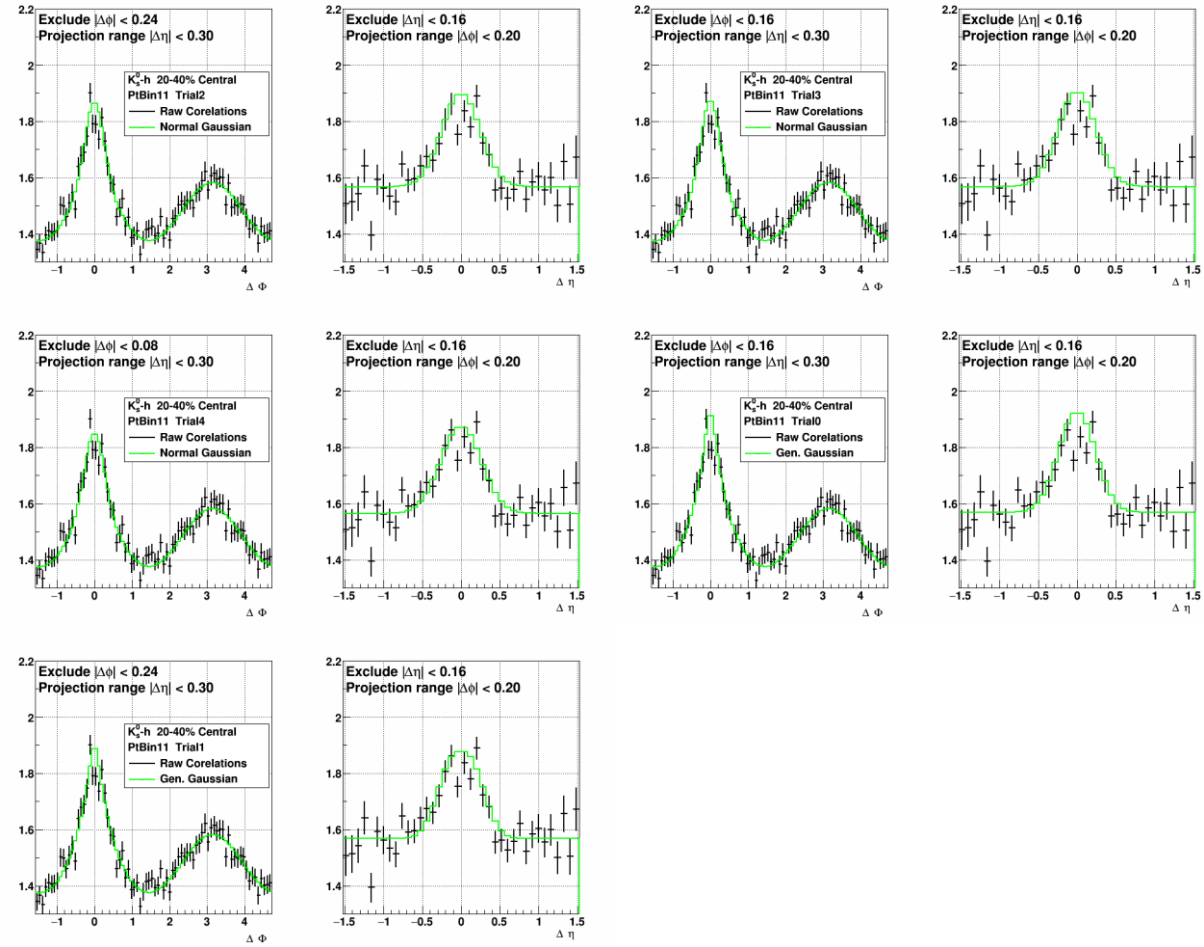

APPENDIX B (Continued)

K^0_S-h: 40-80% 3.0 < p_T^{trig} < 3.5 GeV/c

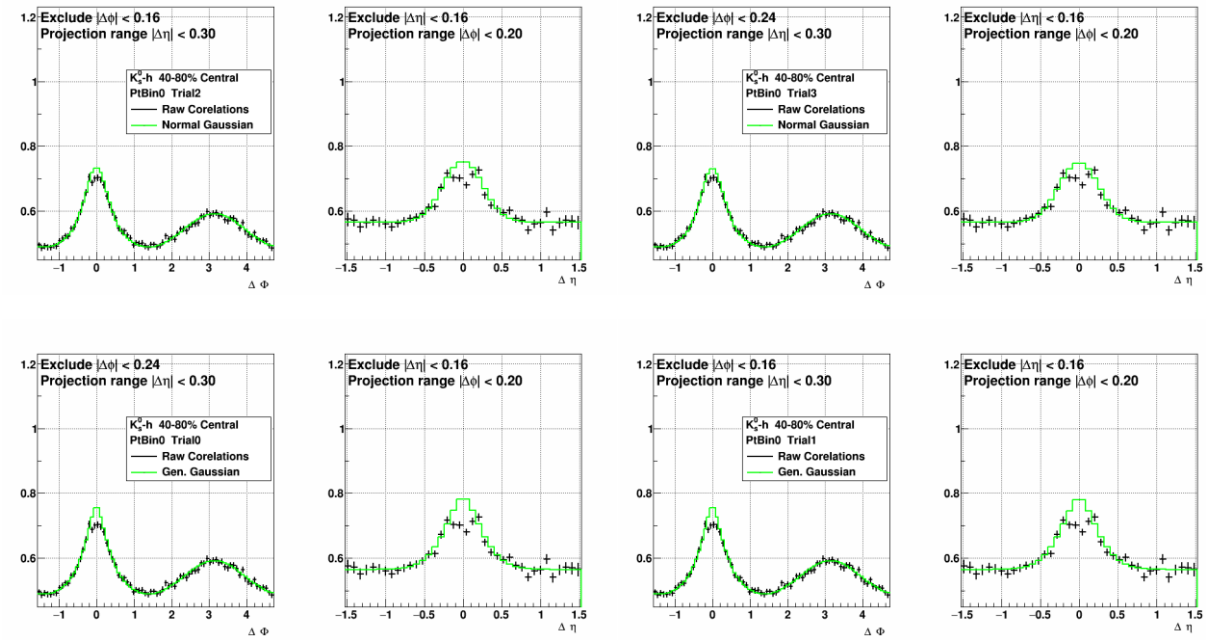

K^0_S-h: 40-80% 3.5 < p_T^{trig} < 4.5 GeV/c

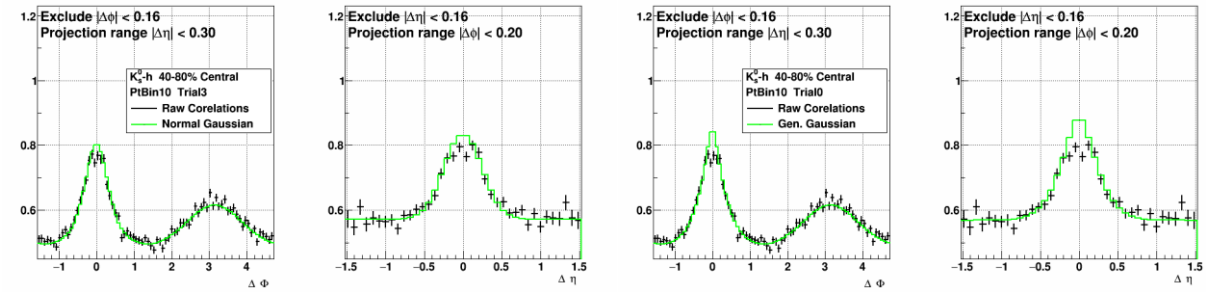

APPENDIX B (Continued)

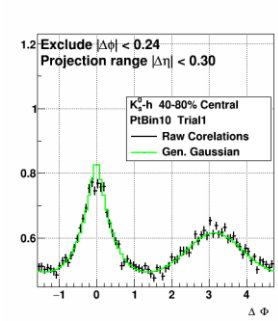

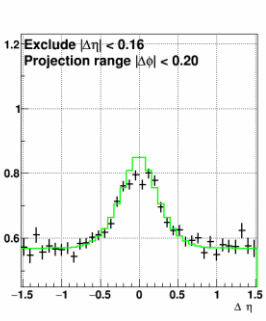

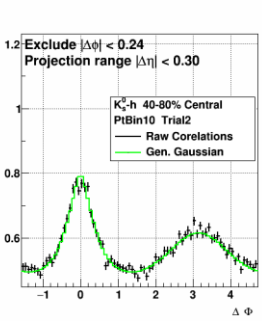

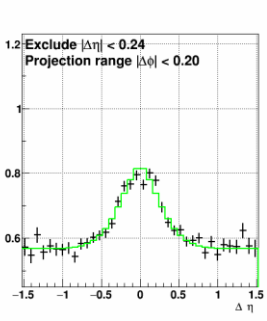

K^0_S-h: 40-80% 4.5 < p_T^{trig} < 5.5 GeV/c

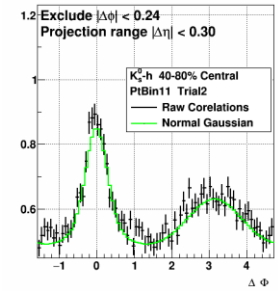

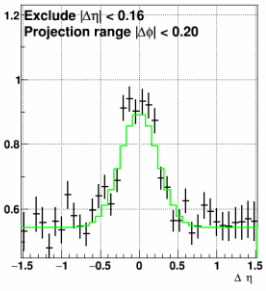

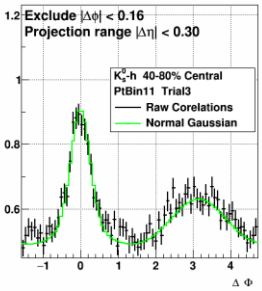

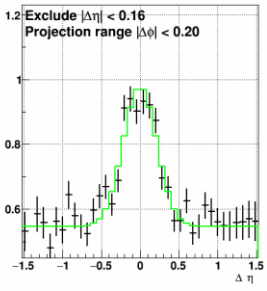

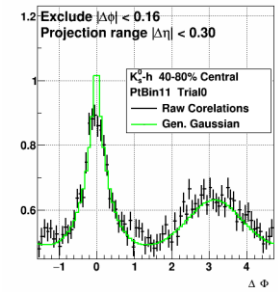

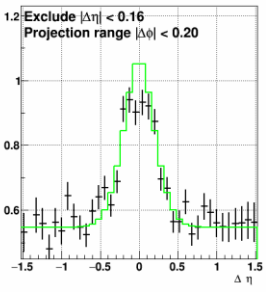

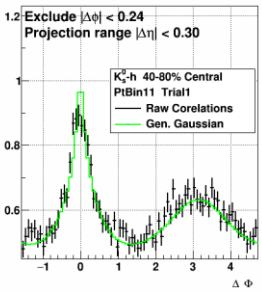

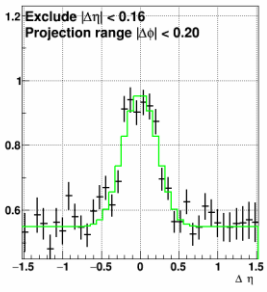

APPENDIX B (Continued)

Λ-h: 0-20% 3.0 < p_T^{trig} < 3.5 GeV/c

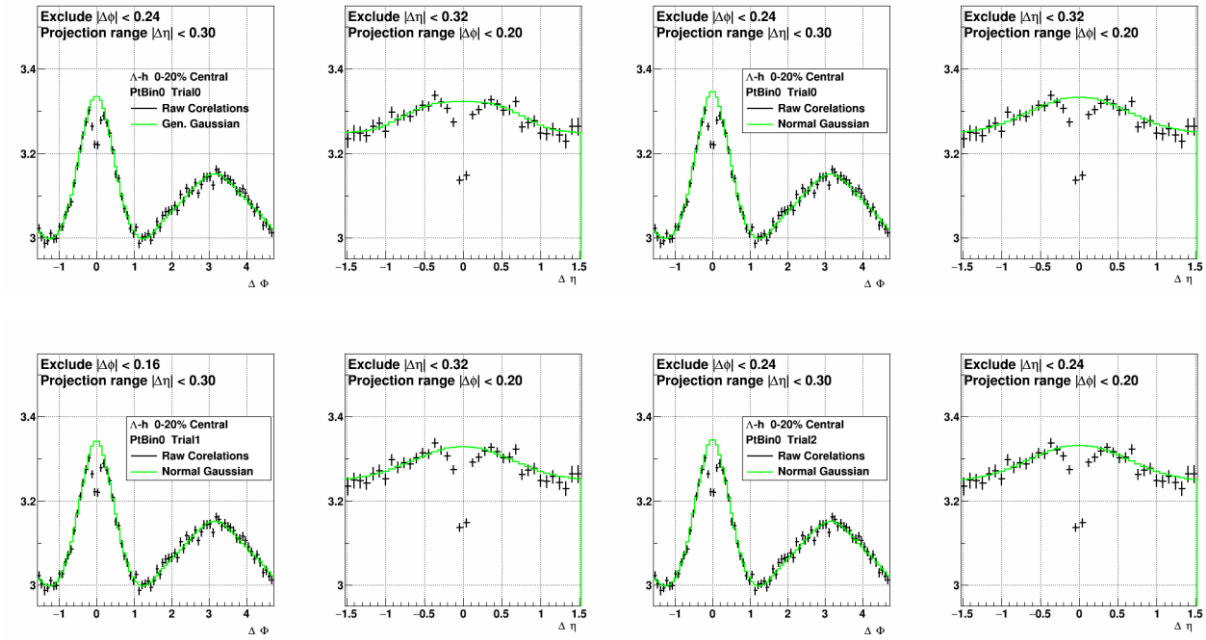

Λ-h: 0-20% 3.5 < p_T^{trig} < 4.5 GeV/c

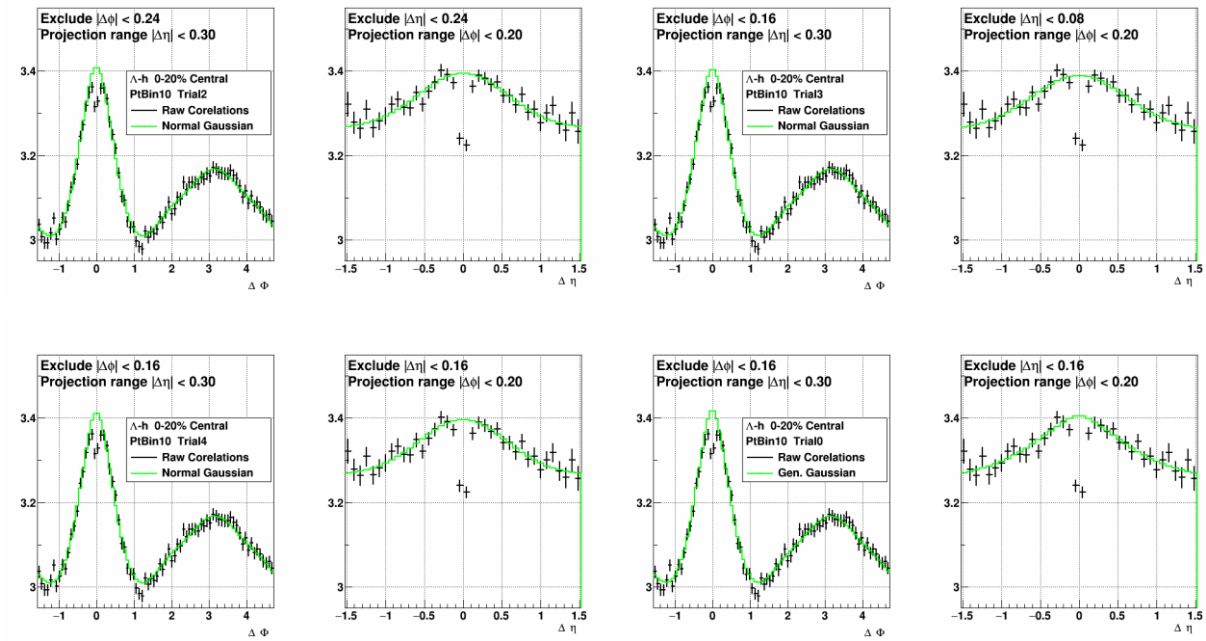

APPENDIX B (Continued)

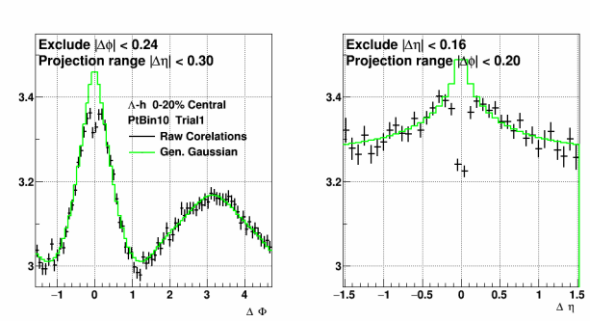

Λ-h: 0-20% 4.5 < p_T^{trig} < 5.5 GeV/c

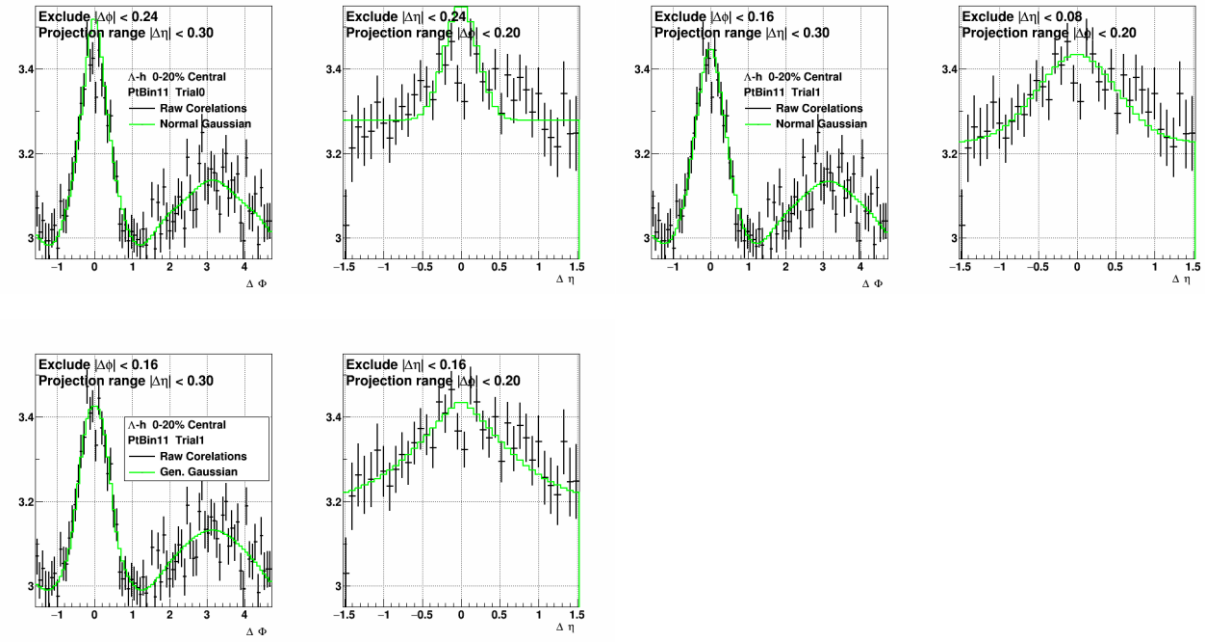

APPENDIX B (Continued)

Λ-h: 20-40% 3.0 < p_T^{trig} < 3.5 GeV/c

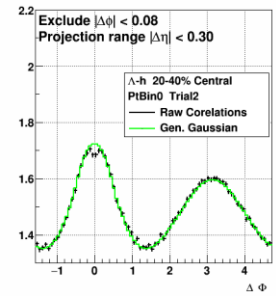

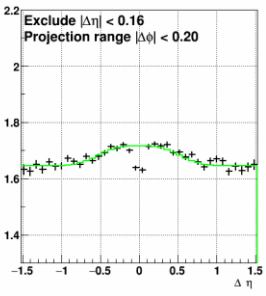

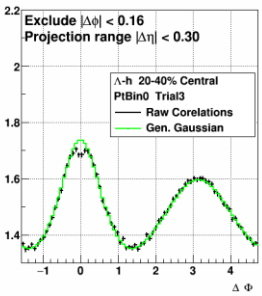

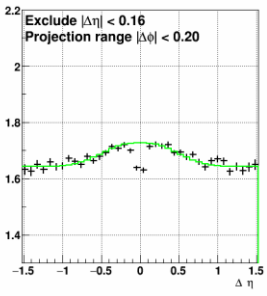

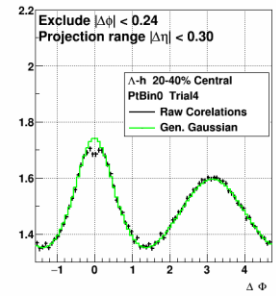

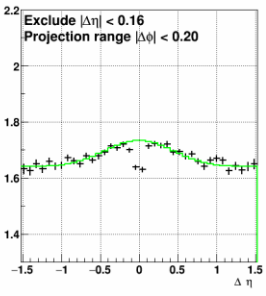

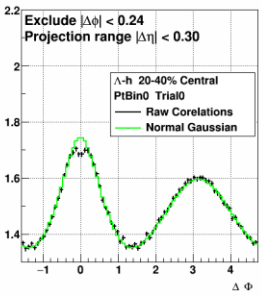

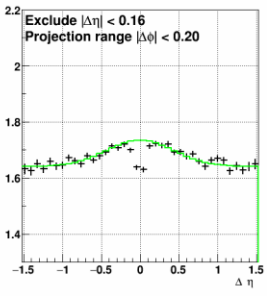

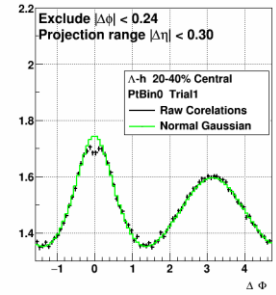

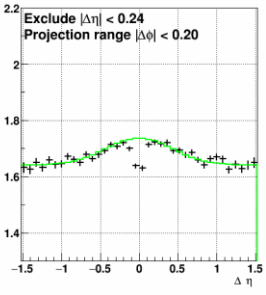

APPENDIX B (Continued)

Λ-h: 20-40% 3.5 < p_T^{trig} < 4.5 GeV/c

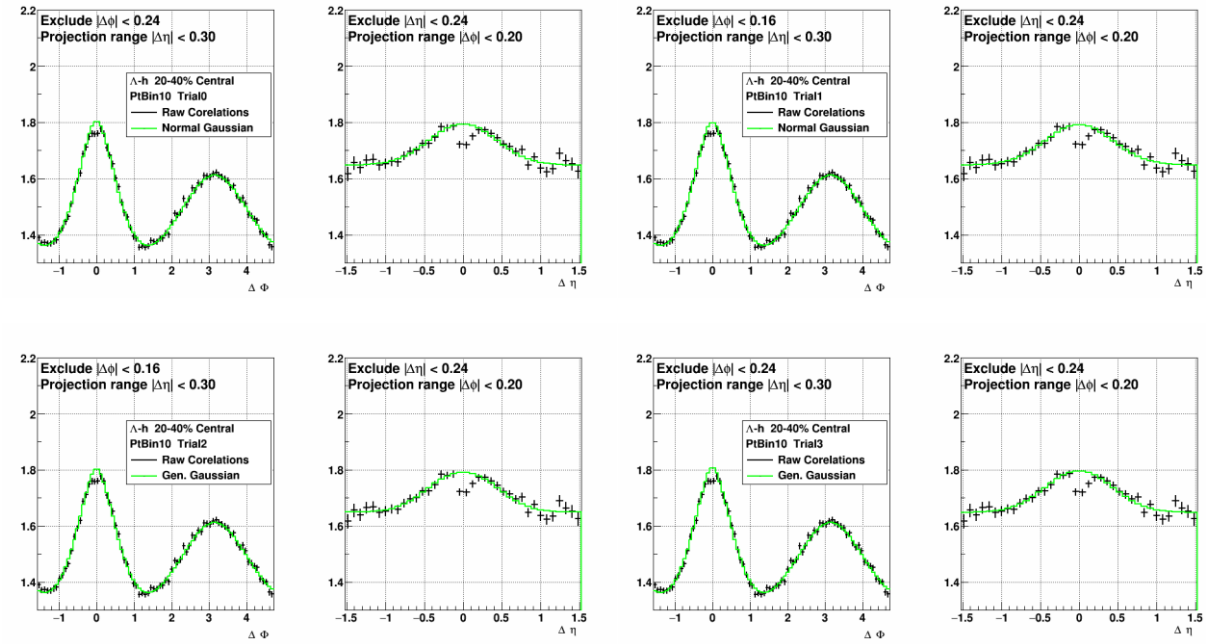

Λ-h: 20-40% 4.5 < p_T^{trig} < 5.5 GeV/c

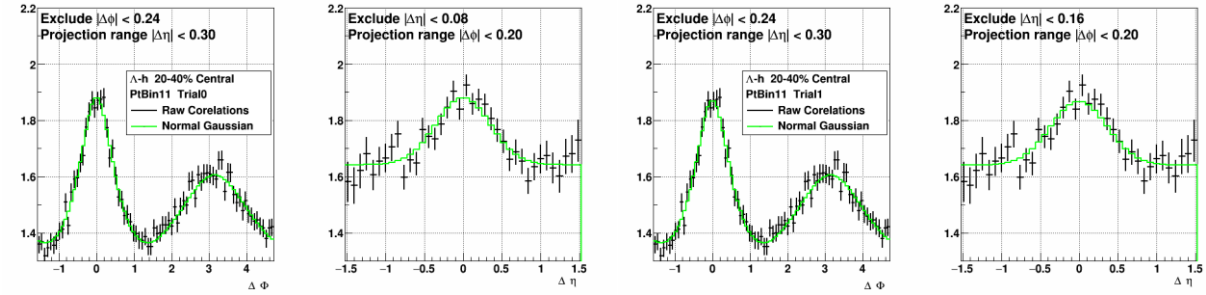

APPENDIX B (Continued)

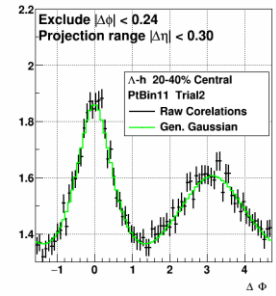

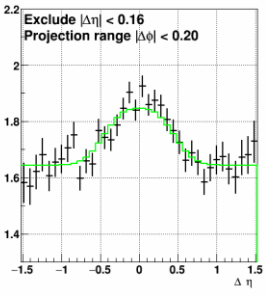

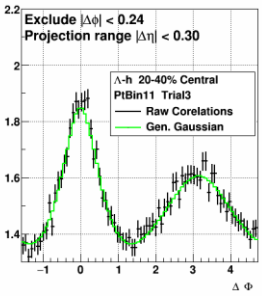

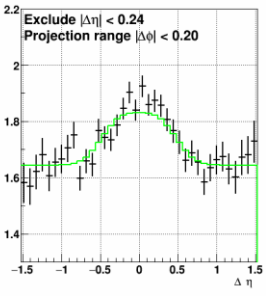

Λ-h: 40-80% 3.0 < p_T^{trig} < 3.5 GeV/c

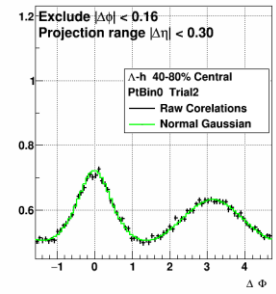

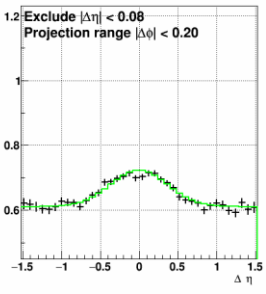

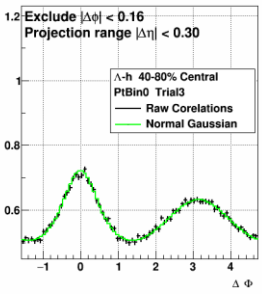

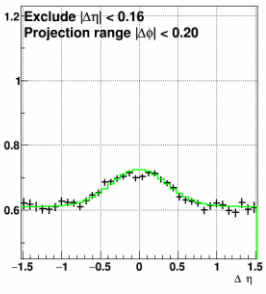

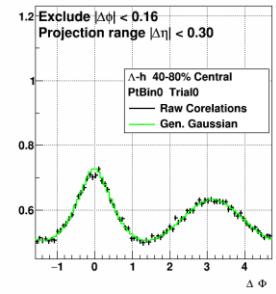

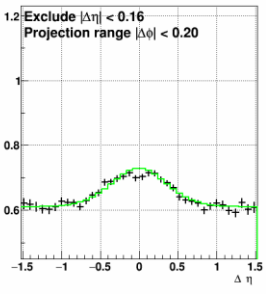

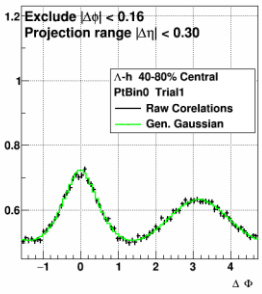

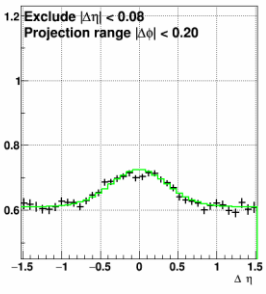

APPENDIX B (Continued)

Λ-h: 40-80% 3.5 < p_T^{trig} < 4.5 GeV/c

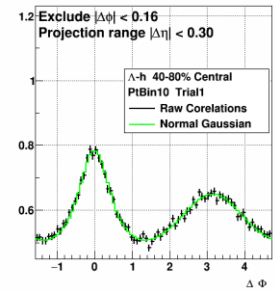

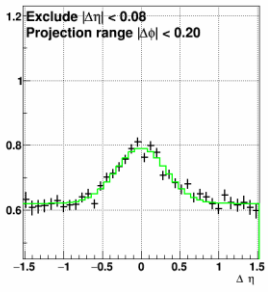

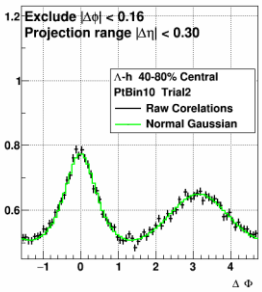

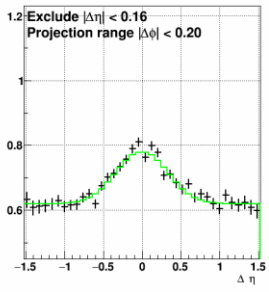

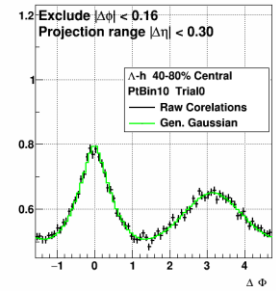

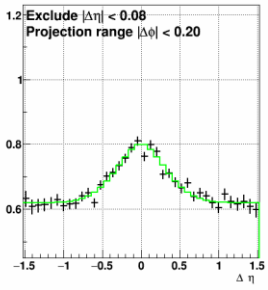

Λ-h: 40-80% 4.5 < p_T^{trig} < 5.5 GeV/c

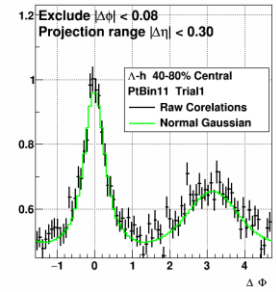

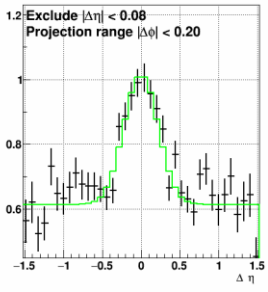

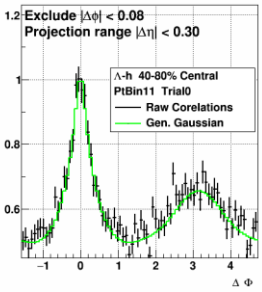

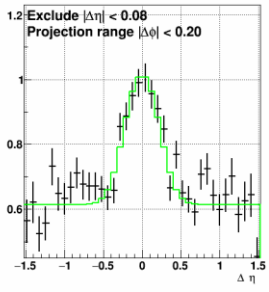

APPENDIX C

BACKGROUND SUBTRACTION – VARY $\Delta\eta$ RANGES

Plots in this appendix show the spread in total associate yield values seen when $\Delta\eta$ ranges were varied to calculate the background level. Mean and sigma of the yield values were used to calculate systematic uncertainties on the final associated yields. Each plots lists the ranges selected, chi squared for the one-dimensional fit used to describe the background, and associated yield calculated by subtracting that background.

K^0_S-h: 0-20%

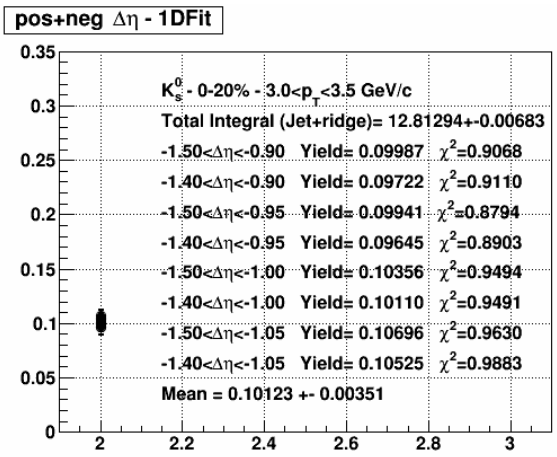

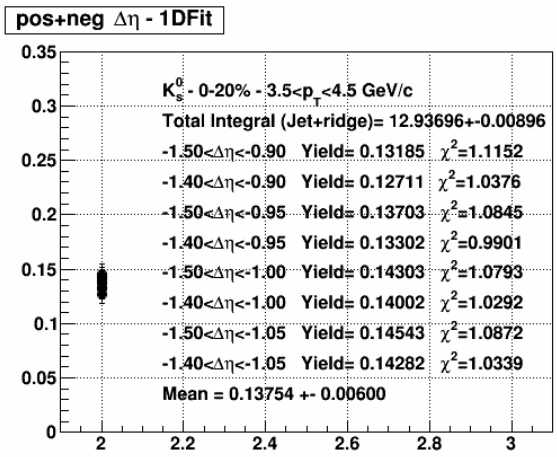

APPENDIX C (Continued)

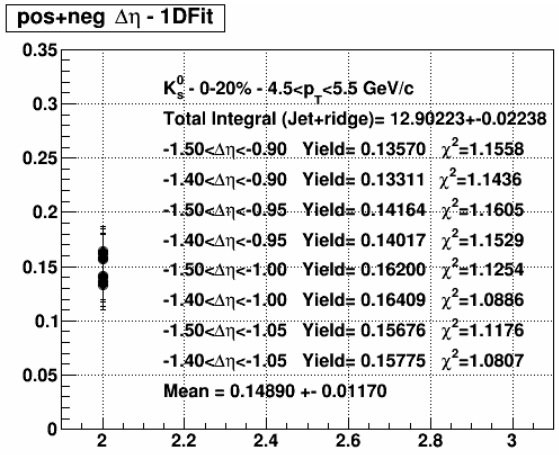

K^0_S-h: 20-40%

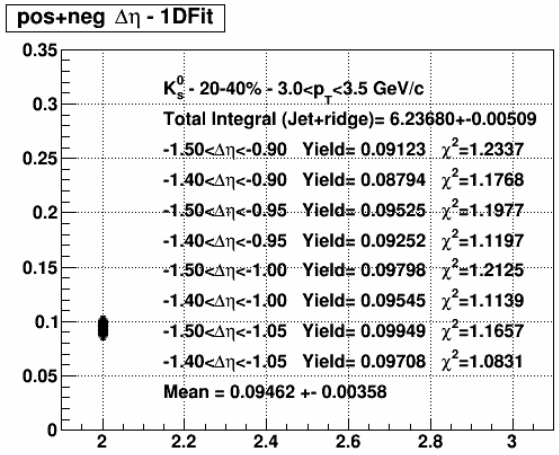

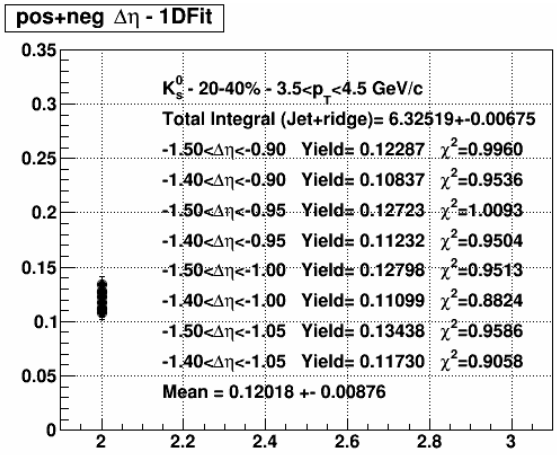

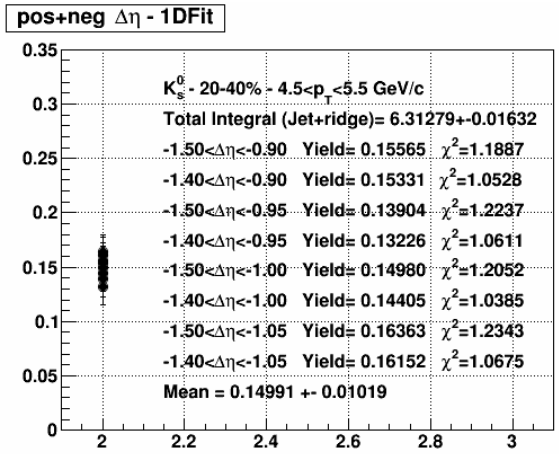

APPENDIX C (Continued)

K^0_S-h: 40-80%

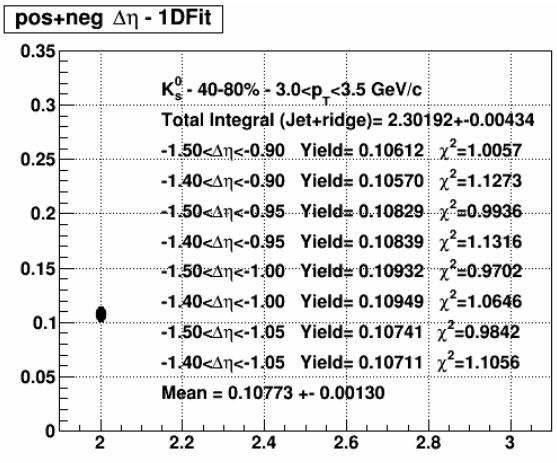

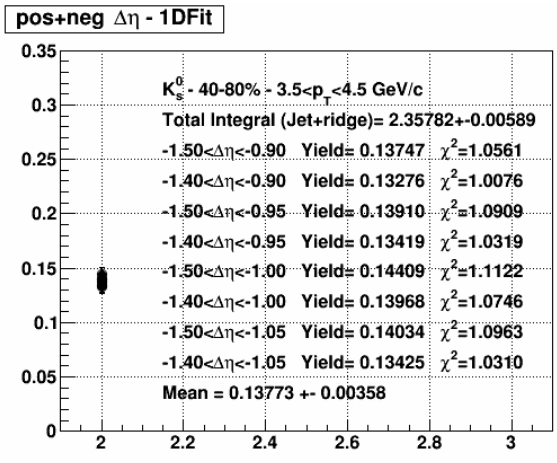

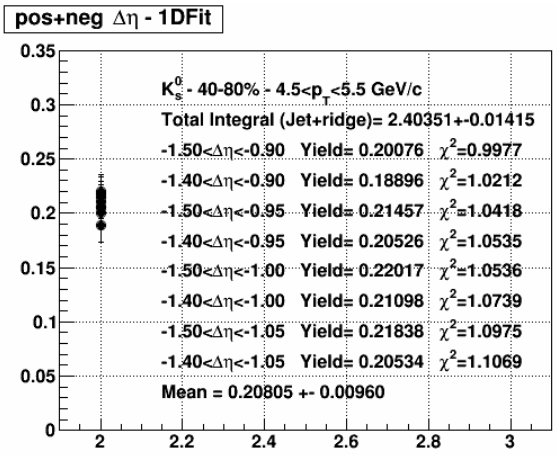

APPENDIX C (Continued)

Λ-h: 0-20%

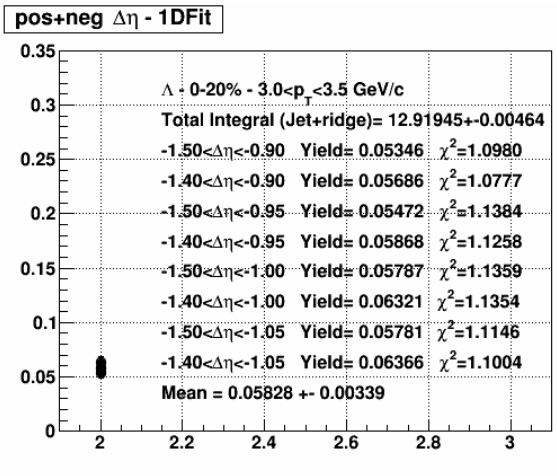

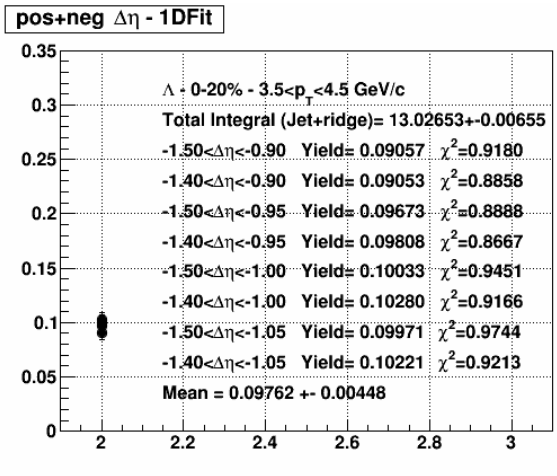

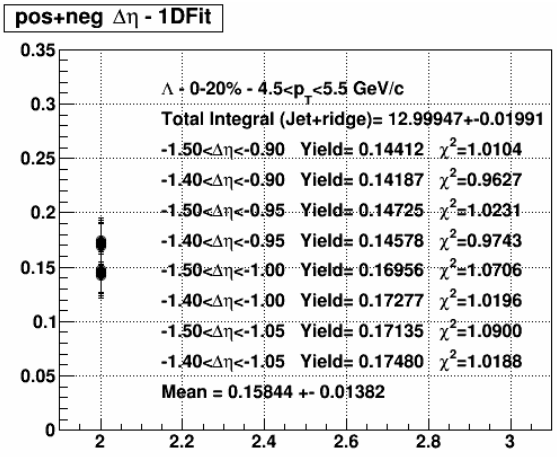

APPENDIX C (Continued)

Λ-h: 20-40%

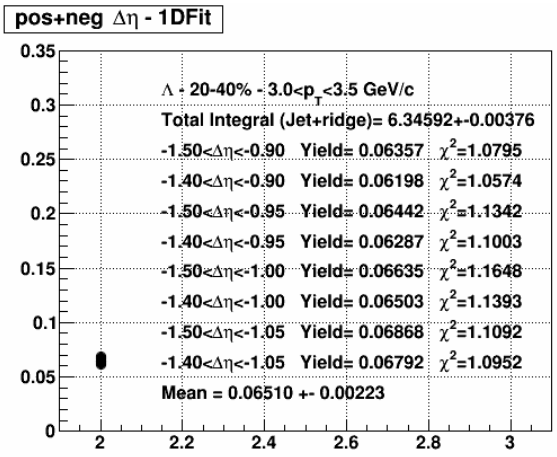

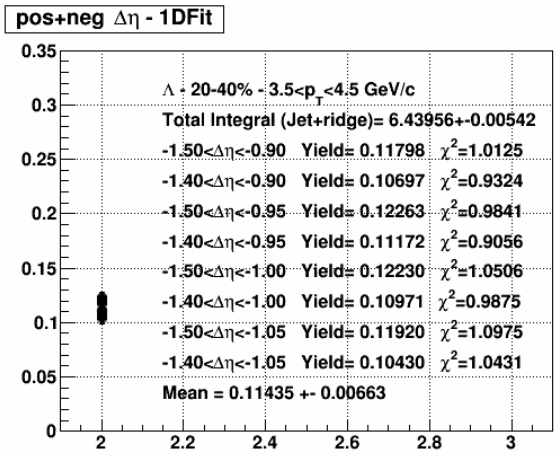

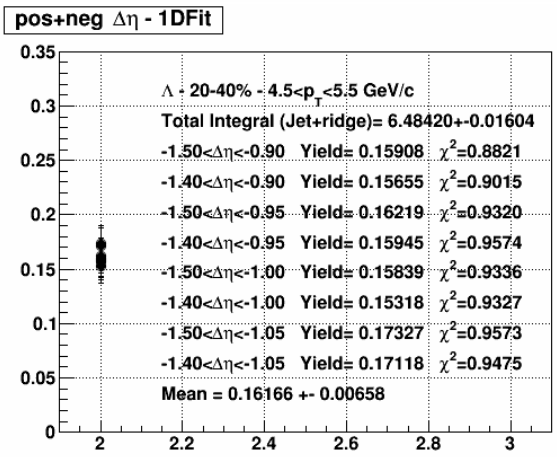

APPENDIX C (Continued)

Λ-h: 40-80%

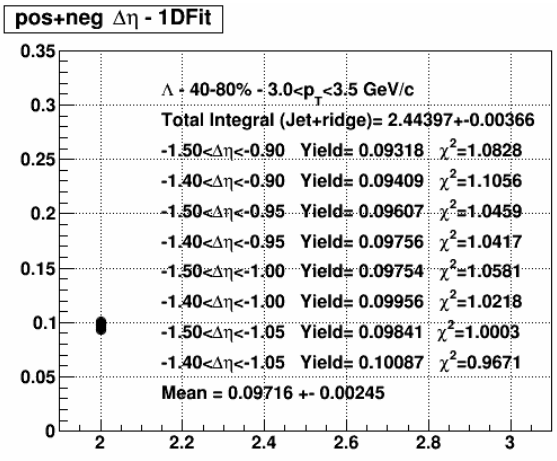

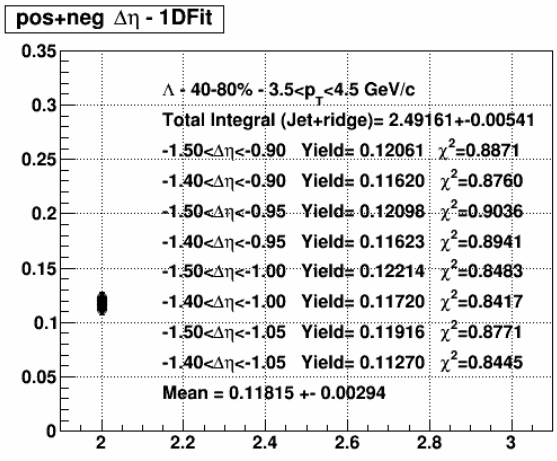

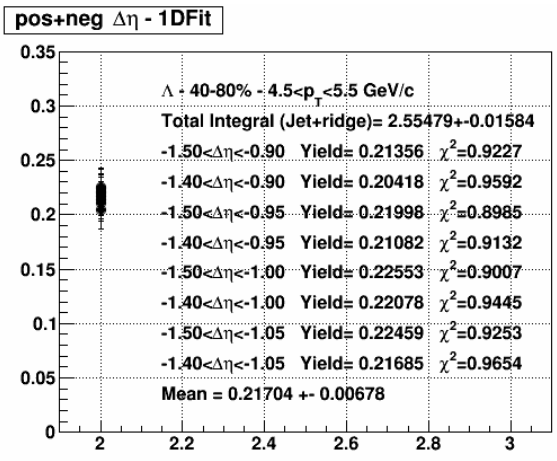

APPENDIX D

BACKGROUND SUBTRACTION – 2D VS. 1D FITS

Plots in this appendix show the differences in the two-dimensional vs. one-dimensional fits used to describe the background.

K^0_S-h: 0-20%

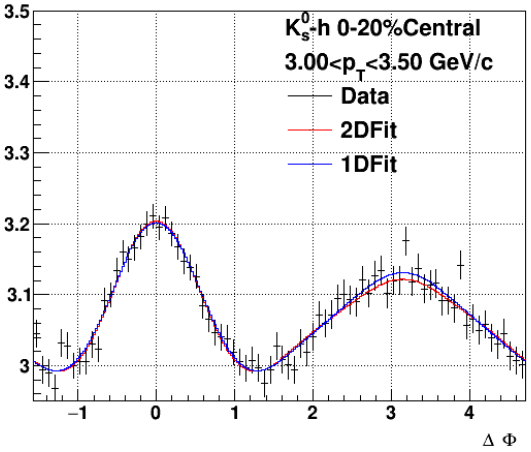

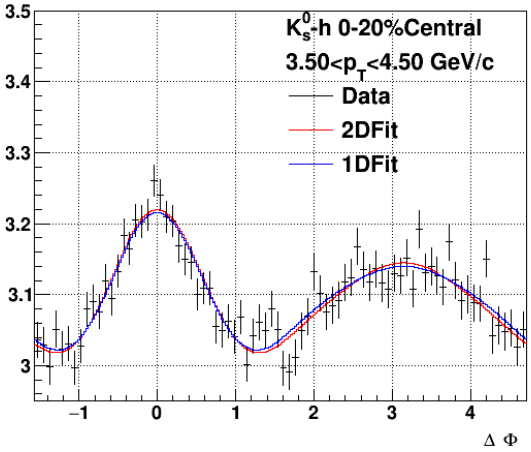

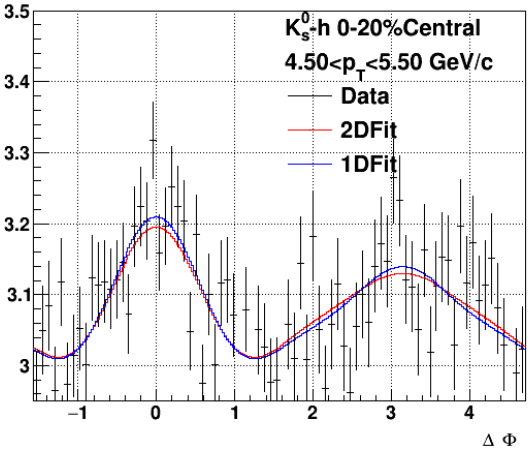

APPENDIX D (Continued)

K^0_S-h: 20-40%

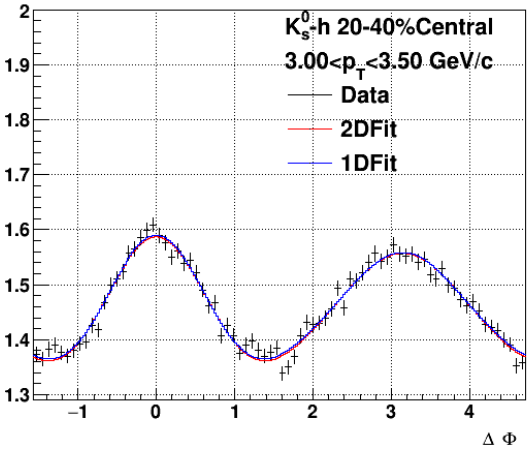

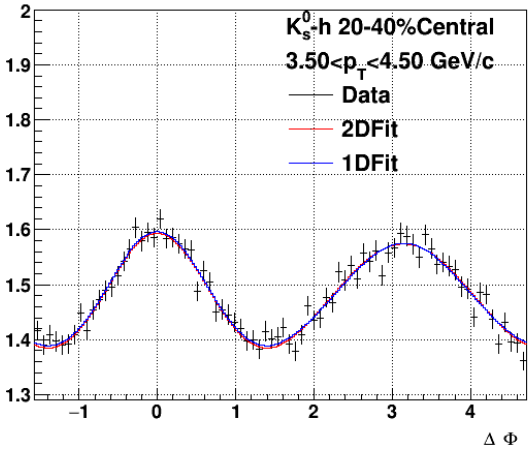

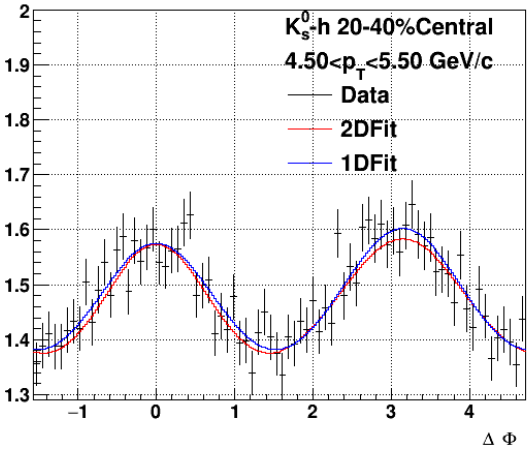

APPENDIX D (Continued)

K^0_S-h: 40-80%

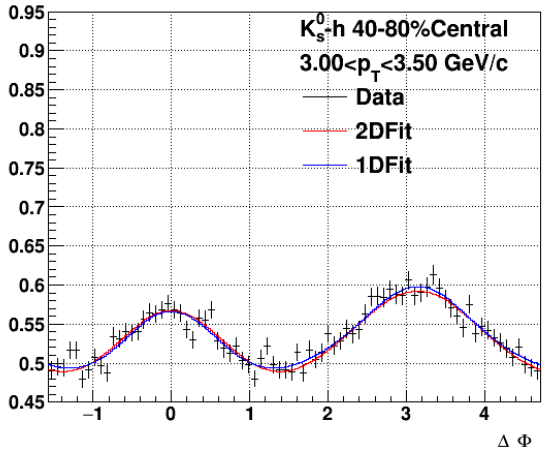

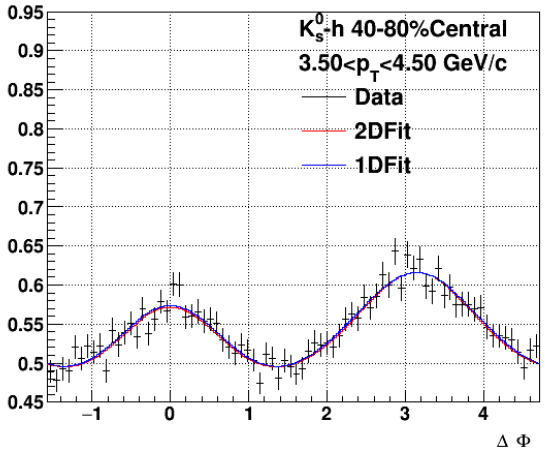

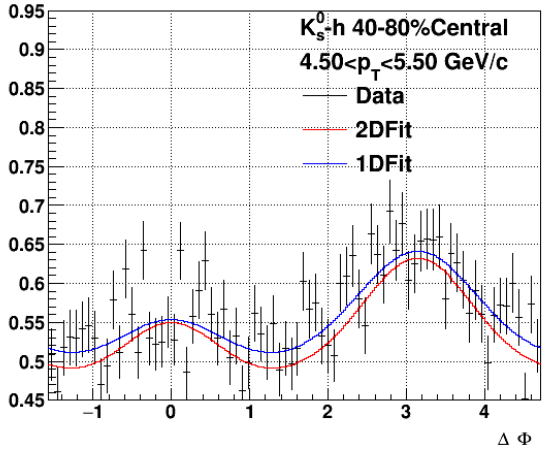

APPENDIX D (Continued)

Λ-h: 0-20%

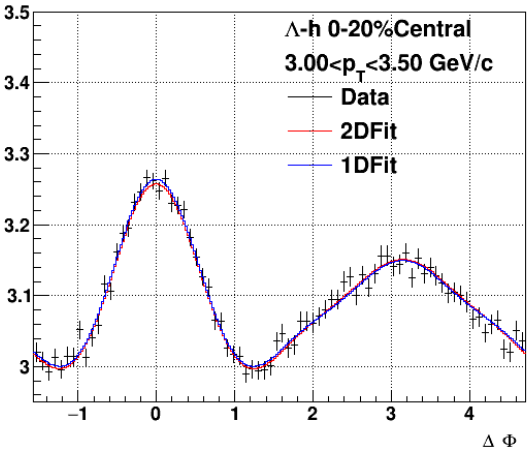

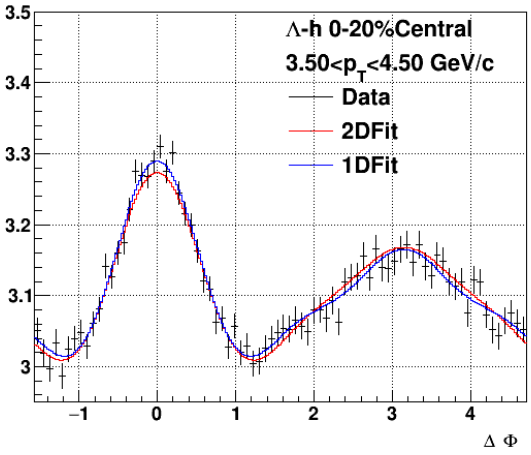

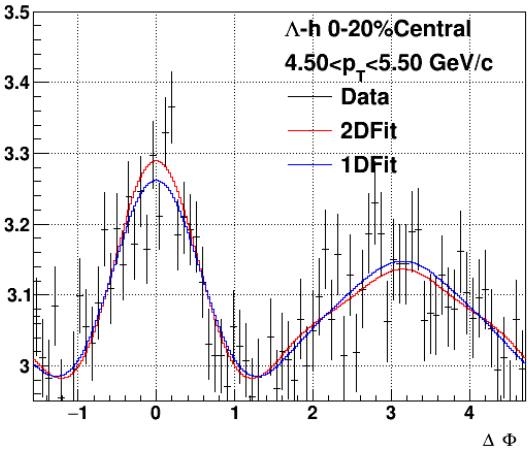

APPENDIX D (Continued)

Λ-h: 20-40%

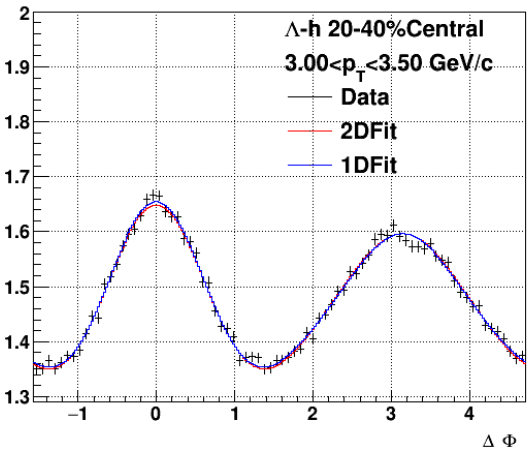

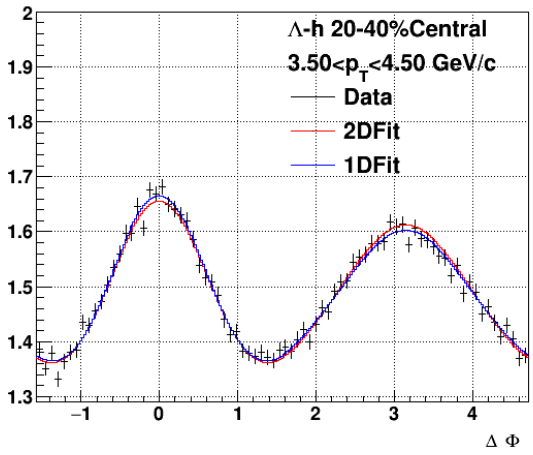

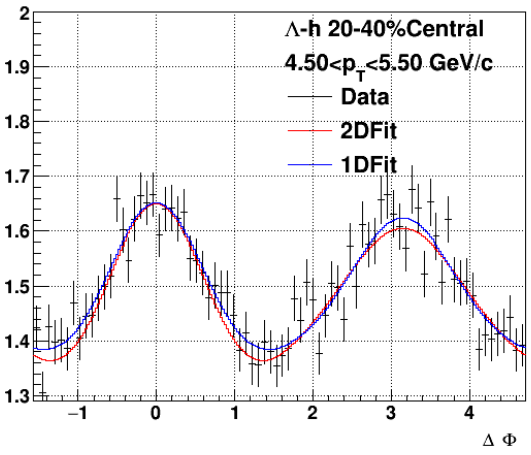

APPENDIX D (Continued)

Λ-h: 40-80%

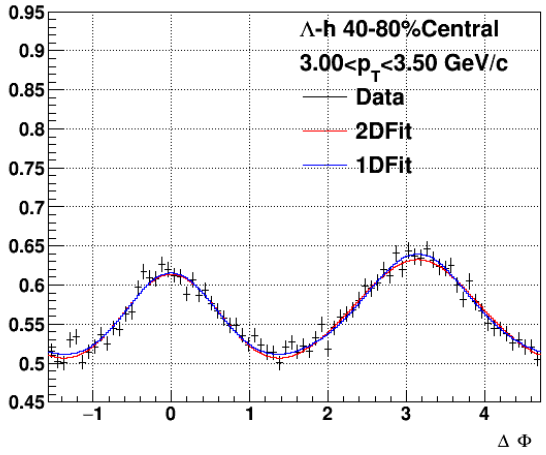

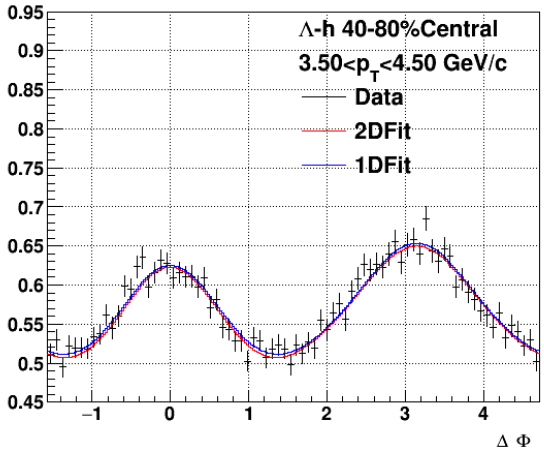

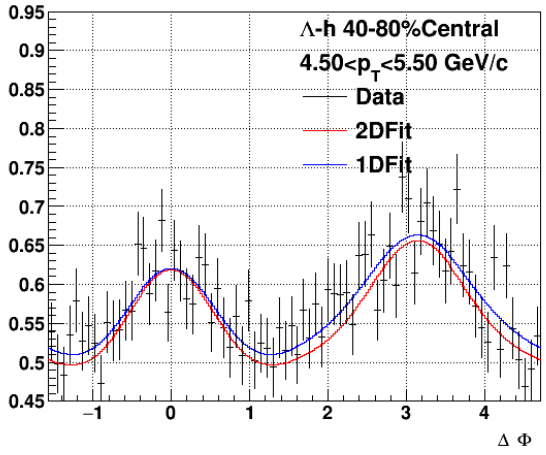

APPENDIX E

'SIDE BAND' CORRELATIONS SUBTRACTION

Invariant mass of K^0_s and Λ in various centrality, magnetic field setting (FF or RFF) and p_T ranges were fitted (as discussed in Section 4.3.7.1) to calculate the scaling factor for the side band correlations. Those fits are shown here, displaying 'peak' and 'side band' ranges and histogram integrals, used to calculate the scaling factor.

K^0_s: 0-20%

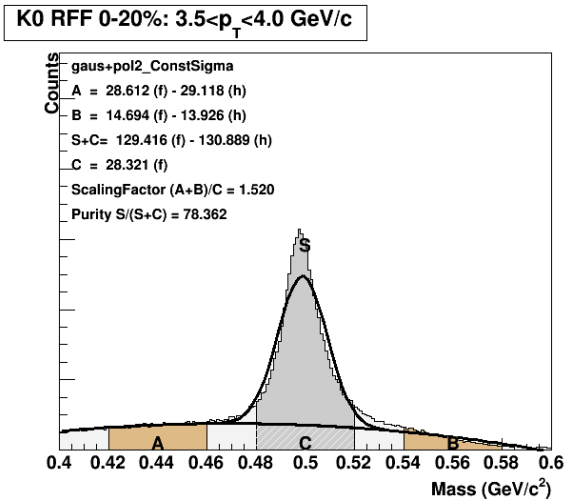

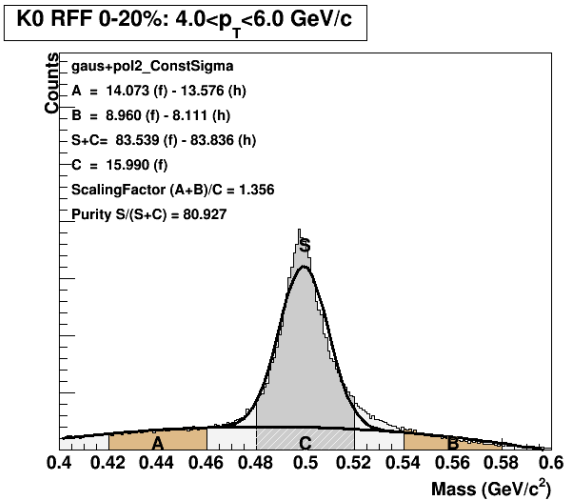

APPENDIX E (Continued)

K0 RFF 0-20%: 3.5<p_T<4.5 GeV/c

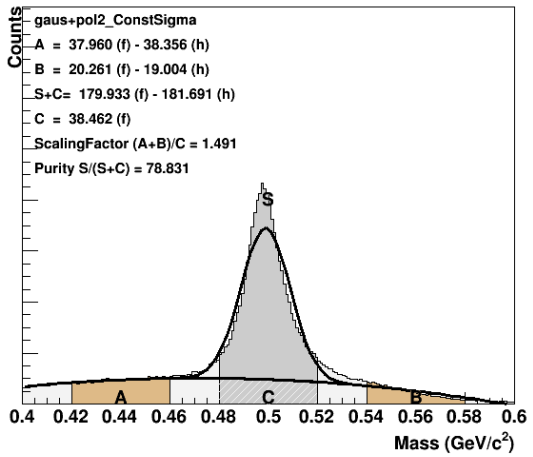

K0 RFF 0-20%: 3.0<p_T<3.5 GeV/c

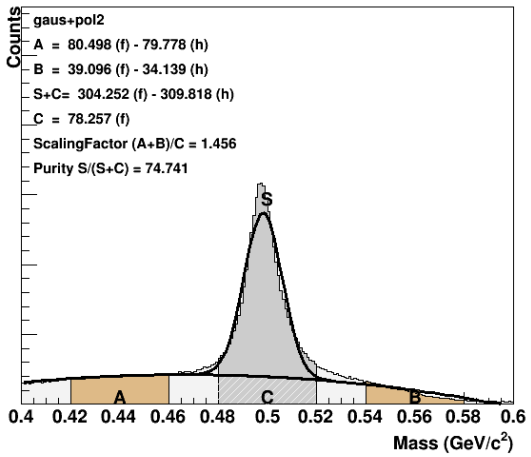

K0 _RFF 0-20%: 3.0<p_T<4.0 GeV/c

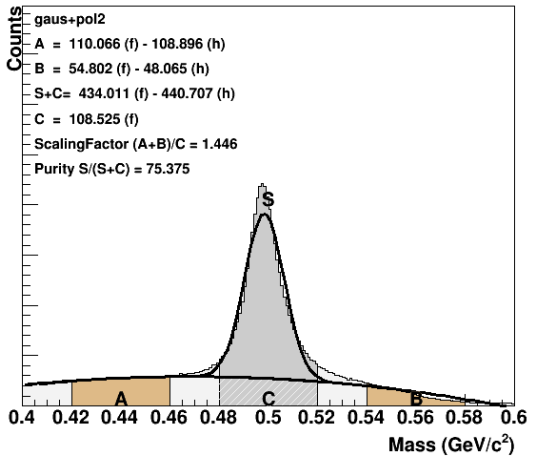

K0 RFF 0-20%: 4.5<p_T<5.5 GeV/c

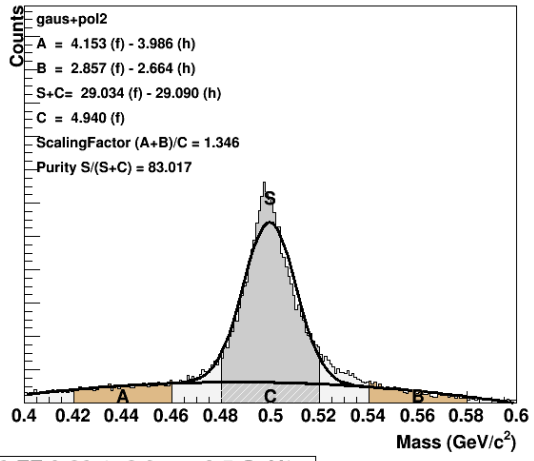

K0 RFF 0-20%: 6.0<p_T<10.0 GeV/c

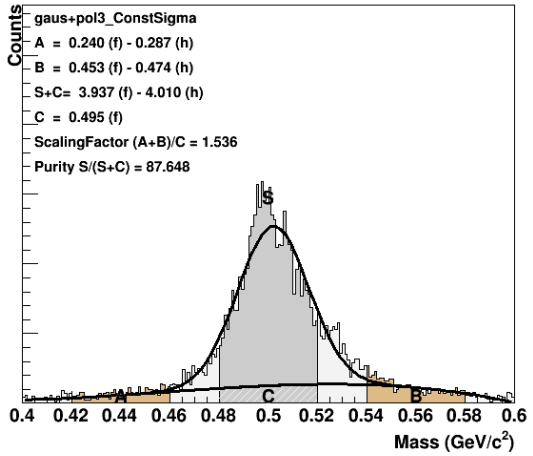

K0 FF 0-20%: 3.0<p_T<3.5 GeV/c

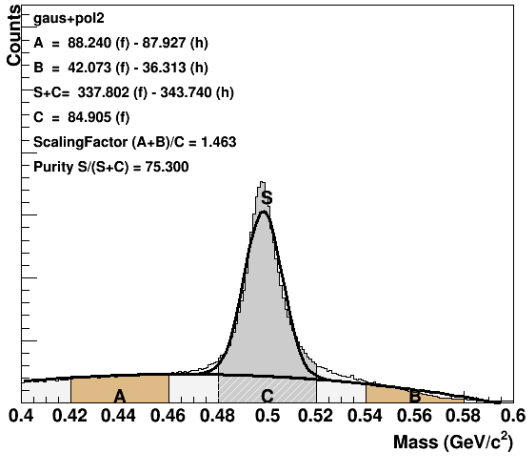

APPENDIX E (Continued)

K0 FF 0-20%: 6.0<p_T<10.0 GeV/c

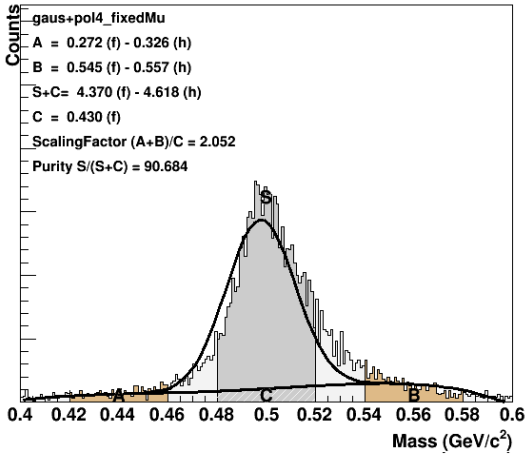

K0 FF 0-20%: 3.5<p_T<4.0 GeV/c

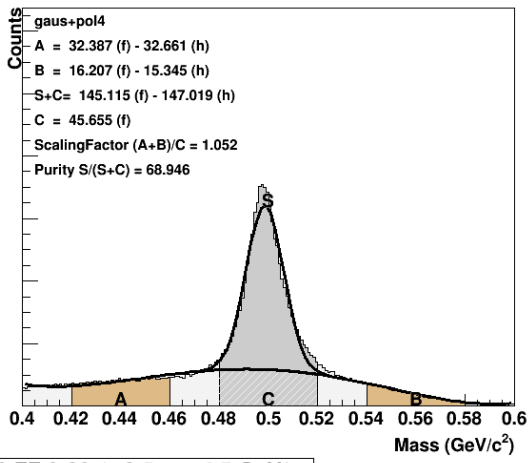

K0 FF 0-20%: 4.0<p_T<6.0 GeV/c

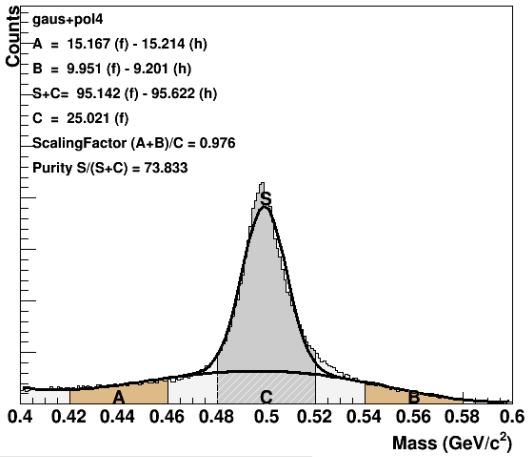

K0 FF 0-20%: 3.5<p_T<4.5 GeV/c

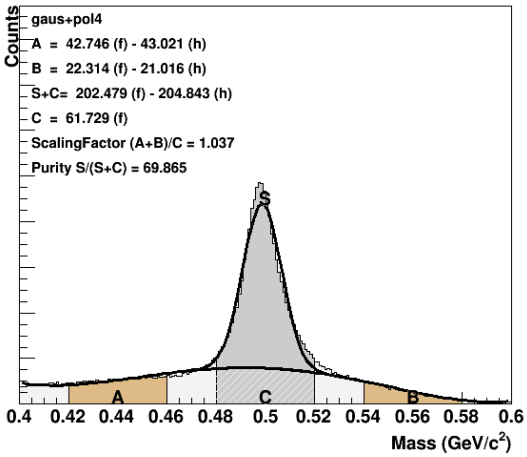

K0 FF 0-20%: 4.5<p_T<5.5 GeV/c

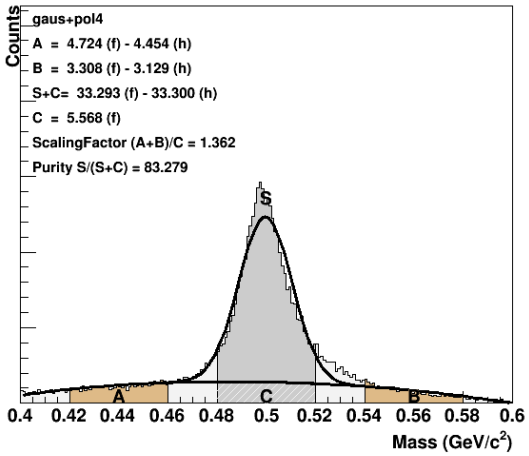

APPENDIX E (Continued)

K^0_S: 20-40%

K0 Mass: 3.0<p_T<3.5 GeV/c

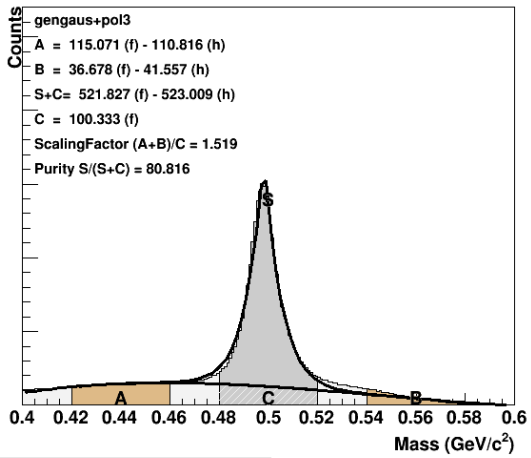

K0 Mass: 3.5<p_T<4.5 GeV/c

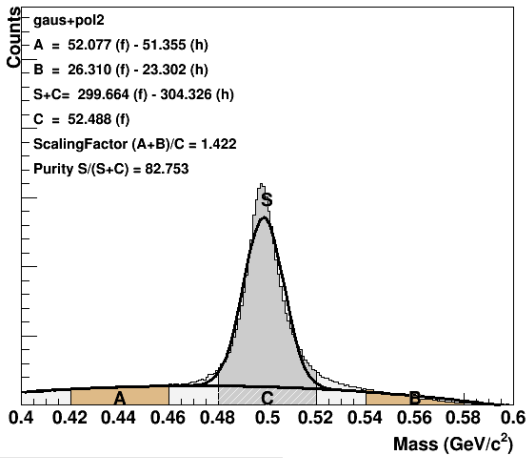

K0 Mass: 4.5<p_T<5.5 GeV/c

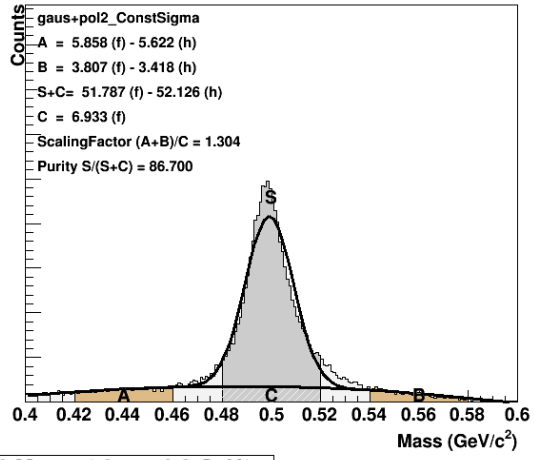

K0 Mass: 6.0<p_T<10.0 GeV/c

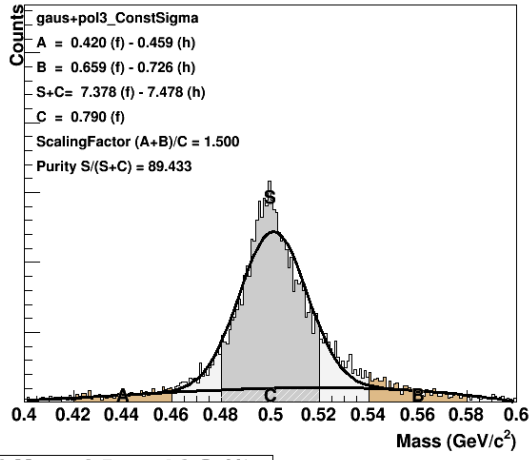

K0 Mass: 4.0<p_T<6.0 GeV/c

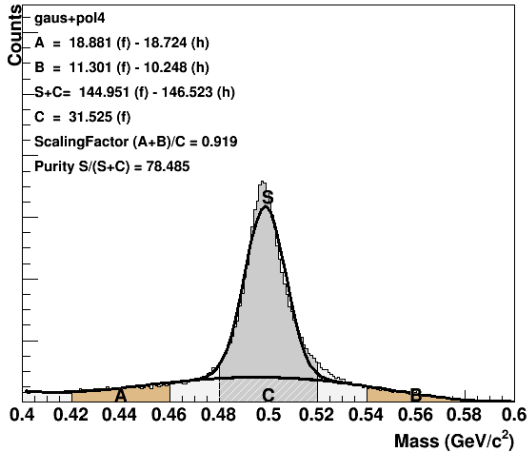

K0 Mass: 3.5<p_T<4.0 GeV/c

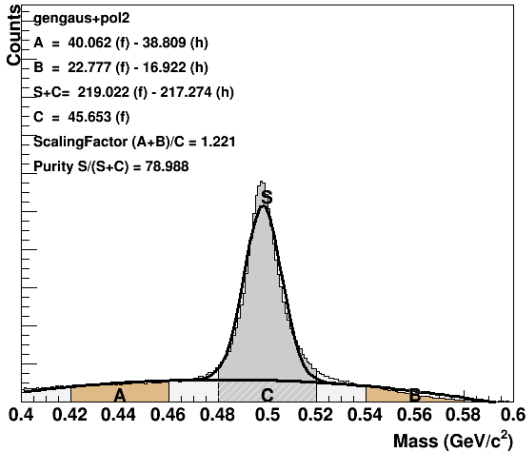

APPENDIX E (Continued)

K^0_S: 40-60%

K0 FF 40-60%: 3.0<p_T<3.5 GeV/c

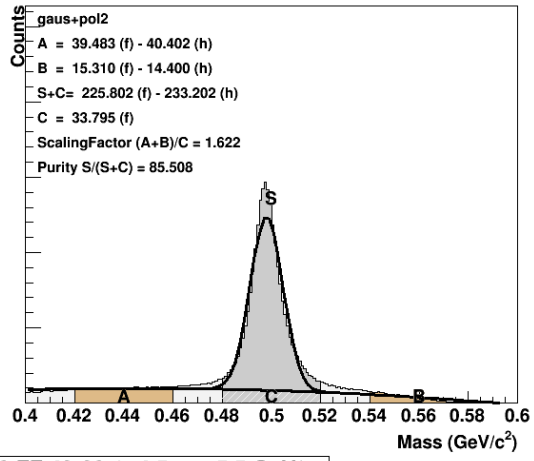

K0 FF 40-60%: 3.5<p_T<4.5 GeV/c

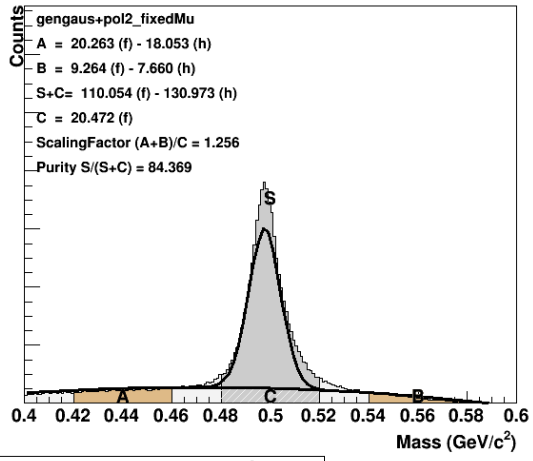

K0 FF 40-60%: 4.5<p_T<5.5 GeV/c

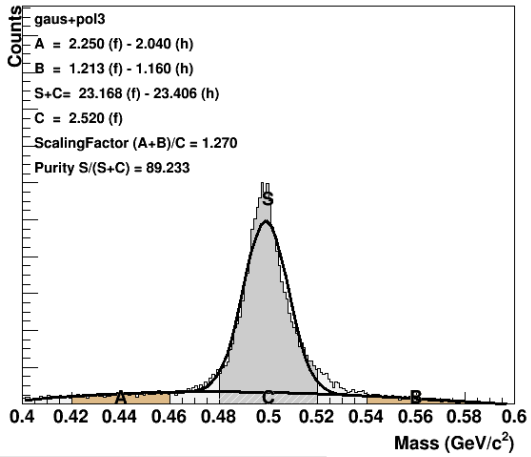

K0 FF 40-60%: 6.0<p_T<10.0 GeV/c

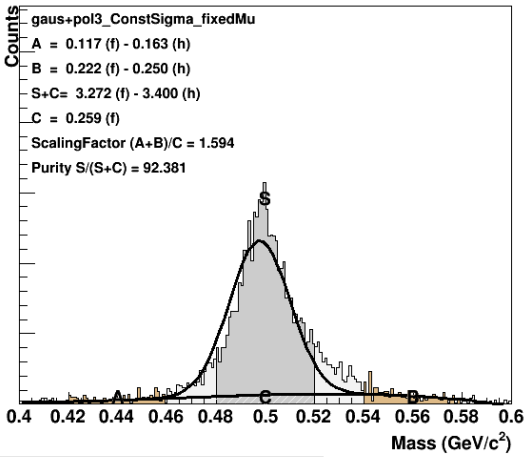

K0 FF 40-60%: 3.5<p_T<4.0 GeV/c

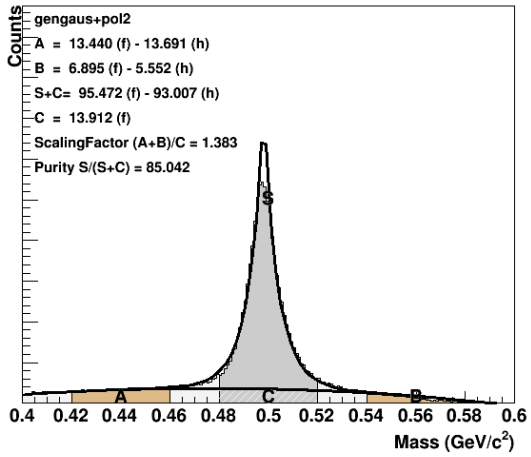

K0 FF 40-60%: 4.0<p_T<6.0 GeV/c

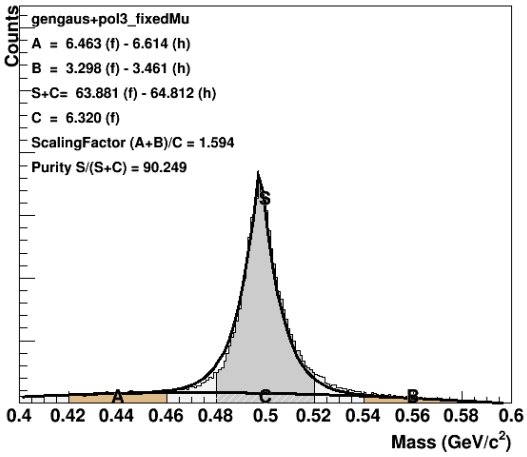

APPENDIX E (Continued)

K^0_S: 40-80%

K0 Mass: 3.0<p_T<3.5 GeV/c

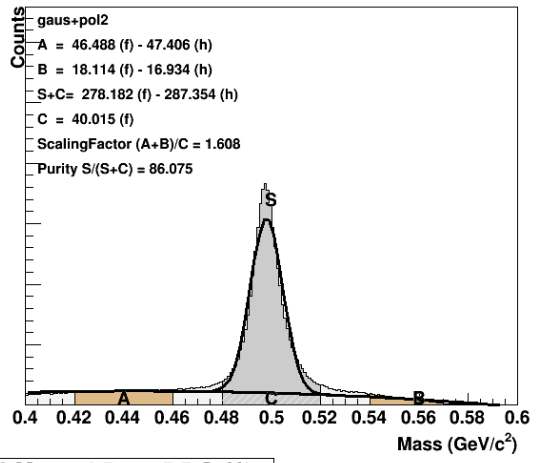

K0 Mass: 3.5<p_T<4.5 GeV/c

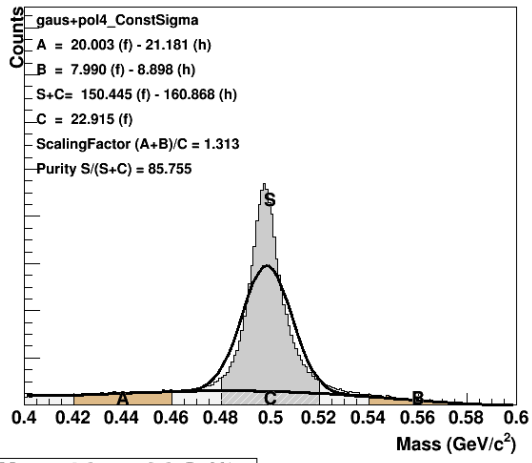

K0 Mass: 4.5<p_T<5.5 GeV/c

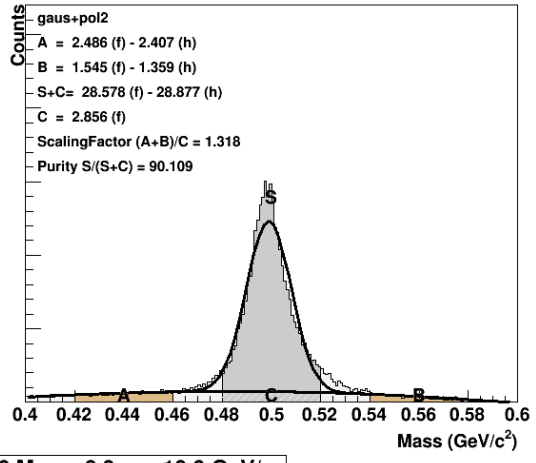

K0 Mass: 4.0<p_T<6.0 GeV/c

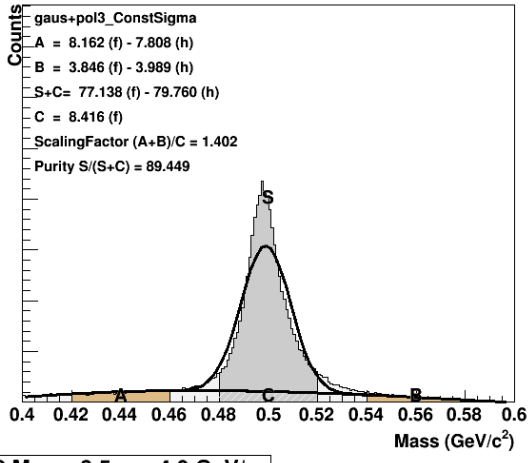

K0 Mass: 6.0<p_T<10.0 GeV/c

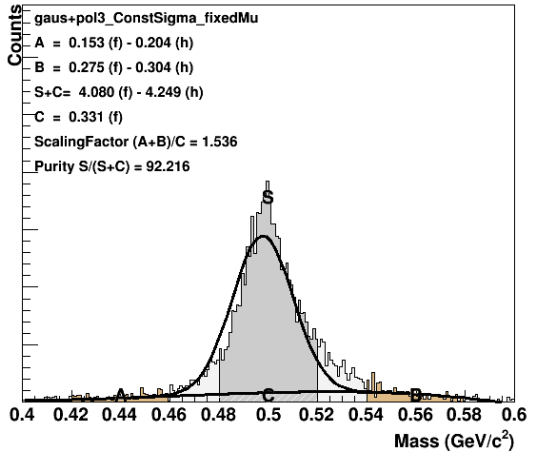

K0 Mass: 3.5<p_T<4.0 GeV/c

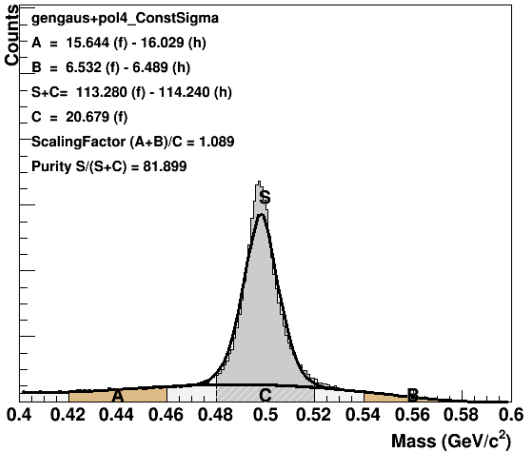

APPENDIX E (Continued)

K^0_S: 60-80%

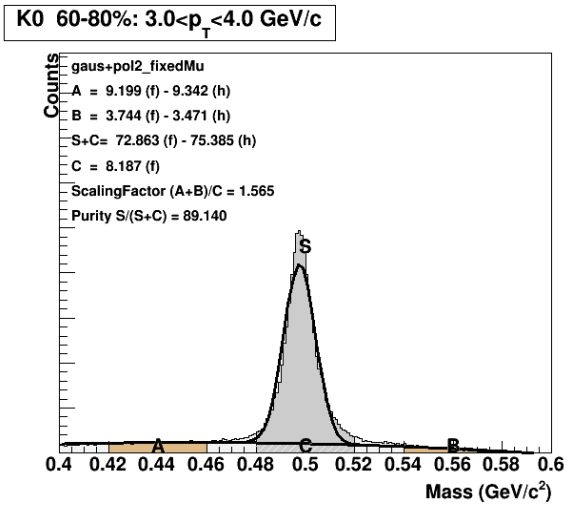

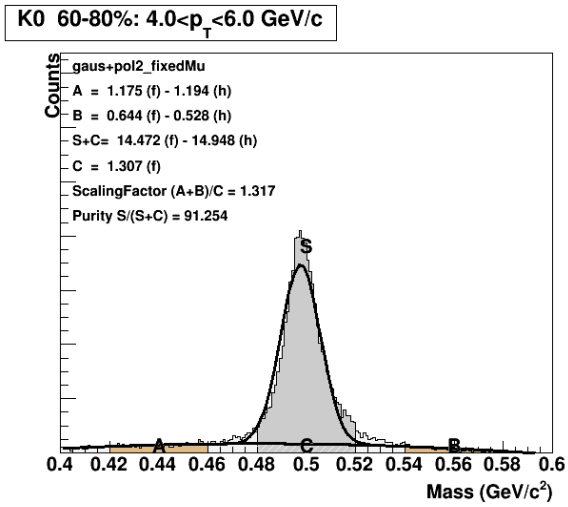

Λ: 0-20%

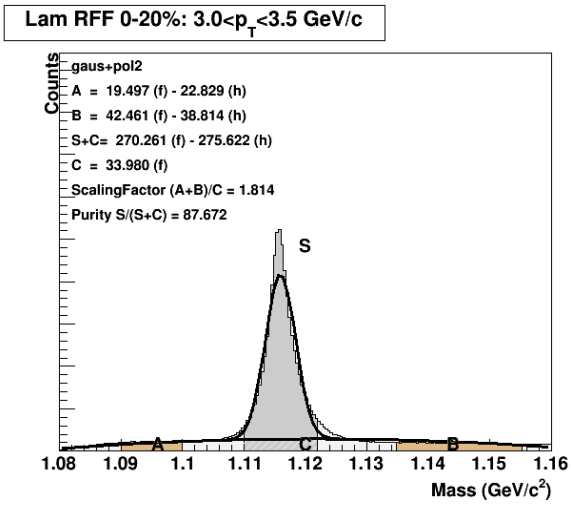

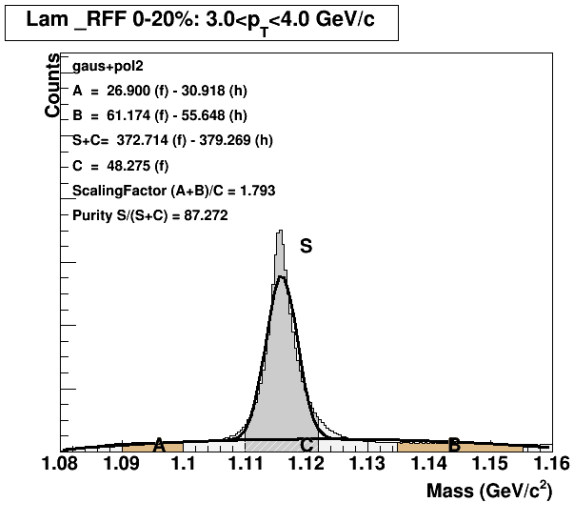

APPENDIX E (Continued)

Lam RFF 0-20%: 6.0<p_T<10.0 GeV/c

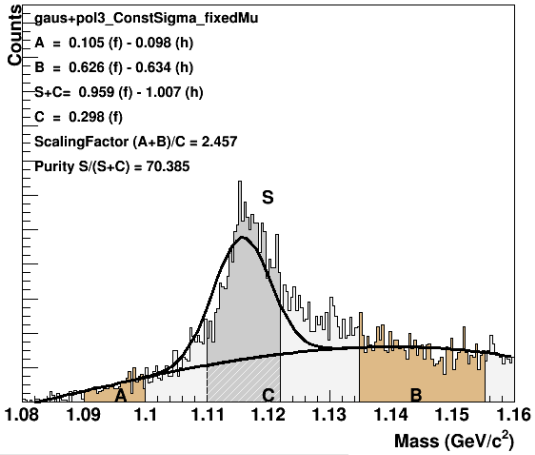

Lam RFF 0-20%: 4.0<p_T<6.0 GeV/c

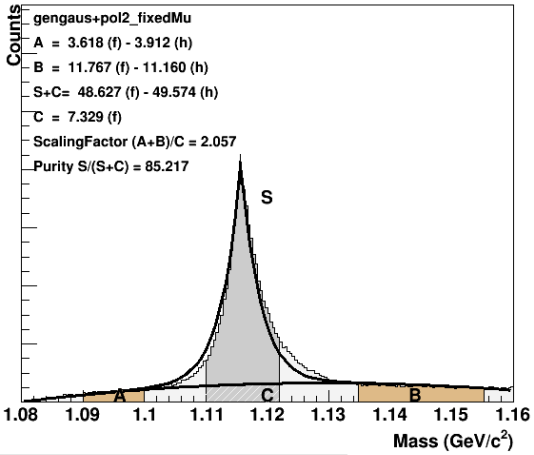

Lam RFF 0-20%: 3.5<p_T<4.5 GeV/c

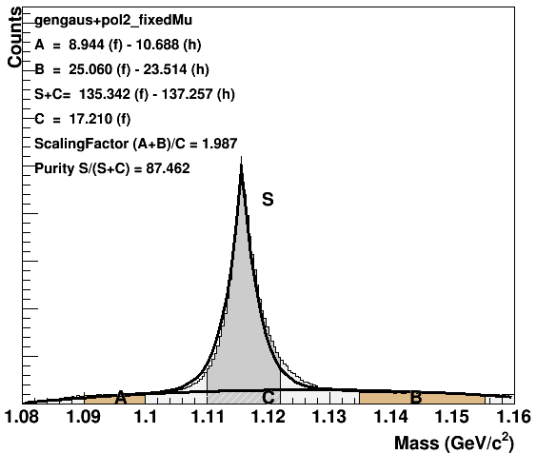

Lam RFF 0-20%: 4.5<p_T<5.5 GeV/c

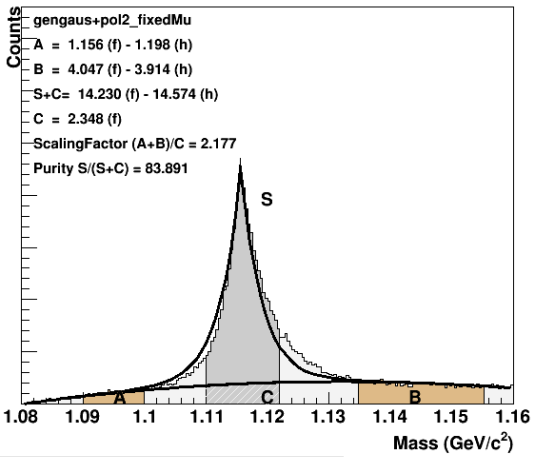

Lam RFF 0-20%: 3.5<p_T<4.0 GeV/c

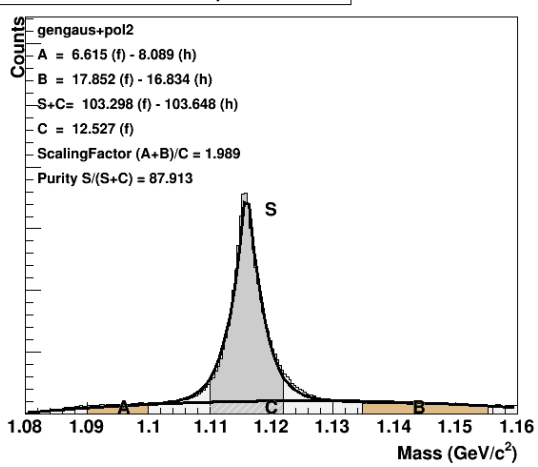

Lam _FF 0-20%: 3.0<p_T<4.0 GeV/c

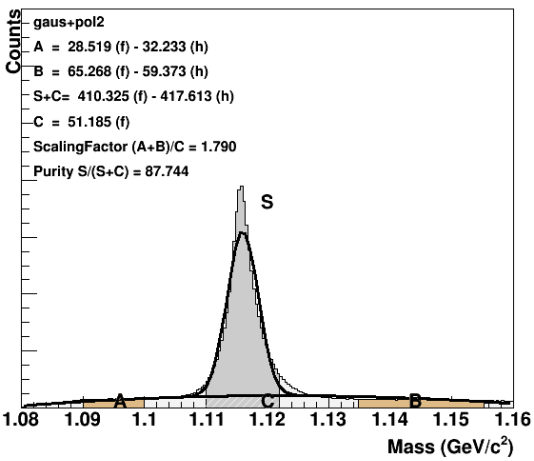

APPENDIX E (Continued)

Lam FF 0-20%: 6.0<p_T<10.0 GeV/c

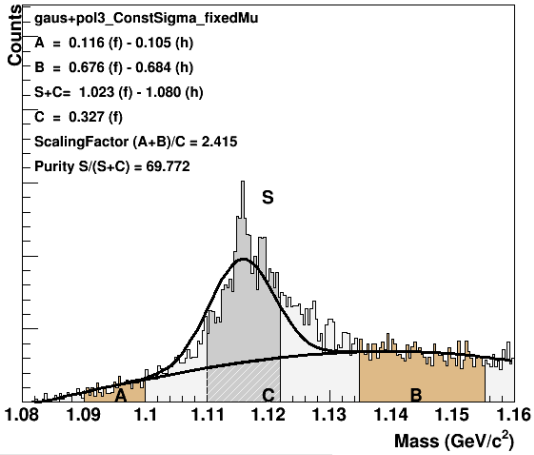

Lam FF 0-20%: 3.0<p_T<3.5 GeV/c

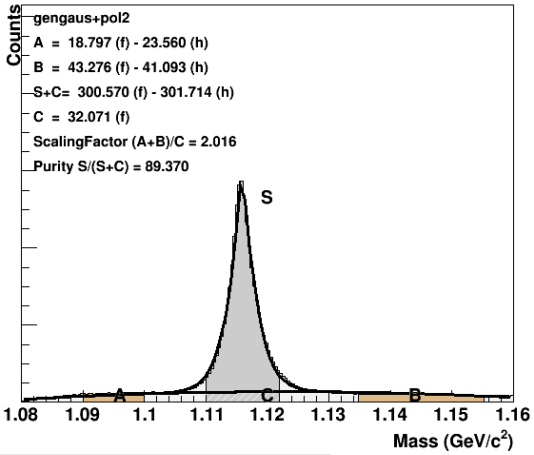

Lam FF 0-20%: 3.5<p_T<4.0 GeV/c

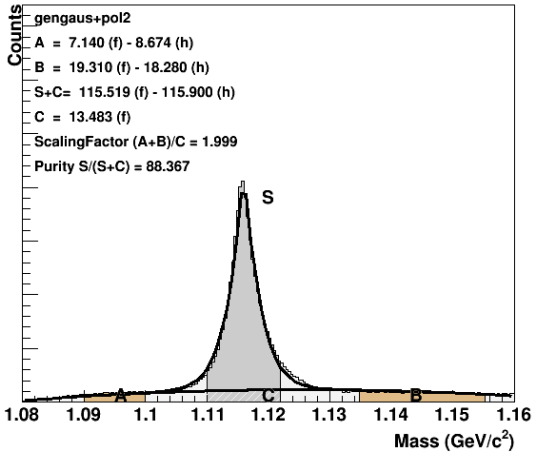

Lam FF 0-20%: 3.5<p_T<4.5 GeV/c

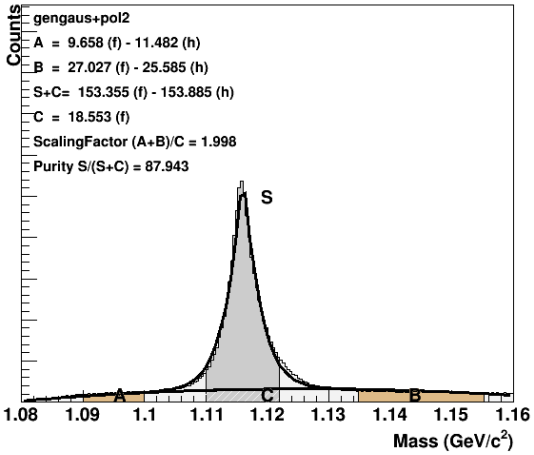

Lam FF 0-20%: 4.0<p_T<6.0 GeV/c

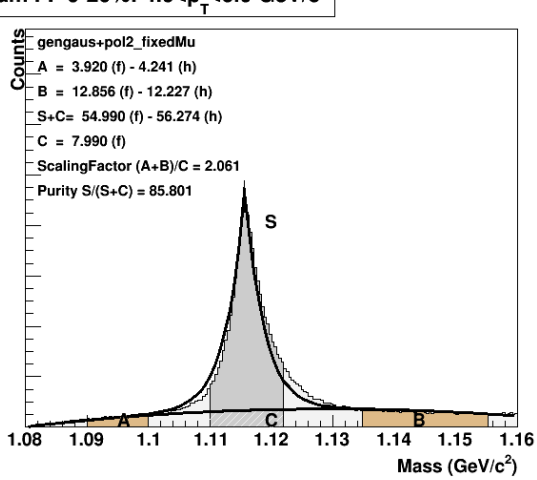

Lam FF 0-20%: 4.5<p_T<5.5 GeV/c

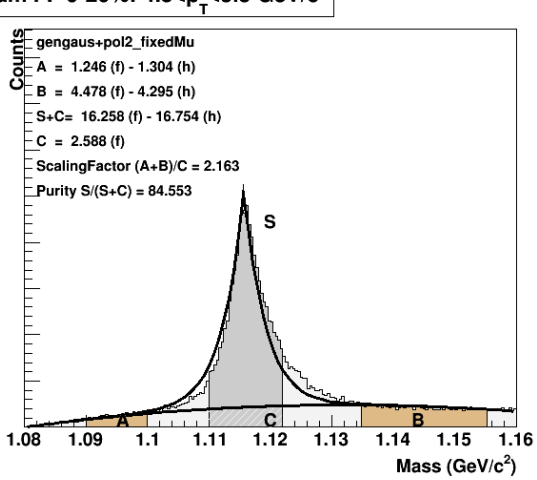

APPENDIX E (Continued)

Λ: 20-40%

Lam Mass: 3.0<p_T<3.5 GeV/c

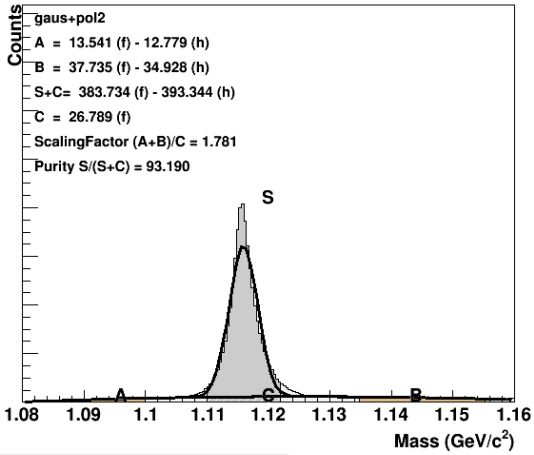

Lam Mass: 3.5<p_T<4.5 GeV/c

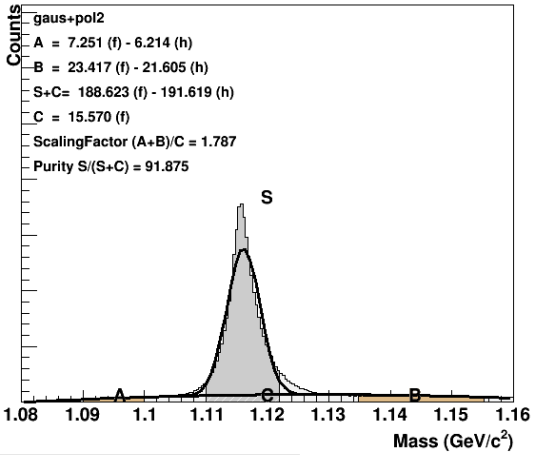

Lam Mass: 4.5<p_T<5.5 GeV/c

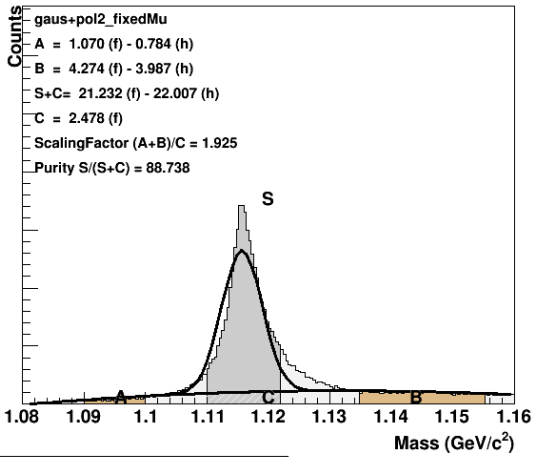

Lam Mass: 6.0<p_T<10.0 GeV/c

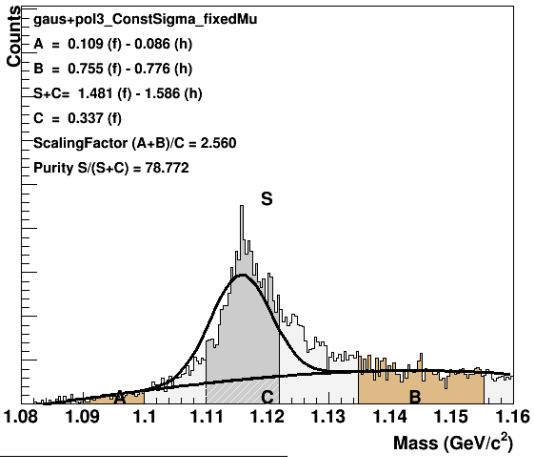

Lam Mass: 3.5<p_T<4.0 GeV/c

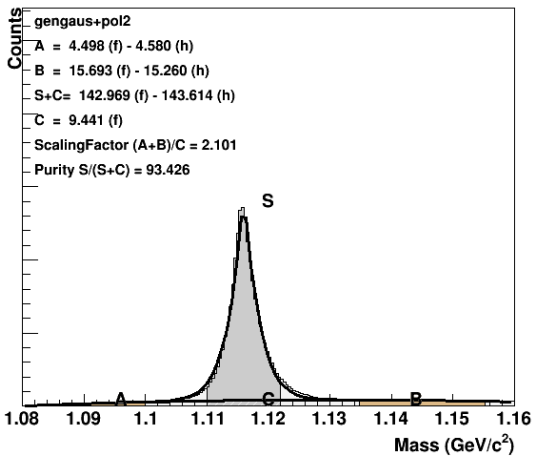

Lam Mass: 4.0<p_T<6.0 GeV/c

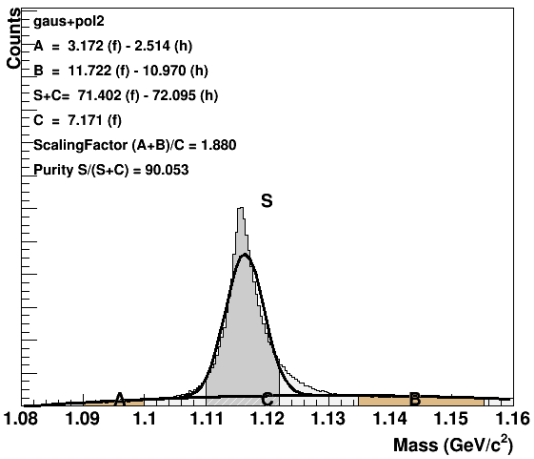

APPENDIX E (Continued)

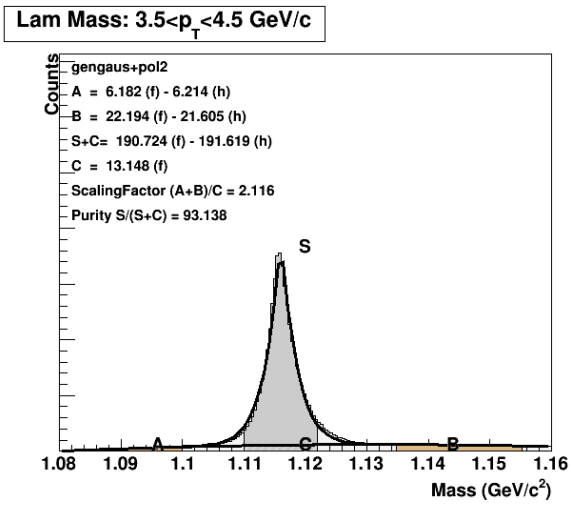

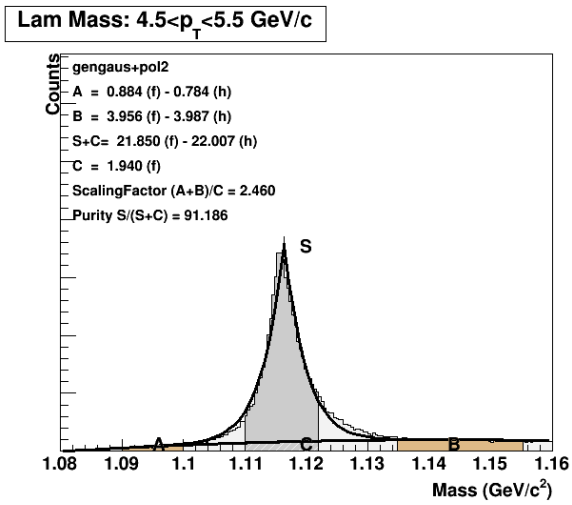

Λ: 40-60%

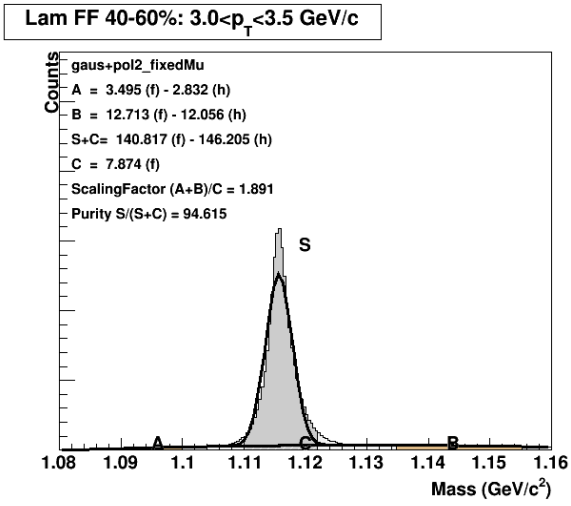

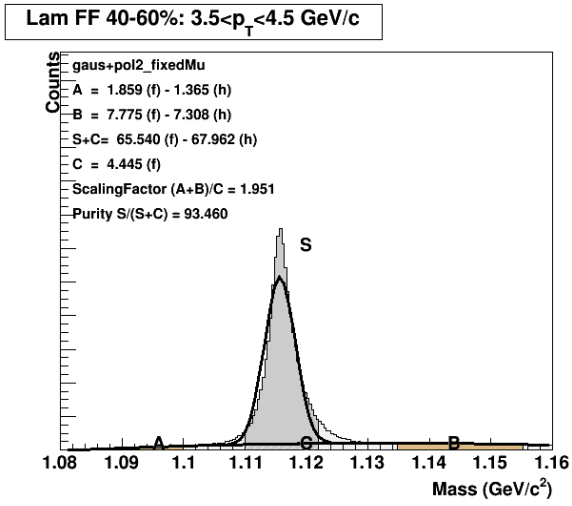

APPENDIX E (Continued)

Lam FF 40-60%: 4.5<p_T<5.5 GeV/c

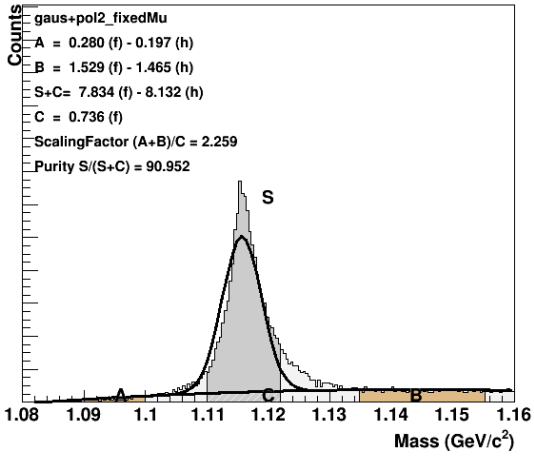

Lam FF 40-60%: 6.0<p_T<10.0 GeV/c

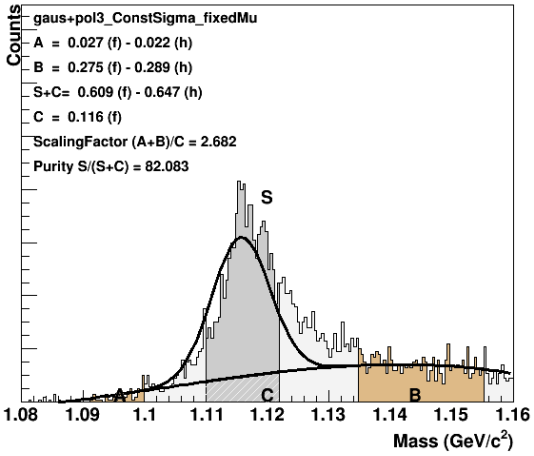

Lam FF 40-60%: 3.5<p_T<4.0 GeV/c

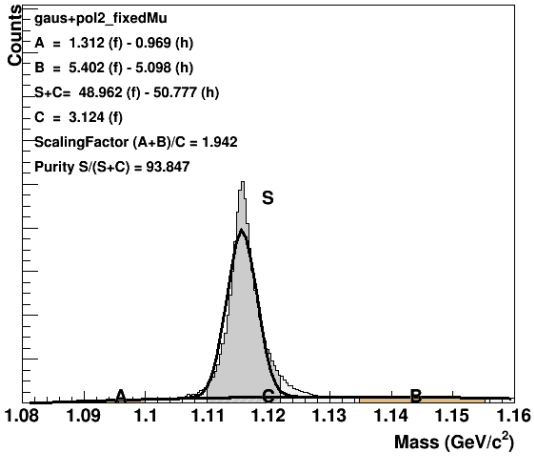

Lam FF 40-60%: 4.0<p_T<6.0 GeV/c

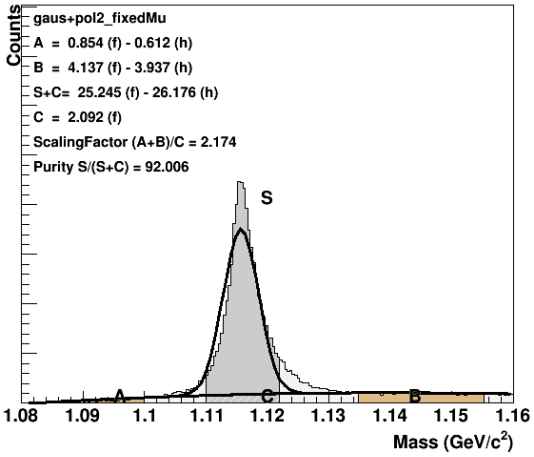

APPENDIX E (Continued)

Λ: 40-80%

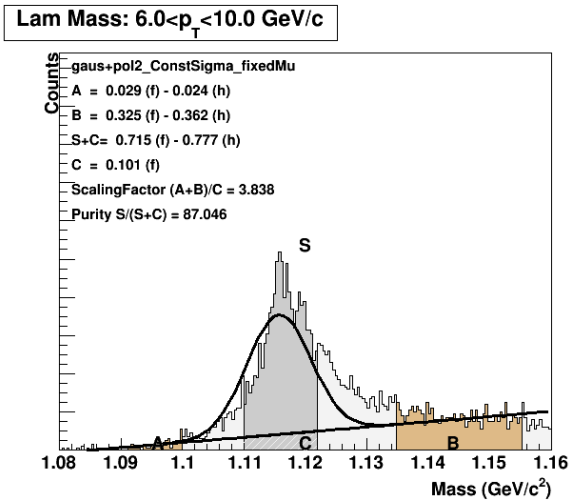

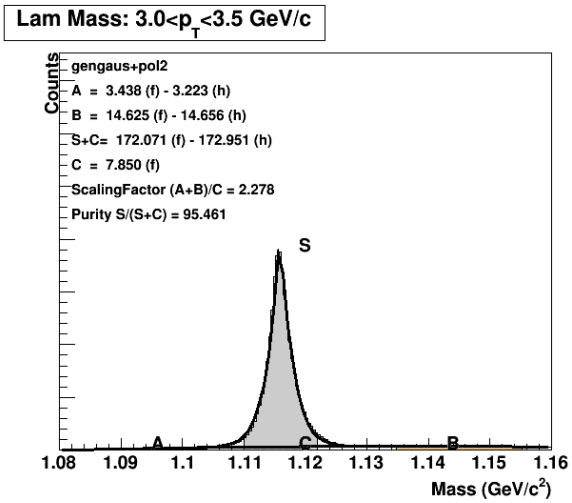

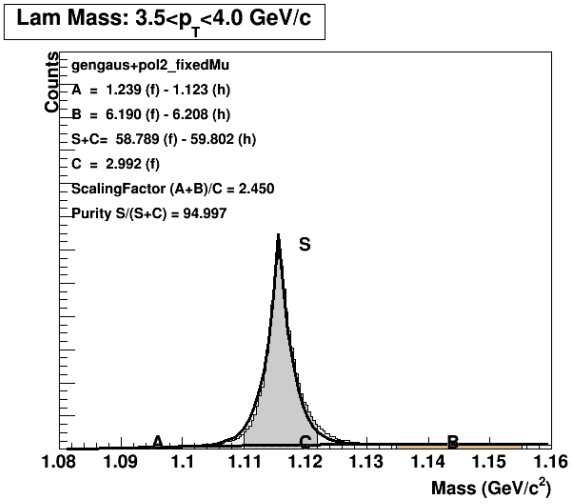

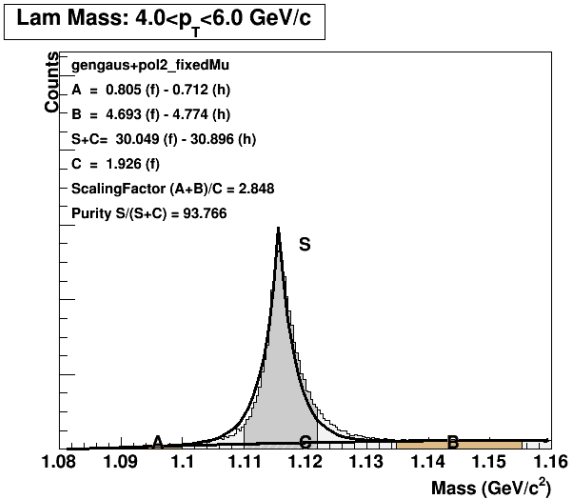

APPENDIX E (Continued)

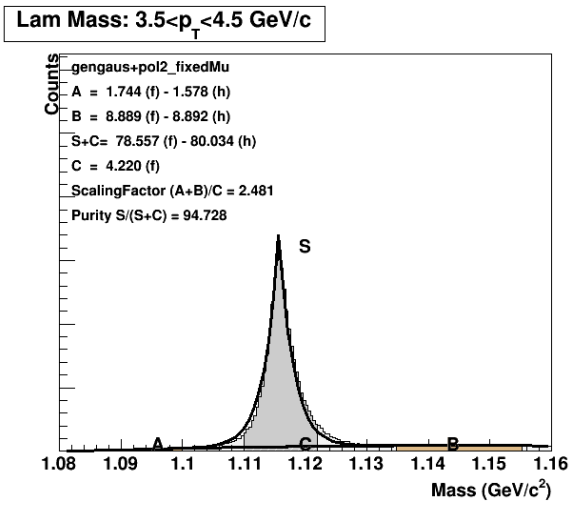

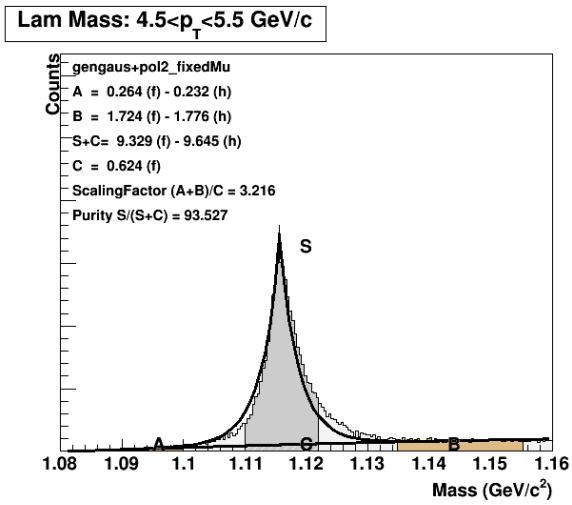

Λ: 60-80%

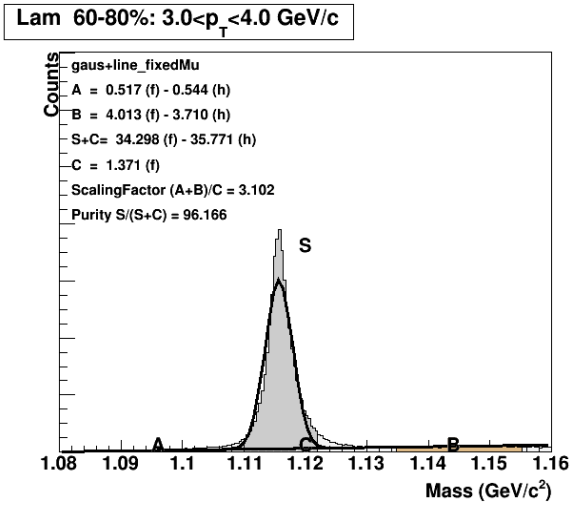

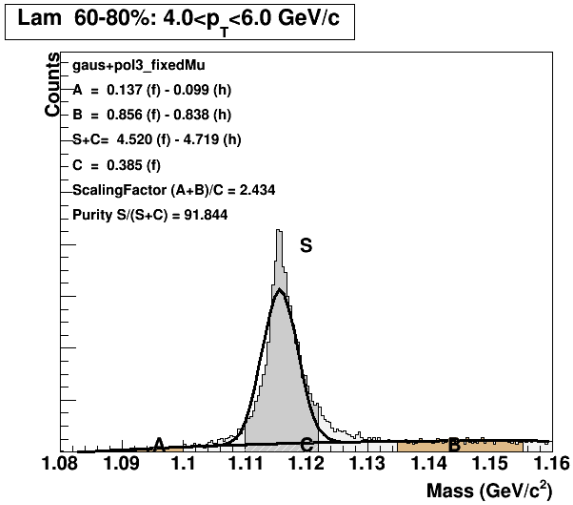

APPENDIX F

ELLIPTIC FLOW FROM ONE-DIMENSIONAL FIT – VARY $\Delta\eta$ RANGES

Plots in this appendix show the spread in the value of elliptic flow seen when $\Delta\eta$ ranges were varied. The standard deviations were used as systematic uncertainties on each p_T bin. Each plots lists the ranges selected, chi squared for the one-dimensional fit used to describe the background, and value of elliptic flow obtained from the fit.

K^0_S-h: 0-20%

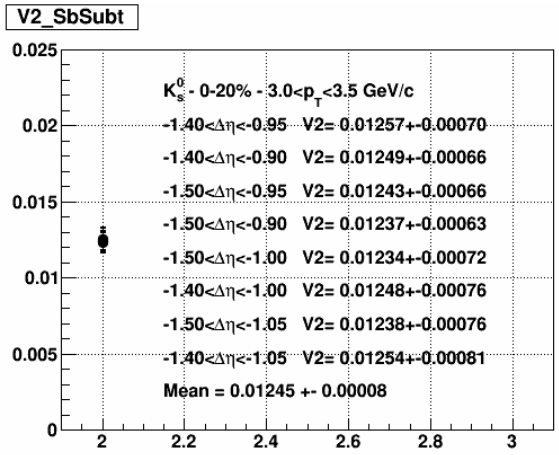

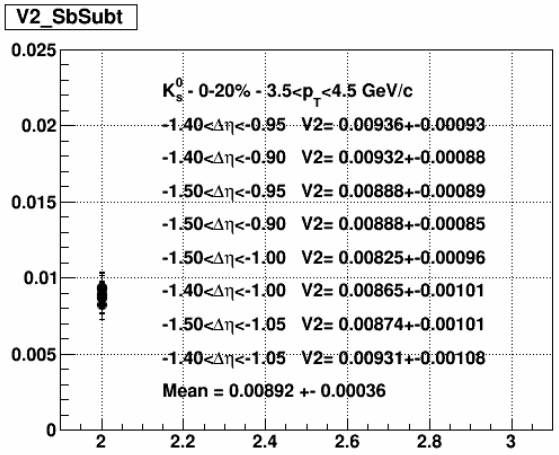

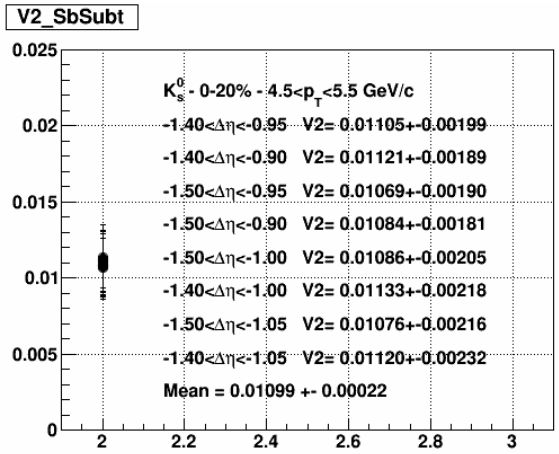

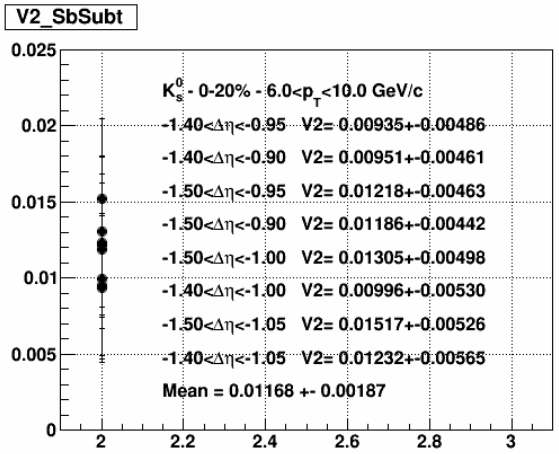

APPENDIX F (Continued)

K^0_S-h: 20-40%

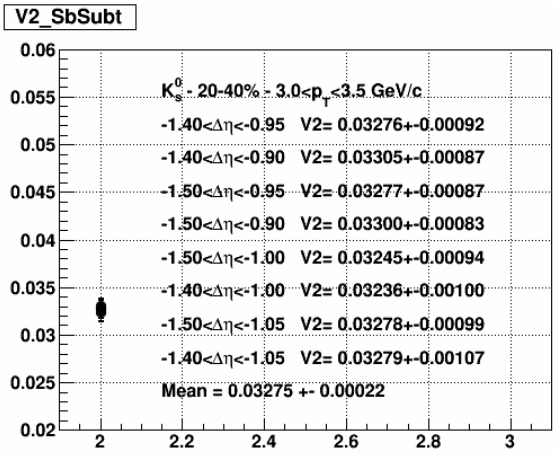

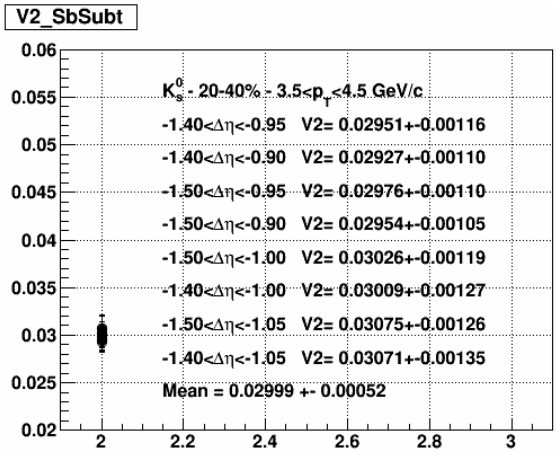

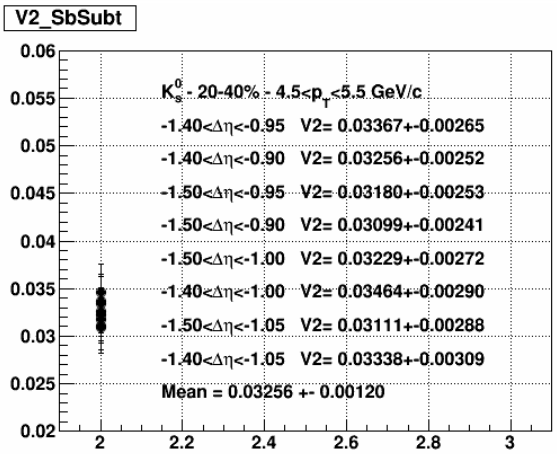

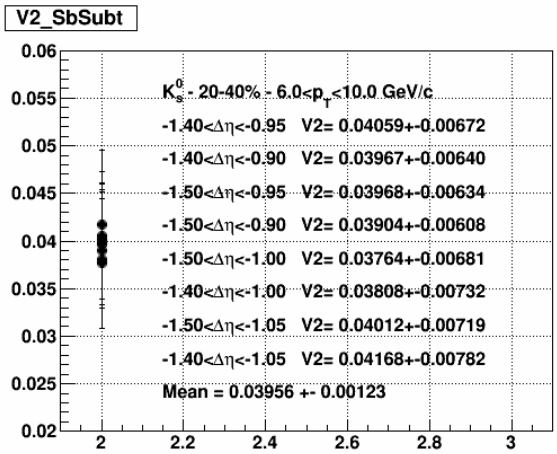

K^0_S-h: 40-60%

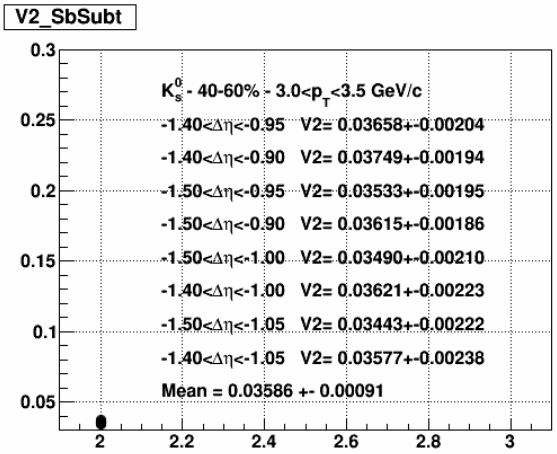

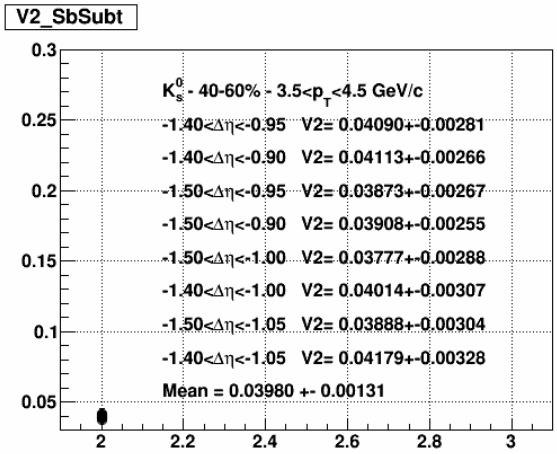

APPENDIX F (Continued)

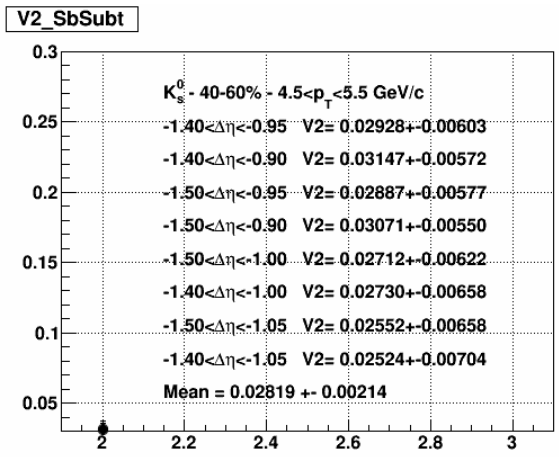

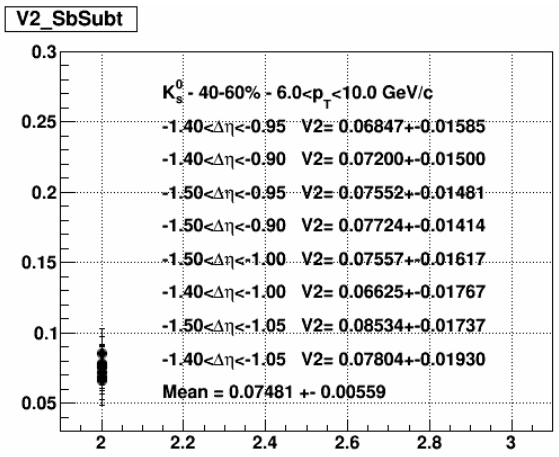

K^0_S-h: 0-80%

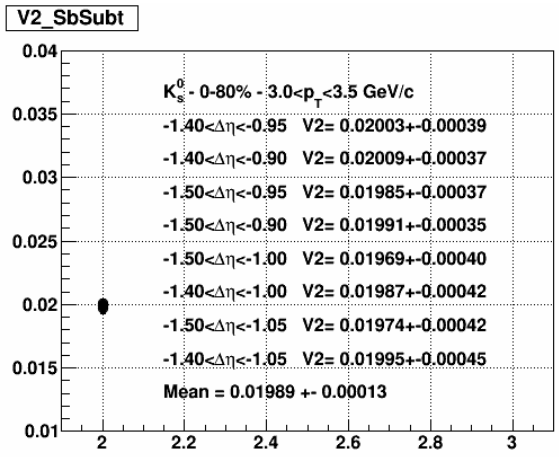

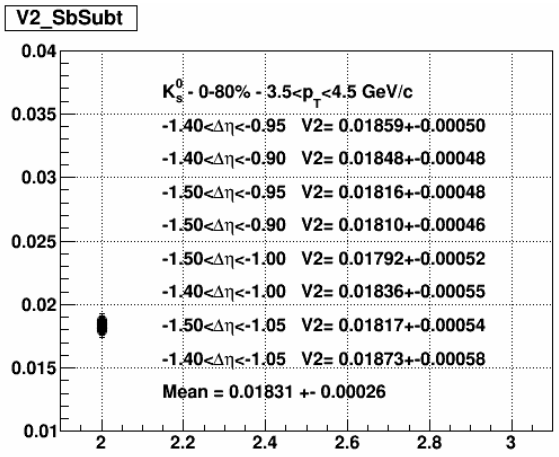

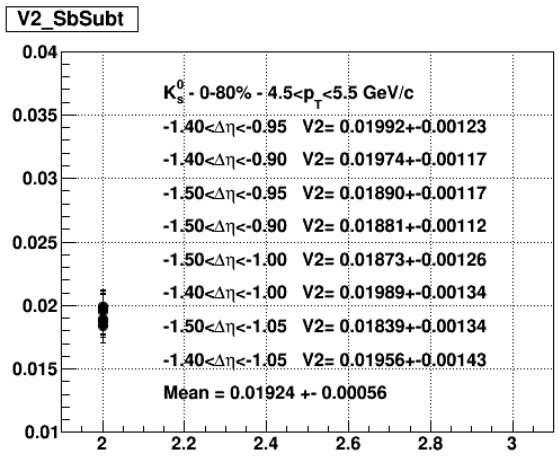

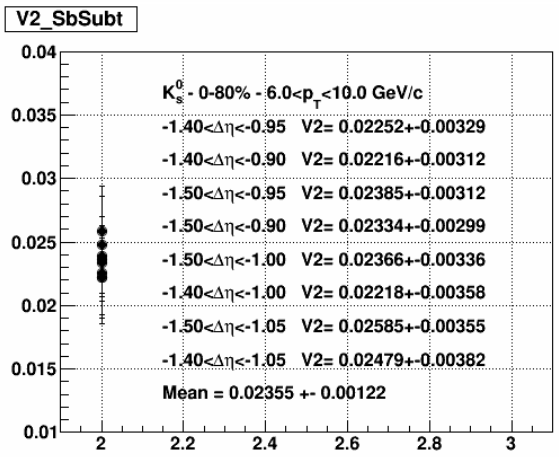

APPENDIX F (Continued)

Λ-h: 0-20%

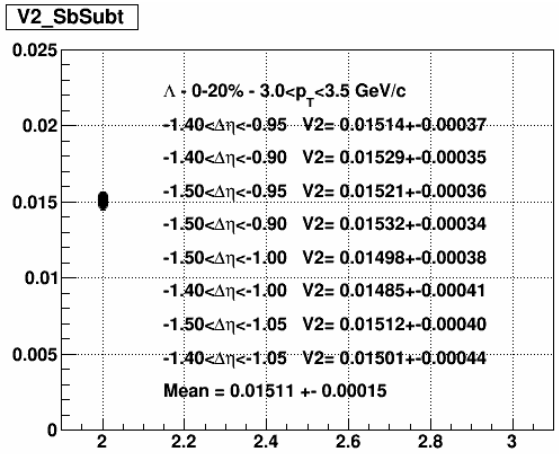

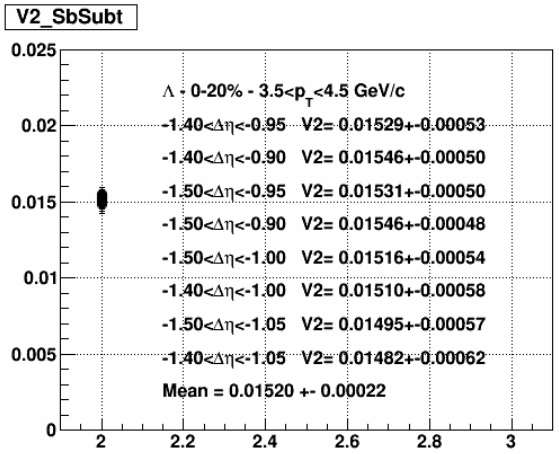

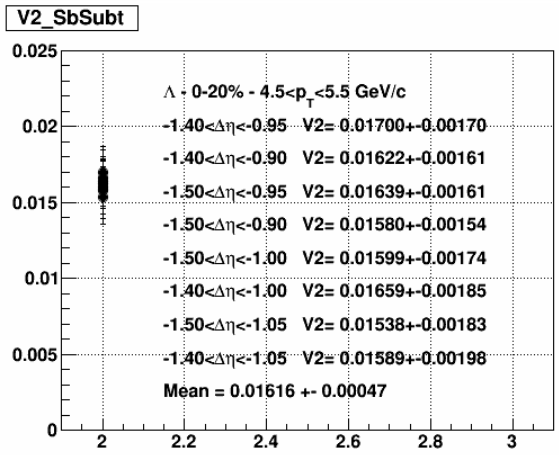

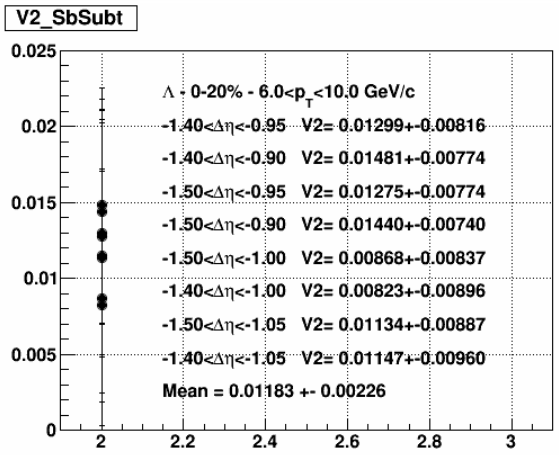

Λ-h: 20-40%

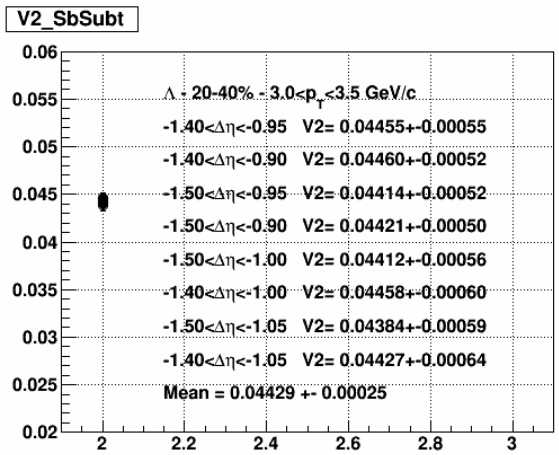

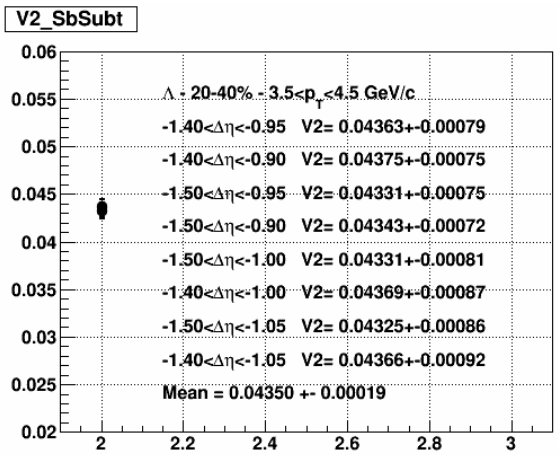

APPENDIX F (Continued)

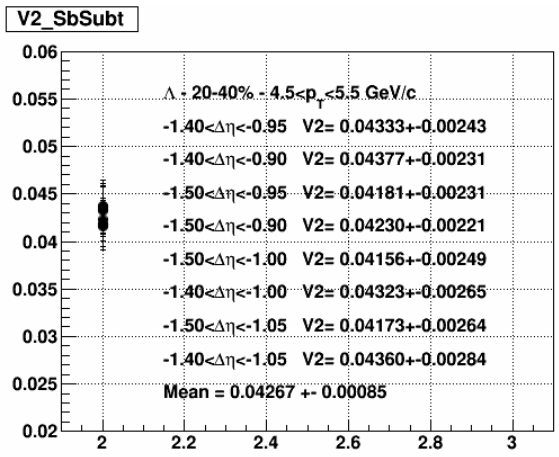

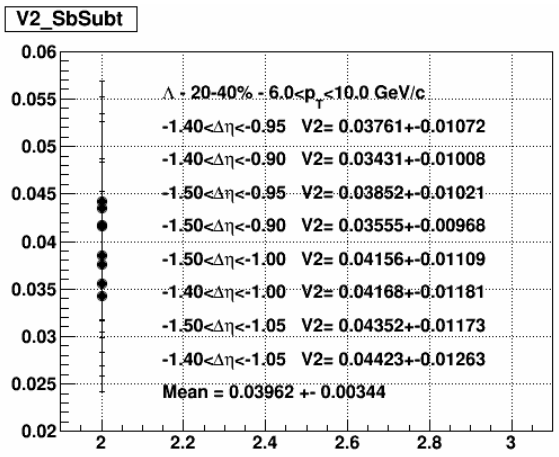

Λ-h: 40-60%

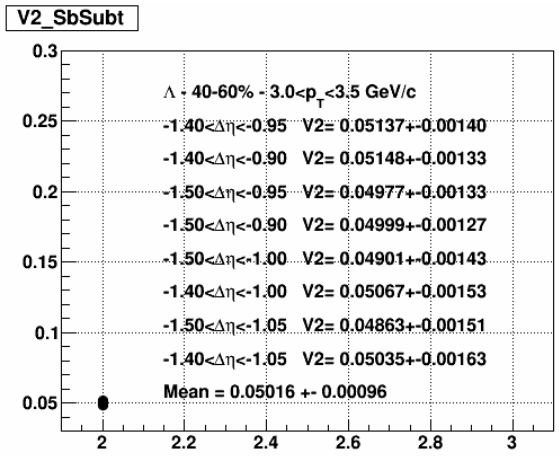

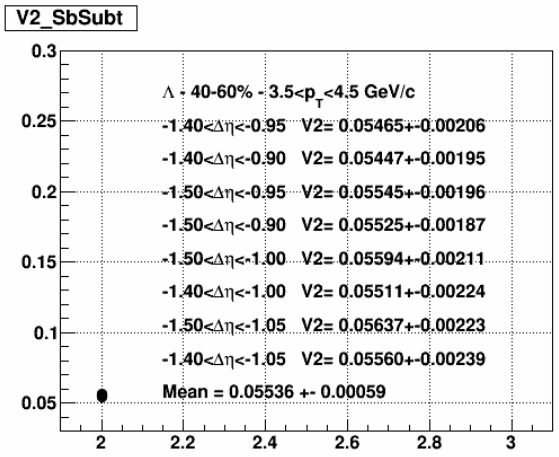

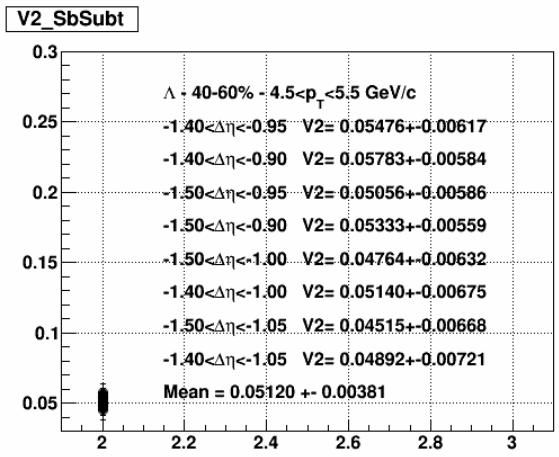

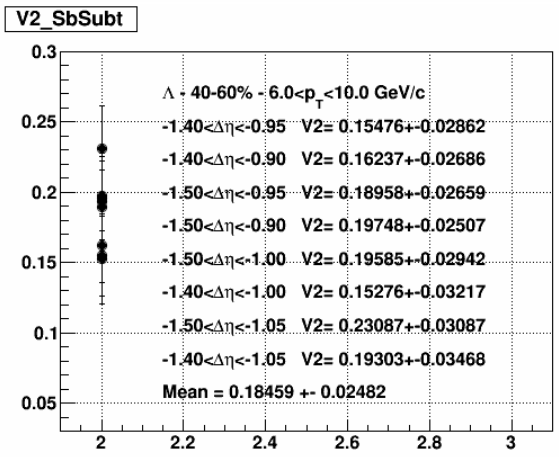

APPENDIX F (Continued)

Λ-h: 0-80%

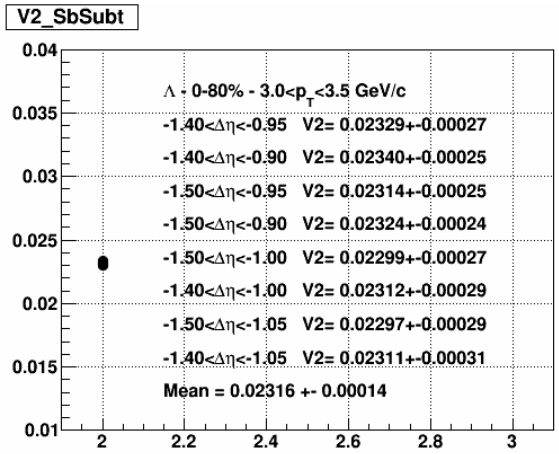

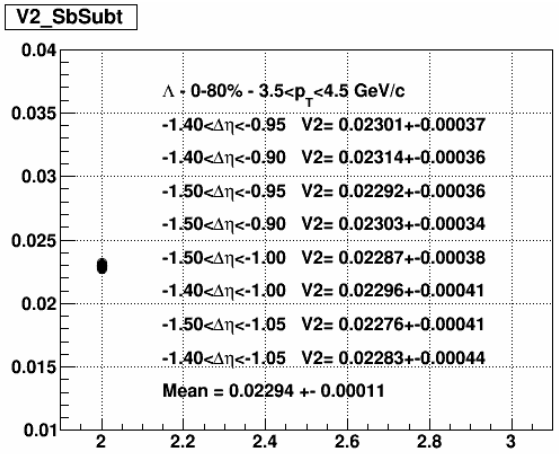

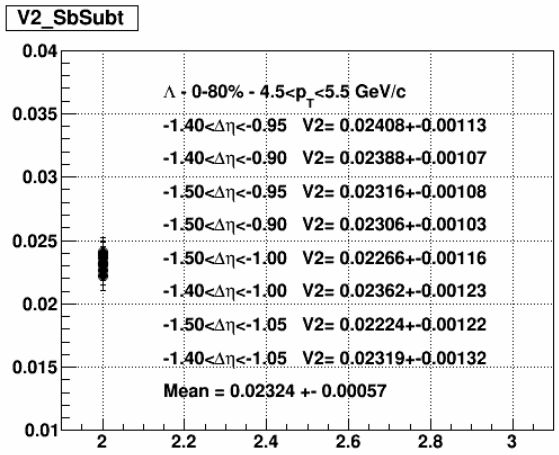

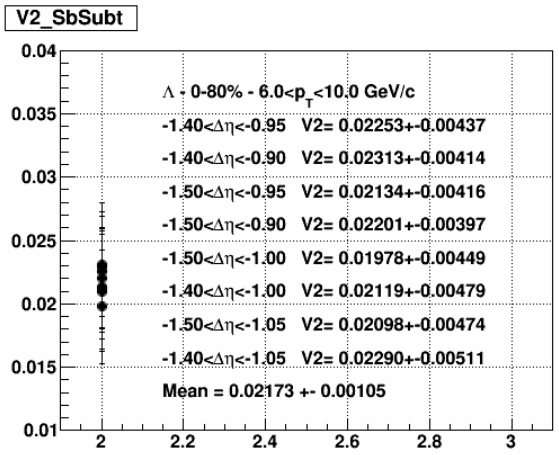

WORKS CITED

[1] C. Shen, The standard model of relativistic heavy ion collisions and electromagnetic tomography. Doctoral dissertaion, The Ohio State University, 2014.

[2] D. H. Perkins, Introduction to High Energy Physics, Addison-Wesley Publishing Company, Inc., 1987.

[3] R. Alkofer, J. Greensite, "Quark Confinement: The Hard Problem of Hadron Physics 21 Dec. 2006.," *arXiv:hep-ph/0610365v2,* 21 Dec. 2006.

[4] A. Deur, et. al., "The QCD Running Coupling," *arXiv:1604.08082v3 [hep-ph],* 15 Aug. 2016.

[5] D. J. Gross, "Twenty Five Years of Asymptotic Freedom," *arXiv:hep-th/9809060v1,* 10 Sept. 1998.

[6] M. Stephanov, "QCD phase diagram: an overview," *arXiv:hep-lat/0701002v1,* 31 Dec. 2006.

[7] P. Braun-Munzinger, K. Redlichb, J. Stachel, "Particle Production in Heavy Ion Collisions," *arXiv:nucl-th/0304013v1,* 3 April 2003.

[8] X. Wang, "QGP and Modified Jet Fragmentation," *arXiv:nucl-th/0510043v1,* 14 Oct. 2005.

[9] J. Kapusta, L McLerran, D. K. Srivastava, "Rates for dilepton production at RHIC and LHC between the J/si and gamma are big," *Physics Letters B 283,* pp. 145-150, 1992.

[10] M. Connors, C. Nattrass, et. al., "Review of Jet Measurements in Heavy Ion Collisions," *arXiv:1705.01974v1 [nucl-ex],* 4 May 2017.

[11] A. Palmese, G. Pagliara, A. Drago, O. Linnyk and W. Cassing, "Strangeness production in heavy-ion collisions," *arXiv:1506.04653v1 [hep-ph],* 15 June 2015.

[12] M. L. Miller, K. Reygers, et. al., "Glauber Modeling in High-Energy Nuclear Collisions," *Annu. Rev. Nucl. Part. Sci. 57,* pp. 57:205-43, 2007.

[13] I. Arsene, et. al., "Quark Gluon Plasma and Color Glass Condensate at RHIC? The perspective from the BRAHMS experiment," *arXiv:nucl-ex/0410020v1,* 14 Oct. 2004.

[14] G. M. Garcia, "Advances in Quark Gluon Plasma," *arXiv:1304.1452v1 [nucl-ex],* 4 Apr. 2013.

[15] M. Horner, Systematic Studies of Low- and Intermediate-pT Correlated Angular Distributions in Au+Au Collisions at √sNN= 200GeV from the STAR Experiment. Doctoral dissertation, University of Cape Town, 2007.

[16] C. Blume, and C. Markert, "Strange hadron production in heavy ion collisions from SPS to RHIC," *arXiv:1105.2798v2 [nucl-ex],* 19 Aug 2011.

[17] U. Heinz, and R. Snellings, "Collective Flow and Viscosity in Relativistic Heavy-ion Collisions," *arXiv:1301.2826v1 [nucl-th],* 13 Jan 2013.

[18] K. Kauder, Di-Hadron Angular Correlation Dependence on Leading Hadron Identity in Relativistic Heavy Ion Collisions. Doctoral dissertation, University of Illinois at Chicago, 2015.

[19] R. S. M. Miller, "Eccentricity fluctuations and its possible on elliptic flow measurements," *arXiv:nucl-ex/0312008v2,* 11 Dec. 2003.

[20] K. Adcox, et. al., "Formation of dense partonic matter in relativistic nucleon-nucleon collisions at RHIC," *Experimental evaluation by the PHENIX Collaboration. Nuclear Physics A 757,* p. 184–283, 2005.

[21] M. Gyulassy, "The QGP Discovered at RHIC," *arXiv:nucl-th/0403032v1,* 12 Mar 2004.

[22] E. Iancu, "Nonlinear Gluon Evolution in the Color Glass Condensate," *arXiv:hep-ph/0011241v1,* 20 Nov. 2000.

[23] J. Schaffner-Bielich, "What is so special about strangeness in hot matter?," *J. Phys. G: Nucl. Part. Phys. 30,* p. R245–R262, 2004.

[24] J. Adams, et. al., "Experimental and theoretical challenges in the search for the quark-gluon plasma: The STAR Collaboration's critical assessment of the evidence from RHIC collisions," *Nuclear Physics A 757,* pp. 102-183, 2005.

[25] K. Redlick, and A. Tounsi, "Strangeness Enhancement in Heavy Ion Collisions," *arXiv:hep-ph/0105201v1,* 19 May 2001.

[26] E. L. Bratkovskaya, M. Bleicher, M. Reiter, S. Soff, and H. Stöcker, "Strangeness dynamics and transverse pressure in relativistic nucleus-nucleus collisions," *Physical Review C 69, 054907,* 2004.

[27] R. Fires, V. Greco, P. Sorensen, "Coalescence Models for Hadron Formation from Quark-Gluon Plasma," *Annu. Rev. Nucl. Part. Sci. 58,* pp. 177-205, 2008.

[28] K. S. Lee, S. Bass. B Muller, and C. Nonaka, "Hadronization via recombination," *J. Phys. G: Nucl. Part. Phys. 36 064034,* 2009.

[29] B. I. Abelev, et. al., "Identified Baryon and Meson Distributions at Large Transverse Momenta from Au+Au Collisions at √sNN = 200 GeV," *Phys. Rev. Lett.,* vol. 97, no. 152301, Oct. 2006.

[30] R. J. Fires, B. Muller, and C. Nonaka, "Hadron production in heavy ion collisions: Fragmentation and recombination from a dense parton phase," *arXiv:nucl-th/0306027v3,* 12 June 2003.

[31] A. Adare, et. al., "Scaling Properties of Azimuthal Anisotropy in Au+Au and Cu+Cu Collisions at √sNN =200 GeV," *Phys. Rev. Lett., 98:162301,* Apr. 2007.

[32] X. Wang, "Effects of jet quenching on high pT hadron spectra in high-energy nuclear collisions," *arXiv:hep-ph/9804357v3,* 12 Aug 1998.

[33] A. Adare, "High-pT jet fragmentation in Au+Au collisions," *J. Phys. G: Nucl. Part. Phys. 35 104089,* 2008.

[34] ALICE Collaboration, "Suppression of charged particle production at large transverse momentum in central Pb–Pb collisions at √sNN = 2.76 TeV," *Physics Letters B 696,* pp. 30-39, 2011.

[35] X. Wang, "Why the observed jet quenching at RHIC is due to parton energy loss," *arXiv:nucl-th/0307036v2,* 1 Aug. 2003.

[36] I. Vitev, and M. Glyulassy, "High-pT Tomography of d+Au and Au+Au at SPS, RHIC, and LHC," *Phy. Rev. Lett., Volume 98, Number 25,* 16 Dec. 2002.

[37] J. Alessi, E. Beebe, S. Binello, et al., "PERFORMANCE OF THE NEW EBIS PREINJECTOR," in *In Proceedings of IPAC'11*, 2011.

[38] H. Hahn, E. Forsyth, H. Foelsche, et al., "The RHIC design overview," *Nuclear Instruments and Methods in Physics Research Section A. Volume 499, Issues 2–3,* 1 March 2003.

[39] M. Harrison, T. Ludlam, S. Ozaki, "RHIC Project Overview," *Nuclear Instruments and Methods in Physics Research Section A. Volume 499, Issues 2–3,* pp. 235-244, 1 March 2003.

[40] G.J. Marr, L. Ahrens, M. Bai, et al., "RHIC PERFORMANCE FOR FY2011 Au+Au HEAVY ION RUN," in *In Proceedings of IPAC'11*, 2011.

[41] W. Fischer, M. Blaskiewicz, A. Fedotov, H. Huang, C. Liu, G. Marr, M. Minty, V. Ranjbar, D. Raparia, "RHIC Collider Projections (FY 2017 – FY 2027)," [Online]. [Accessed 2 May 2017].

[42] F. Bergsma, C. Blyth, R. Brown, et al., "The STAR detector magnet subsystem," *Nuclear Instruments and Methods in Physics Research A. Volume 499,* p. 633–639, March 2003.

[43] F.S. Bieser, H.J. Crawford, J. Engelage, et al., "The STAR Trigger," *Nuclear Instruments and Methods in Physics Research A. Volume 499,* p. 766–777, March 2003.

[44] C. Adler, A. Denisov, E. Garcia, et al., "The RHIC zero degree calorimeters," *Nuclear Instruments and Methods in Physics Research Section A. Volume 499,* pp. 433-436, 2002.

[45] "Index of/protected/common http://www.star.bnl.gov/protected/common/," [Online]. [Accessed 2017].

[46] W. J. Llope, J. Zhou, T. Nussbaum, et al., "The STAR Vertex Position Detector," *arXiv:1403.6855 [physics.ins-det],* March 2014.

[47] L. Kotchenda, S. Kozlov, P. Kravtsov, et al., "STAR TPC Gas System," *Nuclear Instruments and Methods in Physics Research Section A. Volume 499,* pp. 703-712, 2003.

[48] M. Anderson, J. Berkovitz, W. Betts, et al., "The STAR time projection chamber: a unique tool for studying high multiplicity events at RHIC," *Nuclear Instruments and Methods in Physics Research Section A. Volume 499,* p. 659–678, March 2003.

[49] A. Rose, "STAR integrated tracker," *Computing in High Energy and Nuclear Physics,* March 2003.

[50] "http://www.star.bnl.gov/protected/bulkcorr/wanghui6/my_talks/Run11_200GeV_refMult.pdf," [Online]. [Accessed 2017].

[51] H. Long, Mid-rapidity Lambda and anti-Lambda Production in Au+Au Collisions at the Relativistic Heavy Ion Collider. Doctoral dissertation, University of California, 2002.

[52] P. Jacobs and D. Irmscher, "GSTAR: A Geant-based detector simulation chain for STAR. STAR Note # 235," 2 Feb. 1999. [Online]. [Accessed May 2017].

[53] Y. Pandit, Azimuthal Anisotropy in Heavy Ion Collisions. Doctoral disseration, Kent State University, 2012.

[54] ALICE Collaboration, "Anomalous evolution of the near-side jet peak shape in Pb-Pb collisios at √sNN = 2.76 TeV," *arXiv:1609.06643v1 [nucl-ex],* 21 Sep 2016.

[55] B. Abelev, L. Adamczyk, et. al., "Near-side azimuthal and pseudorapidity correlations using neutral strange baryons and mesons in d+Au, Cu+Cu, and Au+Au collisions at √sNN=200 GeV," *arXiv:1603.05477v4 [nucl-ex],* 1 Aug 2016.

[56] J. Adams, C. Adler, et. al., "Particle-type dependence of azimuthal anisotropy and nuclear modification of particle production in Au+Au collisions at √sNN = 200 GeV," *arXiv:nucl-ex/0306007v3,* 3 Feb 2004.

[57] J. Adams, M. M. Aggarwal, et. al., "Azimuthal anisotropy in Au+Au collisions at √sN N = 200 GeV," *PHYSICAL REVIEW,* vol. C 72, no. 014904, 2005.

[58] M. Gyulassy, I. Vitev and X. Wang, "High pT Azimuthal Asymmetry in Non-central A+A at RHIC," *arXiv:nucl-th/0012092v2,* 7 Mar 2001.

[59] H. Long, Mid-rapidity Lambda and Lambda-bar Production in Au+Au Collision at the Relativistic Heavy Ion Collider. PhD Dissertation., Los Angeles: University of California, 2002.

[60] D. d'Enterria, "QCD HARD SCATTERING RESULTS FROM PHENIX AT RHIC," *arXiv:nucl-ex/0401001v1,* 5 Jan 2004.